Design and performance of alternative cementitious materials using industrial solid wastes

CARBONATION AND CHEMICAL ACTIVATION

Yanjie Tang

Bouwstenen 399

Design and performance of alternative cementitious materials using industrial solid wastes

Carbonation and chemical activation

Yanjie Tang

This research is part of the project (T22019) in the framework of the Research Program of the Materials innovation institute (M2i) (www.m2i.nl) supported by the Dutch government.

CIP-DATA LIBRARY TECHNISCHE UNIVERSITEIT EINDHOVEN

Design and performance of alternative cementitious materials using industrial solid wastes - carbonation and chemical activation by Yanjie Tang

A catalogue record is available from the Eindhoven University of Technology Library

ISBN: 978-90-386-6192-6

Bouwstenen 399

NUR 955

Cover design: Yanjie Tang & Yufei Xiong

Ph.D. thesis, Eindhoven University of Technology, the Netherlands

Design and performance of alternative cementitious materials using industrial solid wastes

Carbonation and chemical activation

PROEFSCHRIFT

ter verkrijging van de graad van doctor aan de Technische Universiteit Eindhoven,
op gezag van de rector magnificus prof.dr. S.K. Lenaerts,
voor een commissie aangewezen door het College voor Promoties,
in het openbaar te verdedigen op woensdag 6 november 2024 om 13:30 uur

door

Yanjie Tang

geboren te Changzhou, China

Dit proefschrift is goedgekeurd door de promotoren en de samenstelling van de promotiecommissie is als volgt:

Voorzitter:	Prof. dr. ir. T.A.M. Salet
1e Promotor:	Prof. dr. ir. H.J.H. Brouwers
2e Promotor:	Prof. dr. S.R. van der Laan
Copromotor:	Asst. Prof. dr. K. Schollbach
Promotiecommissieleden:	Prof. dr. H. Justnes (Norwegian University of Science and Technology)
	Prof. dr. L.M. Ottosen (Technical University of Denmark)
	Prof. dr. W. Chen (Wuhan University of Technology)
	Prof. dr. ir. E.J.M. Hensen

Het onderzoek of ontwerp dat in dit proefschrift wordt beschreven is uitgevoerd in overeenstemming met de TU/e Gedragscode Wetenschapsbeoefening.

Preface

With the completion of this thesis, a significant milestone is within reach, and I am profoundly grateful to all those who have supported and guided me throughout Yanjie's PhD journey.

Firstly, I would like to express my sincere appreciation to my promoter and supervisor, Prof. H.J.H. (Jos) Brouwers. Four years ago, you provided me with the invaluable opportunity to join this group. Throughout my PhD study, you ensured I had all the necessary resources for my research. Your invaluable guidance, unwavering support, and continuous encouragement have been fundamental to my progress. Your insightful suggestions consistently offered new perspectives, greatly enhancing both my study and this thesis. Your recommendation enabled me to collaborate with experts from various industrial companies, from whom I have learned and benefited immensely. This experience has enriched my research and broadened my professional network, for which I am deeply grateful.

I would also like to express my heartfelt thanks to my daily supervisor, Dr. Katrin Schollbach, and my second promotor, Prof. Sieger van der Laan. Your professional knowledge and suggestions have been crucial in the completion of my PhD study and thesis. Katrin, you significantly contributed to the writing and revising of my scientific papers. I am incredibly fortunate to have had you as my daily supervisor. You provided me with enough freedom and trust to complete my research over these four years. Sieger, I have thoroughly enjoyed our conversations about life and work, both current and past. Your enthusiasm and passion for science are truly impressive, and I have learned a great deal from you.

My great gratitude goes to my PhD supervisor in Wuhan University of Technology, Prof. Wei Chen, who is also my committee member. Your insights have always sparked new perspectives in my work and life. Your work ethic and life philosophy have been a profound source of inspiration, motivating me to strive for excellence both academically and personally. Your support and wisdom have been invaluable throughout this journey.

I would like to extend my sincere appreciation to my promotion committee: Prof. Dr. Harald Justnes (Norwegian University of Science and Technology), Prof. Dr. Lisbeth M. Ottosen (Technical University of Denmark), and Prof. Dr. Ir. Emiel J.M. Hensen (Eindhoven University of Technology) for their precious time in reviewing my thesis and providing valuable comments and suggestions to improve its quality.

I am sincerely thankful to Prof. Zhonghe Shui, Prof. Jianfeng Fan, Prof. Qiu Li, Prof. Quantao Liu, Prof. Wenbin Hu, Prof. Shi Tian, Dr. Peiliang Shen, as well as my tutor Guofang Shen, Xiong Zhou, for your support and suggestions during my bachelor and PhD studies.

I am also grateful to my colleagues and collaborators, whose contributions were instrumental in the completion of this thesis. Being a member of the Building Materials group, an exceptional international team, fills me with both pride and gratitude. Prof. Qingliang Yu, your dedication to academic research and hardworking nature serves as constant sources of inspiration for me. I cherish the insightful conversations we have had about various aspects of life and work. Dr. Gauvin Florent, I appreciate your assistance and technical support regarding SEM tests, and I enjoy playing tennis with you. I extend my thanks to all the technicians, especially Ing. A.C.A. Delsing and Mr. H.L.W. Smulders, for their assistance and technical support throughout my research. To my wonderful colleagues and friends, Alex, Anna, Beatrice, Bo, Ceren, Charles, Daoru, Fan, Felix, Gang, Helong, Hossein, Iris, Jawad, Jia, Jiale, Jinyang, Jonathan, Kinga, Leila, Marc, Marina, Naomi, Natalyia, Pei, Peipeng, Quan, Ricardo, Samantha, Samuel, Shaohua, Shashank, Tao, Winnie, Xu, Xuan, Yan, Yangyueye, Yanshuo, Yilu, Yuxuan, Zhengyao, Zhihan, Zixiao, Zixing. I am lucky to have shared this time with you over the past four years. Mengyan, Tingting, Luyang, Lili, Peng, Xiaoxiao, Guang, Yutian, Jian, Feiyu, Yanan, Zicheng, Jian and Liang, I treasure the memories we have created together. My appreciation also goes to Huiqing, Jingrui & Jin, Haibo, Xinglong, Pengrong, Dongyu, Yang, and Shaojuan. I wish you all the best in the future and a wonderful life.

I also extend my gratitude to my friends in China: Bo, Luyao, Kefeng, Xueying, Xiang, Jing, Hao, Zonggang, and Haosen, for your support and help; Wenjie, Jie, Lu, and Qian, friends since high school. I am happy to have you, and I am sure these friendships will last a lifetime.

Finally, and most importantly, I give my thanks from the bottom of my heart to my Mom (Xifang) and Dad (Zhiqing). Thank you for your support and encouragement in every choice and decision I have made. My thanks also go to my sister (Yingya) and her husband (Rui) for taking care of our parents during these years, and my lovely niece (Tata) for the happiness you bring to our family. Finally, I would like to thank my wife, Yufei. Thank you for your company and support. Yufei, the world is big, and I look forward to exploring it further with you.

Yanjie Tang

Eindhoven, August 2024

Summary

Intending to reduce the environmental impact of the cement and concrete industry, including reduction of CO_2 emissions as well as the consumption of substantial volumes of raw materials and energy, alternative clinker making, partial replacement by artificial aggregates and supplementary cementitious materials (SCMs), and fully replacement by cement-free binder, can be the effective strategies. This thesis studies the structure of calcium silicate hydrate (C-S-H) with magnesium which may come from low grade limestone, explores the use of concrete waste as artificial aggregates or new supplementary cementitious materials (SCMs) in blended Portland cement via carbonation and develops BOF slag as a cement-free binder through chemical activation.

The first section of the thesis examines the structure of calcium silicate hydrate (C-S-H), the main binding phase produced during Portland cement hydration. The alternative clinker originated from low grade limestone may introduce significant amounts of magnesium. Investigating the structural evolution of C-S-H in the presence of magnesium provides fundamental insights into the hydration of new magnesium-rich cement. Magnesium chloride hexahydrate, calcium oxide, and silica fume are used to prepare Mg^{2+} modified C-S-H. Results indicate that the mineralogical composition of synthesized C-S-H is closely related to the initial concentration of Mg^{2+}. Large additions of Mg^{2+} lead to C-S-H instability, while magnesium can be incorporated into the C-S-H structure. A heterogeneous distribution of elemental Mg in the C-S-H phase at the nanoscale is observed.

The second section focuses on the application of waste concrete fines via carbonation. The primary components of waste concrete powder are hydrated cement paste (HCP). This study used laboratory-made cement paste instead of real demolished concrete to obtain HCP, allowing better control over the chemical composition of the waste concrete fines by eliminating the variability present in materials recovered from demolished structures. By combining cold-bonding technology with carbonation curing, artificial lightweight aggregates (LWAs) can be produced from HCP with low energy consumption. Both CEM I 52.5 R and CEM III/A 52.5 N were chosen as starting materials because the hydration products of CEM I and CEM III differ, especially in the amount of portlandite. A comparative study was conducted to determine the effects of portlandite on aggregate production under carbonation curing. The results show that the optimal carbonation periods can be determined based on varying amounts of portlandite. HCP I-type aggregates achieved 3.14 MPa strength after 7 days of carbonation and contained 35.60 wt.% calcium carbonates. The remaining 13.95 wt.% portlandite indicated significant potential for increasing strength and CO_2 capture capacity through optimized carbonation curing. Conversely, HCP III-type aggregates reached 2.97 MPa after 1 day of carbonation, with further carbonation decomposing C-S-H and leading to the formation of calcite and

amorphous silica gel, significantly increasing the specific surface area (from 10.69 to 42.96 m^2/g). These results provide a low carbon footprint and sustainable method for HCP powder application and LWAs production. In addition to preparing aggregates, using waste concrete fines as ingredients in building materials is also explored. To investigate the effects of semi-dry carbonation on recycled concrete fines containing supplementary cementitious materials (SCMs) in new concrete production, recycled blended cement paste powders (RBCPs) containing granulated blast furnace slag (GBS), fly ash (FA), or recycled glass powder (RGP) were prepared in the lab. The performance of mortars produced from carbonated recycled blended cement paste powder (C-RBCPs) and RBCP-blended cement is evaluated. C-RBCPs exhibit superior performance in workability and mechanical properties compared to carbonated OPC powder. The RBCPs show a lower carbonation degree (less than 53.4%) and CO_2 uptake than neat Portland cement samples due to the lower availability of Ca in the blended cement after incorporating GBS, FA, and RGP. Calcite, aragonite, and vaterite, the main carbonation products, are observed in C-RBCPs. The type of SCMs significantly influences the polymorphs of calcium carbonate and the reactivity of C-RBCPs in blended cement mortars.

The third section moves towards developing alternative binders using the by-product BOF slag via chemical activation. This includes investigating and optimizing the addition of phosphates to the BOF slag system, understanding the mechanisms by which phosphates affect BOF slag hydration and applying phosphate-activated steel slag to control vanadium leaching. To prepare a Portland cement-free BOF slag binder, the activation of C_2S and $C_2(A,F)$ is emphasized because BOF slag is rich in these phases (>50 wt.%) and the RO phase is quite inert. Phosphates interact strongly with iron, aluminum, and calcium through ligand exchange, precipitation, and coprecipitation, facilitating phosphate fixation, which are key constituents of BOF slag. Therefore, phosphate can be a promising activator to synergistically activate C_2S and $C_2(A,F)$. This study shows that the addition of phosphate promotes the dissolution and hydration of C_2S and $C_2(A,F)$, enhancing mechanical properties. The main hydration products include pyroaurite, hydrotalcite, hydrogarnet, C-S-H gel, and hydroxyapatite. The high reaction degree with phosphate addition has been confirmed by comprehensive analytic methods. However, the hydration kinetics of BOF slag pastes strongly depend on the initial pH of the added phosphates. Low pH (pH<9) retards hydration with an equal amount of phosphate, prolonging the induction period to 23 days. Conversely, higher pH (pH>12) accelerates early-stage hydration and enhances the overall hydration extent of C_2S and $C_2(A,F)$, thereby producing more hydration products and exhibiting better mechanical performance. The use of BOF slag as a building material is restricted by its leaching performance. The leaching behavior, which is pH-controlled, becomes more severe after weathering, such as when the slag reacts with water and CO_2. The leaching behavior of phosphate activated BOF slag pastes is evaluated before and after carbonation. Results show that phosphate can maintain a stable high pH during carbonation. The noticeable pH decreases in reference samples (BOF slag mixed with water) from 12.6 to 11.4 contrasts with the slight drop in pH from 13.2 to 13.0 in phosphate-containing samples.

High pH can lower or inhibit the overall carbonation of hydration products like portlandite, the dissolution of which is a key step in the carbonation of hydration products. The leaching of phosphate activated BOF slag pastes after carbonation meets legislative requirements.

Contents

CHAPTER 1

1. Introduction

1.1. Background and motivation

Concrete is widely used in significant volumes because of its unique features of low cost, abundance, strength, robustness, and durability etc. For these reasons it has and will continue to be the foundation of society. Growth in societal need for cement and concrete is expected due to population growth and urbanization. According to a forecast by the Global Cement and Concrete Association (GCCA), the global demand for concrete is expected to increase from the current 14.0 billion m^3 to approximately 20 billion m^3 by 2050 [1]. This increase in cement and concrete demand is projected to result in 3.8 Gt of CO_2 emissions as well as the consumption of substantial volumes of raw materials and energy, assuming current practices remain unchanged [1].

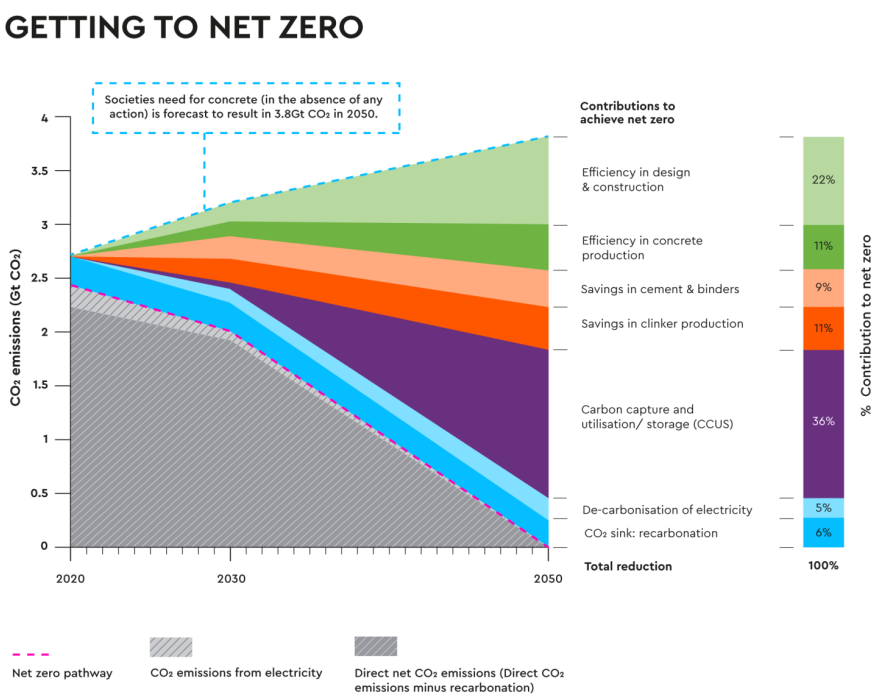

Fig. 1.1 *The net zero pathway by GCCA [1].*

Clinker, the primary constituent of cement, is produced by heating a mix of limestone and other minerals in a kiln at approximately 1450 °C, transforming them into complex reactive minerals. This process requires a lot of raw materials and energy, and generates significant CO_2 emissions, primarily from two sources: the heated limestone itself (approximately 60%) and the combustion of fuels used in the cement kiln and other plant processes (approximately 40%) [1].

To reduce the environmental impact across the entire life cycle of cement and concrete, various strategies are being pursued, as shown in ***Fig. 1.1***. Given that clinker production is a major source of CO_2 emissions, energy use and natural materials consumption, the cement industry is increasingly focusing on minimizing and optimizing clinker use. Effective strategies to reduce the environmental impact include alternative clinker production using low-grade limestone, partial replacement of clinker with SCMs, and the full replacement of clinker with cement-free binders, which represents a promising avenue for sustainable construction. Additionally, the replacement of natural aggregates with artificial aggregates originated from industrial wastes can also minimize the environmental impact. It is important to note that different industrial wastes have varying chemical and mineralogical compositions, and therefore, different disposal and valorization strategies must be selectively applied to maximize their potential as sustainable construction materials.

Generally, this thesis investigates several key areas: it examines the structure of calcium silicate hydrate (C-S-H) when modified by magnesium, which may be introduced through the use of low-grade limestone for alternative clinker production; it explores the valorization of concrete waste by using it as artificial aggregates or new SCMs in blended Portland cement through carbonation; and more radically, it develops basic oxygen furnace (BOF) slag as a cement-free binder through chemical activation. The detailed background and motivation of using different industrial solid wastes are presented below.

- ***Alternative clinker production using low-grade limestone***

High-grade limestone, essential for traditional cement production, is not abundant in all regions. As a result, alternative carbonate sources with higher magnesium content have become the focus of ongoing research [2]. Additionally, the production of MgO requires a lower temperature compared to the calcination of $CaCO_3$ in Portland cement production. This leads to significant energy savings and reduced CO_2 emissions, positioning magnesium-based cement as a promising eco-friendly alternative [3]. Often referred to as "carbon-neutral" cement, magnesium-based cement has the potential to absorb nearly as much CO_2 during its service life as is emitted during its production [4].

However, direct replacement of CaO with MgO in Portland cement production is not feasible due to significant differences in their chemical behavior and phase formation, as illustrated in ***Fig. 1.2***. The respective (MgO, CaO)-SiO_2-Al_2O_3 ternary phase diagrams reveal some magnesium silicate phases forming at elevated temperatures. However, they do not exhibit the hydraulic properties characteristic of the calcium-rich phases in the

CaO-SiO_2-Al_2O_3 system [3,5]. Key hydraulic phases in Portland cement, such as Ca_2SiO_4, Ca_3SiO_5, and $Ca_3Al_2O_6$, are not replicated in magnesium-dominant regions, underscoring the challenges of directly substituting CaO with MgO [3,5].

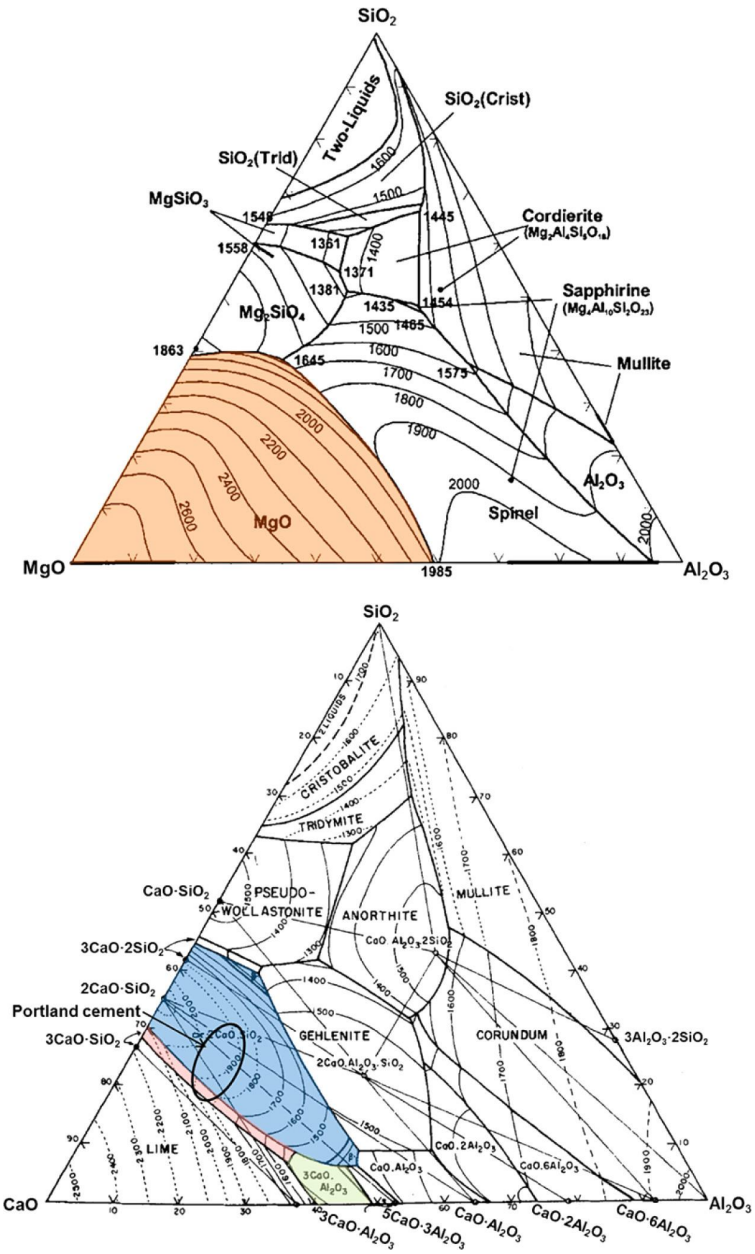

Fig. 1.2 Ternary phase diagrams in units of weight percent ((MgO, CaO)- SiO_2-Al_2O_3 system) [3].

Given these challenges, it is clear that directly substituting CaO with MgO in clinker production will not yield the desired hydraulic properties. As a result, the focus has shifted towards understanding the effect of magnesium on the structure and chemical composition of calcium silicate hydrate (C-S-H), the primary hydration product of Portland cement. C-S-H plays a pivotal role in the material's binding capacity, and any modifications induced by the presence of magnesium ions warrant intensive investigation.

- ***Valorization of waste concrete powder***

Besides, one common strategy to optimize clinker use and reduce CO_2 emissions is to incorporate supplementary cementitious materials (SCMs). Currently, widely used by-products such as fly ash (FA) and ground granulated blast furnace slag (GBS) are highly valued in the market due to their excellent properties and limited availability. To further enhance this approach, there is potential in utilizing currently unused by-products.

Waste concrete powder can be the alternative SCMs for clinker replacement instead of commonly used FA and GBS. Cities are facing the renewal of buildings, roads, and infrastructure due to urbanization and development, leading to the demolition of many old concrete structures and generating over 4 billion m^3 of solid waste annually [6]. Developed recycling technologies can effectively extract steel, bricks, and natural aggregates for reuse in new concrete structures, and thus leave 10-20% of fine concrete waste powder [7,8]. The main component in waste powder is hydrated cement paste (HCP) but the exact composition can depend on the crushing and heating methods used to recycle concrete [9–12]. However, the presence of HCP in recycled concrete significantly affects the performance of recycled concrete materials [13]. The porous structure of cement hydration products often results in poor workability of fresh recycled concrete mixtures [14]. Furthermore, C-(A)-S-H, calcium hydroxide, and other hydrates in concrete wastes exhibit very limited reactivity, negatively impacting the microstructure and mechanical performance of new concrete [15,16]. These properties of hydrated cement waste strictly limit the high-end utilization of recycled concrete wastes, resulting in a low recycling rate of less than 40% in many countries [17].

In addition to neat Portland cement, blended cement is produced by mixing supplementary cementitious materials (SCMs) with ordinary Portland cement clinker, typically with a replacement ratio of 30-60% by mass [18,19]. These blended cements often exhibit superior performance compared to traditional cement and concrete [20–22]. For instance, granulated blast furnace slag (GBS) blended cement concrete demonstrates excellent resistance to ion penetration, extending the service life of buildings in coastal or saline environments [23,24]. The use of coal fly ash (FA) in blended cement concrete effectively reduces the heat release during hydration, helping to prevent the formation of cracks due to internal temperature loads [10,25]. Additionally, recycled glass powder (RGP) has been extensively studied as a new SCM candidate due to its ability to modify the microstructure of cement composites [26,27].

The application of these blended cements has gained a mature market presence because it effectively reduces the CO_2 emissions associated with buildings and construction. Consequently, the valorization of concrete wastes should consider the influence of these various SCMs to maximize environmental and performance benefits [28].

- ***High-end application of BOF slag***

Moreover, the development of cement (clinker)-free binders based on industrial by-products offers a promising alternative to conventional cement. This strategy not only reduces cement usage but also alleviates land pressure from temporary storage and adds value to industrial waste.

Steel slags, by-products of steel manufacturing, are produced in substantial quantities annually and should be considered a green resource. Modern steels can be broadly categorized into four types: carbon, alloy, stainless, and tool steels. Steel is produced either in a basic oxygen furnace (BOF) or an electric arc furnace (EAF) and then refined in a ladle furnace (LF) to achieve its compositional specifications [29–31]. During steel manufacturing, large quantities of steel slag are produced, amounting to about 15-20% of the total mass of steel output (***Fig. 1.3***). The compositions of steel slags are highly variable and are generally classified into BOF slag, EAF slag, and LF slag [29–31]. Annual global steel production is currently approximately 1,732 million tons and is projected to increase to around 2,000 million tons by the next decade [30]. This increase is expected to generate approximately 237-275 million tons of steel slag per year [30]. About 70% of total steel slag production comes from BOF slag, generated from refining molten pig iron into crude steel in the basic oxygen furnace process, also known as the Linz-Donawitz steelmaking process [29,32–35]. The valorization of this substantial amount of BOF slag is both essential and critical.

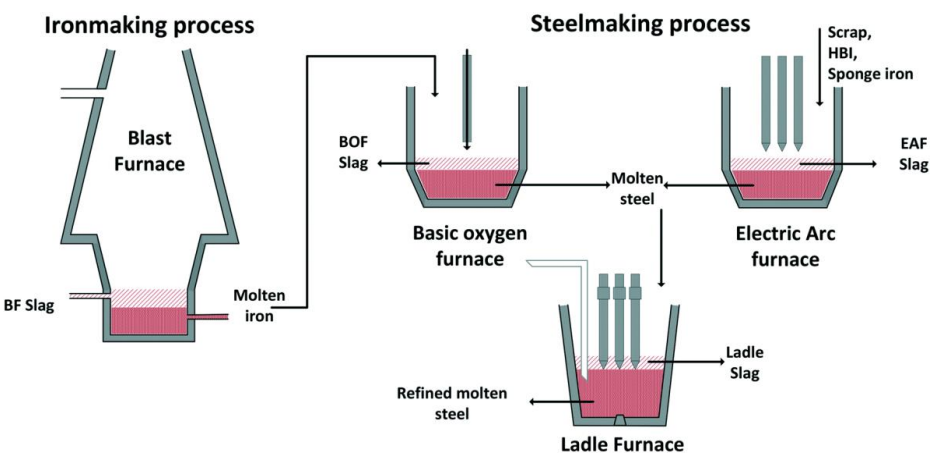

Fig. 1.3 *Generation of various slags from the steel industry* [30].

The annual production of BOF slag in Europe is approximately 10 million tons [34,35]. However, a significant portion of BOF slag, around 27.6% of the total mass, is currently

landfilled or temporarily stored [35], leading to environmental pollution and landscape degradation [36,37]. Moreover, BOF slag is predominantly utilized for low-end applications, such as road construction aggregates and backfill materials [35,38], which do not fully exploit its potential. Utilizing BOF slag as a binder constituent offers a promising alternative to conventional cement, promoting both valorization and sustainability.

BOF slag typically exhibits high concentrations of CaO and Fe_2O_3 (30-50 wt.%), with lesser amounts of SiO_2 and MgO (10-20 wt.%), alongside minor oxides such as MnO, Al_2O_3, P_2O_5, and TiO_2 (2-5 wt.%) [32]. Its mineral composition includes C_2S, $C_2(A,F)$, and an RO phase (a solid solution of CaO–FeO–MgO–MnO, crystallized in a wuestite structure), with negligible C_3S content [31,39]. This mineral assemblage makes BOF slag a promising substitute for Portland cement in cementitious applications. However, its hydraulic activity is limited due to impurities in C_2S and the elevated iron content in $C_2(A,F)$ [40–42]. Additionally, contamination with heavy metals, particularly vanadium and chromium, poses challenges to its use as a binder constituent [29,36].

Extensive studies on BOF slag blended cements with replacement levels below 30 wt.% indicate that, compared to Portland cement, the addition of BOF slag results in a prolonged induction period and delayed setting time [29,40–43]. This delay is due to the slowed depletion of gypsum, reduced formation of ettringite, and significant inhibition of the precipitation of portlandite and calcium silicate hydrate (C–S–H) gel [44,45]. Consequently, the amount of BOF slag used as supplementary cementitious materials (SCMs) in Portland cement must be strictly limited to achieve performance comparable to that of standard cement. Therefore, the development of a cement-free BOF slag binder warrants more attention than its use as an SCM like ground granulated blast furnace slag (GBS) or fly ash (FA) in conventional cement.

1.2. Scopes and objectives

Intending to reduce the environmental impact of the cement and concrete industry, this thesis has three primary objectives. First, it focuses on understanding the structure of calcium silicate hydrate (C-S-H) in the presence of Mg. Second, it explores the application of concrete waste as artificial aggregates and new supplementary cementitious materials (SCMs). Finally, it proposes the design of new alternative binders using basic oxygen furnace (BOF) slag. These objectives are addressed through the following topics:

- ***Investigation into the effects of magnesium on calcium silicate hydrate (C-S-H) structure***

Calcium silicate hydrate (C-S-H) gel is the primary binding phase formed during Portland cement hydration, characterized by its poorly crystalline structure and variable composition [46–50]. The presence of various ions can modify the structure and chemical composition of C-S-H phases during hydration [51–55]. The alternative clinker originated from low grade limestone may introduce significant amounts of magnesium. Investigating

the structural evolution of C-S-H in the presence of magnesium provides fundamental insights into the hydration of new magnesium-based cement. This study explores the CaO-SiO_2-H_2O system containing Mg^{2+} by mixing calcium oxide, silica fume, and magnesium chloride solution. The structural features of Mg^{2+} modified C-S-H and the potential incorporation of Mg into the C-S-H structure were examined.

- ***Production of artificial LWAs and new SCMs***

Recent years have seen the introduction of carbonation treatment in the recycling of concrete wastes, resulting in notable improvements in reducing water demand, densifying microstructure, and enhancing mechanical behavior [56,57]. Using laboratory-made cement pastes instead of actual demolished concrete to obtain hydrated cement paste (HCP) powder allows for better control over the chemical composition of the waste powder, eliminating the variability associated with recovered demolished materials. The valorization of HCP was divided into two parts, including production of lightweight aggregates (LWAs) as the alternative aggregates for concrete and development of new SCMs to replace cement.

The first part aims to produce lightweight aggregates (LWAs) by combining cold-bonding technology and carbonation treatment. Researchers typically focus on HCP powder from CEM I, which contains few supplementary cementitious materials (SCMs), although CEM III is also widely used and deserves more attention in LWA production. Consequently, both CEM I 52.5 R and CEM III/A 52.5 N were selected as starting materials. A comparative study was conducted to evaluate the properties of artificial LWAs derived from HCP I and HCP III under carbonation curing. Additionally, silica fume was added to produce LWAs under normal curing to assess its potential pozzolanic properties, given the high residual portlandite content. The study investigated the mechanical performance and microstructural evolution of artificial LWAs.

The second part aims to produce alternative SCMs from different hydrated blended cements with GBS, FA, and RGP. The carbonation products, reactivity, and leaching properties of blended cements and neat cement after carbonation treatment were comprehensively compared. Furthermore, as new SCMs, carbonated blended cement and neat cement were examined for their effects on hydration kinetics, hydration products, mechanical performance, and sustainability efficiency. These aspects were thoroughly investigated and discussed.

- ***Development of cement free binder***

In this part, an alternative BOF binder is developed to fully replace Portland cement. Unlike hydrated cement pastes, BOF slag has hydraulic properties due to the significant presence of brownmillerite and belite. To harness this potential, appropriate additives are needed to activate brownmillerite and belite, whose reactivity is otherwise limited by impurities and high iron content [40–42]. Phosphates are known to interact strongly with iron, aluminum, and calcium through ligand exchange, precipitation, and coprecipitation,

facilitating phosphate fixation [58,59]. Thus, phosphates were selected as additives to enhance the hydration of BOF slag to activate both belite and brownmillerite.

The initial evaluation focuses on the feasibility of using monopotassium phosphates (MKP) as a novel activator for cement-free BOF slag binding materials. This involved investigating the microstructure and strength development of BOF slag pastes with varying MKP dosages.

BOF slag contains heavy metals, including vanadium (V), chromium (Cr), and molybdenum (Mo), whose leachability affects the industrial applicability of slag-based building products. Although heavy metal ions are generally stable in the BOF slag matrix, carbonation can reactivate their leaching. Notably, the leaching of heavy metals, particularly vanadium, can increase significantly, potentially exceeding legal thresholds in the Dutch one-batch leaching test. Consequently, further work focuses on the leaching behavior of dipotassium phosphate (DKP)-activated BOF slag before and after carbonation.

Additionally, differences in the hydration behavior of BOF slag with acidic versus alkaline phosphates were observed. Building on previous research, reactions between BOF slag and phosphate are studied across a pH range of 4.2 to 12.8, considering factors such as reaction extent, product identification, heat release, and pore structure.

1.3. Outline of the thesis

The research framework is illustrated in ***Fig. 1.4***, and the contents of each chapter are summarized as follows:

Chapter 2 explores the impact of varying Mg^{2+} concentrations on the formation of C-S-H phases through simplified synthesis conducted at elevated temperatures and ambient pressure. This chapter characterizes both solid and liquid phase of C-S-H synthesis to investigate the structural modifications induced by Mg^{2+} and magnitude of incorporation into the C-S-H structure.

Chapter 3 examines the mechanisms behind the mechanical performance and microstructural development of artificial aggregates produced from hydrated cement paste (HCP) powder. This chapter presents a comparative study on the effects of portlandite content in CEM I and CEM III on aggregate production under carbonation curing and evaluates its potential pozzolanic properties with the addition of silica fume (SF). The study investigates the mechanical properties, reaction products, and microstructure using techniques such as X-ray diffraction (XRD) and Fourier-transform infrared spectroscopy (FTIR) to understand the re-cementation effects of carbonation and pozzolanic reactions inside these lightweight aggregates (LWAs).

Chapter 4 assesses the role of mixed ground granulated blast furnace slag (GBS), coal fly ash (FA), and recycled glass powder (RGP) in the recyclability of hydrated blended cement composites compared to neat hydrated Portland cement. This chapter utilizes semi-dry

carbonation to recycle and apply hydrated cement with or without GBS, FA, and RGP as new supplementary cementitious materials (SCMs). It analyzes hydration kinetics, hydration products, mechanical performance, and sustainability efficiency of mortars produced with these new SCMs.

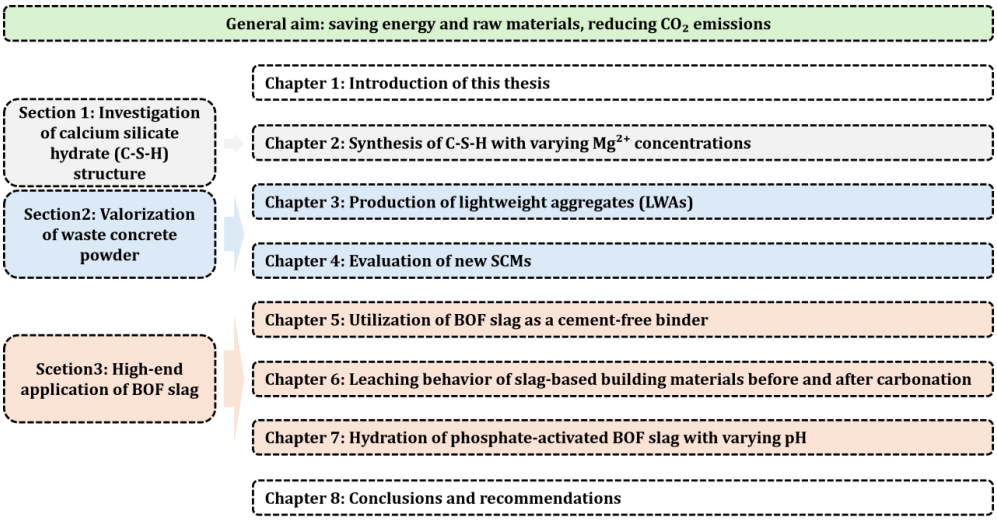

Fig. 1.4 *Outline of this thesis.*

Chapter 5 introduces a novel approach to utilize BOF slag as a cement-free binder in combination with monopotassium phosphate (MKP). This chapter evaluates the activation of BOF slag with low MKP additions at ambient temperature. It employs a comprehensive multi-technique approach, including QXRD, SEM/EDX, and phase mapping with PARC software, to analyze the microstructure and strength development of BOF slag pastes with varying MKP dosages below 10 wt.%.

Chapter 6 addresses the leaching of heavy metals, including vanadium (V), chromium (Cr), and molybdenum (Mo), in BOF slag before and after accelerated carbonation. The chapter examines the carbonation behaviors of both reference and dipotassium phosphate (DKP)-activated BOF slag samples, focusing on differences in mineralogical composition, pH, carbonation depth, and porosity.

Chapter 7 builds on previous research by studying the reactions between BOF slag and phosphates across a pH range of 4.2 to 12.8, highlighting the critical role of pH in phosphate additives. A comprehensive multi-technique approach is employed to elucidate the effects of acidic and alkaline phosphates on hydration kinetics, microstructure, and strength development, including early-stage dissolution, reaction extent, product identification, heat release, and pore structure.

Chapter 8 presents the overall conclusions of the research and provides recommendations for future studies.

CHAPTER 2

2. Effects of soluble magnesium on the structure of calcium silicate hydrate

This chapter aims to investigate the impact of soluble magnesium on the structure of C-S-H formed at elevated temperature. Magnesium chloride hexahydrate, calcium oxide and silica fume were used in the preparation of Mg^{2+} modified C-S-H. The obtained solid and liquid phases from C-S-H synthesis were characterized with XRD, FTIR, TGA, etc. to investigate the structural features of Mg^{2+} modified C-S-H. Results show that the mineralogical compositions of the synthesized C-S-H are highly related to the initial concentration of Mg^{2+}. Large additions of Mg^{2+} lead to the instability of C-S-H. Meanwhile, magnesium can be incorporated into the structure of C-S-H. A heterogenous distribution of elemental Mg in C-S-H phase on nanoscale is observed.

This chapter is reproduced from: Y. Tang, K. Schollbach, H.J.H. Brouwers, W. Chen, Effects of soluble magnesium on the structure of calcium silicate hydrate, Constr. Build. Mater. 302 (2021) 124402. https://doi.org/10.1016/j.conbuildmat.2021.124402.

2.1. Introduction

Calcium silicate hydrate (C-S-H) gel is the main binding phase produced by Portland cement hydration, which has a poorly crystalline structure with a variable composition [46–50]. With the presence of minor ions, the structure and chemical composition of C-S-H phases can be modified during the hydration of Portland cement. The impact of Cl^-, SO_4^{2-}, Na^+, etc. ions on the structure of C-S-H phases has been discussed intensively in recent literature [51–55].

Magnesium is also a common element from dolomite as well as seawater and groundwater, and researchers have paid much attention to the effects of magnesium oxide (MgO) on C-S-H phases. It has been reported that addition of MgO has little effect on the structure of C-S-H gels synthesized with low CaO/SiO_2 molar ratio under hydrothermal conditions [60]. The formation of pure magnesium silicate hydrates (M-S-H) is only detected for the lowest CaO/SiO_2 molar ratio (0.66) while magnesium ions are suggested to be incorporated into four-fold coordinated sites of C-S-H gel with the highest CaO/SiO_2 molar ratio (1.8) [60]. The magnesium ions might be incorporated into the octahedral sites in the interlayer space of the dreierketten pattern or the gap of the Q^{2b} silicon tetrahedron as tetrahedral magnesium, which is largely determined by the CaO/SiO_2 ratio [61]. In addition, Tobermorite bears great resemblance to poorly-crystalline C-S-H phases originating from Portland cement hydration, providing a crystalline model structure for the investigation of interactions between C-S-H phases and other ions [62,63]. Mg-Tobermorite ($Ca_{4.36}Mg_{0.6}Si_{6.02}(OH)_2{\cdot}4H_2O$) can be successfully synthesized in the MgO-CaO-SiO_2-H_2O system at 180 °C, where the extent of MgO contained in Tobermorite is enarly constant if the MgO/CaO molar ratio is varied from 0.2 to 1.0 [64]. Other researchers [62] found the substitution of magnesium for calcium to occur under hydrothermal conditions where MgO replaces 2 mol% of CaO and SiO_2. In XRD analysis, Mg-Tobermorite shows a smaller full width at half maximum (FWHM) and a higher relative intensity of (0 0 2) peak compared to pure Tobermorite indicating an increase of crystallinity. Magnesium elevates the silicate chains polymerization and increases the chain cross-linkage, as a result of the reduction in cation exchange capacity [62].

In contrast with the hydrothermal treatment, the addition of MgO to the CaO-SiO_2-H_2O system at room temperature facilitates the formation of brucite and C-S-H phases. The elevated MgO content leads to an increase of the Ca/Si ratio in C-S-H and shorter silicate chains [65]. The incorporation of Mg ions into the C-S-H is strongly limited by the low solubility of brucite at room temperature and the subsequent low concentration of magnesium in the solution [66,67]. Obviously, the concentration of Mg that can interact with C-S-H is crucial for the formation of C-S-H phases incorporating Mg.

The use of soluble magnesium salts such as magnesium chloride instead of MgO for synthesis could elevate the concentration of Mg^{2+}. However, the effect of soluble magnesium salts on the structure and chemical composition of C-S-H has been seldomly reported and deserves greater attention. Tobermorite hydrothermally synthesized with

soluble Mg takes up a maximum of 3.5 wt.% of Mg^{2+} after immersion in a solution with an initial concentration of 100-1000 ppm in Mg^{2+} [68]. In general, the uptake of Mg in C-S-H appears to be the joint effects of reversible ion exchange on broken bonds and outer planar surfaces and irreversible reaction of Mg^{2+} with the calcium silicates which leads to release of Ca^{2+} [68]. However, other researchers state that immersing C-S-H into Mg^{2+} solutions at room temperature leads to the formation of brucite and that it is only possible to form M-S-H with a high initial Mg^{2+} concentration, making the incorporation of Mg^{2+} essentially impossible as the dissolution of brucite is very slow at room temperature [65].

For the purpose of figuring out whether the soluble magnesium salts can interact with C-S-H phases, the current study investigates the role of different concentrations of Mg^{2+} on the formation of C-S-H phases using a simplified synthesis at elevated temperatures and ambient pressure. The CaO-SiO_2-H_2O system containing Mg^{2+} was investigated via mixing calcium oxide, silica fume and magnesium chlorides solution at the elevated reaction temperature (80 °C) for 24 hours. The obtained solid and liquid samples of synthetic C-S-H were characterized to investigate the structural features of Mg^{2+} modified C-S-H and the possibility of Mg incorporation into the structure of C-S-H.

2.2. Materials and experiments

2.2.1. Materials

Magnesium chloride hexahydrate ($MgCl_2 \cdot 6H_2O$, 99.5%, ACROS ORGANICS), calcium oxide (CaO, VWR CHEMICALS) and silica fume (SiO_2, Sipernat 50S, chemically prepared) were used. CaO was calcined at 750 °C for 5 hours to remove potential CO_3^{2-} and -OH groups.

2.2.2. Experiments

The reference C-S-H was synthesized following the routine reported in literature [69] with a Ca/Si molar ratio of 0.83 (4.648g CaO, 6g SiO_2) and sufficiently deionized water (200 ml) in an oil bath at 80 °C with a stirring rate of 700 rpm, benefiting the formation of Tobermorite-like C-S-H [49,70]. Different Mg/Si molar ratios (0.05, 0.15, 0.30, 0.45) were used while preparing the Mg^{2+} modified C-S-H with a fixed Ca/Si molar ratio of 0.83. The samples are labelled according to the nominal Mg/Si molar ratios of the samples, i.e., M0, M0.05, M0.15, M0.30 and M0.45, respectively, as shown in ***Table 2.1***.

Solutions with different Mg^{2+} concentration (0.025, 0.075, 0.150, 0.225 $mol \cdot l^{-1}$) were prepared with $MgCl_2 \cdot 6H_2O$ in volumetric flasks. 200 ml deionized water or prepared Mg^{2+} solution was added with CaO and silica fume powder. The amount of solution is determined by ensuring sufficient water for dissolution and reaction [71]. The samples were synthesized in conical flasks equipped with a condenser pipe, which was used to prevent water loss due to evaporation. The entire system was well sealed with glass stoppers to minimize CO_2 contamination. All samples were matured in an oil bath at 80 °C with a stirring rate of 700 rpm. After reaction for 24 hours, suspension of C-S-H was obtained. All suspensions were vacuum filtered with 0.45 μm Nylon filter after 24 hours

reaction. The residues were rinsed with 50 ml 94% ethanol solution to terminate hydration and then 50 ml deionized water to remove adsorbed ions from the particle surface as much as possible. The volume of filtrate was determined with graduated cylinder after cooling down to 20 °C and preserved in a vacuum container before Ion Chromatography (IC) testing. The obtained solids were vacuum dried at 40 °C until the weight of solid samples was constant. The solids were weighed and then ground in an agate mortar by hand. All samples were stored in desiccators, using a drying agent ($CaCl_2$ pellets) and sodium hydroxide pellets as CO_2 trap.

Table 2.1 *Mix proportions.*

Mg/Si molar ratio	Sample	Weight/g		Deionized water volume/ml	Mg^{2+} solution volume/ml	Mg^{2+} concentration/mol·l^{-1}
		CaO	SiO_2			
0	M0	4.648	6	200	-	-
0.05	M0.05	4.648	6	-	200	0.025
0.15	M0.15	4.648	6	-	200	0.075
0.30	M0.30	4.648	6	-	200	0.150
0.45	M0.45	4.648	6	-	200	0.225

2.2.3. Analysis techniques

The reaction products were analyzed with X-ray diffraction (XRD, Bruker D2 PHASER) with a Co tube (λ = 1.79 Å, 20 kV, 10 mA), between the scanning range from 10 to 70 °2θ, with a step of 0.02° and 1 s/step measuring time. A further set of samples was prepared to perform quantitative phase analysis with the Rietveld method [72]. For the quantification of the amorphous and crystalline content, 10 wt.% of Si (Siltronix, France) was added into the sample as an internal standard with a relative error below 5 % following literature [73]. The quantification was carried out with the software TOPAS 4.2 from Bruker Corporation [74]. The synthesized C-S-H is a nanostructural material with low crystallinity. In order to quantify it, the CSH 1 (Ca/Si = 1) structure from Battocchio et al. [72] was used, which is based on Tobermorite due to the low crystallinity the synthesized C-S-H appears partially X-ray amorphous. Therefore, the quantified CSH 1 and the amorphous content can be regarded as the same phase. It is possible that the amorphous content also contains other phases, such as amorphous silica, that the XRD cannot distinguish, however there is no indication this is the case based on the other analytical methods.

Fourier transform infrared spectroscopy (FTIR) spectra of samples were collected using a Varian 3100FTIR Spectrometer. All spectra were obtained with 20 scans per spectrum. The scanning electron microscopy (SEM) analysis was performed using a Phenom ProX

scanning electron microscope to observe the surface and morphology of solid samples. Transmission electron microscope (TEM) images were obtained with JEM 2100F microscope at 200Kev after powder samples were ultrasonically dispersed in ethanol for one minute. The suspensions were deposited on a copper holder for TEM imaging. Chemical analysis was performed with energy dispersive spectrometry (EDS) with an EDAX Elite T detector. Nitrogen sorption analysis was performed using a Brunauer-Emmett-Teller (BET) specific surface area and porosity instrument (TriStar II 3020, Micrometrics). The surface area was calculated with the Brunauer-Emmett-Teller method [75] using the adsorption branch. The pore size distribution (from 1 nm to 50 nm) was determined with the Barrett–Joyner–Hallenda method [76,77] from the adsorption branch. Thermogravimetric analyses (TGA) were done on ground powder (10~20 mg) using a heating rate of 10 °C/min from 40-1000 °C in nitrogen atmosphere (gas flow rate = 20 ml/min) with a STA 449 F1 instrument (Netzsch). The amount of Mg in form of Brucite was quantified from the water loss around 330-420 °C, which was determined with derived thermogravimetric analysis (DTG) and calculated according to:

$$W_{Mg\ in\ Brucite} = \frac{\text{Water loss}_{Brucite}}{M_{H_2O}} \times M_{Mg} \times 100\% \qquad \textbf{(2.1)}$$

where $W_{Mg\ in\ Brucite}$ corresponds to the magnesium amount in the total mass fraction, M_{H_2O} is molar mass of the water, equal to 18.02 g/mol, M_{Mg} is the molar mass of Mg, equal to 24.31 g/mol.

The pH values of the initial solution and the filtrate were tested at ambient temperature with a VOLTCRAFT PH-100ATC pH meter. The pH values were determined three times respectively and the mean is given. The initial concentrations of Mg^{2+} and Cl^- in the magnesium chloride solution and the concentrations of Mg^{2+} and Cl^- in the filtrates were determined with a Thermo Scientific Dionex ICS-1100 ion chromatography (IC) system, respectively. All liquid samples were undiluted or diluted by a factor of 10. Independent measurements of solutions with known compositions indicated a measurement error ≤ 10%. All concentrations have been determined three times respectively and the mean is given.

The amount of Mg taken up in C-S-H was calculated with:

$$M_{Mg\ in\ CSH} = C_{Initial} \times V_{Initial} - C_{Filtrate} \times V_{Filtrate} - W_{Mg\ in\ Brucite} \times M_{Total} \qquad \textbf{(2.2)}$$

where $M_{Mg\ in\ CSH}$ corresponds to the mass in g of Mg which was incorporated into C-S-H structure. $C_{Initial}$ and $C_{Filtrate}$ were determined with IC test, in $mg \cdot l^{-1}$. $V_{Initial}$ and $V_{Filtrate}$

in ml were measured at ambient temperature with a graduated cylinder. M_{Total} in mg was determined immediately after solid samples were vacuum dried and cooled down.

2.3. Results and discussion

2.3.1. Phase identification

Fig. 2.1 shows the XRD patterns of the Mg^{2+} modified C-S-H samples. The wide diffraction peaks of the reference C-S-H (M0 Sample) at 19.4, 34.0, 37.3, 58.7 and 64.8 °2θ are attributed to a poorly-crystalline C-S-H phase CSH 1 reported in [72]. Calcite is also present in small amounts as the sample has become slightly carbonated during sample preparation. It has a peak at around 34 °2θ, which is also the main peak of the C-S-H phase, making it difficult to see. The XRD patterns of samples synthesized with Mg^{2+} solution show the Bragg diffraction peaks in the same positions as the reference C-S-H. The intensity of CSH 1 peaks decreases with the increase of the initial Mg concentration due to the increasing presence of brucite and decreasing crystallinity indicative of an increasing amorphous content.

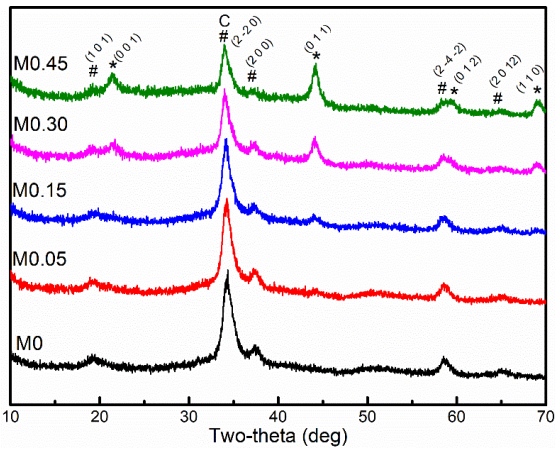

Fig. 2.1 *XRD pattern of Mg^{2+} modified C-S-H samples (# = C-S-H, * = Brucite, C = Calcite).*

The mineralogical compositions, which were quantified with the Rietveld method, are presented in ***Table 2.2***. The X-ray diffractograms of the synthesized C-S-H and the peak fit calculated with TOPAS are shown in ***Fig. 2.2***. The content of CSH 1 decreases from 63.88 % in the M0 sample to 9.88 % in the M0.45 sample. Meanwhile, the amorphous phase increases from 35.23 % to 74.46 %. The amount of brucite increases from 2.63 % to 13.85 % with the elevation of the initial Mg^{2+} concentration. The amount of calcite is around 1 % in all samples, indicating that all samples were slightly carbonated. The addition of Mg^{2+} leads to the transformation of CSH 1 to amorphous phase. M0.05 sample consists of 47.42 % CSH 1, 49.02 % amorphous phase and 2.63 % brucite. Comparing that with the composition of M0 sample, it can be concluded that even minor initial Mg^{2+} input

decreases the crystallinity of the C-S-H, which is reflected by the increase in amorphous content in the XRD.

Table 2.2 *Rietveld refinement results of Mg^{2+} modified C-S-H samples.*

Sample	CSH 1	Amorphous phase	Brucite	Calcite	GOF	Rexp	Rwp
	[wt.%]						
M0	63.9±2.0	35.2±2.1	-	0.9±0.2	1.72	4.81	8.30
M0.05	47.4±1.8	49.0±1.9	2.6±0.5	0.9±0.3	1.84	4.75	8.74
M0.15	48.2±2.2	44.7±2.1	5.7±0.5	1.5±0.3	1.64	4.66	7.64
M0.30	35.2±2.1	52.1±2.1	11.7±0.3	1.0±0.3	1.63	4.44	7.24
M0.45	9.9±1.2	74.5±1.2	13.9±0.3	0.7±0.2	1.58	4.26	6.71

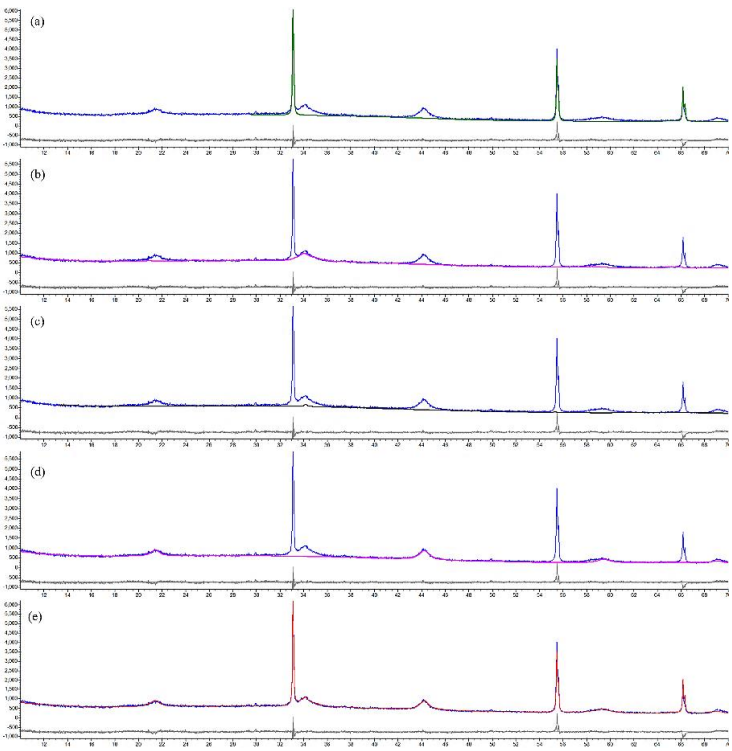

Fig. 2.2 *Peak fit as calculated with TOPAS. Measured X-ray diffractogram of the synthesized C-S-H (blue line) and (a) silicon (green line), (b) CSH 1 (pink line), (c) calcite (black line), (d) brucite (pink line), (e) the calculated spectrum (red line).*

2.3.2. FT-IR analysis

The reference C-S-H sample (M0) without Mg^{2+} (***Fig. 2.3***) shows a OH stretching vibrations at 3442 cm^{-1} and H-OH bending vibrations of molecular water at 1634 cm^{-1}. Furthermore, the spectrum contains a Si-O-Si bending band at 670 cm^{-1} and Si-O stretching vibration bands at 970 cm^{-1} (Q^2 tetrahedra) and 830 cm^{-1} (Q^1 tetrahedra) [65,71]. The bands at 443 cm^{-1} correspond to the deformation of SiO_4 tetrahedra form, which are shown in all samples [78].

The spectra of samples containing magnesium show great similarities to that of reference C-S-H, indicating that C-S-H remains the major reaction product with magnesium. Mg-OH stretching vibration bands centered at approximately 3680 cm^{-1} are associated with the formation of brucite, whose intensity increases with increasing Mg content. The small shift from 830 cm^{-1} to 870 cm^{-1} occurs when the Mg/Si ratio is elevated to 0.30. The shifts towards higher frequency can be attributed to a lower Ca/Si ratio of the C-S-H [78]. The band at 670 cm^{-1} disappears gradually with increasing Mg content, consistent with decreased ordering with increasing cross-linking of the silicate chains [78]. Thus, the reference C-S-H sample is the most ordered, corresponding to the XRD results where the M0 sample contains the least amount of X-ray amorphous phase. The Si-O band at 970 cm^{-1} becomes broader with increasing Mg content and the shoulder at 1030 cm^{-1} is only observed in the M0.45 sample. This difference reflects its higher average silicate polymerization due to more Q^3 sites caused by the addition of high magnesium content [78]. It is also possible that a new phase is formed with abundant Mg^{2+} but in this case it would be X-ray amorphous.

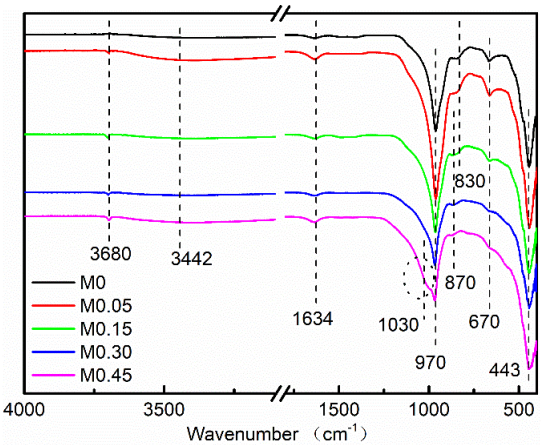

Fig. 2.3 *FT-IR spectra of Mg^{2+} modified C-S-H samples.*

2.3.3. Thermogravimetric analysis

Different materials can be identified based on their thermal characteristics with thermogravimetric analysis (TGA) and its first derivative (DTG) signal [79], which can measure the weight loss and the rate of weight loss with temperature during analysis in a

fast and direct way. ***Fig. 2.4*** show the TGA-DTG data of Mg^{2+} modified C-S-H samples with different Mg/Si ratios. In general, the weight loss occurs in three stages: the loss of free water or loosely bound interlayer water between 40 and 330 °C; weight loss between 330 °C and 420 °C is associated with the dehydroxylation of magnesium hydroxide phase in Mg^{2+} modified C-S-H samples and the further weight loss is corresponding to the dehydroxylation of the silanol groups in the reference C-S-H and magnesium modified C-S-H [71,73]. The small weight loss at approximately 750 °C is associated with the presence of calcite due to the slight carbonation.

The M0 sample shows a main water loss between 40 and 330 °C, which can be attributed to the mass loss of free water and the dehydration of loosely bound water [80]. No weight loss is observed at 400 °C in the M0 sample, indicating that calcium hydroxide is absent and all calcium is bound in the C-S-H, which is in line with the absence of $Ca(OH)_2$ peaks in the XRD data. As research by Jin et al. [81] showed, small peaks at around 520-570 °C can be attributed to the loss of coordinated water in pure M-S-H. These peaks are not visible in ***Fig. 2.4(b)***, demonstrating that no pure M-S-H phases were formed, or the amount of pure M-S-H is negligible.

Table 2.3 *Weight loss of Mg^{2+} modified C-S-H samples calculated from TGA.*

Sample	Chemically bound water (wt. %)	OH group in brucite (wt. %)	Amount of brucite (wt. %)	Total (wt. %)	a/b (%)*
M0	11.20	-	-	19.74	11.2
M0.05	11.88	0.97	3.35	21.40	12.3
M0.15	11.12	1.71	5.52	22.73	11.8
M0.30	9.33	3.89	12.60	21.35	10.7
M0.45	8.50	4.83	15.65	21.00	10.1

**a/b refers to the amount of chemically bound water divided by the amount of CSH 1 plus amorphous phase.*

The amount of chemically bound water, the amount of brucite and the total weight loss are calculated from TGA data and summarized in ***Table 2.3***. Researchers are holding different opinions on the temperature boundary of the chemically bound water in thermogravimetric study. In this study, 100 °C was chosen as the starting point of the dehydration of bound water [82]. The mass loss of chemically bound water is determined from 100 to 330 °C. The amount of bound water decreases with increasing Mg content. However, these values are difficult to compare because the C-S-H content is different in all the samples due to the increasing content of brucite. Therefore, the chemically bound water content was normalized by the amount of CSH 1 plus amorphous phases in the sample. As can be seen the same trend still exists indicating that higher additions of Mg

can cause the decomposition of C-S-H because the chemically bound water is highly related to the formation of C-S-H phase [82]. The weight loss due to the OH group in brucite is increasing gradually with the increasing Mg content as expected. In general, the amount of brucite calculated from the results of the TGA test is slightly higher than that obtained from the Rietveld refinement (***Table 2.2***). The amount of brucite in Rietveld refinement is lower because of the low crystallinity of the brucite therefore it's slightly underestimated.

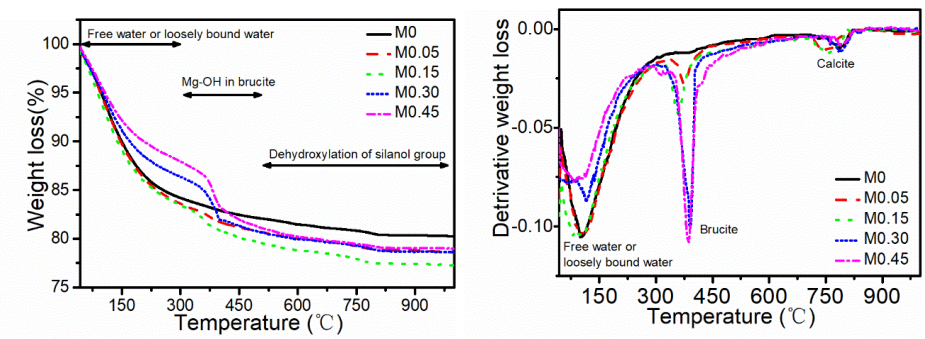

(a) ***(b)***

Fig. 2.4 *(a) Weight loss determined with thermogravimetric analysis (TGA) and (b) its first derivative (DTG) of Mg^{2+} modified C-S-H samples.*

2.3.4. Microstructural analysis

Fig. 2.5 shows the morphology of the reference C-S-H and Mg-modified C-S-H obtained with SEM. The M0 sample exhibits a dense network with a foil-like structure [83–86]. With an Mg/Si ratio of 0.05, the morphology changes to foil-like structures arranged in a dense, laminar pattern. The M0.15 sample is similar in morphology to the M0.05 sample, however the foils are more distinct in a less extended structure. As the Mg/Si ratio is elevated to 0.30, fiber shapes instead of foil-like structures coexist with the gel-like phases. The structure is less extended with some obvious large pores. The tiny fibers are more polydisperse in the M0.45 sample, where the surface of the Mg-modified C-S-H is likely covered and intermixed with crystallite brucite. The reference C-S-H exhibits a more homogenous morphology compared to the other four samples mixed with Mg. More macro capillary pores are found in C-S-H synthesized with magnesium, corresponding to the evaporation of more free water during the drying process [87].

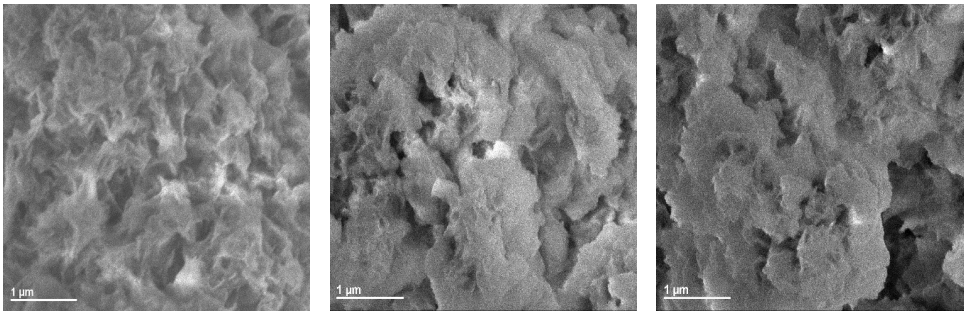

(a) *M0* ***(b)*** *M0.05* ***(c)*** *M0.15*

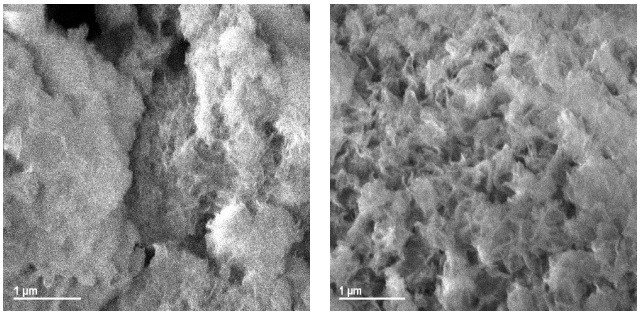

(d) *M0.30* ***(e)*** *M0.45*

Fig. 2.5 *SEM images of Mg^{2+} modified C-S-H samples.*

The BET specific surface area was measured as shown in ***Table 2.4*** and the pore size distribution from 1 nm to 50 nm was measured as shown in ***Table 2.4*** and ***Fig. 2.6*** in order to obtain more details about the pore structure of C-S-H on a nanoscale. A clear trend is visible, the cumulative volume of meso gel pores (1-25 nm) and micro capillary pores (25-50 nm) increases with the addition of Mg [88]. M0 sample exhibits the smallest BET surface area, demonstrating that reference C-S-H contains more chemically bound water, in line with TGA results as pore distribution depends largely on water content [89,90]. Mg^{2+} modified C-S-H contain more free water in capillary and gel pores which was removed during the ethanol drying procedure, leading to a porous structure while the bound water in the reference C-S-H was more stable as a result in the formation of a dense network structure [87]. The M0.30 sample exhibits a larger BET surface area than the M0.45 sample, as the more extended and polymerized morphology of M0.45 sample is observed with SEM. Combined with the results obtained with FT-IR, it can be possibly concluded that a new phase containing a large amount of Mg and Ca formed when the initial Mg/Si ratio is at least 0.45.

Table 2.4 *BET surface area of Mg^{2+} modified C-S-H samples.*

Name	Cumulative pore area (m^2/g)		BET specific surface area (m^2/g)
	1-25 nm	25-50 nm	
M0	29.87	6.24	44.01
M0.05	41.27	7.53	58.25
M0.15	112.02	12.70	131.52
M0.30	179.99	26.47	218.85
M0.45	146.94	25.69	191.40

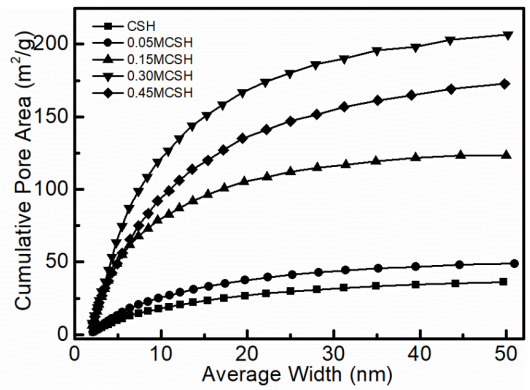

Fig. 2.6 *Cumulative pore area of Mg^{2+} modified C-S-H samples (from 1 to 50 nm).*

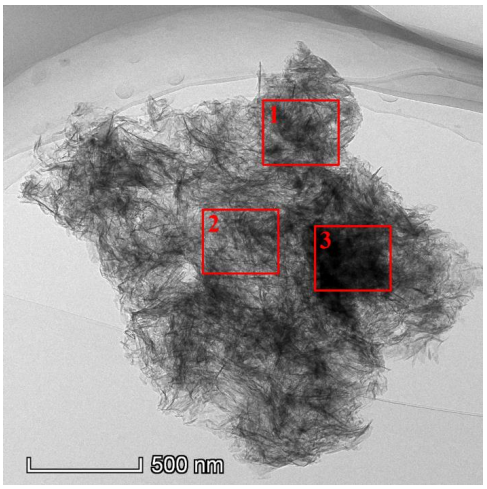

Fig. 2.7 *TEM picture of M0.45 sample.*

In order to gain further insight into the microstructure of the M0.45 sample, TEM analysis was conducted. ***Fig. 2.7*** and ***Fig. 2.8*** show the TEM image and mapping results of the M0.45 sample, respectively. ***Fig. 2.7*** illustrates that the Mg modified C-S-H exhibits a disorganized layered texture. The EDS mapping was conducted to further investigate the chemical element distribution. ***Fig. 2.8*** shows the homogeneous distribution of Ca and Si while Mg is only detected in some areas, showing a heterogenous distribution. The atomic fraction of Mg, Ca and Si in the areas shown in ***Fig. 2.7*** are listed in ***Table 2.5***. After normalization, the calculated Mg:Ca:Si molar ratio is 0.41:0.40:1, 0.07:0.39:1 and 0.33:0.34:1 in area 1, 2 and 3, respectively. The atomic fraction of Ca is relatively fixed, indicating that the detected phase is C-S-H. The atomic fraction of Mg is close to Ca in area 1 and 3, demonstrating that large amounts of Mg were incorporated into the structure of C-S-H during the synthesis process. TEM electron diffraction analyses performed on the detected C-S-H phase are shown in ***Fig. 2.9***. No diffraction spots are detected, indicating that the synthesized C-S-H is cryptocrystalline in nature and that no crystalline brucite is contained in the C-S-H phase. Silicate tetrahedrons are balanced by H^+ in the interlayer space, which could be substituted by Ca^{2+} as the Ca/Si atomic ratio is elevated [49]. With the increasing Mg addition, it is likely that H^+ ions are substituted by Mg^{2+} and Ca^{2+} ions together.

Table 2.5 *Calculated parameters from TEM-EDS results of sample M0.45 (%).*

Element	Atomic fraction		
	Area 1	Area 2	Area 3
Mg	7.88	1.48	7.05
Ca	7.70	8.66	7.22
Si	19.05	21.94	21.51
Element	Normalization		
	Area 1	Area 2	Area 3
Mg	0.41	0.07	0.33
Ca	0.40	0.39	0.34
Si	1	1	1

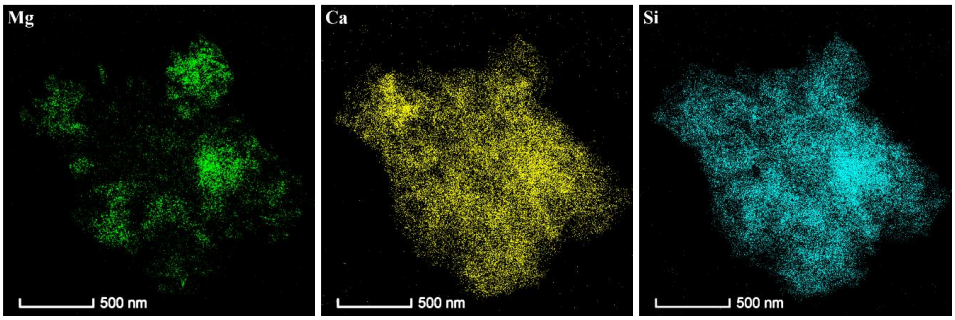

Fig. 2.8 *TEM-EDS mappings of magnesium, calcium and silicon in M0.45 sample.*

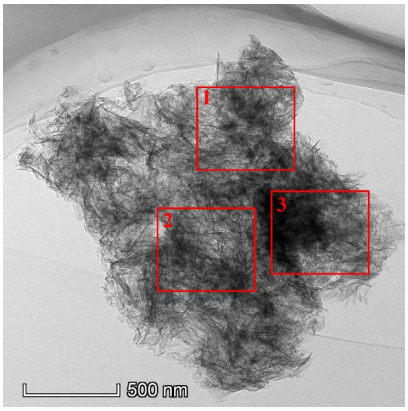

(a)

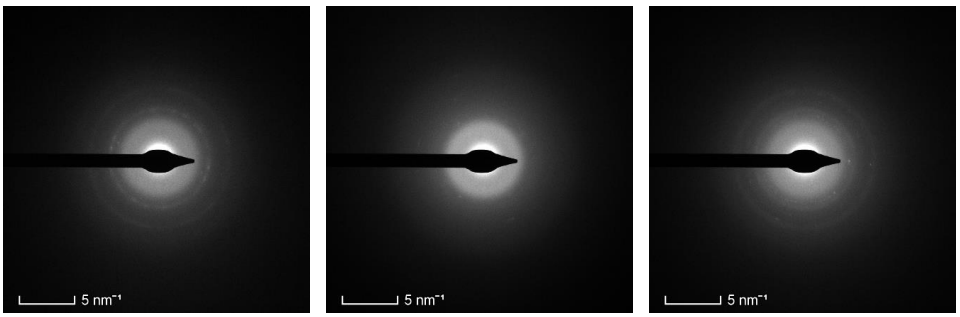

(b) *Area 1* ***(c)*** *Area 2* ***(d)*** *Area 3*

Fig. 2.9 *TEM image of the detected C-S-H phase and electron diffraction patterns ((a) TEM image, (b) electron diffraction pattern of Area 1, (c) electron diffraction pattern of Area 2, (d) electron diffraction pattern of Area 3).*

2.3.5. Aqueous solution and Mg uptake in C-S-H

The amount of Mg bound in the C-S-H excluding Mg in the form of brucite and the Mg in the filtrate is calculated according to ***Eq. (2.2)*** and listed in ***Table 2.6***. In terms of the

amount of brucite, the quantification results obtained from TGA data are considered more accurate than the Rietveld refinement for this system due to the low crystallinity or small crystalline size of brucite and TGA analysis is not influenced by these factors. Therefore, the TGA data was chosen for the calculation of the uptake of Mg in C-S-H.

Table 2.6 *The amount of Mg in Mg modified C-S-H.*

Sample	$C_{Initial}$ /mg·l^{-1}	$V_{Initial}$ /ml	$C_{Filtrate}$ /mg·l^{-1}	$V_{Filtrate}$ /ml	$W_{Mg\ in\ Brucite}$ /wt. %	M_{Total} /mg	$M_{Mg\ in\ CSH}$ /mg	a/b* (%)
M0	-	200	0.82±0.04	228	-	12311.3	-	-
M0.05	627.00±3.12	200	0.86±0.07	244	1.31	12383.8	-36.52	-29.1
M0.15	1762.12±14.83	200	1.17±0.04	239	2.30	13376.9	44.20	12.5
M0.30	3806.00±15.03	200	3.04±0.07	238	5.25	12463.2	105.88	13.9
M0.45	5575.62±88.49	200	1.47±0.01	246	6.52	13660.1	223.92	20.1

**a/b refers to $M_{Mg\ in\ CSH}$ divided by the amount of the initial amount of Mg.*

Table 2.7 *Mass balance of Cl^- and pH changing.*

Sample	Initial concentration /mg·l^{-1}	Initial volume /ml	Filtrate concentration /mg·l^{-1}	Filtrate volume /ml	a/b (%)	Initial pH	Final pH
M0	-	200	60.76±0.68	228	-	7.2±0.1	10.2±0.1
M0.05	1760.21±6.66	200	1191.03±6.30	244	17.5	6.1±0.0	9.6±0.0
M0.15	4366.98±13.20	200	3748.74±38.30	239	-2.5	5.8±0.0	9.2±0.0
M0.30	10577.55±62.90	200	7660.34±119.46	238	13.8	5.3±0.1	8.3±0.0
M0.45	16199.67±72.54	200	10161.89±64.25	246	22.8	4.2±0.1	7.3±0.0

**a/b refers to the difference of the initial and filtrate amount of Cl^- divided by the initial amount of Cl^-.*

The concentrations of Mg^{2+} in the filtrate are similar and it can be seen that most of Mg is incorporated in the solid phase of the sample. The amount of Mg in the C-S-H increases from -36.52 to 223.92 mg with the increasing initial concentration of Mg^{2+}. The negative Mg content in sample M0.05 is possibly because the weight loss in the corresponding temperature range in TGA is not only associated with the dehydration of $Mg(OH)_2$, but also the hydroxylation of C-S-H itself [73]. 20.1 % Mg of the initial input Mg has been incorporated into the structure of C-S-H. However, as shown in ***Table 2.7***, a maximum of 22.8 % Cl^- still exists in the M0.45 sample, indicating that the Cl^- ions were not totally

washed out by rinsing. The increased specific surface area detected in BET analysis can promote the ions absorption capacity of the Mg-modified C-S-H. Therefore, the considerable uptake of Mg in C-S-H might be partly caused by surface absorption.

The pH values of the initial and final liquid phase are shown in ***Table 2.7***. The addition of Mg^{2+} undoubtedly decreases the pH value of the solutions. The final pH of the reference C-S-H filtrate is 10.2 while that of the M0.45 sample is only 7.3. The low pH can increase the instability of C-S-H structure and contribute to the decomposition of C-S-H, in accordance with the reduction of crystallinity of C-S-H phases.

2.4. Conclusion

The mineralogical composition of $CaO\text{-}SiO_2\text{-}H_2O$ system is obviously modified when the aqueous solution contains Mg^{2+} ions. The reference C-S-H (M0 sample) can be refined using the crystal structure of CSH 1 (Ca/Si = 1) based on Tobermorite. According to the quantitative phase analysis with the Rietveld method, minor amounts of Mg^{2+} can greatly increase the content of X-ray amorphous phase and decrease the content of CSH 1. With increasing Mg^{2+} content, more brucite is formed.

The gradual disappearance of the band at 670 cm^{-1} in the FTIR patterns confirms that high Mg^{2+} concentrations add to the instability of C-S-H. The amount of chemically bound water in M0.30 and M0.45 samples is obviously less than that in the other samples, further indicating structural change of C-S-H.

The BET specific surface areas of the synthesized C-S-H show a clear trend that the cumulative volume of meso gel pores (1-25 nm) and micro capillary pores (25-50 nm) increases with the addition of Mg except M0.45 sample. M0.45 sample has a lower BET specific surface area than M0.30 sample, indicating that the microstructure of Mg^{2+} modified C-S-H with initial Mg/Si ratio of 0.45 has been changed. A new phase containing large amounts of Ca and Mg is possibly formed in M0.45 sample. More evidence is found in TEM-EDS mapping results that large amount of Mg is heterogeneously distributed within the C-S-H phase. TEM diffraction indicates that this is not due to the presence of brucite. Mass balance calculation between filtrate, solid phase (both chemical analysis) and brucite (TGA/QXRD) of Mg uptake in C-S-H confirms that Mg can be incorporated into the structure of C-S-H.

Based on the results discussed above, the following conclusions can be drawn:

The mineralogical compositions of the synthesized C-S-H are highly related to the initial concentration of Mg^{2+} of the aqueous phase. Addition of Mg decreases the content of CSH 1 and increases the content of X-ray amorphous solid phase and of brucite.

Elevating Mg^{2+} concentration leads to decreased ordering with increasing cross-linking of the silicate chains in the synthesized C-S-H. Large additions of Mg^{2+} lead to the instability of C-S-H.

A heterogenous distribution of elemental Mg in C-S-H phase on nanoscale is observed. Phase separation of C-S-H is caused by incorporating magnesium into the structure of C-S-H. The considerable uptake of Mg in C-S-H is also possibly caused by surface absorption.

The synthesized C-S-H with initial Mg/Si molar ratio of 0.45 shows special microstructure characteristics, indicating that a new phase is possibly formed. The occurrence of the broad band at 1030 cm^{-1} in FT-IR analysis and the smaller BET specific surface area obtained via BET test further confirm the hypothesis. The exact structure and formation process of the synthesized C-S-H remains unclear due to its disordered, partially X-ray amorphous nature. Synchrotron experiments combined with Scanning transmission X-Ray microscopy or Rietveld refinements may be able to offer further insights. Solid-state nuclear magnetic resonance spectroscopy may also help to resolve the key atomic structural details within the synthesized C-S-H via obtaining detailed information about local structure, reaction mechanisms and kinetics, understanding composition–structure–property relationships.

CHAPTER 3

3. Re-cementation effects by carbonation and the pozzolanic reaction on LWAs produced by hydrated cement paste powder

This chapter aims to evaluate lightweight aggregates produced with hydrated cement paste powder (HCP) using both carbonation and normal curing. The comparative study was conducted to figure out the effects of the portlandite amount in HCP I and HCP III on the aggregates during carbonation curing. The addition of up to 10 wt.% silica fume to HCP I was attempted to make full use of the considerable amount of portlandite to prepare artificial aggregates under normal curing. The mechanical properties, reaction products and microstructure were analyzed and the results show that the optimal carbonation period for HCP I- and HCP III-type aggregates are different due to different amounts of portlandite. HCP I-type aggregates can gain 3.14 MPa after 7-day carbonation and contain 35.60 wt.% calcium carbonates. The remaining 13.95 wt.% portlandite shows the enormous potential in elevating the strength and CO_2 capture capacity jointly via the optimized carbonation curing method. On the contrary, HCP III-type aggregates gained 2.97 MPa after 1-day carbonation and further carbonation decomposed C-S-H and lead to the formation of calcite and amorphous silica gel with significantly elevated specific surface area (from 10.69 to 42.96 m^2/g). Additionally, the individual strength development of the prepared aggregates containing silica fume benefits from the sufficiently available portlandite due to the formation of secondary C-S-H, obtaining 2.39 MPa after 28-day normal curing.

This chapter is reproduced from: Y. Tang, G. Liu, K. Schollbach, Y. Chen, W. Chen, H.J.H. Brouwers, Re-cementation effects by carbonation and the pozzolanic reaction on LWAs produced by hydrated cement paste powder, J. Clean. Prod. 377 (2022) 134529. https://doi.org/10.1016/j.jclepro.2022.134529.

3.1. Introduction

As a newly developed building material, lightweight concrete shows some extraordinary properties such as extremely low density, excellent sound absorption, and thermal insulation [91–94]. The main ingredients for a lightweight concrete design are cement and lightweight aggregates (LWAs) [91–94]. Generally, LWAs have a porous structure and low bulk density (less than 1200 kg/m^3) and thus reduce the density of concrete structure effectively [95]. However, the commercial LWAs, for instance, expanded clay, expanded glass and perlite, consume huge amounts of energy, as well as natural resource due to the production at high temperatures (700 - 1400 °C) [96]. Consequently, some studies started focusing on the development of a low-carbon footprint and sustainable LWAs.

Cold-bonding technology has been proposed and developed for the purpose of low energy consumption during LWAs manufacture [97–99]. Combined with a pelletizing process, pellets in different sizes with porous structure were produced and then applied as LWAs [100]. Some industrial solid wastes can be utilized in LWAs as well, for examples, bottom ash, concrete waste powder, and fly ash [101–105]. Since these solid wastes show a low or non-hydraulic reactivity, the incorporation of cement, additional curing strategies, or chemical additives in cold-bonded LWAs are commonly used to form extra hydration products and optimize pore structure in order to achieve adequate mechanical performance. Steam curing was applied to improve the properties of cold-bonded LWAs produced with cement waste slurry and bottom ash [100]. Portlandite and alkali solution were also used to promote the reaction in blast furnace slag or fly ash-based LWAs [106,107]. However, the use of additional binders, alkali activators or other curing regimes can result in long curing period, high costs, high CO_2 emission and safety risks.

The main components in waste powder are hydrated cement paste (HCP) but the exact composition can depend on the crushing and heating methods used to recycle concrete [9–12].The difficulty lies in applying waste concrete powder to normal concrete production without further treatment or activation [92–94]. The HCP contains mainly calcium silicate hydrate (C-S-H) gels, calcium hydroxide, AFt, AFm and some unreacted clinker phases. Gas-solid and aqueous carbonation were reported to be effective to utilize HCP powders as the SCMs [108]. The workability and mechanical property of cement paste blended with carbonated HCP powder can be enhanced via the formation of calcium carbonates which can act as fillers and then optimize the pore structure [109,110]. Carbonation can also lead to the formation of silica gel with pozzolanic properties due to the decomposition of calcium silicate phases [111–113]. The reaction between portlandite and silica gel, has been widely applied to improve the bonding performance of recycled concrete aggregate in new concrete due to the formation of secondary C-S-H gel [114]. Furthermore, these re-cementation effects may make it possible to produce HCP powder based cold-bonded LWAs without cement and alkali activator addition, by using carbonation or the addition of silica fume only. The current research on the effects of carbonation and pozzolanic reactions on mechanical and microstructure development of

cold-bonded HCP powder-based LWAs is still limited and the effects need to be further investigated.

For the purpose of investigating the mechanism of the mechanical and microstructure development of the artificial aggregates under carbonation or pozzolanic reaction, this study used laboratory-made cement paste instead of real demolished concrete to obtain HCP powder and then produce LWAs, which allows for better control of the chemical composition of the waste powder by eliminating the variability of its properties when recovered from demolished materials. Additionally, researchers preferred to investigate the properties of HCP powder from CEM I which contains few SCMs, whereas CEM III is also widely used and deserves more attention in the production of LWAs. Therefore, both CEM I 52.5 R and CEM III/A 52.5 N were chosen as the starting materials. The amount of hydration products from CEM I and CEM III is different, especially the amount of portlandite. Therefor a comparative study has been conducted to find out the effects of portlandite amount in HCP I and HCP III on the aggregates production under carbonation curing. Addition of up to 10 wt.% silica fume into HCP I was also attempted to make full use of the considerable amount of portlandite in the preparation artificial aggregates and evaluate their pozzolanic property under normal curing. The mechanical properties, reaction products and microstructure were investigated via XRD, FTIR etc. to determine the re-cementation effects of carbonation and pozzolanic reactions on LWAs produced with HCP powder. The results provide a low carbon footprint and sustainable method of HCP powder application and LWAs production.

3.2. Experiments and methodology

3.2.1 Raw materials

Silica fume (SF) was used as a part of the binder to produce aggregates, which was provided by Sika. The HCP powder was produced in the laboratory from cement paste which was prepared from CEM I 52.5 R or CEM III/A 52.5 N (provided by ENCI, the Netherlands). The used CEM I 52.5 R and CEM III/A 52.5 N in this study contain 0 wt.% and 36-65 wt.% ground granulated blast furnace slag (GBS) according to European standard EN 197-1, respectively. All cement pastes were prepared with a water to cement ratio of 0.5 and then demolded 24 hours after mixing, followed by ambient curing in resealable bags for at least 3 months. The HCP was crushed manually and sieved to a size of below 5 mm. The sieved material was then oven dried at 105 °C until the weight was constant. Disc milling (Retsch, RS300XL) for 10 min was applied to obtain the waste cement paste powder for the tests. The milled HCP powder originating from CEM I and CEM III was labelled as HCP I and HCP III, respectively. The chemical composition of SF, HCP I and HCP III was analysed with X-ray fluorescence (XRF, Model Axios Advanced, PANalytical.B.V), as shown in ***Table 3.1***. The mineral composition of HCP I and HCP III was determined using X-ray diffraction (XRD) analysis, which is shown in ***Fig. 3.1(a)*** and ***(b)***, respectively. The particle size distribution of SF, HCP I and HCP III analysed with a

laser particle size analyser (Model Malvern Mastersizer 2000, Malvern PANalytical) is presented in ***Fig. 3.2***.

Table 3.1 *The chemical composition of raw materials for preparation of aggregates.*

Materials (wt.%)	CaO	SiO_2	Al_2O_3	Fe_2O_3	SO_3	MgO	MnO	TiO_2	Others
SF	0.90	93.06	-	2.06	1.28	0.70	0.07	-	1.93
HCP I	65.96	17.42	7.57	3.51	3.08	1.43	0.08	0.44	0.51
HCP III	49.32	27.10	12.02	1.24	4.83	4.24	0.17	0.55	0.53

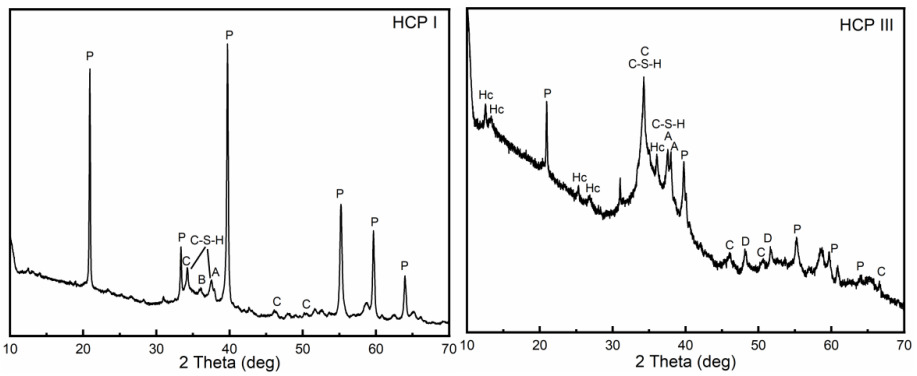

(a) ***(b)***

Fig. 3.1 *XRD patterns of HCP I (a) and HCP III (b) (P=portlandite, A=alite, B=belite, C=calcite, Hc=hemicarbonate, D=dolomite, C-S-H=calcium silicate hydrates).*

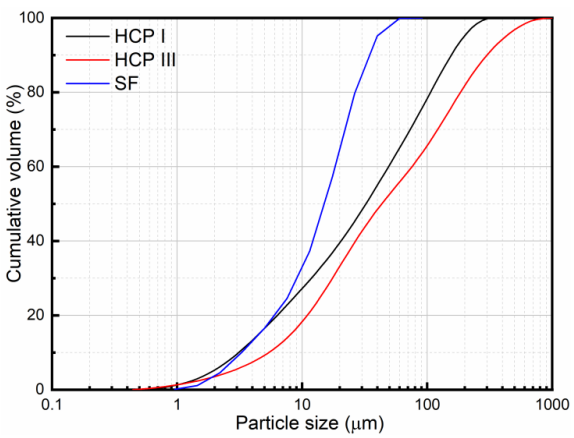

Fig. 3.2 *Particle size distribution of silica fume (SF), milled hydrated cement paste powder I (HCP I) and milled hydrated cement paste powder III (HCP III).*

3.2.2 Pelletizing procedure

The disc pelletizer was used to produce artificial aggregates. The model was D-7736, Maschinenfabrik Gustav Eirich, Germany with a disk/pan size of 40 cm in diameter and 10 cm collar height. The vertical angle of the pan is 75° and the rotating speed was set as 60 rpm during the production process. 500 grams of HCP were placed on the rotating pan. After about 3 min of rotating, 50 grams of distilled water was sprayed slowly over 10 min onto the mixed powder in the pan using a spray bottle. After the aggregation was observed, the pan continued running for 5 min to form the pellets. The as-prepared aggregates drop out of the pan automatically once they reached sufficient size and were collected. The next batch was made with the addition of another 500 grams of dry powder and following the same procedure. The freshly prepared LWAs were placed in a CO_2 chamber with a CO_2 concentration of 5% and a relative humidity of 75% and carbonated for 1, 3 and 7 days, respectively for carbonation curing. The temperature during curing was constant, around 20 °C. The prepared aggregates, which originated from HCP I and HCP III, and were carbonated for 1, 3 and 7 days are labelled as C1A I, C3A I, C7A I, C1A III, C3A III and C7A III, respectively, as shown in ***Table 3.2***.

Table 3.2 *Mix proportion of aggregates prepared from different curing regimes.*

Curing regime	Sample	HCP I/g	HCP III/g	SF/g	Water/g	Curing time/day
CO_2 curing	C1A I	500	-	-	50	1
	C3A I	500	-	-	50	3
	C7A I	500	-	-	50	7
	C1A III	-	500	-	50	1
	C3A III	-	500	-	50	3
	C7A III	-	500	-	50	7
Normal curing	S0A I	500	-	-	50	28
	S5A I	475	-	25	50	28
	S10A I	450	-	50	50	28

To obtain aggregates containing SF, the SF and HCP I was first mixed in a Planetary mixer. Then around 500 grams of mixed powder was placed on the rotating pan. The pelletizing procedure followed was the same as mentioned above. The obtained fresh aggregates were then placed in sealed plastic bags for 28 days until further testing. The aggregates

containing SF were labelled as S0A I, S5A 1 and S10A I, respectively, according to the different proportions of SF partially replacing HCP I in the mix, being 0%, 5% and 10% of mass respectively, as shown in ***Table 3.2***.

3.2.3. Properties of prepared LWAs

3.2.3.1. Water absorption and loose bulk density

After curing, the prepared aggregates were dried in an oven at 105 °C until a constant mass. The loose bulk density test was carried out according to EN 1097-3. The water absorption test was carried out according to EN 1097-6.

3.2.3.2. Mechanical property

The mechanical properties of individual pellets with different diameters were tested in an MTS Criterion electromechanical testing machine equipped with a load cell of 100 kN at a speed of 0.6 mm/min until collapse. The maximum compression load was used to calculate the individual crushing strength with [115]:

$$\sigma = 2.8P/\pi h^2 \qquad \textbf{(3.1)}$$

where σ (MPa) is the crushing strength of each pellets tested, P (N) is the maximum compression load each pellet can withstand, h (mm) is the diameter of the round pellet produced.

20 pellets were chosen as representatives for each group of prepared LWAs.

3.2.3.3. Characterization of reaction products and microstructure

Different artificial aggregates were crushed manually and ground finely to pass a sieve of 68 μm. Afterwards, samples were immersed in isopropanol for 30 min to eliminate hydration according to literature [73] and then dried in an oven at 40 °C until a constant mass. All samples were stored in desiccators, using a drying agent ($CaCl_2$ pellets) and sodium hydroxide pellets as a CO_2 trap until further tests.

The crystalline phases of the prepared aggregates were detected by X-ray diffraction (XRD, Bruker D2 PHASER) analysis. The parameters chosen were as follows: Co tube, 40KV, 30 mA, 0.02°/ step, 0.2°/min, with variable divergence slits V20.

Fourier transform infrared spectroscopy (FTIR) was conducted using a Varian 3100 FTIR Spectrometer. All spectra were obtained with 30 scans per spectrum and a resolution of 1 cm^{-1}.

The microstructure was observed with scanning electron microscopy (SEM), using a JEOL JSM-5600 instrument at an accelerating voltage of 15 kV.

Nitrogen sorption analysis was performed using a Brunauer-Emmett-Teller (BET) specific surface area and porosity instrument (TriStar II 3020, Micrometrics). The surface area was calculated with the Brunauer-Emmett-Teller method [77] using the adsorption branch. The pore size distribution was determined from the adsorption branch with the Barrett–Joyner–Hallenda method [76].

Thermogravimetric analyses (TGA) were conducted using a NETZSCH STA 449 F1. Ground powder samples (30~40 mg) were prepared, and a heating rate was used of 10 °C/min from 40-1000 °C in a nitrogen atmosphere. The temperatures selected for the quantification of $Ca(OH)_2$, $CaCO_3$ and chemically bound water were determined with differential thermogravimetric analysis (DTG), and are 400-500 °C, 600-800 °C and 75-550 °C respectively according to literature [73,116,117]. The weight loss between 75-550 °C is considered to represent the amount of chemically bound water in hydration products such as C-S-H, ettringite, AFm phases, portlandite etc.

The quantification of the amount of portlandite was according to:

$$W_{Ca(OH)_2} = \frac{Water\ loss_{OH\ group\ in\ Ca(OH)_2}}{M_{H_2O} \times M_{800\ °C}} \times M_{Ca(OH)_2} \times 100\% \quad \textbf{(3.2)}$$

where $Water\ loss_{OH\ group\ in\ Ca(OH)_2}$ corresponds to the weight loss from approximately 400 to 500 °C in the total mass, $M_{800\ °C}$ is the sample mass at 800 °C, M_{H_2O} is molar mass of the water, equal to 18.02 g/mol, $M_{Ca(OH)_2}$ is the molar mass of $Ca(OH)_2$, equal to 74.09 g/mol.

The quantification of the amount of calcium carbonate was according to:

$$W_{CaCO_3} = \frac{Mass\ loss_{CO_3\ group\ in\ CaCO_3}}{M_{CO_2} \times M_{800\ °C}} \times M_{CaCO_3} \times 100\% \quad \textbf{(3.3)}$$

where $Mass\ loss_{CO_3\ group\ in\ CaCO_3}$ corresponds to the weight loss from approximately 600 to 800 °C in the total mass, $M_{800\ °C}$ is the sample mass at 800 °C, M_{CO_2} is molar mass of CO_2, equal to 44.01 g/mol, M_{CaCO_3} is the molar mass of $CaCO_3$, equal to 100.09 g/mol.

Notably, the quantification of the amount of chemically bound water excluding portlandite in the prepared samples before and after curing under different conditions was according to [118]:

$$W_{Chemically\ bound\ water} = \frac{Water\ loss_{75-550\ °C} - Water\ loss_{OH\ group\ in\ Ca(OH)_2}}{M_{800\ °C}} \times 100\% \quad \textbf{(3.4)}$$

where $Water\ loss_{105-600\ °C}$ corresponds to the weight loss from approximately 75 to 550 °C in the total mass, $M_{800\ °C}$ is the sample mass at 800 °C, $Water\ loss_{OH\ group\ in\ Ca(OH)_2}$ corresponds to the weight loss approximately from 400 to 500 °C in the total mass fraction.

3.3. Results

3.3.1. Loose bulk density and water absorption of the produced LWAs

The loose bulk density and water absorption are essential parameters for evaluating cold-bonding lightweight aggregates and have a significant influence on their application. Both parameters are shown in ***Table 3.3***.

Table 3.3 *Physical properties of the produced LWAs.*

Curing regime	Sample	Bulk density (kg/m^3)	Water absorption (%)	Average individual strength (MPa)
CO_2 curing	C1A I	614.6±2.0	33.6±0.6	1.60±0.32
	C3A I	668.6±3.0	32.2±0.4	1.95±0.82
	C7A I	738.4±1.8	29.8±0.4	3.14±0.78
	C1A III	753.6±4.5	25.9±0.5	2.97±0.98
	C3A III	715.8±3.6	26.3±0.8	2.03±0.66
	C7A III	605.3±2.2	30.2±0.1	0.57±0.22
Normal curing	S0A I	576.0±2.6	39.5±0.2	0.83±0.16
	S5A I	637.5±1.2	33.7±0.2	2.39±0.60
	S10A I	637.7±2.0	30.7±0.1	2.22±0.31

It can be seen that all the samples have a loose bulk density of around 576.0-753.6 kg/m^3, which is below 1200 kg/m^3 and thus satisfies the density requirement for lightweight aggregates according to EN 13055-1 (2002). The bulk density is highly related to the total mass of the carbonated aggregates, which was determined by the CO_2 uptake and water evaporation after drying. The carbonated samples show an increasing bulk density with increasing CO_2 curing duration in the samples containing HCP I, indicating that more carbonation products were formed with increased CO_2 curing duration, where portlandite was the main reactive phase to form calcium carbonates, elevating total mass directly

[101,119]. However, the HCP III group shows the opposite trend because portlandite was consumed after 1-day carbonation and the longer carbonation resulted in the decomposition of C-S-H gel and other hydration products, producing silica or aluminium gel containing abundant evaporation water [119,120]. These reactions lead to a reduction of the total mass during the drying process preceding the bulk density measurement. Internal cracks and pores significantly decrease the bulk density of the aggregates originated from HCP III after 7-day carbonation [121]. The density of the normal cured samples increases with the addition of SF, which can help promote the formation of C-S-H and modify the microstructure of the aggregates.

Additionally, LWAs produced with HCP I and HCP III show different trends in the water absorption, which is related to the microstructure evolution with carbonation. It is discussed further in the following sections. The formation of various carbonation products fills the pores inside the artificial aggregates if the carbonation level is appropriate, effectively lowering the internal porosity [78,101]. The water absorption of the studied artificial aggregates is higher than that of other reported artificial lightweight aggregates, which is commonly around 15% [101,115]. It might be attributed to not only the water absorption by the porosity but also water consumption by the rehydration of the dehydrated phases and reformation of ettringite in the 105 °C-dried aggregates [48,122].

3.3.2. Mechanical properties

Fig. 3.3 shows the maximum compression load of each produced aggregate in relation to diameters. The results illustrated in ***Fig. 3.3(a), (b)*** and ***(c)*** show the obvious trend that the compression load increases with the increasing diameter of the aggregates for both the CO_2 cured and normal cured samples, in agreement with the results reported in [123,124]. ***Table 3.3*** shows the average individual strength of all the produced aggregates and ***Fig. 3.4*** shows the strength of each individual aggregate. The average individual strength of the aggregates produced with HCP I increases with the increasing carbonation period while the aggregates produced with HCP III shows the opposite trend, which is illustrated in ***Fig. 3.4(a)*** and ***(b)***. The carbonation curing can contribute to the formation of calcium carbonates and then fill some pores to reduce the overall porosity and enhance the mechanical property. However, the aggregates obtained from HCP III may suffer carbonation shrinkage and internal cracking during carbonation process, leading to the reduction of individual strength. The addition of SF elevates the individual pellet strength of the produced aggregates as shown in ***Table 3.3*** and ***Fig. 3.4(c)***, which is attributed to the formation of C-S-H gel generated from the reaction between SF and portlandite produced by the hydration of Portland cement [117]. The advantage of carbonation is the fast strength development of the LWAs produced with HCP I and HCP III, especially if the carbonation time is optimized. The SF can also benefit the strength development but the pozzolanic reaction takes much longer under normal curing to gain adequate strength.

The average crushing strength in different diameter ranges has been calculated and is shown in ***Fig. 3.5***. The aggregates with a size from 5 to 7 mm show a dominant crushing strength compared to the aggregates with larger sizes. Similar results are reported by G. Perumal et.al [125]. They show that crushing strength of individual pellets does not increase with the increasing size of the aggregates.

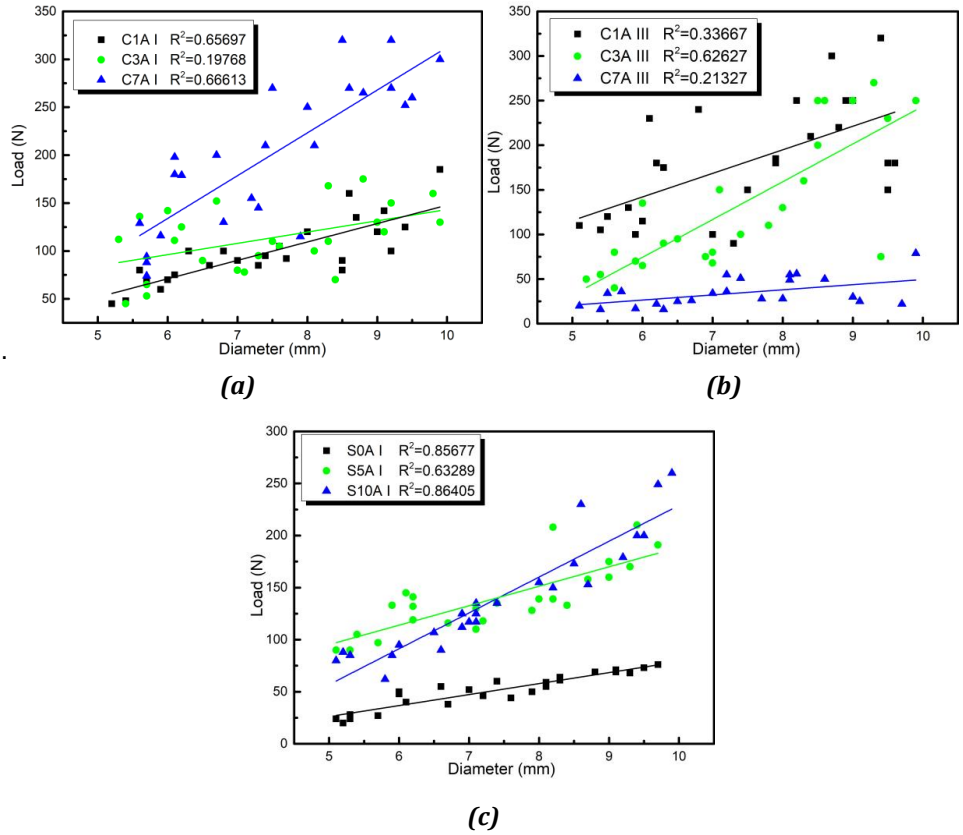

Fig. 3.3 *Compression load of the produced aggregates.*

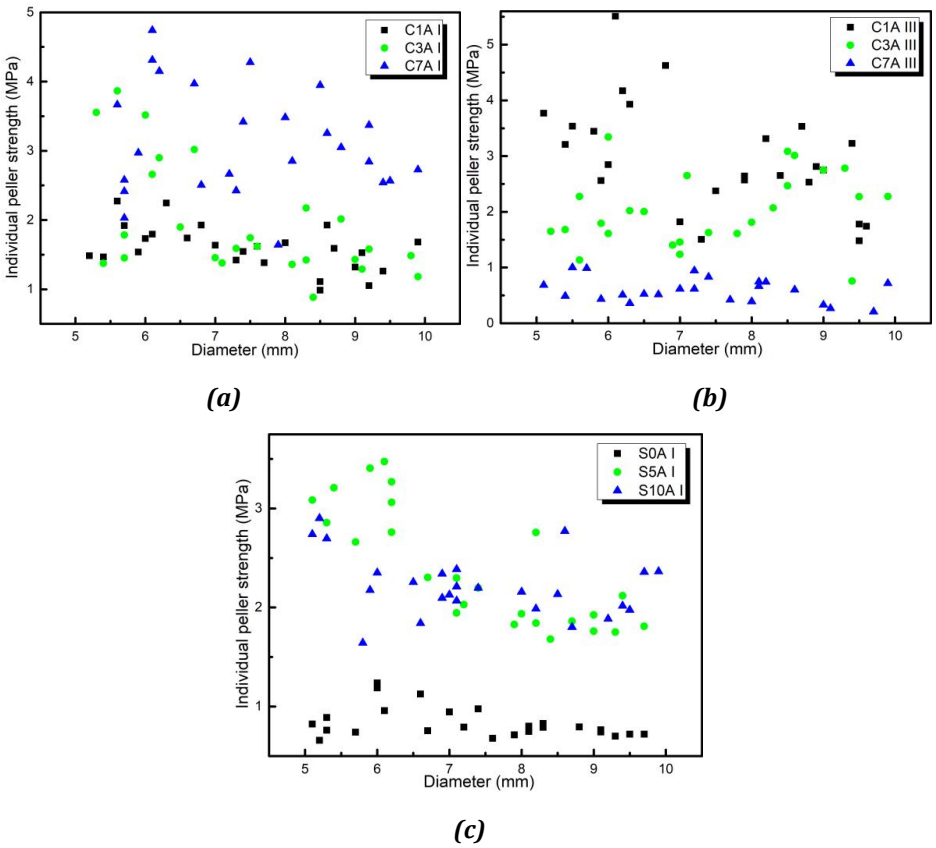

Fig. 3.4 *Individual pellet strength of the produced aggregates.*

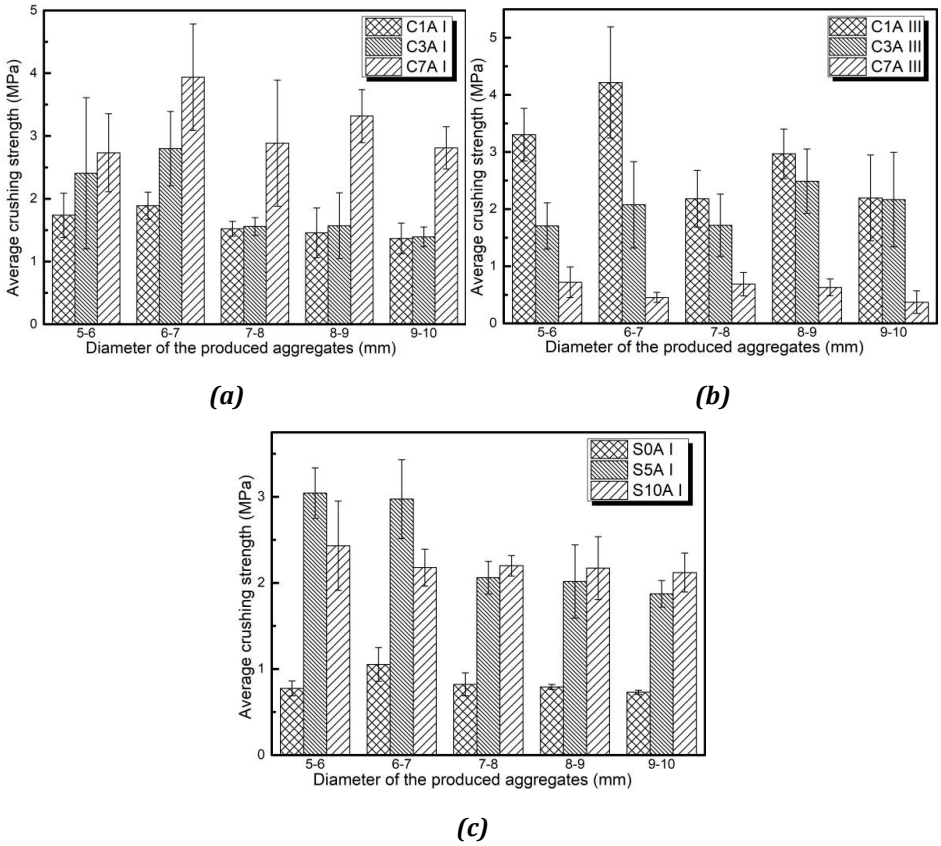

Fig. 3.5 *Average crushing strength of the produced aggregates.*

3.3.3. Reaction products and CO_2 uptake

3.3.3.1. Phase identification

The main mineral phases of HCP I and HCP III include C-S-H gel, portlandite, calcite, hemicarbonate, and unhydrated alite, belite as shown in ***Fig. 3.1***. ***Fig. 3.6(a)*** and ***(b)*** show XRD patterns of the carbonated aggregates of HCP I and HCP III, respectively. It can be seen that the intensity of diffraction peaks of portlandite decreases while calcite increases significantly with the increasing CO_2 curing duration. This is due to the formation of calcite during the carbonation reaction, which consumed portlandite in hydrated cement. The content of portlandite in HCP III is less than that in HCP I due to the high volume of ground granulated blast furnace slag (GBS) contained in CEM III [126]. The GBS also consumed the portlandite because it is pozzolanic, further reducing the portlandite content [22].

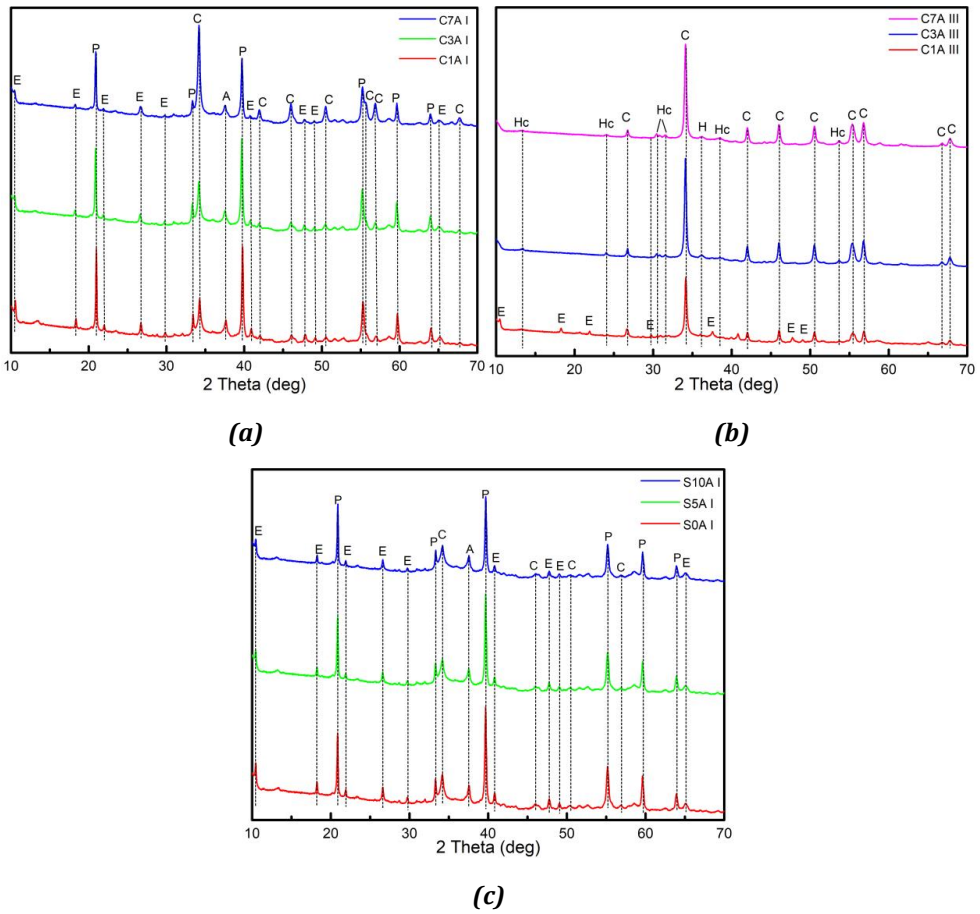

Fig. 3.6 *XRD patterns of the produced aggregates (P=portlandite, E=ettringite, A=Alite, C=calcite, Hc=hemicarbonate).*

The carbonation does not only consume portlandite but also affects ettringite, alite and C-S-H, which can account for the decreasing intensity of those peaks in the corresponding XRD curves [119,127]. The characteristic diffraction peak of ettringite around 10.51 °2θ is not visible in HCP I and HCP III before pelletization but occurs in C1A I and C1A III in line with the reformation of ettringite due to the high moisture content [24,122]. During the carbonation process, portlandite is able to delay ettringite carbonation because it acts like a buffer due to its higher reaction rate with CO_2 [128]. Therefore, the diffraction peaks of ettringite can be detected in all samples obtained from HCP I but disappear in samples obtained from HCP III after 3-day carbonation, because the overall portlandite content is much lower.

Fig. 3.6(c) shows XRD pattern of the aggregates produced with the mixtures of HCP I and SF. After another 28-day curing, the addition of SF preserves the original mineral composition of S0A I but changes the relative intensity of the peaks of portlandite in the

corresponding XRD curves, indicating that SF consumed portlandite to generate C-S-H gel, which can effectively glue particles together and provide additional strength [117].

3.3.3.2. Thermogravimetric analysis

Fig. 3.7 shows the TGA-DTG results of the produced aggregates. In general, the weight loss of the produced aggregates occurs in three stages: the loss of chemically bound water approximately between 75 and 550 °C; weight loss between 400 and 500 °C associated with the dehydroxylation of portlandite and a further weight loss approximately between 600 and 800 °C due to the decomposition of the carbonate groups in calcium carbonates [73,116–118].

Fig. 3.7(a) and ***(b)*** show the TGA-DTG curves of the carbonated aggregates produced with HCP I and HCP III, respectively. The intensity of the decomposition peaks of chemically bound water occurring around 75-300 °C and portlandite around 400-500 °C decreases with the increasing carbonation period, indicating the simultaneous carbonation of portlandite, C-S-H, AFt and AFm phases, etc. [119,129]. The significant difference between HCP I and HCP III systems is that no weight loss is observed around 400-500 °C in the HCP III system, demonstrating that calcium hydroxide content is negligible due to the reaction with CO_2, which is in line with the absence of portlandite peaks in the XRD data. The further weight loss peaks attributed to the decomposition of calcium carbonates become broader and sharper during the carbonation process. For instance, the decomposition temperature of calcium carbonates starts at around 460 °C and continues till 810 °C as shown in C7A III. This could indicate the presence of amorphous or poorly crystalline calcium carbonate that can decompose at lower temperatures, as reported in the literature [130]. The TGA-DTG curves of the aggregates under normal curing are similar and show the typical weight loss peaks of chemically bound water, portlandite and calcium carbonate. The intensity of the decomposition peak of chemically bound water occurring between 75-300 °C increases with the addition of SF due to the formation of secondary C-S-H gel via the reaction between SF and portlandite. The portlandite decomposition peak (400-500 °C) decreases because of the lower initial HCP I content and its consumption via the pozzolanic reaction, which is also in accordance with the above XRD results.

The amount of $Ca(OH)_2$, $CaCO_3$ and chemically bound water is calculated from TGA data and summarized in ***Table 3.4***. The amount of $Ca(OH)_2$ in carbonated aggregate samples decreases with the increased carbonation duration. Besides, an obvious increase of the amount of $CaCO_3$ is observed, from 5.20 to 35.60 wt.% in the HCP I system and from 2.55 to 48.57 wt.% in the HCP III system. The considerable change demonstrates that calcium hydroxide is not the only hydration product reacting with CO_2 during the carbonation process [119]. The addition of SF undoubtedly consumed portlandite and then contributed to the formation of C-S-H gel as illustrated in ***Table 3.4***.

Table 3.4 *Weight loss calculated from TGA (wt.%).*

Sample	$Ca(OH)_2$	$CaCO_3$	Chemically bound water
HCP I	24.17	5.20	15.42
HCP III	2.53	2.55	8.63
C1A I	21.20	12.63	31.74
C3A I	19.14	14.86	24.55
C7A I	13.95	35.60	18.73
C1A III	-	22.30	28.83
C3A III	-	44.52	21.54
C7A III	-	48.87	18.17
S0A I	23.64	5.41	28.71
S5A I	21.03	4.49	32.26
S10A I	17.30	4.02	32.80

Table 3.4 shows the amount of chemically bound water in the cement hydration phases like C-S-H gel, AFt, hemicarbonate, etc. which benefit the mechanical property [48,73]. The amount of chemically bound water increases after 1-day carbonation from 15.42 (HCP I) and 8.63 wt.% (HCP III) to 31.74 (C1A I) and 28.83 wt.% (C1A III), respectively, which is in contrast to the results reported in [131,132]. This can be attributed in part to the reformation of ettringite [122,133] according to XRD results. On the other hand, HCP I and HCP III were treated at 105 °C while the prepared samples were dried at 40 °C, contributing to the higher amount of chemically bound water determined from 75 to 550 °C. After 3- and 7-day carbonation, the chemically bound water decreases because further carbonation contributed to the decalcification or decomposition at a more extensive level of all hydration products [119]. The addition of SF elevates the amount of chemically bound water due to more C-S-H gel being formed.

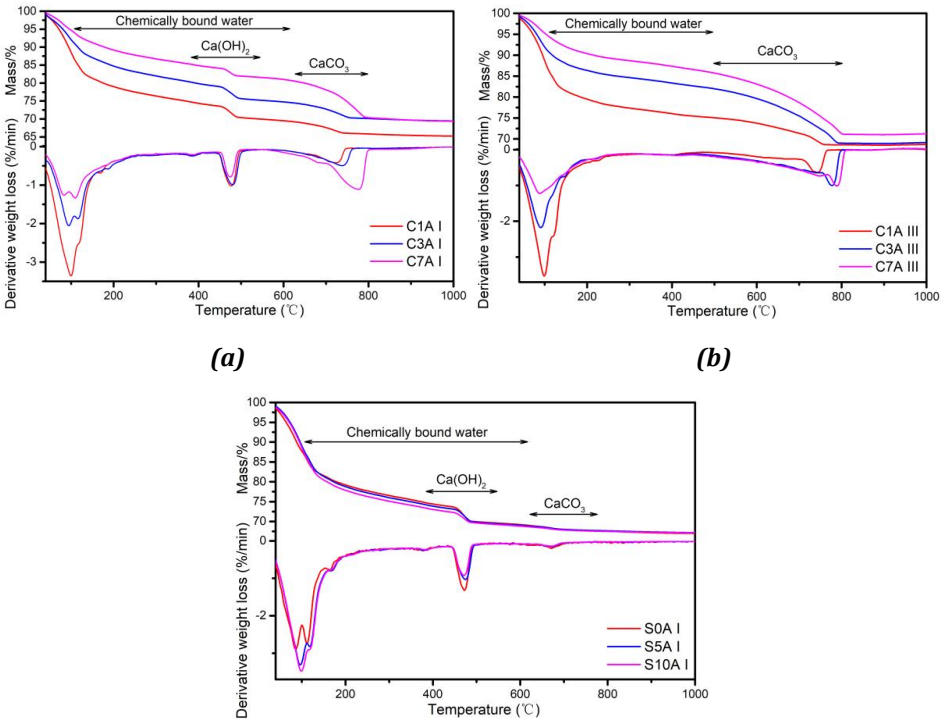

Fig. 3.7 *Weight loss determined with thermogravimetric analysis (TGA) and the first derivative of TGA (DTG) of the produced aggregates.*

3.3.3.3. FTIR analysis

The results of FTIR are presented in general terms by examining the infrared transmittance spectra in the region of 4000–400 cm^{-1} as shown in ***Fig. 3.8***. The broad bands at around 3410, 1658, 1640 cm^{-1} are associated with the O-H groups in water [134] as shown in all samples. Furthermore, the bands at 1107 cm^{-1} shown in ***Fig. 3.8(a), Fig. 3.8(c)*** and the shoulder at 1129 cm^{-1} detected in ***Fig. 3.8(b)*** can be attributed to S–O stretching vibrations of the sulphate phases [135]. The absorption peak at 3640 cm^{-1} originates from the O–H bond in $Ca(OH)_2$ in the samples containing HCP I [131]. This absorption peak disappears in the spectra of the aggregates out of HCP III, in accordance with the above XRD and TGA results that show portlandite was completely consumed after the 1-day carbonation treatment.

The broad bands detected in the range of 1400-1500 cm^{-1} and the peaks located at 870, 711 cm^{-1} are related to the CO_3 bending vibration [136–138]. The accelerated carbonation resulted in the formation of a large amount of calcium carbonates, visible in FTIR and verified by the above TGA and XRD results.

The typical sharp peak located at around 958 cm^{-1} is associated with the asymmetric stretching vibration of Si-O bonds in the C-S-H gel Q^2 units [78,139]. This peak shifts from 958 cm^{-1} to 1026 cm^{-1} after carbonation treatment, in line with the severe decomposition of C-S-H and formation of highly polymerized and elongated form of amorphous silica gel [131,136]. The absence of portlandite makes C-S-H gel the dominant carbonated subject during the carbonation process [119]. The formation of silica gel as seen with FTIR can explain the decreasing crushing strength of the aggregates containing HCP III after carbonation curing. The formation of silica gel ruined the structure of C-S-H which is commonly considered as a binding phase.

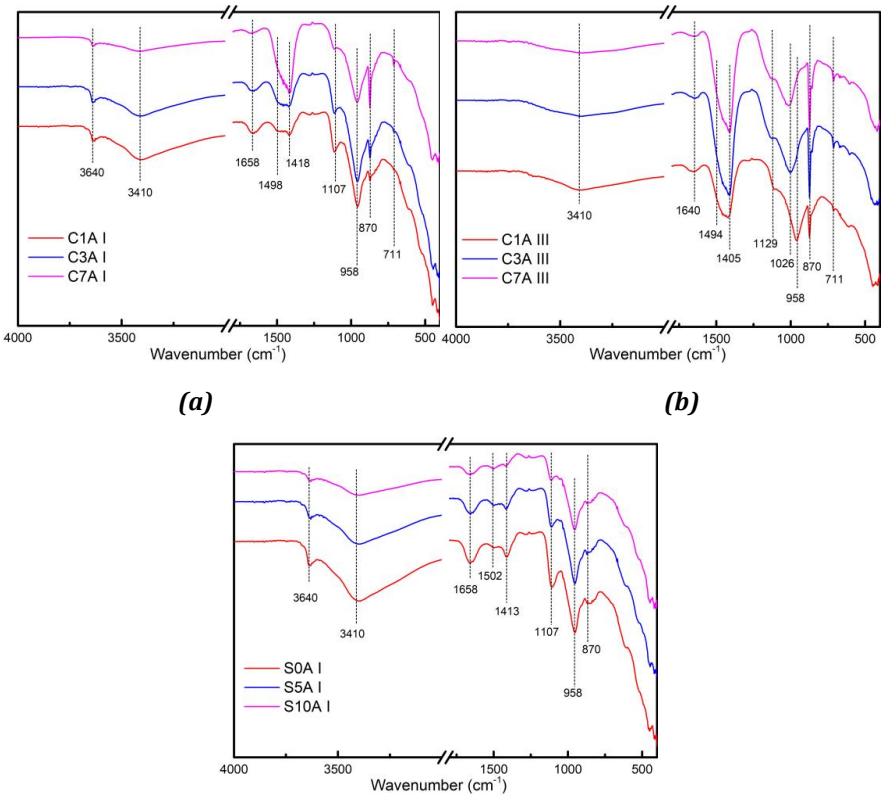

Fig. 3.8 *FTIR spectra of the produced aggregates.*

3.3.3.4. Nitrogen physisorption analysis

The BET specific surface area and pore size distribution were measured as shown in ***Fig. 3.9*** in order to obtain more details about the pore structure of the produced aggregates on a nanoscale.

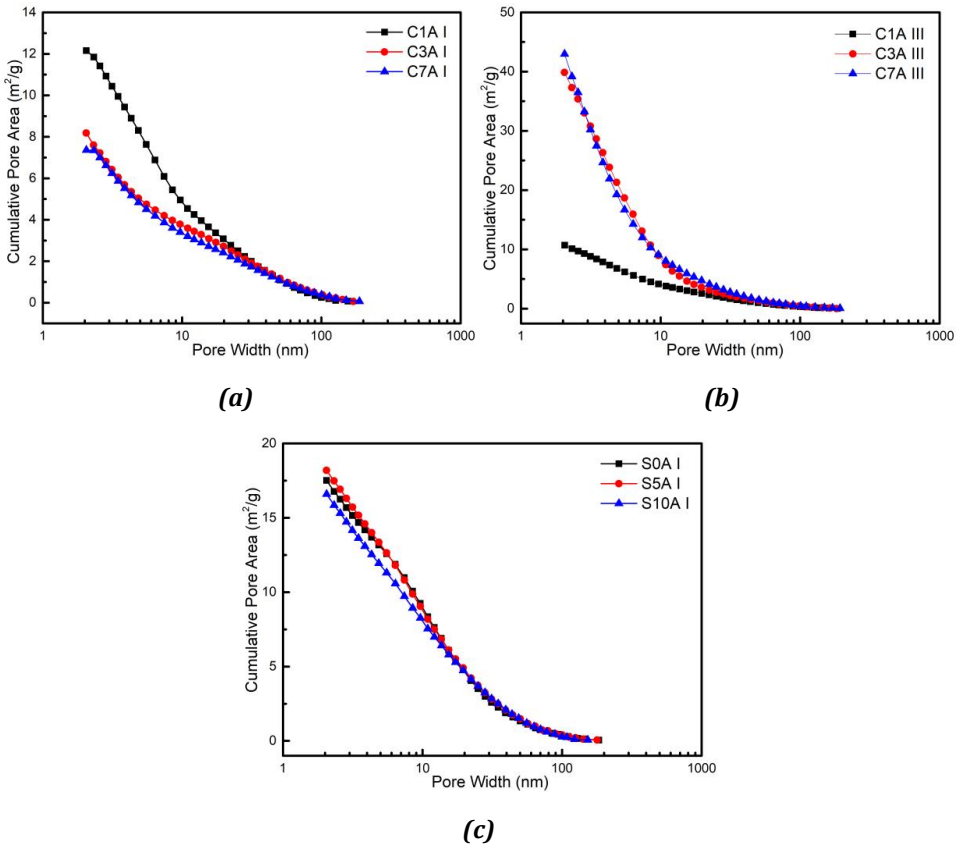

Fig. 3.9 *Cumluative pore area of the produced aggregates.*

The specific surface area of the carbonated aggregates containing HCP I decreases with the carbonation duration as shown in ***Fig. 3.9(a)***. C-S-H gel contains large amounts of gel pores with relatively higher specific surface area than other hydration products [48]. The carbonation leads to the partial decalcification of C-S-H gel and the reduction of gel pores [140,141]. The carbonated aggregates obtained from HCP III instead shows a much higher specific surface area of C3A III and C7A III compared to C1A III. It is reasonable to assume that C_3A III and C7A III are strongly affected by the severe decomposition of C-S-H gel as analysed in FTIR results and the subsequent formation of silica gel, which increases the porosity. The addition of SF shows little effects on the specific surface area of the normal cured aggregates as shown in ***Fig. 3.9(c)***. The cumulative pore area slightly increases and then decreases with the addition of SF. 5% addition of SF undoubtedly contributed to the formation of C-S-H gel, in line with the results obtained from TGA. However, more addition of SF may not benefit the formation of more C-S-H gel as the chemically bound water only increases from 32.26 to 32.80 wt.% in TGA results. A SF powder content level of 10% might affect the optimal pore size distribution as reported in [142].

3.3.3.5. SEM

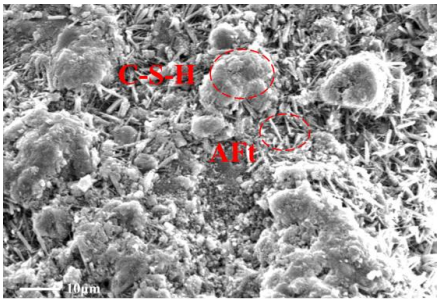

(a) *C1A I*

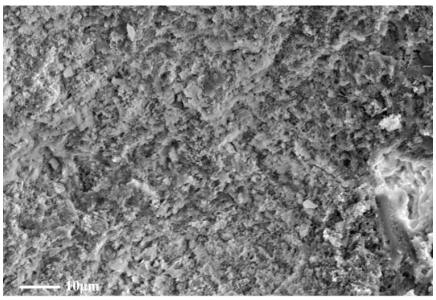

(b) *C7A I*

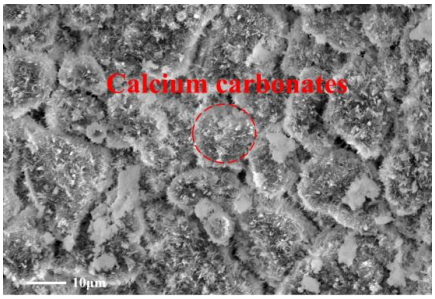

(c) *C7A III*

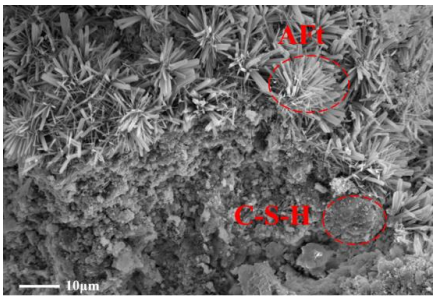

(d) *S5A I*

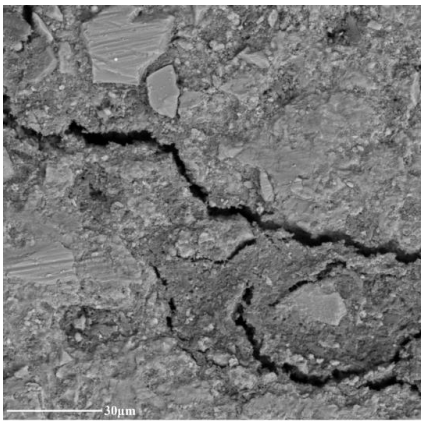

(e) *C3A III*

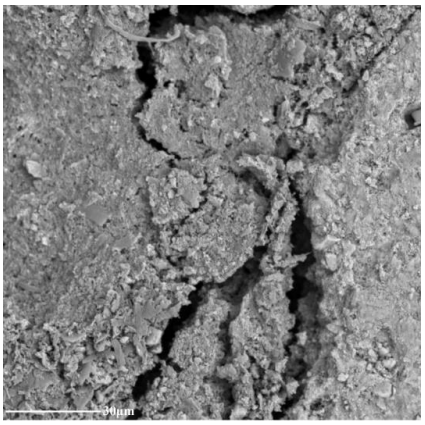

(f) *C7A III*

Fig. 3.10 *SEM picture of the produced LWAs.*

Fig. 3.10(a) and ***(b)*** show the morphology of the produced aggregates originating from HCP I after 1- and 7-day carbonation, respectively. The needle-like ettringite grows across C-S-H phases, arranged in a dense structure as shown in ***Fig. 3.10(a)*** while after 7-day carbonation, ettringite phases seem to have disappeared almost entirely (***Fig. 3.10(b)***).

S5A I shows a similar morphology to C1A I, where the ettringite is denser and larger than in C1A I. Notably, the 7-day carbonated aggregates obtained from HCP III shows an entirely different morphology as shown in ***Fig. 3.10(c)***. The plate-like calcium carbonates are covered by tiny-needle-like phases which can be attributed to the crystallite calcium carbonates or silica gel, arranged in a loose structure due to the degeneration of C-S-H structure. The carbonation caused the decalcification of the interlayer calcium and then the degeneration of C-S-H dense network structure, in accordance with the FTIR results. Moreover, ***Fig. 3.10(e)*** and ***(f)*** were obtained based on Backscattered Electrons (BSE) mode to illustrate the visible internal cracks in HCP III-type aggregates after 3- and 7-day carbonation, further confirming carbonation shrinkage and cracking due to the severe decomposition of C-S-H.

3.4. Discussion

The individual strength of the carbonated aggregates originated from HCP I increases from 1.60 to 3.14 MPa after 7-day carbonation, in line with the re-cementation effects of carbonation. Without carbonation, the normal cured aggregates (S0A I) only reach 0.83 MPa, indicating that carbonation can benefit the strength development. A reduction of porosity is observed most likely because the volume of the carbonates formed is 11–12% greater than the volume of portlandite as reported in [119,143], which can optimize the pore structure and then enhance the mechanical property. However, the HCP III system shows the opposite results, where the individual strength of the carbonated aggregates decreases from 2.97 to 0.57 MPa, despite more carbonation products being formed over time. This is caused by the decomposition of C-S-H. It is suggested that carbonation of C-S-H is accompanied by a decalcification process. The decomposition of C-S-H gel can happen at a high calcification level [144]. In HCP I system, the large amounts of portlandite (24.17 wt.%) acted as a buffer and were carbonated preferentially, protecting C-S-H from decomposition while densifying the microstructure at the same time [119]. In HCP III system, however, the small amount of portlandite (2.55 wt.%) was consumed rapidly resulting in the decomposition of C-S-H followed by severe carbonation shrinkage and cracking [144] and an increase in porosity because of it. This increased porosity also made further carbonation even easier. This is supported by TG results where the portlandite content in HPC I is still 13.95 wt.% after 7-day carbonation, while no portlandite is detectable in HCP III after only 1-day carbonation. The peak shift from 958 to 1026 cm^{-1} in FTIR and the significantly elevated specific surface area from 10.69 to 42.96 m^2/g after carbonation treatment of HCP III also support this. On all account, the aggregates obtained from HCP III suffered carbonation shrinkage and internal cracking during carbonation process, leading to the reduction of individual strength and increasing water absorption [127] as shown in ***Fig. 3.11*** and ***Fig. 3.12***.

The addition of SF undoubtedly increases the individual strength of the produced aggregates from 0.83 to 2.39 MPa due to the formation of new C-S-H gel to create a dense structure as shown in ***Fig. 3.11***. The sufficient portlandite content plays an important role

in the pozzolanic reaction with silica fume to promote the formation of C-S-H gel [117], in line with the increasing content of chemically bound water from 28.71 to 32.80 wt.%. Furthermore, the individual strength of S10A I is a little lower than S5A I. As can be seen in ***Table 3.4***, the amount of portlandite decreases from 21.03 to 17.30 wt.% and the amount of chemically bound water increases slightly from 32.26 to 32.80 wt.%, indicating the minor increasing content of C-S-H gel, AFt phases, etc. when the addition of SF is elevated from 5 to 10%. The slight increase of hydration phases seems to play little role in the enhancement of mechanical property. As reported in [115], the excess use of silica fume with a high surface area is not conducive to producing a compact structure during pelletization. It can be supposed that the strength development of the aggregates originated from HCP I and SF depends on the formation of C-S-H gel and the compaction between SF and HCP I powder.

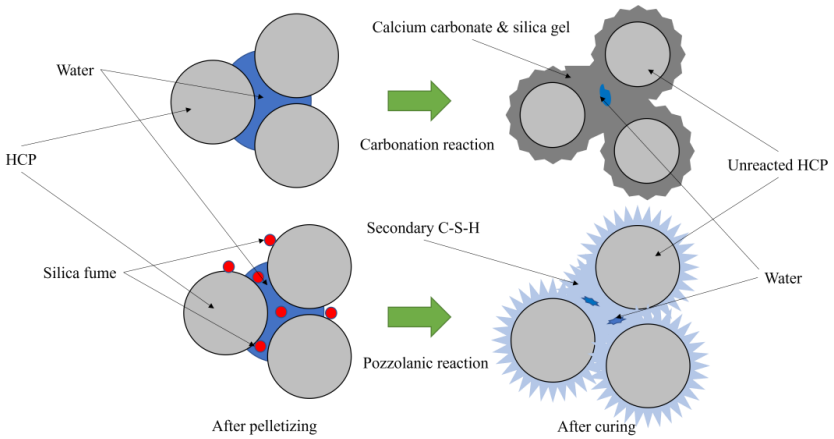

Fig. 3.11 *Schematic of the re-cementation of the aggregates by carbonation and pozzolanic reaction.*

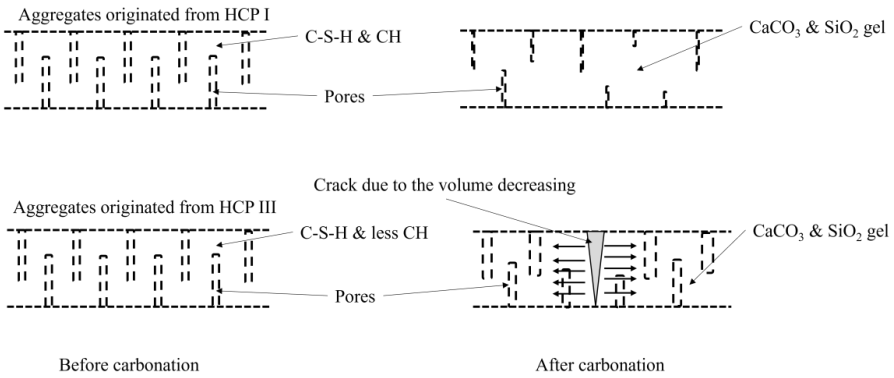

Fig. 3.12 *Schematic of microsturcture of the produced aggregates before and after carbonation.*

Carbonation and pozzolanic reaction are both beneficial to the strength development while carbonation is faster and more sustainable. The addition of silica fume undoubtedly elevates the raw materials cost and extends the curing period, thus increasing the total manufacturing cost of LWAs. Meanwhile, using CO_2 uptake to enhance the mechanical property is a proven emissions reduction solution, permanently removing CO_2 from the atmosphere. However, taking the mechanical performance into account, the carbonation curing period should be optimized to show the jointly positive effects on both CO_2 capture amount and strength development. Hence, carbonation might be an inappropriate curing method for HCP III-type aggregates due to destruction of C-S-H and the resulting strength loss. HCP I, as a Ca-rich waste solid containing abundant portlandite, shows an enormous potential for producing high strength LWAs and CO_2 capture capacity at the same time via the optimized carbonation curing method. For instance, Jiang and Ling [145] produced steel slag based artificial aggregates to achieve an optimal strength value of 5.24 MPa via post carbonation method, significantly increasing the strength compared to the synchronized carbonation during granulation. However, the optimal carbonation period should be emphasized in any case to avoid affecting negatively the resulting mechanical performance of the artificial aggregates even though CO_2 uptake is continuously increasing [146].

3.5. Conclusions

The comparative study was conducted to figure out the effects of the portlandite amount in HCP I and HCP III on the aggregates under carbonation curing. The addition of up to 10 wt.% silica fume into HCP I was attempted to make full use of the considerable amount of portlandite to prepare artificial aggregates under normal curing. The effects of re-cementation during carbonation and pozzolanic reactions on physical properties and mineral composition, microstructure of the produced aggregates have been investigated, which can be crucial and essential for the performance prediction of LWAs originated from the real demolished materials. Based on the findings from this study, the following conclusions can be drawn:

Carbonation reaction benefits the fast strength development because the formation of calcium carbonates decreases the porosity, optimizing the pore structure and then benefiting the mechanical property. However, carbonation curing is more appropriate for HCP I-type aggregates than HCP III-type aggregates due to the different amount of portlandite. HCP I-type aggregates show enormous potential in elevating the strength along with CO_2 capture capacity via the extended carbonation curing until the optimal curing period is reached. The optimal curing period for HCP III-type aggregates is short so that the individual strength and CO_2 uptake are undoubtedly limited.

The sufficiently available portlandite acts like a buffer to prevent decomposition in C-S-H and other phases caused by carbonation. The lack of available portlandite makes C-S-H the dominant phase subjected to carbonation, along with the decomposition of C-S-H at

the extensive carbonation calcification. Consequently, shrinkage and internal cracking during carbonation can occur, leading to a significant reduction of individual strength.

Addition of silica fume elevates the individual strength of the aggregates originated from HCP I after normal curing due to the formation of C-S-H gel. 5% addition of silica fume is the optimal dosage, and S5A I shows the highest individual strength among the normal cured aggregates in this study. 10% of silica fume is harmful to the compaction of the mixed powder during pelletizing, which leads to a reduction of strength performance.

Carbonation and pozzolanic reaction are both beneficial to the strength development while carbonation takes the advantages in sustainable development and sustainability in this study, which can reduce CO_2 emissions and manufacturing cost of LWAs.

CHAPTER 4

4. Recycling and valorization of hydrated cement blends in mortars via semi-dry carbonation – the role of waste glass, granulated blast furnace slag and fly ash

The recycling technology of demolished concrete wastes in building materials manufacture provides a possibility of achieving sustainable constructions. Carbonation pre-treatment helps to enhance the performance of recycled concrete fines effectively. To investigate the effects of semi-dry carbonation on the utilization of recycled concrete fines containing supplementary cementitious materials (SCMs) in new concrete production, recycled blended cement paste powder (RBCPs) containing granulated blast furnace slag (GBS), fly ash (FA), or recycled glass powder (RGP) were prepared in the lab. The performance of mortars produced by carbonated recycled blended cement paste powder (C-RBCPs) and RBCPs blended cement were evaluated. C-RBCPs exhibit superior performance in workability and mechanical properties of prepared mortars compared to carbonated OPC powder. The results indicate that the RBCPs exhibit a lower carbonation degree (less than 53.4%) and CO_2 uptake compared to OPC samples due to the lack of available Ca in the originally blended cement after incorporation of GBS, FA and RGP. As the main carbonation products, calcite, aragonite, and vaterite are all observed in C-RBCPs, the category of SCMs exhibited visible influences on the crystal format of calcium carbonate, as well as the reactivity of C-RBCPs in blended cement mortars. Overall, semi-dry carbonation can promote the reactivity of C-RBCPs efficiently. The effects of the SCMs category should be considered in the recycling processes of cement wastes. The application of GBS, FA, and RGP in blended cement can help to achieve excellent sustainability of C-RBCPs blended mortars after semi-dry carbonation pre-treatment.

This chapter is reproduced from: G. Liu, Y. Tang, J. Wang, Recycling and valorization of hydrated cement blends in mortars via semi-dry carbonation – The role of waste glass, granulated blast furnace slag and fly ash, Constr. Build. Mater. 401 (2023) 132987. https://doi.org/10.1016/j.conbuildmat.2023.132987.

4.1. Introduction

Carbonation treatment has been introduced in the recycling of concrete wastes in recent years. Recycled concrete wastes after carbonation treatment exhibit a significant improvement in reducing water demand, densifying microstructure, and promoting mechanical behaviour (see ***Table 4.1***).

Table 4.1 *Summary of carbonation treatment of recycled concrete wastes in literature.*

References	Research objective	Treatment conditions	Notes
Xuan et al. [57]	Recycled concrete aggregates (5 mm-20 mm)	25°C, CO_2 100%, 0.1bar and 0.5 bar	Pure CO_2 and a high-pressure chamber were needed.
Bal et al. [8]	Recycled cement pastes powder based on OPC (< 75 um)	20°C, CO_2 100%, RH 60±5% (semi-dry carbonation)	Pure CO2 was needed. Silica gel was extracted.
Zajac et al. [147]	Recycled cement pastes powder based on CEM III (< 150 um)	20°C, CO_2 10%, water environment (wet carbonation)	Water disposal was needed. The pozzolanic reactivity of carbonated powder was proved.
Ouyang et al. [148]	Recycled cement pastes powder based on OPC (<150 um)	20°C, CO_2 20±3%, RH 70±5%, 0.1MPa (semi-dry carbonation)	Strong bonding between the surface of carbonated powder and C-S-H was proved.
Peiliang et al. [149]	Recycled cement pastes fines based OPC (<150 um)	Ambient temperature, CO_2 99%, water environment (wet carbonation)	Nano-silica was produced. Chemical solution disposal was needed.

Zhan et al. finds the hydrated cement in concrete wastes presented a high carbonation reactivity, the calcium carbonates formation can effectively densify the micro-pores, and then reduce the water absorption after carbonation [56,57]. Shi et al. points out that the presence of amorphous silica gel from the carbonation of C-S-H can exhibit a high pozzolanic reactivity [8]. Zajac et al. investigates the hydration process of blended cement containing carbonated cement powder, the amorphous silica-aluminate gel can be fast reacted in the first curing days, more C-S-H gels can be produced [118,150,151]. These studies effectively prove the feasibility of the application of pre-carbonation treatment to enhance the recyclability of waste hydrated cement wastes. As is well known, the chemical compositions and hydration products of blended cement can be modified by the addition of SCMs. Many previous investigations have confirmed the variation of Ca/(Si+Al) in C-(A)-S-H gels after SCMs incorporation, for example, a high volume of FA and RGP in blended cement increases the available Si and reduces the Ca at the same time, the average Ca/Si ratio in reaction products decreases to 1.3 compared to normal OPC samples [152]. On the other hand, portlandite is significantly consumed by the pozzolanic reaction of

SCMs particles [26]. Therefore, the carbonation mechanisms of hydrated blended cement materials could be different to normal OPC. The latest study reveals that blended cement composites exhibit a poor carbonation resistance compared to OPC due to the less available Ca in reaction products [153,154]. Furthermore, Ca/Si ratio of C-S-H gel is also identified to be a critical factor during carbonation, consequently, the carbonation products and structures can be influenced [155]. The engineering applications and studies of SCMs in cement concrete are relatively prevalent. However, most of the existing studies of demolition concrete wastes recycling by carbonation pre-treatment focus on the neat OPC based materials. The influences of SCMs on recyclability of carbonated cement-based wastes in the new concrete production are still unclear. The carbonation mechanism of hydrated SCMs-cement composites and the performance evaluation of recycled concrete need to be investigated.

This study aims to investigate the role of mixed SCMs (GBS, FA and RGP) in recyclability of hydrated blended cement composites by semi-dry carbonation pre-treatment. In addition, recycling and application of treated fines in production of new blended mortars were evaluated. The effects of mixed GBS, FA, and RGP on carbonation products, reactivity and leaching properties of recycled blended cement paste powders (RBCPs) were characterized and addressed. Hydration kinetics, hydration products, mechanical performance and sustainability efficiency of recycled blended cement paste powders (C-RBCPs)-cement composites were analyzed and discussed. The related results can contribute to a deep understanding of blended cement concrete recycling by carbonation, and their high-end application in low carbon footprint building materials.

4.2. Materials and methods

4.2.1. Materials

The applied ordinary Portland cement (CEM I 52.5 N) was provided by ENCI, the Netherlands. The supplementary cementitious materials (SCMs) for the preparation of various blended cement were ground granulated blast furnace slag (GBS), fly ash (FA), and recycled waste glass powder (RGP). The chemical and mineral compositions of materials are shown in ***Table 4.2*** and ***Fig. 4.1***. The particle size distributions of powders are presented in ***Fig. 4.2***.

Table 4.2 *Chemical composition of raw materials [wt.%].*

Chemical composition	CEM I 52.5 R	RGP	GBS	FA
Na_2O	-	14.651	-	-
MgO	1.712	1.298	8.57	1.141
Al_2O_3	3.793	1.93	13.214	26.98
SiO_2	16.188	68.328	29.407	51.442
SO_3	4.055	0.086	2.639	1.121
K_2O	0.187	0.702	0.424	1.84
CaO	67.968	11.904	42.665	5.83
TiO_2	0.277	0.062	1.487	1.78
Cr_2O_3	0.01	0.117	0.001	0.034
MnO	0.094	0.022	0.398	0.057
Fe_2O_3	3.589	0.364	0.366	8.271
ZnO	0.1	0.009	-	0.022
BaO	0.005	0.061	0.081	-
PbO	0.005	0.05	-	0.009
P_2O_5	0.42	-	-	0.849
Cl	0.041	0.019	0.011	-
LOI	0.72	1.34	1.15	2.27

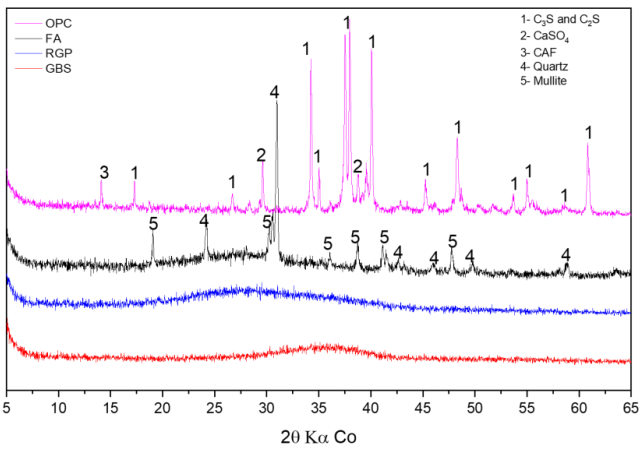

Fig. 4.1 *XRD patterns of cement, FA, GBS and RGP.*

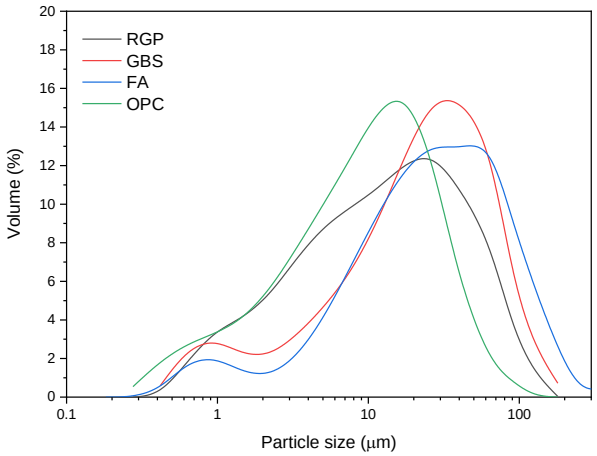

Fig. 4.2 *Particle size distribution of RGP, GBS, FA and cement.*

4.2.2. Preparation of RBCPs and C-RBCPs

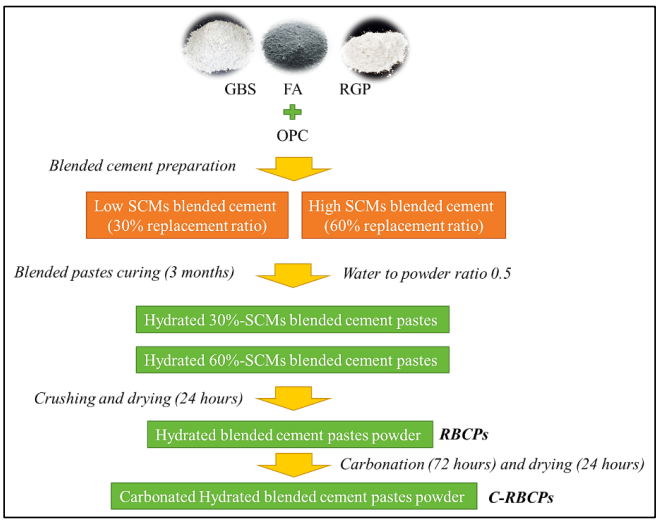

Fig. 4.3 *Preparation process of RBCPs and C-RBCPs.*

The preparation of RBCPs and C-RBCPs is shown in ***Fig. 4.3***. Different cement blends were prepared by mixing dry ordinary Portland cement (CEM I 52.5 R) and GBS, FA, or RGP. The cement replacement ratio was 30% (labeled as 'L') and 60% (labeled as 'H'), respectively. Then, the cement blends were mixed homogenously with distilled water (w/b =0.5). At the same time, pure cement paste (labeled as OPC) was prepared as the reference. The curing duration lasted for 3 months. Afterward, the hardened pastes samples were crushed and milled into powder by using a disc mill and dried in the oven at 105 °C for 24 hours. At last, RBCPs were collected.

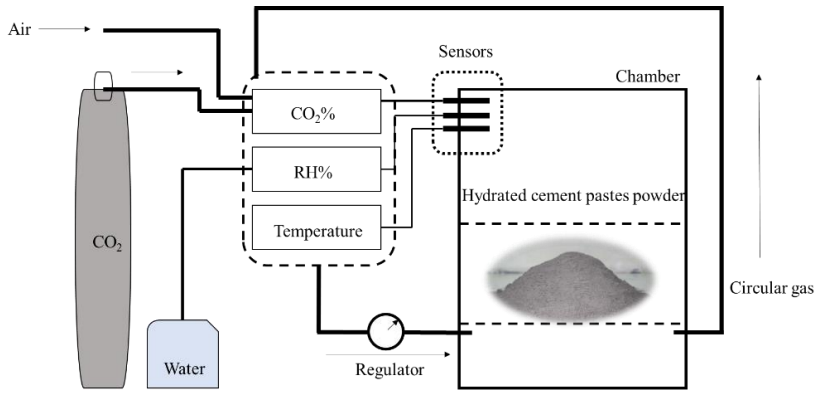

Fig. 4.4 *Equipment for carbonation pre-treatment.*

C-RBCPs were produced by the carbonation of RBCPs in a climate chamber with CO_2 flow gas. At first, RBCPs were placed in a stainless-steel plate and moved into the climate chamber. The carbonation conditions were set as 20% CO_2, 25 °C, and RH 75% for 3 days. Then, the carbonated powder was dried in the oven at 105°C for 24 hours to remove free water. Then, the collected dry powder was used for other tests. Sample code labeled with a 'C' indicated that it was carbonated. The schematic picture of carbonation is shown in ***Fig. 4.4***. The particle size distributions of RBCPs and C-RBCPs are shown in ***Fig. 4.5***.

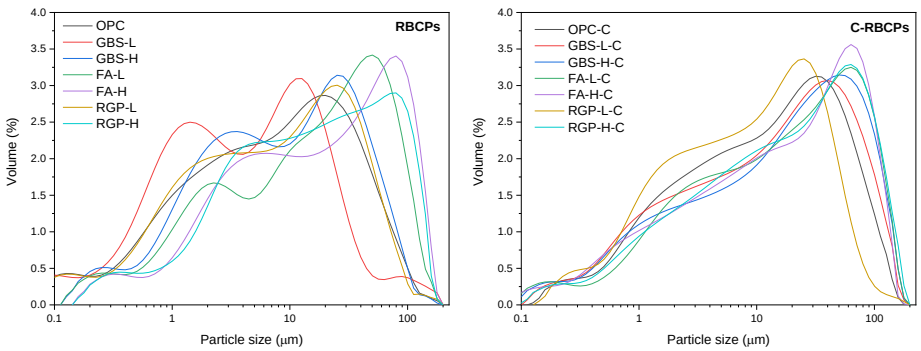

Fig. 4.5 *Particle size distribution of RBCPs and C-RBCPs.*

4.2.3. Mix design of mortars containing RBCPs and C-RBCPs

RBCPs and C-RBCPs were utilized to replace ordinary Portland cement in the production of blended cement mortars. The replacement ratio was set as 30%, the water to binder ratio was 0.5, standard sand to binder ratio was 3 (standard mortar). The mix design of blended mortars is shown in ***Table 4.3***.

Table 4.3 *Mix design of blended mortars (kg/m³).*

Sample ID	Cement (kg)	RBCPs (kg)	C-RBCPs (kg)	Standard sand (kg)	Water (kg)
RGP-L-M	339.85	145.65		1456.50	242.75
RGP-H-M	340.05	145.73		1457.34	242.89
GBS-L-M	340.80	146.06		1460.56	243.43
GBS-H-M	341.84	146.50		1465.02	244.17
FA-L-M	339.75	145.61		1456.07	242.68
FA-H-M	340.05	145.73		1457.34	242.89
OPC-M	339.55	145.52		1455.21	242.54
RGP-L-C-M	340.52		145.94	1459.37	243.23
RGP-H-C-M	340.89		146.09	1460.94	243.49
GBS-L-C-M	341.84		146.50	1465.02	244.17
GBS-H-C-M	342.40		146.74	1467.44	244.57
FA-L-C-M	340.43		145.90	1458.97	243.16
FA-H-C-M	340.71		146.02	1460.17	243.36
OPC-C-M	341.59		146.39	1463.94	243.99

4.2.4. Test methods

4.2.4.1. Fresh and hardened behaviours of RBCPs and C-RBCPs blended mortars

The slump-flow of fresh mortars was conducted by using the flow table test, according to EN 1015-3. An average value of two tested diameters was recorded by using a standard conical ring. The flow ability enhancement ratio was calculated according to the following:

$$Flow\ ability\ enhancement\ ratio\ (\%) = \frac{d_{RBCP} - d_{C-RBCP}}{d_{RBCP}} \times 100\% \qquad \textbf{(4.1)}$$

d_{RBCP}- slump flow of mortars containing RBCP

d_{C-RBCP}- slump flow of mortars containing C-RBCP

The mechanical properties of blended cement mortars were evaluated by compressive strength after 7, 28 and 90 days of normal curing. A strength test bench of concrete was used. 3 parallel cube samples (40 mm × 40 mm × 40 mm) were prepared for the

compressive strength test. The value of compressive strength was recorded by the average strength of 3 mortar cubes.

The SAI of various recycled pastes powder was evaluated by the compressive strength of blended mortars after 7, 28, and 90 days of curing. Ordinary Portland cement (CEM I 52.5 N) mortar was selected as the reference, the calculation was accorded with the following equation:

$$SAI = \frac{M_S}{M_{OPC}} \times 100\% \quad \textbf{(4.2)}$$

SAI- strength activity index of RBCPs or C-RBCPs

M_S- compressive strength of RBCPs or C-RBCPs blended mortar

M_{OPC}- compressive strength of reference mortar

4.2.4.2. Hydration heat flow of RBCPs and C-RBCPs blended cement

The reaction heat of blended cement was recorded by using an isothermal calorimeter (TAM Air). The blended cement was mixed with water until homogeneously in the plastic cup, then the paste samples were poured into the glass ampoules carefully. Afterwards, the ampoules were sealed and loaded into the test channels. The test was running at 20 °C and lasted for 50 hours.

4.2.4.3. Characterization of reaction products

The chemical compositions of cement, GBS, FA and RGP were tested by using X-ray fluorescence (PANalytical Epsilon 3XL). The powder was mixed with wax binder homogenously, then the mixture was pressed into tablet sample for XRF test. The results were calculated and collected from the Epsilon software.

To characterize the variation of mineral composition in RBCPs and C-RBCPs, and the relevant reaction products in hydrated blended cement, a Brucker D4 was applied. The hydrated paste samples after 28 days of curing were crushed and immersed into acetone for 7 days to exchange the free water in samples to cease the hydration reaction. Then the mixtures were moved to the oven to remove the evaporable water at 40 °C for 24 hours. Afterward, the dried samples were milled into powder by using an XRD mill (Retsch McCrone Micronizer mill) for scanning. The setting of XRD was 0.018 °/step and 0.4 s/step with 40 KV.

To further observe the chemical bond change in samples. The Frontier transform infrared spectroscopy (FTIR) test was performed in a Varian 3100 instrument with powdered samples. The test parameters were set to a scanning range of 4000 to 400 cm^{-1}, and a resolution of 2 cm^{-1}.

For the calculation of calcium hydroxide consumption and carbonation degree of recycled powders. The thermogravimetric analysis (TGA) was conducted by using an STA 449 F1 instrument. The test temperature range was set from 40 to 1000 °C. The heating rate was 10 °C/minute and N_2 was applied as the carrier gas.

4.2.4.4. Leaching properties of RBCPs and C-RBCPs

The leaching behaviour of RBCPs and C-RBCPs was evaluated by using Inductively Coupled Plasma Atomic Emission Spectrometry (ICP-OES) and Ion Chromatography (IC). The leachates were filtered by using a 0.017-0.030 nm membrane filter from the mixtures of distilled water and powder samples (L/S=10) after a dynamic shaking (250 rpm, 24 hours). For the ICP-OES test, the filtrates were acidified with HNO_3 until the pH<2.

4.2.4.5. Evaluation of calcium carbonate formation

Due to the poorly crystallized calcium carbonate formed in this study, the calculation of total calcium carbonate in C-RBCPs included 2 parts according to TG results. Poorly crystallized calcium carbonate was calculated by the decomposition between 520 and 720 °C, while the well-crystallized calcium carbonate was evaluated by the decomposition between 720 and 950 °C [156]. Then CO_2 uptake ability was roughly evaluated by the decomposition of all calcium carbonate during TGA test according to:

$$CO_2\ uptake\ (\%\ in\ gram\ of\ unreacted\ cement\ blends) = \left(\frac{M^c_{520}-M^c_{950}}{M^c_{950}} - \frac{M_{520}-M_{950}}{M_{950}}\right) \times 100\% \quad \textbf{(4.3)}$$

$M^c_{520} - mass\ ratio\ of\ C-RBCPs\ at\ 520\ °C$

$M^c_{950} - mass\ ratio\ of\ C-RBCPS\ at\ 950\ °C$

$M_{520} - mass\ ratio\ of\ RBCPs\ at\ 520\ °C$

$M_{950} - mass\ ratio\ of\ RBCPs\ at\ 950\ °C$

The proportion of poorly crystallized calcium carbonate in total calcium carbonate was calculated according to:

$$Poor\ crystallized\ calcium\ carbonate\ (\%) = \frac{M_{520}-M_{720}}{M_{720}-M_{950}} \times 100\% \quad \textbf{(4.4)}$$

The increased carbonation degree of C-RBCPs was calculated according to the following two equations:

$$Carbonation\ degree\ (\%\ in\ gram\ of\ unreacted\ cement\ blends) = \frac{\frac{M_{520}-M_{950}}{M_{950}}}{\frac{M_{CaO}\times 44}{56}} \times 100\% \quad \textbf{(4.5)}$$

$M_{520} - mass\ ratio\ at\ 520\ °C$

$M_{720} - mass\ ratio\ at\ 720\ °C$

$M_{950} - mass\ ratio\ at\ 950\ °C$

$M_{CaO} - mass\ ratio\ of\ CaO\ from\ XRF\ test$

$44 - molar\ mass\ of\ carbon\ dioxide$

$56 - molar\ mass\ of\ CaO$

$$Increased\ carbonation\ degree\ (ICD)(\%) = CD_{before} - CD_{after} \quad \textbf{(4.6)}$$

CD_{before}- Carbonation degree of RBCP

CD_{after}- Carbonation degree of C-RBCP

4.2.4.6. Evaluation of sustainability efficiency

The sustainability efficiency (MPa/(kg CO_2/m^3))was calculated by the ratio of compressive strength (90 days) to total CO_2 emission of 1 m^3 of blended mortar, which indicates the value of strength gaining (MPa) by per kilograms of CO_2 emission (modified from [157]) The CO_2 emission of cement, sand, and water production are 930 kg/ton, 4 kg/ton, and 0.196 kg/ton, respectively [37]. The CO_2 for carbonation pre-treatment was also considered in this study, the CO_2 emission of inlet CO_2 gas during production is around 23.8 kg/ton [158]. The CO_2 emission of RBCPs recycling and transportation was around 21.2 kg/ton [159].

4.3. Results

4.3.1. Characterization of RBCPs and C-RBCPs

4.3.1.1. XRD and FTIR analysis

The mineral compositions of various recycled pastes powder before and after carbonation treatment are shown in ***Fig. 4.6***. Peaks of portlandite (PDF#00-004-0733) and C-S-H are

commonly identified in all hydrated pastes powder, which was derived from the hydration reaction of cement clinker and pozzolanic reaction [26,160]. In GBS blended samples, hydrotalcite was generally formed, while quartz and mullite were addressed in FA-cement blends. In cement blends with the high volume of GBS, FA or RGP, a weak intensity of portlandite was performed compared to the samples with a low replacement ratio of them. After carbonation, the peak intensity of portlandite was barely observed in ***Fig. 4.6(b)***, while the peak intensity of calcium carbonate grows significantly. Three polymorphs of calcium carbonate can be found in carbonated pastes powder, which is related to calcite (PDF#00-005-0586), aragonite (PDF#00-005-0453) and vaterite (PDF#00-024-0030). Aragonite and calcite were observed in carbonated GBS blended cement pastes powder and pure OPC sample, while calcite was the only calcium carbonate phase in FA blended cement pastes. A trace of vaterite was found in carbonated RGP blended samples. Aragonite and calcite were commonly observed in carbonated cement concrete [56,57]. However, the presence of vaterite was rarely reported, this could be induced by the sodium in RGP, which played as a structure modifier in calcium carbonate formation [161].

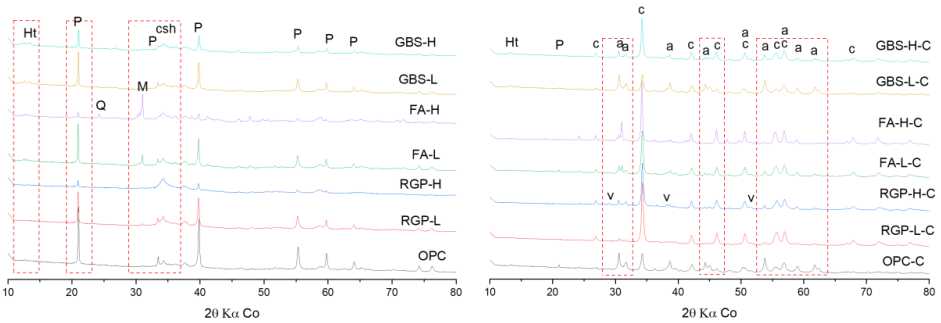

(a) ***(b)***

Fig. 4.6 *XRD patterns of RBCPs and C-RBCPs (Ht-hydrotalcite, P-portlandite, Q-quartz, M-mullite, csh-calcium silicate hydrate, c-calcite, a-aragonite, v-vaterite).*

The FTIR results (see ***Fig. 4.7***) further confirmed the presence of various calcium carbonates. The absorptions at 700 and 713 cm^{-1} are related to the presence of C-O in aragonite, while 713 and 745 cm^{-1} for calcite and vaterite, respectively [162]. The wavenumbers of 854 and 874 cm^{-1} are related to the C-O in aragonite and calcite [37]. Besides, a broad absorption band between 1018 to 1036 cm^{-1} indicates the formation of high polymerized silica-alumina, it can be induced by the decalcification of C-(A)-S-H in hydrated blended cement [147,148]. In addition, this amorphous silica-alumina gel was pointed out to show a high reactivity in cement blends [147].

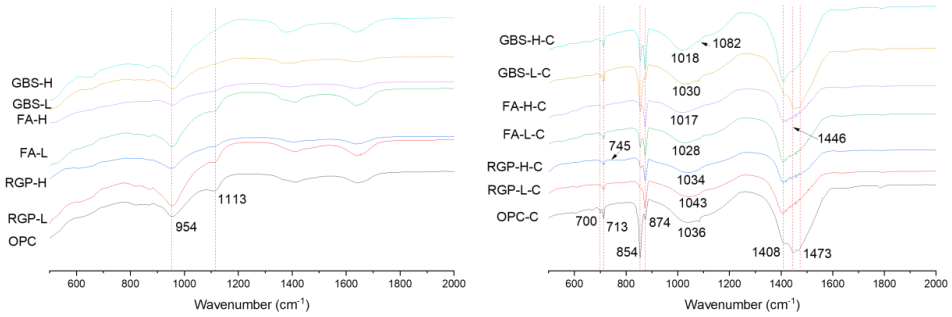

(a) ***(b)***

Fig. 4.7 *FTIR results of RBCPs (a) and C-RBCPs (b).*

4.3.1.2. Thermogravimetric test of RBCPs and C-RBCPs

The TGA results of RBCPs are illustrated in ***Fig. 4.8***, the hydrated cement pastes before carbonation exhibited typical mass loss curves during the test. The first significant mass loss corresponded to the dehydration of C-(A)-S-H, which derived from the hydration of cement clinker and pozzolanic reaction [26,160]. The following decomposition was induced by the water loss of calcium hydroxide. Afterward, the small decrease of mass around 700 °C was due to the decomposition of calcium carbonate [129]. After carbonation treatment, a huge mass loss from 400 to 900 °C was observed, which was related to the formation of various calcium carbonates. It is noticed that calcium hydroxide decomposition can be barely visible after carbonation. Instead of it, poorly crystallized calcium carbonate was formed that can be decomposed at relatively low temperature (520-720 °C), while CO_2 in vaterite, aragonite and calcite can be emitted at higher temperature (720-950 °C) [163]. Overview, the SCMs in RBCPs strongly reduced the amount of calcium carbonate formation compared to OPC sample. The variation of the decomposition temperature range of calcium carbonates indicated the change of calcium carbonate polymorphs, which could be affected by the incorporation of SCMs categories.

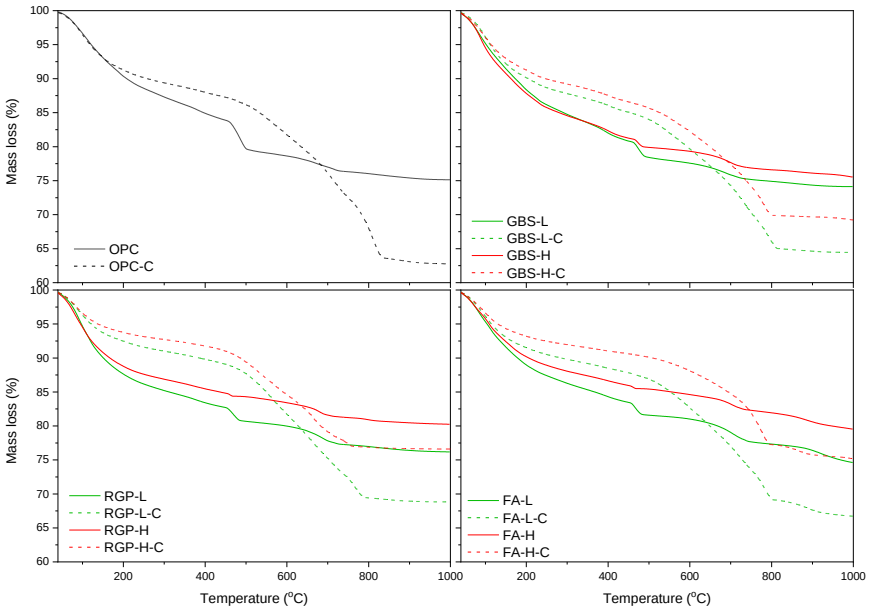

(a)

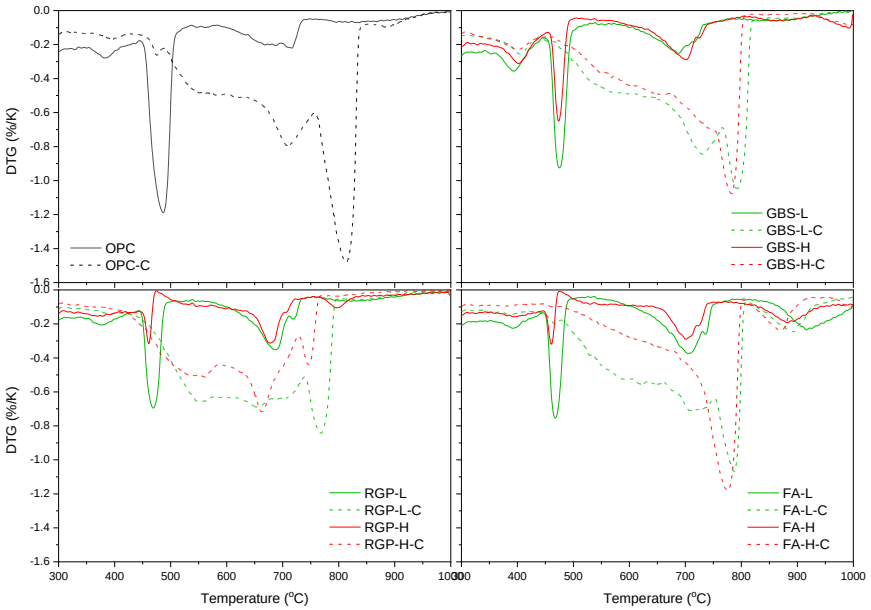

(b)

Fig. 4.8 *TG analysis of RBCPs and C-RBCPs (a) mass loss, and (b) derivative thermogravimetric.*

4.3.1.3. Leaching properties of RBCPs and C-RBCPs

The leaching behaviours of RBCPs and C-RBCPs in distilled water are shown in ***Fig. 4.9***. As illustrated in ***Section 4.3.1.1***. and ***Section 4.3.1.2***., the mineral compositions of RBCPs were considerably modified by carbonation pre-treatment. The consumption of portlandite during carbonation also can effectively decrease the alkalinity of recycled cement-based powders [164]. Therefore, leachable alkali ions, Si and Al, which are sensitive to alkalinity, presented a visible variation of concentration in the leachates of RBCPs and C-RBCPs. K concentration in RBCPs and C-RBCPs showed no significant relevance to SCMs amount and categories because of its limited content in raw materials as shown in XRF results. Na concentration presented an extremely high content in leachates of RGP specimens. This can be induced by soluble sodium from the destroyed glass phase in RGP particles [165], which was hard to be solidified by the hydration products and carbonation products. Meanwhile, Mg concentration also increased significantly in all C-RBCPs due to the consumption of calcium hydroxide. On the other hand, due to the decalcification of C-(A)-S-H gel and the formation of polymerized silica gel after carbonation, the dissolved Si amount in C-RBCPs was also enhanced. However, there is a decline of Al concentration after carbonation treatment, this could be induced by the identical amphoteric behaviour at low alkalinity environment [166]. These changes agree with the previous research on carbonated cement-based materials [164].

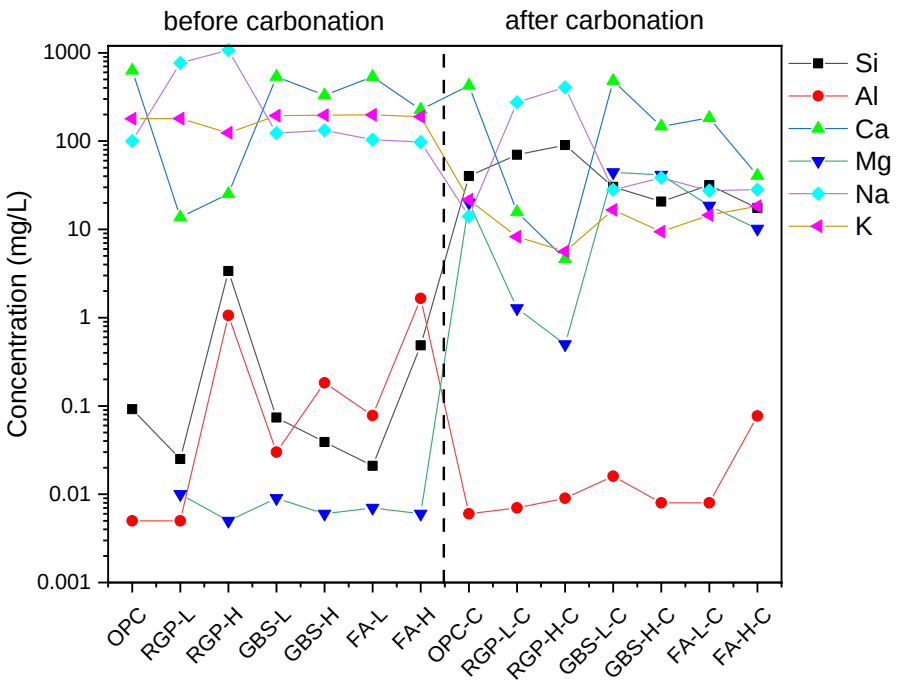

Fig. 4.9 *Leaching properties of various recycled powders.*

4.3.2. Recycling of RBCPs and C-RBCPs as SCMs in blended mortars production

4.3.2.1. Reaction kinetics of RBCPs and C-RBCPs blended cement

The reaction heat flows of blended cement pastes in the first 50 hours of hydration are shown in ***Fig. 4.10***. A slight acceleration in the hydration process can be found in OPC and GBS-based carbonated RBCPs blended mixtures. The time to reach the first reaction peak was reduced, and the peak intensity was increased slightly for OPC-C, GBS-L-C and GBS-H-C mixtures. Meanwhile, the carbonated FA-L, FA-H, RGP-L and RGP-H showed slightly suppress the reaction intensity and delay the time to reach the first reaction peak of related cement blends. It can be attributed to the high reactivity of unreacted GGBS particles compared to RGP and FA in cement-based blends [167,168]. In many previous studies, carbonation of hydrated OPC has been proven to increase its reactivity of it, as well as the acceleration effect on the heat of cement hydration [8]. However, the heat releasing of RBCPs blended mixtures showed acceleration or retardation depending on the SCMs incorporation in sourced cementitious systems. This should be considered during the recycling of RBCPs in new concrete production by carbonation pre-treatment.

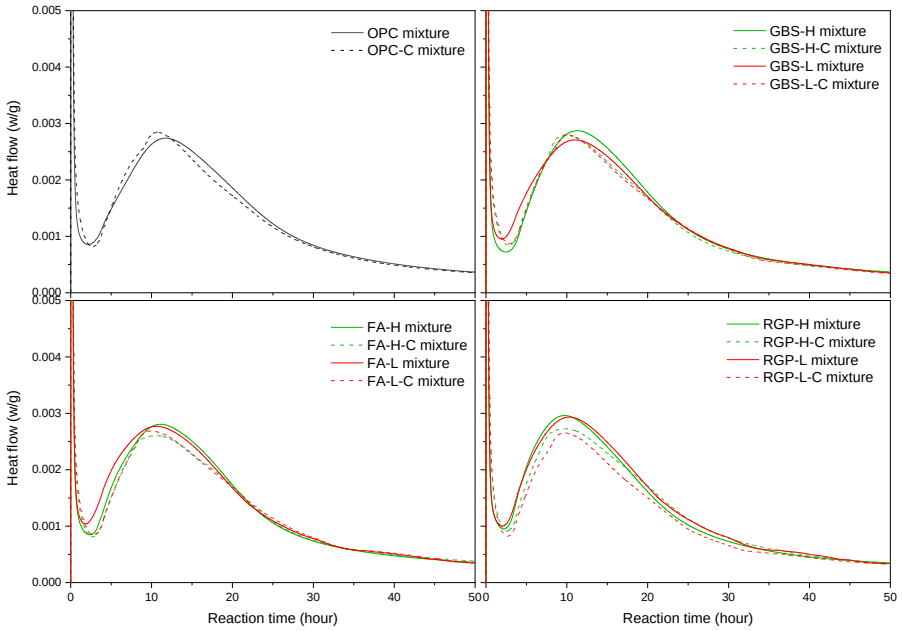

Fig. 4.10 *Heat flow of blended mixtures.*

4.3.2.2. Reaction products of RBCPs and C-RBCPs blended cement

To investigate the reaction products of RBCPs and C-RBCPs blended cement, X-ray diffractions and thermal gravimetric tests were applied, and the test results were performed in ***Fig. 4.11*** and ***Fig. 4.12***. The main reaction products of RBCPS and C-RBCPs

blended cement after 28-day hydration were mainly calcium hydroxide (PDF#00-004-0733), belite (PDF#33-302) and a small trace of alite (PDF#01-070-8632), which are all typical products in hydrated cement concrete [169]. Besides, the hump around 34 °2θ is related to the C-(A)-S-H formation, which was generally observed in ordinary Portland cement-based cementitious materials [10,129]. For C-RBCPs blended cement mixtures, a new significant peak corresponding to the formation of Mc can be observed around 13.4 °2θ (summarized in ***Fig. 4.12***) in all samples. It was formed by the reaction between calcium carbonate, calcium hydroxide and alumina-containing phases [170–172]. It has been reported in many previous studies of limestone blended cement, the reaction process can be described as the following equations:

$$C_3A + 0.5Cc + 0.5CH + 11.5H \rightarrow C_4Ac_{0.5}H_{12} \quad \textbf{(4.7)}$$

$$AS_2 + 0.5Cc + 3.5CH + 8.5H \rightarrow C_4Ac_{0.5}H_{12} \quad \textbf{(4.8)}$$

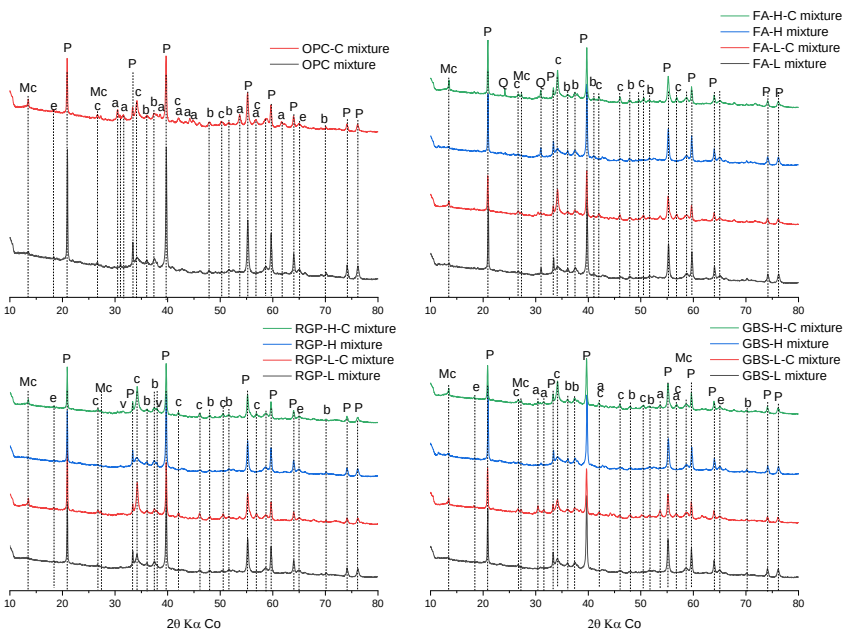

Fig. 4.11 *XRD patterns of RBCPs and C-RBCPs blended cement pastes after 28 days of normal curing (Mc-mono-carboaluminate, e-ettringite, a-aragonite, v-vaterite, c-calcite, P-portlandite, b-belite).*

Calcium carbonate can be reacted with calcium aluminate or amorphous alumina-silicate phases, while calcium hydroxide was further consumed during this process. The formation of hemi-carboaluminate only appeared at the early age of hydrated cement blends, as the progressing of cement hydration, it converts to mono-carboaluminate at late ages, for example, after 28 days [170]. This also explains that only Mc was identified in C-RBCPs blended cement.

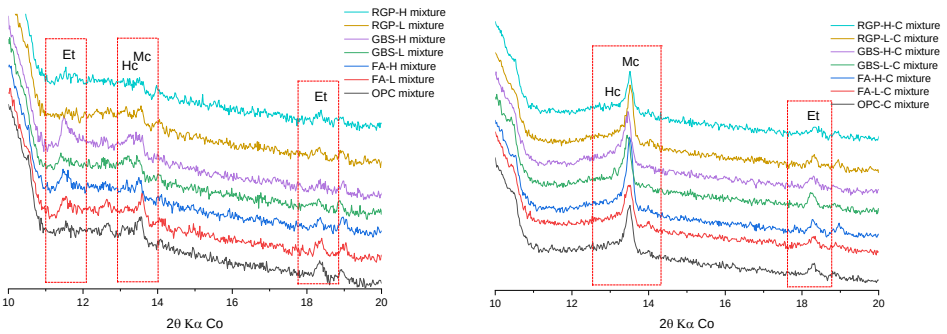

(a) ***(b)***

Fig. 4.12 *Identification of Ettringite, Mc and Hc in (a) RBCPs and (b) C-RBCPs blended cement samples (Et- ettringite, Mc-mono-carboaluminate, Hc- hemi-carboaluminate).*

A Thermogravimetric test was conducted to know more information about hydrates in RBCPs and C-RBCPs blended cement after 28 days of hydration (see ***Fig. 4.13***). Several main decomposition peaks are clearly observed in all blended cement samples, which are located at the temperature ranges of 40 ~ 240 °C, 430 ~ 500 °C, and 600 ~ 850 °C, respectively. The first decomposition was assigned to the dehydration of C-S-H, ettringite and Mc [173], after that, the second peak was induced by the water loss of calcium hydroxide [26]. The third largest peak corresponded to the CO_2 released from calcium carbonates. It is clear to see that the decomposition between 40 and 240 °C significantly increased in samples containing C-RBCPs compared to RBCPs. This was caused by the additional formation of C-(A)-S-H and Mc in blended cement by the presence of silica-alumina gel and calcium carbonate in C-RBCPs. On the other hand, calcium hydroxide also can be consumed by the reactive products in C-RBCPs, which resulted in the reduction of decomposition between 430 and 500 °C. This indicated that the application of C-RBCPs not only can effectively promote the hydration of cement, but also reduce the calcium hydroxide content.

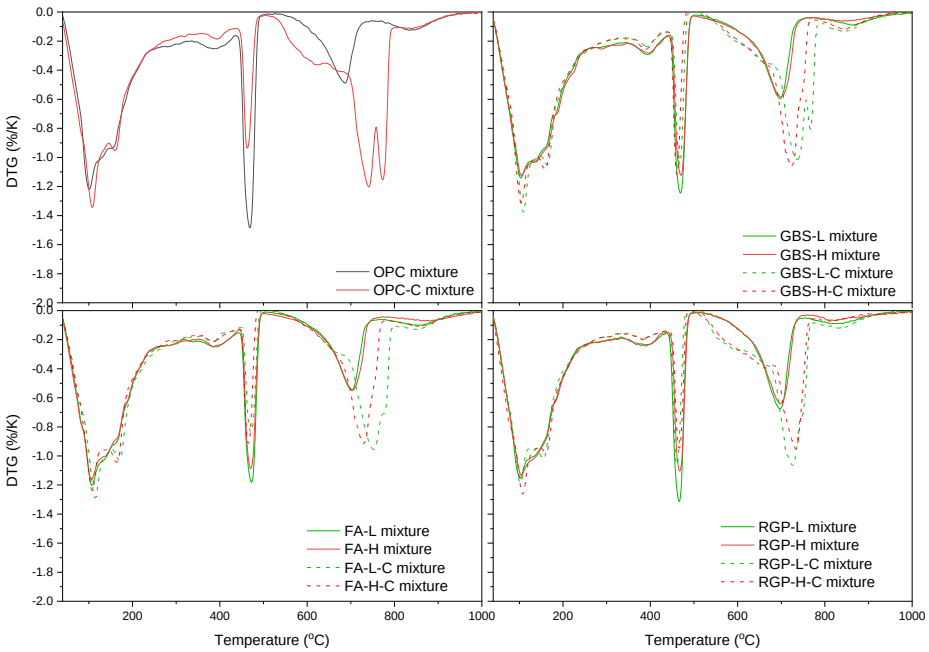

Fig. 4.13 *TG analysis of hydrated recycled powder blended cement (30% powder + 70% CEM I) after 28-day normal curing.*

4.3.2.3. Workability of RBCPs and C-RBCPs blended cement mortars

The flow ability is a critical behavior of workability to evaluate the fresh performance of cement composites. The properties of additives and SCMs can change the workability effectively due to the chemical and physical effects on fresh cement mixtures [174,175]. As shown in ***Fig. 4.14(a)***, the addition of RBCPs in cement mortars caused poor performance of flowability. The best flowability of 14 cm was found in RGP-H-M, while GBS-L-M presented the poorest workability of 12.25 cm. The hydrated blended cement pastes were reported to present a strong water absorption ability [176]. Consequently, the application of RBCPs can result in a strong reduction of water between particles, which decreased the flowability of blended mortars. Meanwhile, it is noticeable that the carbonation pre-treatment could effectively modify the water demand of RBCPs, which was presented as an improved flowability compared to untreated powders. ***Fig. 4.14(b)*** performs the flowability enhancement ratio of C-RBCPs blended mortars. OPC-C-M exhibited the highest flowability enhancement ratio. For other C-RBCPs blended mortars, the improvements were not so significant, in addition, the high-volume SCMs containing RBCPs resulted in a limited enhancement on the flowability of blended mortars after carbonation pre-treatments. This indicates that the SCMs categories and volume in hydrated blended cement can effectively influence the treatment efficiency of pre-carbonation treatment.

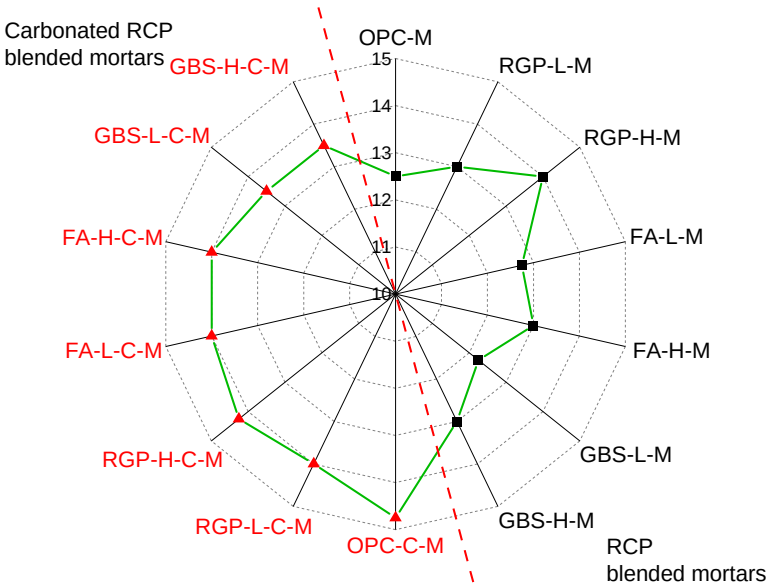

(a)

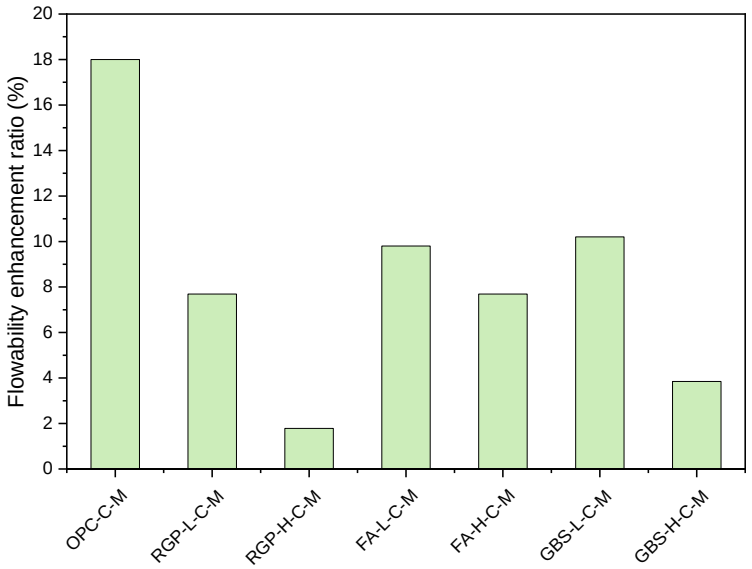

(b)

Fig. 4.14 *(a) Flowability of various RCP blended mortars and (b) flowability enhancement ratio after incorporating RBCPs carbonation treatment based on* ***Table 4.3****.*

4.3.2.4. Mechanical performance of RBCPs and C-RBCPs blended cement mortars

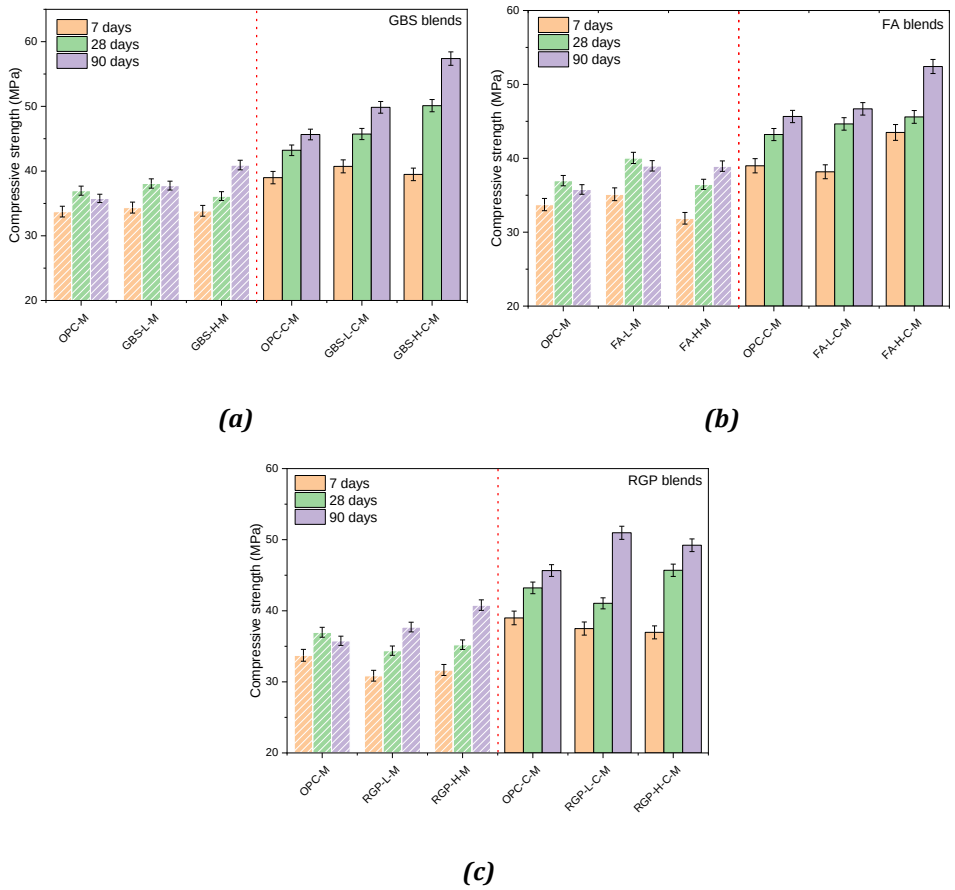

Fig. 4.15 *Compressive strength of mortars after 28 days of curing based on* ***Table 4.3****.*

The compressive strength of RBCPs and C-RBCPs blended mortars was tested, and the results are presented in ***Fig. 4.15***. The recycled OPC powder blended mortar exhibited the compressive strength of 33.7, 36.9 and 35.78 MPa after 7, 28 and 90 days, respectively. Comparable mechanical performance was observed in blended mortars containing GBS-RBCPs after curing for 7 and 28 days. It is interesting to see that the compressive of GBS-RBCPs exhibited a further improvement at a late age (90 days). GBS-L-M and GBS-H-M achieved 37.7 and 40.9 MPa after 90 days, which increased 6% and 14% compared to OPC-M. A similar observation also can be found in FA and RGP-RBCPs blended mortars. This indicated that the RBCPs can participate the further reactions after 28 days to contribute to a better mechanical performance at a late age. For SCMs blended cement concrete, the reaction degree of GBS only reached less than 60%, while only 30% for FA and RGP in the previous reports [168,177,178]. So, the gradually increasing compressive strength at late age can be caused by the pozzolanic reaction of unreacted SCMs particles

in RBCPs. On the other hand, C-RBCPs blended mortars presented obviously superior mechanical performance compared to RBCPs cement blends. Especially for GBS and FA blends, for example, GBS-H-C-M presented a compressive strength of 57.4 MPa, while FA-H-C-M reached 52.4 MPa after 90 days. The OPC-C-M exhibited a compressive strength of 45.6 MPa after 90 days, which was considerably lower than other C-RBCPs blended mortars. This can be attributed to the improved flowability and the reactive products in C-RBCPs.

4.4. Discussion

4.4.1. Effects of SCMs particles on the reactive agents of C-RBCPs

As is well known, the incorporation of SCMs can significantly modify the mineral and chemical composition of hydrated blended cement. Pozzolanic reaction of SCMs produced secondary C-(A)-S-H with a modified Ca/(Si+Al) ratio, and partially unreacted SCMs particles usually occurred in old blended concrete [168]. During recycling and utilization, all calcium-containing phases in cement clinker hydration and pozzolanic reaction products provided a possibility of CO_2 sequestration [113,179]. The phase transformation in RBCPs after carbonation produced more reactive agents such as calcium carbonate and silica-alumina gel compared to old calcium-containing hydrates (e.g. C-S-H, portlandite, ettringite) in new concrete production as shown in ***Fig. 4.16*** and ***Fig. 4.17***. Furthermore, in previous studies, the SCMs reaction degree only reached 20% to 60% in old concrete [168], after recycling, the unreacted SCMs particles could be reacted again. The improvement of mechanical performance at late age in both RBCPs and C-RBCPs blended mortars in this study also could be induced by the secondary reaction of previous unreacted SCMs particles.

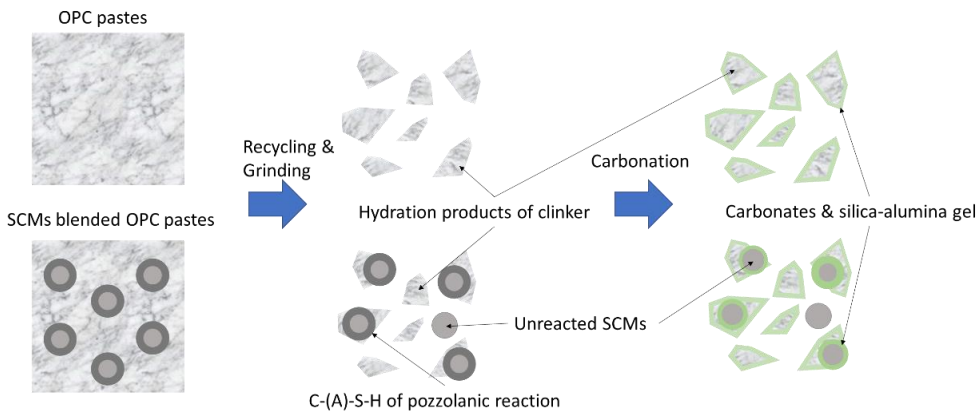

Fig. 4.16 *Schematic recycling process of OPC and SCMs blended cement pastes.*

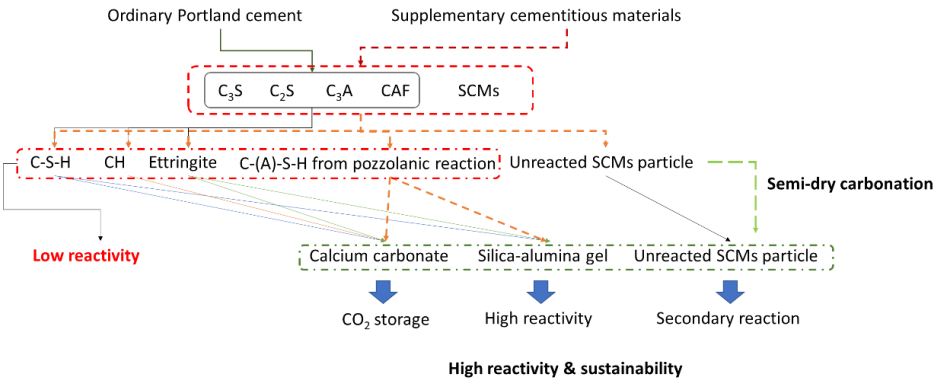

Fig. 4.17 *Carbonation treatment mechanism of hydrated SCMs blended cement.*

4.4.2. Effects of SCMs on carbonation products and reactivity of C-RBCPs particles

The total Ca, Si and Al proportions in initially prepared blended cement were changed after the incorporation of SCMs as shown in ***Fig. 4.18***. For instance, the incorporation of RGP considerably increased Si and decreased Ca in blended cement, as well as for FA blends. GBS blended cement presented a closer location to OPC in the ternary diagram due to the similar Ca/(Si+Al) ratio, however, Ca content in GBS was still lower than ordinary portlandite cement. Therefore, the increase of SCMs volumes indicated the reduction of clinker and available Ca in blended cement. Consequently, their theoretical CO_2 uptake ability presented a significant reduction compared to OPC (see ***Fig. 4.19***). However, the lowest solidified CO_2 still can exceed 10 %. On the other hand, the increased carbonation degree (ICD) of RBCPs after semi-dry carbonation exhibited an obvious variation depending on the SCMs categories and volumes. FA and RGP blended samples exhibited an overall higher ICD compared to OPC sample, and the high volume (60%) FA and RGP contributed to a lower ICD compared to normal volume (30%) samples. On the other hand, GBS blended samples achieved a lower ICD than OPC sample, which is due to the amount of Ca remaining in unreacted GBS particles. This observation also confirms the results of previous studies [180], the C-S-H with lower Ca/Si experienced a slow carbonation process compared to the C-S-H with higher Ca/Si due to the slow dissolution rate of Ca. The Ca was more difficult to be removed in C-S-H with low Ca/Si in GBS, FA and RGP blended cement samples compared to hydrated OPC powder under the same conditions.

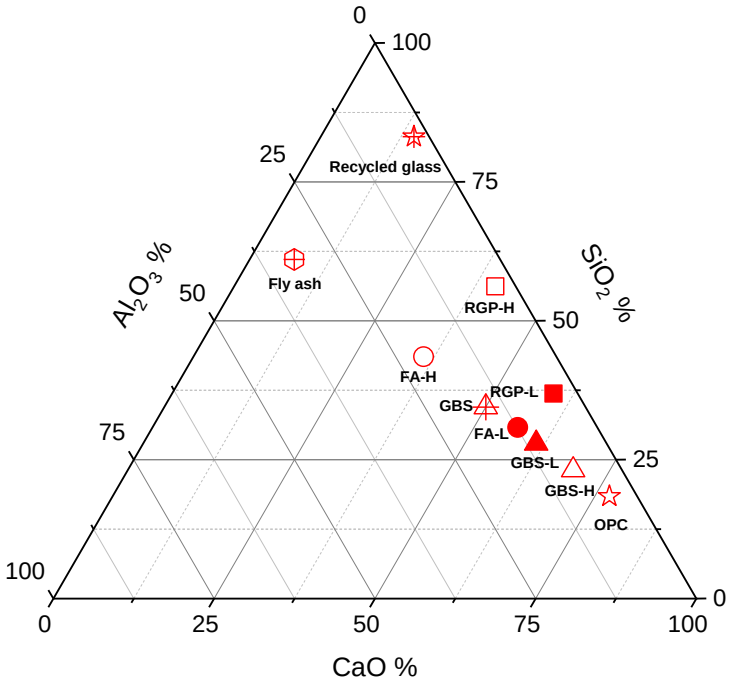

Fig. 4.18 *Compositions of various blended cement paste powder.*

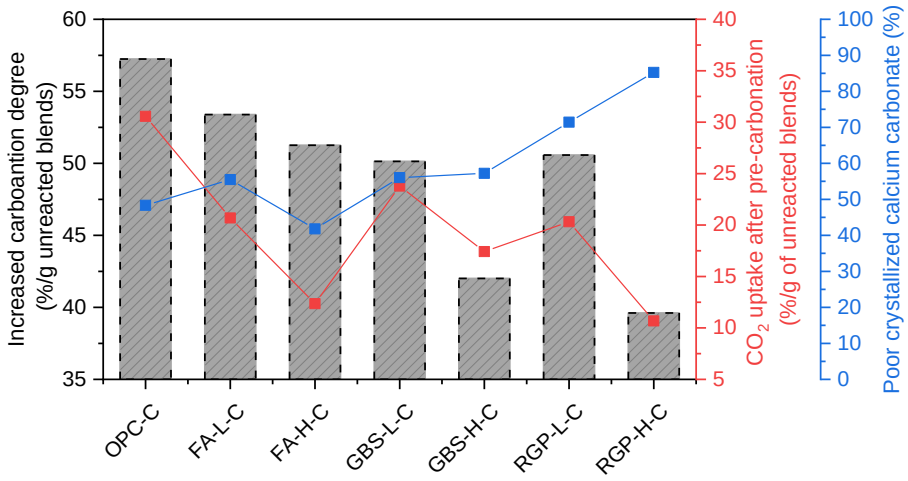

Fig. 4.19 *Carbonation degree, CO_2 uptake ability and poor crystallized calcium carbonate of C-RBCPs.*

Besides, the formation of calcium carbonate also was indicated to be influenced by the various SCMs in RBCPs. Poor crystallized calcium carbonate amount was calculated and

shown in ***Fig. 4.19***. FA and GBS exhibited a limited influence on the formation of calcium carbonate, the proportion of poorly crystallized calcium carbonate slightly lower or higher than carbonated OPC. However, RGP presented a remarkable effect on calcium carbonate formation. The poorly crystallized calcium carbonate reached 71% and 85% in RGP-L-C and RGP-H-C, respectively. The crystallization of calcium carbonate could be influenced by many conditions such as temperature, ion concentration and CO_2 dosage [161]. Liu et al. investigated the carbonation behaviour of alkali-activated GGBS-RGP mixtures, it indicated that the Na released from reacted RGP particles can inhibit the formation of well-crystallized calcium carbonate because of the pH buffer capacity [181]. The leaching test in ***Fig. 4.9*** also confirmed the high sodium ions in RGP blends. Furthermore, the presence of a high amount of poorly crystallized calcium carbonate also explains the limited improvement of RGP blends on the workability of new mortars after carbonation, which usually shows a high surface area.

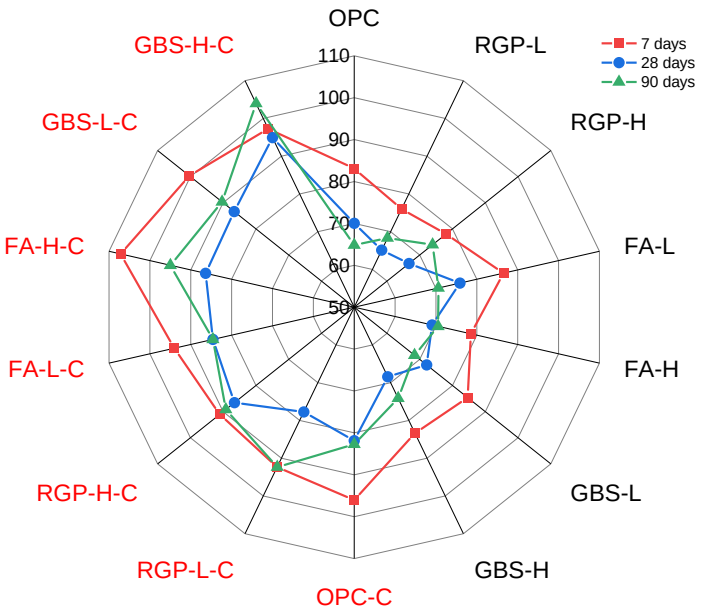

Fig. 4.20 *Strength activity index of RBCPs and C-RBCPs in blended cement mortars.*

The formation of silica-alumina gel and calcium carbonates in C-RBCPs resulted in a considerable improvement on their reactivity agents, consequently, the SAI of C-RBCPs at different ages was obviously enhanced (see ***Fig. 4.20***). The presence of amorphous silica-alumina gel contributed to an extremely higher SAI compared to powder without carbonation pre-treatment. Zajac et al. have confirmed the high reactivity of silica-alumina gel in carbonated normal cement paste powder, which can be fast reacted in the first week of hydration [147]. It is noticed that the FA-H-C presented the highest SAI (103) after 7 days, this can be induced by the synergetic effects between a high amount of

unreacted FA and calcium carbonate. This observation also agrees with the previous studies of cement-limestone-fly ash ternary binder systems [182]. Afterward, the hydration of clinker and reactivity of residue SCMs particles kept promoting the increase of mechanical strength at a late age. SAI of C-RBCPs at a late age (90 days) well corresponded with the reactivity of SCMs, which was commonly presented as GBS>FA>RGP in many studies [168]. The SCMs application in old concrete could effectively influence the SAI in new cement products after recycling by carbonation pre-treatment. However, the strength performance is only a primary evaluation of C-RBCPs blended cement mortars. Further investigations will be needed to have more quantitative analysis and tests in future studies.

4.4.3. Effects of SCMs on sustainability coefficient of C-RBCPs blended mortars

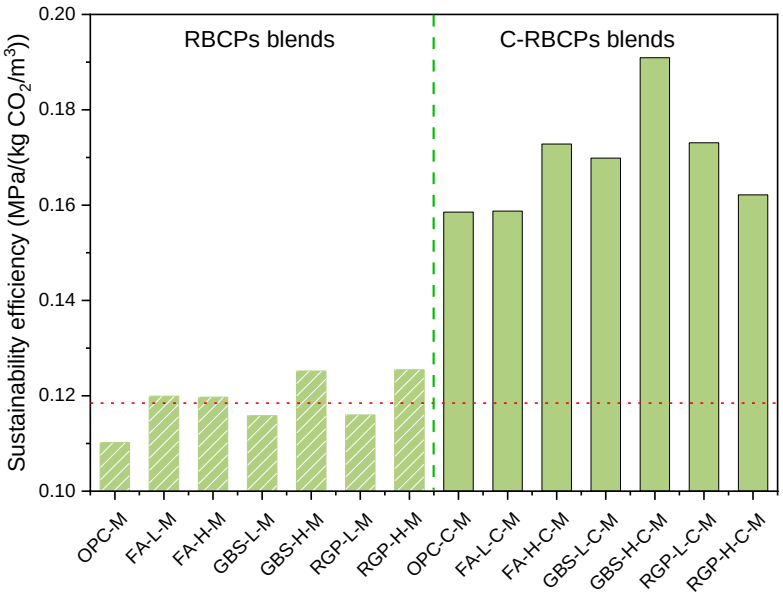

Fig. 4.21 *Sustainability efficiency of RBCPs and C-RBCPs blended mortars based on* ***Table 4.3****.*

The recycling and utilization of demolition concrete wastes have been proven to be sustainable conservation of the environment [12,183,184]. The red dot line in ***Fig. 4.21*** indicates the sustainability efficiency (SE) of normal ordinary Portland cement mortar. The utilization of RBCPs in blended mortars resulted in a SE around to the normal ordinary Portland cement mortars, which contributed to slightly positive or even negative effects on sustainability. The replacement of cement clinker by RBCPs did reduce the CO_2 emission of blended mortars, even though, the poor strength performance of RBCPs blended samples resulted in a comparable SE to normal cement mortars. Carbonation has been proven to efficiently improve the quality of recycled concrete wastes, for instance,

recycled aggregates and fines [185]. Similar to the normal carbonated recycled concrete wastes, the reactivity and workability of RBCPs can be improved due to the existence of hydration products of cement clinker, as well as being a feedstock of CO_2. Besides, residue unreacted SCMs particles can also have a second chance to react with calcium hydroxide in new cement blends. Consequently, C-RBCPs showed a superior SE compared to RBCPs in concrete production. The SCMs application not only reduced the CO_2 emission of blended cement building materials but also considerably promoted their recyclability for secondary applications after carbonation pre-treatment.

4.5. Conclusions

This study investigates the valorization of recycled hydrated blended cement paste powder containing GBS, FA, and RGP in new cement-based mortars through a pre-carbonation modification. The effects of semi-dry carbonation on properties of RBCPs were characterized and evaluated. Afterward, the performances including reaction kinetics, hydration products, workability, mechanical performance, and sustainability of new cement composites prepared by C-RBCPs were evaluated and analyzed. The following conclusions can be addressed:

- Polymorphs of calcium carbonate in C-RBCPs can be influenced by the categories of SCMs. Calcite and aragonite were formed in C-RBCPs containing GBS and FA, while the incorporation of RGP resulted in the formation of vaterite and large amount of poor crystallized calcium carbonate (>70%).
- The CO_2 uptake ability (10-25%) of RBCPs was reduced due to the presence of SCMs particles compared to normal hydrated OPC sample (30.5%), as well as the total carbonation degree. Leachable Si in C-RBCPs was significantly improved due to the carbonation of C-(A)-S-H. C-RBCPs containing RGP presented a higher Si leaching than samples containing FA and GBS, meanwhile, a high amount of Na leaching was observed.
- C-RBCPs contributed to the formation of mono-carboaluminate and more hydrates in hydrated cement blends. The flowability of C-RBCPs blended cement mortars was considerably improved compared to RBCPs. However, high volume of SCMs in C-RBCPs resulted in lower enhancement ratio of flow ability. The application of C-RBCPs containing RGP resulted in a poorer flow ability compared to samples with FA and GBS.
- Carbonation was an efficient pre-treament to enhance the reactivity of RBCPs in cement composites. The unreacted SCMs particles contributed to a fast strength development of C-RBCPs blended cement mortars. The presence of GBS was related to a higher strength activity index of C-RBCPs than FA and RGP.

The unreacted GBS, FA and RGP were important reactive agents in C-RBCPs, their reaction mechanisms in the new cementitious systems and contributions to the recyclability of carbonated powders still need more focus in the future study.

CHAPTER 5

5. A novel BOF slag binder based on monopotassium phosphate activation

This chapter proposes a novel method to utilize BOF slag as cement-free binding materials through chemical activation with monopotassium phosphate (MKP) to achieve high-end applications. The microstructure and strength development of BOF slag pastes with MKP dosages below 10 wt.% were investigated using a multi-technique approach. Results indicate that MKP facilitates the dissolution and hydration of $C_2(A,F)$ and C_2S, enhancing mechanical properties. Principal hydration products identified include hydrotalcite, hydrogarnet, C-S-H gel, and hydroxyapatite. A 2.5 wt.% MKP addition shows little effect on 7-day hydration but still enhances overall hydration at 28 days. Optimization of pore structure is attained with 5 wt.% MKP, yielding maximum strength at both 7 and 28 days (19.9 and 44.5 MPa). Excessive MKP addition (10 wt.%) induces a drastic early-stage reaction, creating unexpected large pores and hindering strength development. Furthermore, Ca over-capture from hydroxyapatite formation reduces available Ca for C-S-H, addressing the importance of the balance between Si, Al, and Fe dissolution and Ca fixation by phosphate.

This chapter is reproduced from: Y. Tang, METHOD FOR ACTIVATING BASIC OXYGEN FURNACE STEEL SLAG, WO 2024/052265 A1, 2024. (International patent); Y. Tang, K. Schollbach, S.R. van der Laan, W. Chen, H.J.H. Brouwers, A novel BOF slag binder based on monopotassium phosphate activation, 2024 (submitted).

5.1. Introduction

A pressing need to explore high-end applications for BOF slag as potential candidate for clinker replacement is discussed. For preparing a Portland cement-free BOF slag binder, the activation of the hydraulic phases C_2S and $C_2(A,F)$ attracts the most attention because they make up > 50 wt.% and RO phase is quite inert [186]. It has been reported that C_2S hydration can be accelerated in the presence of Na_2CO_3 and Na_2SO_4 while the positive role of NaOH in the activation of C_2S remains controversial [187–189]. Notably, both carbonates and sulfate can strongly retard the hydration of $C_2(A,F)$ creating a prolonged induction period [190,191]. Other admixtures, including $CaCl_2$, NaCl, Na_2SiO_3, high alumina cement, and commercial accelerator have also been shown to affect the hydration of BOF slag only slightly [186,192]. BOF slag was found to be preferentially activated by citrates and alkanolamines like triethanolamine, triisopropanolamine etc. due to the chelating effects on Al, Fe and Ca [39,193]. They primarily activate $C_2(A,F)$ while the contribution to C_2S hydration is minor [39,193]. The synergetic activation of both C_2S and $C_2(A,F)$ remains challenging.

Phosphates interact strongly via ligand exchange, precipitation, and coprecipitation with iron, aluminum, and calcium [58,59], which are main constituents of BOF slag. The development of chemically bonded phosphate ceramics (CBPCs) utilizing BOF slag further demonstrates the feasibility of activating C_2S, $C_2(A,F)$, and wuestite with phosphates or phosphoric acids at ambient temperature to produce insoluble phosphate hydrates [194–196]. These reaction products form via an acid-base reaction, distinct from the hydration kinetics of Portland cement [48,195]. It is known that excessive phosphate addition, typically above 15 wt.% of BOF slag, inhibits C_2S and $C_2(A,F)$ hydration, yielding iron/calcium phosphates, $Al(OH)_3$, $Fe(OH)_3$, and H_4SiO_4 as primary hydration products instead of C-S-H gel and hydrogarnet [194,196]. Therefore, optimizing phosphate dosages and exploring lower phosphate inputs for BOF slag hydration merit attention.

This study presents a novel approach to utilize BOF slag as cement-free binding materials with monopotassium phosphate (MKP) playing a crucial role in promoting hydration, investigating the microstructure and strength development of BOF slag pastes with varying MKP dosages below 10 wt.% using a comprehensive multi-technique approach. This includes quantitative XRD analysis, SEM/EDX large area phase mapping combined with PhAse Recognition and Characterization (PARC) software, thermogravimetric analysis (TGA), calorimetric measurements, and porosimetry (MIP), for the solid samples. Ion chromatography (IC) and inductively coupled plasma atomic emission spectrometer (ICP-OES) were employed to analyze corresponding aqueous solutions. This research yields new insights into the reactions involving BOF slag and varying phosphate quantities below 10 wt.%, offering a promising activation method for BOF slag using low phosphate additions at ambient temperature [197].

5.2. Experiments and methodology

5.2.1. Raw materials and mix design

BOF slag used in this study was collected from standard production, provided by Tata steel (The Netherlands). A disc milling (Retsch, RS300XL) for 15 min was applied to obtain BOF slag powder. The particle size distribution of BOF slag powder analysed with a laser particle size analyser (Model Malvern Mastersizer 2000, Malvern PANalytical) is presented in ***Fig. 5.1***. The chemical composition of BOF slag powder was analysed with X-ray fluorescence (XRF, Model Axios Advanced, PANalytical.B.V) and the mineral composition was determined with quantitative X-ray diffraction (QXRD) analysis as shown in ***Table 5.1***. Monopotassium dihydrogen phosphate (MKP, KH_2PO_4) was chosen as the additive, which is a commercially available technical grade product (VWR Chemicals BDH®, purity >99.0%).

MKP of amounts equivalent to 0, 2.5, 5, 10 wt.% of BOF slag, was first mixed with BOF slag powder at a low speed for 30 seconds to obtain a homogenous distribution. Water was then added to the dry mixture with a water to solid ratio (BOF slag + MKP) of 0.2. Mixing for 30 seconds with low speed, subsequently manual homogenization for another 30 s and then mixing for 60 seconds with high speed was applied to prepare the MKP-activated BOF slag pastes. The fresh BOF slag pastes were cast into polystyrene molds (40×40×160 mm^3) and then covered with plastic film until demolding. Due to the large variation in setting time, the samples with 5 and 10 wt.% MKP were demolded after 24 hours while the samples with 0 and 2.5 wt.% MKP were carefully demolded after 7 days because of insufficient hardening at earlier ages. To ensure optimal curing conditions after demolding, the pastes were meticulously sealed again with plastic foil and maintained at ambient temperature throughout the testing period. The samples in this study are labelled based on the amount of MKP added, as MKP0, MKP2.5, MKP5, MKP10 for 0, 2.5, 5, 10 wt.% of MKP dosages, respectively.

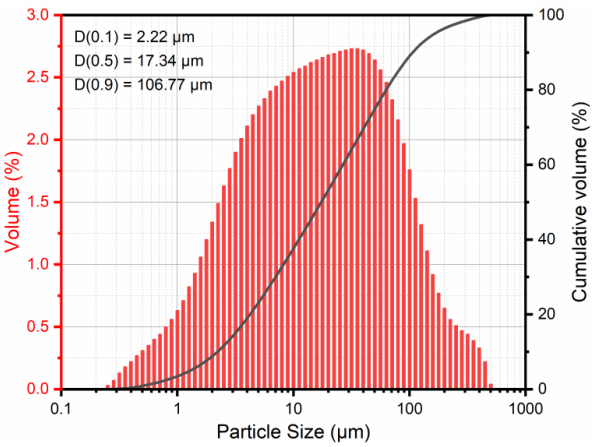

Fig. 5.1 *Particle size distribution of BOF slag.*

Table 5.1 *Mineralogical and chemical composition of BOF slag.*

Mineral compound	Content [wt.%]	Oxide	Content [wt.%]
Brownmillerite ($C_2(A,F)$)	17.1	MgO	6.8
Magnetite	6.4	SiO_2	13.45
C_2S	39.6	Al_2O_3	2.21
Wuestite	20.5	CaO	40.14
Lime	0.9	P_2O_5	1.61
Calcite	0.8	TiO_2	1.39
Portlandite	0.7	V_2O_5	1.05
Amorphous	14.0	Cr_2O_3	0.3
Rwp	2.8	MnO	4.61
		Fe_2O_3	28.32
		Others	0.12
		GOI	1.31

5.2.2. Methodology

The compressive strength of the specimens at 7 and 28 days was assessed following the guidelines of EN 196-1. For the evaluation of compressive strength, a loading rate of 2400 N/s was uniformly applied to all specimens, and the recorded strength values were obtained through triplicate tests.

The rate of heat release during the initial 23 days of hydration was measured using an isothermal conduction calorimeter (TAM Air, Thermometric). To prepare a homogenous paste, BOF slag powders were internally mixed with MKP and distilled water for 1 minute. The heat flow curve was integrated between 45 minutes and 23 days to assess the cumulative heat release. MKP2.5 was measured for 32 days due to a significantly prolonged induction period.

Scanning electron microscopy (SEM) measurements, coupled with energy-dispersive X-ray spectroscopy (EDX) analyses, were conducted on the pastes after 28 days of hydration. Prior to the measurements, the pastes were gently broken into small pieces below 4 mm. Subsequently, these small pieces were immersed in isopropanol for 3 days and subjected to vacuum drying. To facilitate SEM analysis, the small pieces were vacuum-impregnation with epoxy-resin, polished, and coated with a thin layer of carbon. The SEM data, specifically the spectral imaging (SI) data, was acquired using a JEOL JSM-7001F SEM

equipped with two 170 mm^2 Ultim Max SDD detectors and AZtec 6.0 software, both from Oxford Instruments. A focused probe with a beam current of 10 nA and an accelerating voltage of 15 kV was employed for the analyses. The SI imaging was performed with a step size of 1 µm, and each individual SI field consisted of 512 × 384 pixels. For each sample, a total of 9 fields were analyzed to ensure representative and statistically meaningful results.

The PhAse Recognition and Characterization (PARC) software was employed to determine the chemical composition and phase distribution of both the original slag phases and the hydration products. A comprehensive description of the PARC technique can be found elsewhere [198]. The data obtained from the energy-dispersive X-ray spectroscopy (EDS) mapping was processed using the PARC software, which facilitated the grouping of each data point based on its chemical composition into distinct phases. PARC complements the X-ray diffraction (XRD) Rietveld method, providing area proportions (thus volume fractions) of various phases based on chemical composition, including amorphous ones, with a resolution of around 1 µm.

After the designated curing periods, the samples were crushed manually to pass a sieve of 2 mm and then immersed in isopropanol for 24 hours to eliminate hydration, followed by drying in an oven at 45 °C until a constant mass [73]. All dried samples were ground finely to pass a sieve of 63 µm and then stored in desiccators, using calcium chloride pellets as a drying agent and sodium hydroxide pellets as a CO_2 trap until further analyses and tests.

The analysis of crystalline phases in both the raw BOF slag and hydrated slag samples was conducted using a D4 ENDEAVOR X-ray Diffractometer equipped with a LynxEye detector and a Co X-ray tube (operating at 40KV and 40 mA). The diffraction measurements were performed with a step size of 0.019° and a counting time of 1 second per step. Variable divergence slits (V20) were employed, and the scanning range covered 10 to 80 °2θ. A broader range from 10 to 90 °2θ was applied for X-ray quantification.

For quantitative phase analysis using the Rietveld method, an additional set of samples was prepared. To determine the amorphous and crystalline content, 10 wt.% of Si powder (Siltronix, France) was added to the samples as an internal standard. The Si powder was mixed thoroughly with the samples using an XRD-Mill McCrone (RETSCH) operating at 75% speed for 5 minutes to ensure a homogenous distribution of the powders. The quantification of crystalline and amorphous phases was performed using the TOPAS 5.2 software from Bruker Corporation.

The Fourier transform infrared spectroscopy (FTIR) was carried out using a Varian 3100 FTIR Spectrometer. During the analysis, 20 scans were recorded per spectrum, and a resolution of 1 cm^{-1} was employed to ensure high-quality data acquisition.

Nitrogen sorption analysis was performed using a Brunauer-Emmett-Teller (BET) instrument, specifically the TriStar II 3020 from Micrometrics. Based on data obtained

from the adsorption branch of the sorption isotherm, the surface area and pore size distribution were calculated using the Brunauer-Emmett-Teller method [77] and evaluated employing the Barrett–Joyner–Hallenda method [76], respectively.

Thermogravimetric analyses (TGA) were carried out employing a NETZSCH STA 449 F1 instrument. Ground powder samples, each weighing between 30 to 40 mg, were prepared. A heating rate of 10 °C/min was consistently applied in a nitrogen atmosphere spanning the temperature range of 40 to 1000 °C. The specific temperature range chosen for the precise quantification of chemically bound water was determined through derived thermogravimetric analysis (DTG) and references [199].

The porosity of 28-day hydrated samples was obtained by Mercury Intrusion Porosimetry (MIP) measurements using the AutoPore V 9600 Micrometrics Series Mercury Porosimeter with the maximum pressure of 228 MPa.

The leaching test was performed on 2-hour, 7- and 28-day cured slag pastes according to EN 12457–2 (one stage batch leaching test) [200]. Hydrated samples were crushed and sieved below 4 mm. The experiments were performed by mixing sieved samples and deionized water with liquid to solid ratios (L/S) of 10 using a dynamic shaker (ES SM-30, Edmund Buhler GmbH) at a constant speed of 250 rpm for 24 hours. After shaking for 24 hours, leachates were filtered through a syringe filter (pore diameter 0.22 μm, VWR) and then partial leachates were acidified with concentrated HNO_3. The acidified solutions were analyzed with an inductively coupled plasma atomic emission spectrometer (ICP-OES, SPECTROBLUE), according to NEN 6966. The obtained elements concentrations were compared with the limit values specified in the Dutch Soil Quality Decree [201].

The concentrations of Ca^{2+}, K^+ and phosphate in the residual leachate without acidification were determined with a Thermo Scientific Dionex ICS-1100 ion chromatography (IC) system, respectively. All liquid samples were undiluted or diluted by a factor of 10. The pH values were tested at ambient temperature with a VOLTCRAFT PH-100ATC pH meter. The pH values were determined three times respectively and the mean is given.

5.3. Results

5.3.1. Isothermal calorimetry

The isothermal conduction calorimetry results are presented in ***Fig. 5.2***. In the absence of phosphate, flash setting is observed with a subsequent minor peak at approximately 2 days. The introduction of varying amounts of phosphate leads to different induction periods, manifested by distinct heat flow peaks in MKP2.5, MKP5, and MKP10 starting at approximately 23 days, 3 days, and 2 hours, respectively. It is well-established that phosphate retards the hydration process of Portland cement [202]. This effect is also apparent for MKP2.5, which shows a prolonged induction period of 23 days. This makes the cumulative heat of MKP2.5 (~17 J/g) even lower than for the reference sample (~26 J/g) during the first 23 days of hydration. A significant increase in activator dosage to 10

wt.% accelerates the reaction between phosphate and BOF slag. MKP10 manifests three distinct exothermic peaks, with two of them occurring within the initial 24 hours post-mixing. The presence of multiple exothermic peaks implies a complex reaction pathway, where the initially formed metastable phases undergo different stages to convert into stable phases over time, reminiscent of the observed behaviour in MKP5. Although the primary exothermic peak in MKP5 emerges at around 13 days, the cumulative heat release values for MKP5 (108 J/g) and MKP10 (114 J/g) at 23 days are found to be comparable.

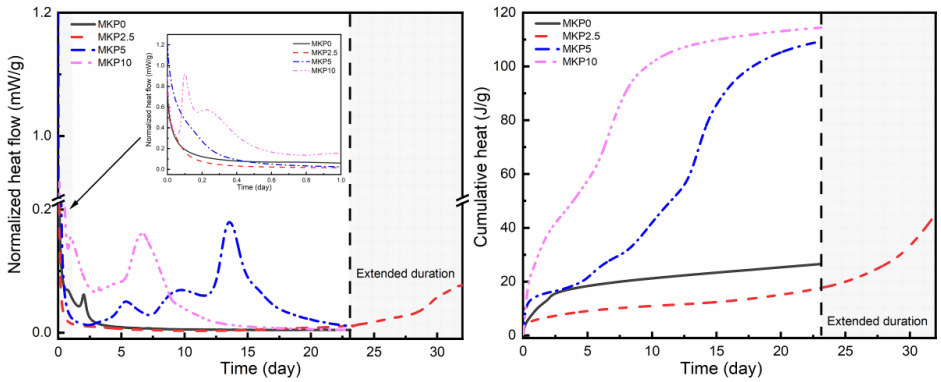

(a) ***(b)***

Fig. 5.2 *(a) Cumulative heat evolution and (b) heat flow of BOF slag pastes with dosages of MKP varying from 0 to 10 wt.%.*

5.3.2. Hydrates assemblage

The X-ray diffraction (XRD) analysis demonstrates the presence of two distinct crystalline hydration products, namely siliceous hydrogarnet, and pyroaurite/hydrotalcite, along with small amounts of poorly crystalline hydroxyapatite as illustrated in ***Fig. 5.3***. Siliceous hydrogarnets, characterized by the general chemical formula $Ca_3(Al_xFe_{1-x})_2(SiO_4)_y(OH)_{4(3-y)}$, have been previously identified in Portland cement systems and slags [34,39,203]. Among numerous iron-rich hydration products, including ferrihydrites, Fe-containing AFm, and Fe-ettringite, hydrogarnets have demonstrated the highest level of stability [199]. Therefore, it is reasonable that hydrogarnet becomes the main crystalline hydration products in BOF slag system. Hydrotalcite and pyroaurite can be theoretically considered as the Al and Fe rich endmembers of a solid solution represented by the general formula $Mg_3(Al,Fe)(OH)_8(CO_3)_{0.5}\cdot nH_2O$. However, the two diffraction peaks at 12.90 and 13.60 °2θ indicate there being two phases. They belong to the layered double hydroxides (LDH), and the formed LDH can be locally different.

The precipitation of hydroxyapatite can be expected under conditions where calcium and phosphate ions are present, particularly in an alkaline environment [204], however only very small amounts are visible in XRD. The pH of the designate binder ultimately increases due to the acid-base neutralization between $H_2PO_4^-$ and BOF slag, and the continuous

hydration of C_2S and $C_2(A,F)$. It is possible that the high pH (above 10) in the system hinders the formation of well-crystalline hydroxyapatite [205], making the hydroxyapatite largely X-ray amorphous. FT-IR spectra (***Fig. 5.4***) reveal characteristic bands corresponding to phosphate groups, further confirming the formation of hydroxyapatite. The infrared peaks associated with the PO_4^{3-} group correspond to the asymmetric stretching vibration (ν3) at 1031 cm^{-1}, and the characteristic bending vibrations (ν4', ν4") at 603 and 563 cm^{-1}, respectively [206]. The absence of the peaks at 1060, 765 and 635 cm^{-1} assigned to PO_4^{3-} bending vibrations excludes the formation of struvite, which is the typical hydration product in magnesium phosphate cement [207]. Even though other calcium phosphates like octacalcium phosphate can have similar IR vibrations, the high pH above 10 excludes the possibility of the existence of other calcium phosphates [206,208].

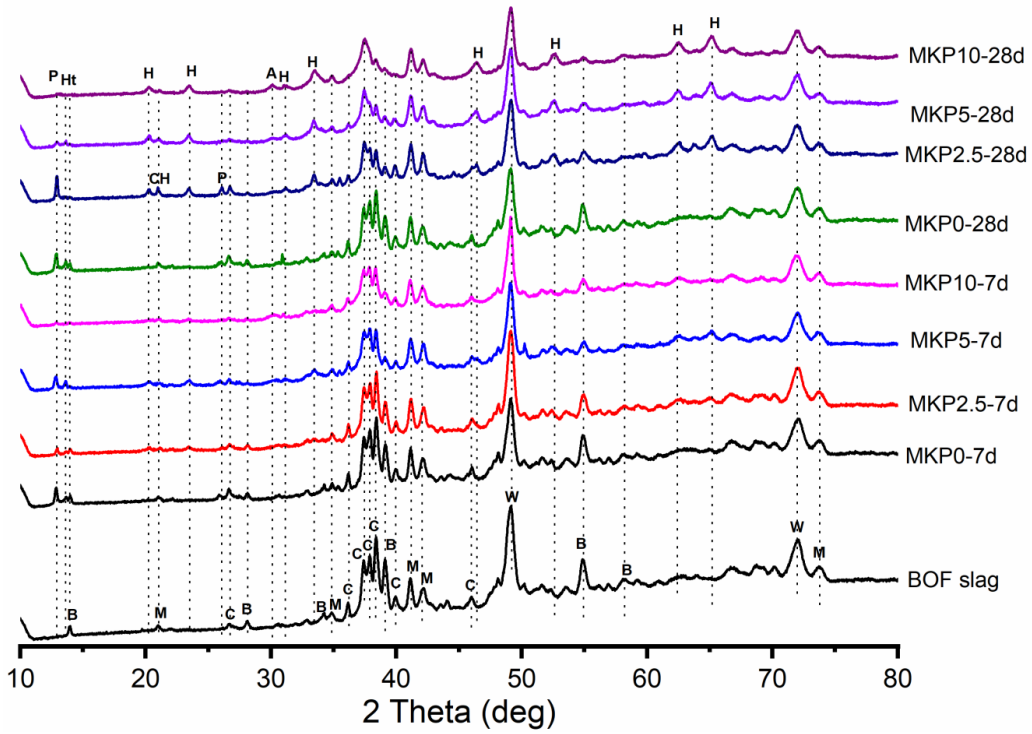

Fig. 5.3 *XRD data of hydrated samples with dosages of MKP (Legend: B-Brownmillerite($C_2(A,F)$), C-C_2S, M-Magnetite, W-Wuestite, P-Pyroaurite, H-Hydrogarnet, Ht-Hydrotalcite, A-Hydroxyapatite, CH-Portlandite).*

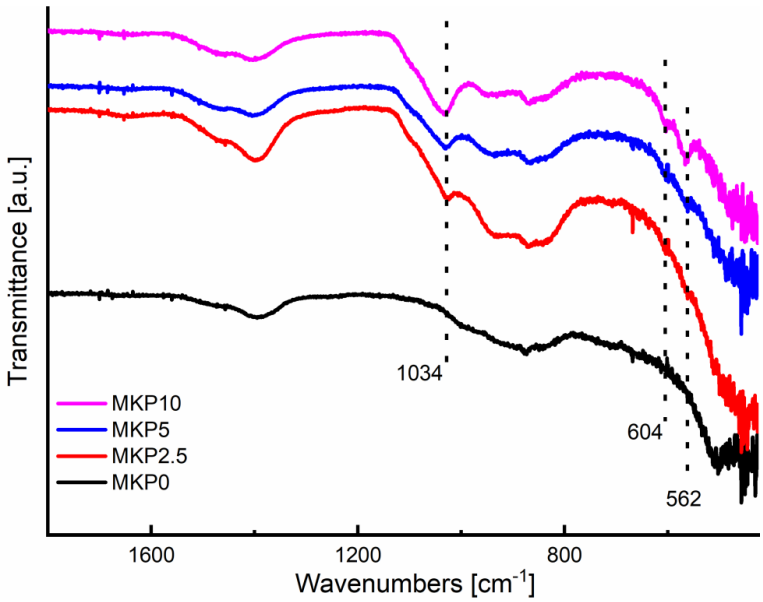

Fig. 5.4 *FTIR spectra of BOF slag pastes with dosages of MKP after 28-day hydration.*

Further insights into the phase amounts of 7 and 28-day hydration products have been gained via XRD-Rietveld analysis as shown in ***Table 5.2***. LDH (hydrotalcite + pyroaurite) and hydrogarnet have been identified as the principal crystalline hydration products in MKP0, aligning with findings of Franco Santos et al. [34]. In comparison to raw BOF slag, there is minimal formation of hydration products for MKP0, signifying its low reactivity in water. The introduction of 2.5 wt.% phosphate results in a slightly lower LDH content at 7 days and a significant increase at 28 days compared to MKP0. The further increase of phosphate to 5 wt.% results in a similar amount of LDH as MKP0 at 7 days. The content of LDH is limited in MKP10 at 7 days, as the diffraction peaks of hydrotalcite and pyroaurite are invisible.

0.8 and 1.8 wt.% of hydrogarnet is formed by the hydration of MKP0 at 7 and 28 days, respectively. The addition of MKP significantly promotes the formation of hydrogarnet at 28 days, whose amount correlates well with the extent of $C_2(A,F)$ hydration, generally increasing with the increased dosage of phosphate. However, elevating the phosphate dosage from 5 to 10 wt.% does not enhance the hydration of $C_2(A,F)$ or improve the formation of hydrogarnet at 7 days. The amount of hydrogarnet in MKP10 at 7 days is only 1.8 wt.%, however a notable increase to 11.8 wt.% at 28 days is observed. In comparison to MKP10, MKP5 achieves a higher hydrogarnet amount of 6.3 wt.% at 7 days and a comparable hydrogarnet of 10.8 wt.% at 28 days. High additions of phosphate may inhibit the formation of hydrogarnet at 7 days even though it activates $C_2(A,F)$, which can be attributed to the formation of other metastable phosphate-containing phases at early ages that slowly transform into the hydrogarnet over time. This explains the presence of multiple exothermic peaks, attributed to that slow conversion process.

Table 5.2 *Phase amounts of 7 and 28-day hydrated samples with varying dosages of MKP determined by XRD-Rietveld analysis.*

Phase	Raw slag	7 days				28 days			
		MKP0	MKP2.5	MKP5	MKP10	MKP0	MKP2.5	MKP5	MKP10
Wuestite	20.5	20.5	21.2	18.2	19.0	20.3	20.0	17.3	18.6
Magnetite	6.4	6.1	5.9	5.6	6.4	5.7	6.3	5.7	6.0
C_2S	39.6	38.8	39.9	26.5	32.0	36.8	28.0	23.5	20.1
$C_2(A,F)$	17.1	15.6	13.3	4.6	7.9	13.1	6.8	4.6	4.6
Lime	0.9	0.5	0.9	0.2	0.2	0.9	0.8	0.5	0.3
Calcite	0.8	0.5	0.6	0.4	0.2	0.4	0.5	1.1	0.6
Portlandite	0.7	0.8	0.0	0.0	0.0	1.1	0.7	0.6	0.1
Hydrogarnet	0.0	0.8	3.2	6.3	1.8	1.8	8.5	10.8	11.8
Hydroxyapatite	0.2	0.0	1.3	1.9	3.1	0.0	1.9	2.4	6.2
LDH	0.0	0.7	0.2	0.6	0.0	0.9	1.9	0.5	0.2
Amorphous	14.0	17.9	17.8	41.8	38.1	21.6	30.4	39.5	39.7

**Note: the amounts of wuestite, magnetite, C_2S and $C_2(A,F)$ were normalized by the mass of water loss and phosphate input.*

Various impurities in C_2S severely constrain its hydration activity [42]. This is evident in the phase amounts of MKP0 where only a limited amount of C_2S has reacted both at 7 and 28 days. The hydration of C_2S in MKP2.5 is also inhibited at 7 days, as indicated by the low amount of C_2S that has reacted compared to MKP5, where a substantial decrease in C_2S content and a notable increase in the amorphous phase occurs. A further increase of MKP does not continue to increase C_2S consumption at 7 days. At 28 days, the consumption of C_2S correlates well with the addition of phosphate, increasing with the increase of phosphate (from 28.0 wt.% in MKP2.5 to 20.1 wt.% in MKP10). However, no significant growth in the amorphous phase from 7 to 28 days is observed for MKP5 and MKP10.

The consumption of C_2S by MKP is enhanced compared to other activators like tripotassium citrate, which is able to promote the $C_2(A,F)$ hydration while the activation of C_2S by citrate by is negligible [39]. The high amorphous content in the MKP samples compared to MKP0 could therefore be due to the formation of C-S-H gel or may more likely involve other phosphate containing x-ray amorphous hydrated phases. Phosphate can bind significant amounts of Ca from C_2S thereby promote the dissolution of C_2S [187,204]. Over time these amorphous metastable phosphate phases could transform into hydroxyapatite, as the further increase in hydroxyapatite is noticed especially for samples containing high phosphate dosage like MKP10.

Magnetite content remains relatively stable in the samples and wuestite exhibits a slight decrease in the presence of 5 and 10 wt.% phosphate. Phosphate interacts with iron, aluminium, magnesium and calcium via adsorption, ligand exchange, precipitation and coprecipitation across a broad pH range, whereas Mg^{2+} is more likely than Fe^{2+} in wuestite to react with phosphate in this system due to the pH limitation [58,209]. Lime and calcite remain low after 28 days of hydration. Notably, no portlandite is present at 7 days in the MKP samples and only appears in small amounts at 28 days.

The TG-DTG method, depicted in ***Fig. 5.5***, provides compelling evidence of hydrogarnet and other hydration products forming in the BOF slag pastes. The final weight loss is low in MKP0 and increases significantly with MKP addition. Notably, a further increase in MKP dosage from 5 to 10 wt.% does not yield a higher final weight loss. The weight loss unfolds in distinct stages, each offering insights into the intricate composition of the hydrated system.

I. 40 to 200 °C: Initial weight loss corresponds to the removal of adsorbed water of hydroxyapatite and the release of chemically bound water from C-S-H gel [73,210,211].

II. 200 to 400 °C: Subsequent weight loss is attributed to the water loss from siliceous hydrogarnet and hydrotalcite-pyroaurite minerals [199,212].

III. 400 to 450 °C: Weight loss is linked to the dehydroxylation of portlandite [73].

IV. 450 to 720 °C: Another weight loss phase signifies the decomposition of carbonate groups in calcium carbonates [73].

V. 720 to 1000 °C: A final weight loss range corresponds to the dehydroxylation from hydroxyapatite [210,211].

MKP0 exhibits a four-stage mass loss, concluding with the decomposition of calcite at 720 °C . In contrast, samples containing MKP display a continuous increase in mass loss beyond 720 °C, corresponding to the dehydroxylation of hydroxyapatite [210]. Notably, in an aqueous environment, CO_3^{2-} can substitute PO_4^{3-} at room temperature, forming B-type carbonated hydroxyapatite [213]. This substitution initiates decarbonation around 500 °C, concluding around 1000 °C [214]. The formed hydroxyapatite may undergo partial carbonation during the curing process, contributing to the observed higher weight loss in the carbonate region in samples containing MKP.

The mass loss observed within the temperature range of 200 to 400 °C predominantly arises from water loss in siliceous hydrogarnet and hydrotalcite-pyroaurite minerals [199,212]. The decomposition of the hydrotalcite-pyroaurite solid solution is dependent on the Al/Fe ratio but always occurs between approximately 200 and 400 °C [215]. However, due to the minor presence of hydrotalcite-pyroaurite minerals, they only have slight effects on the mass loss within the temperature range of 200 to 400 °C in comparison to hydrogarnet for phosphate containing samples. Consistent with XRD

Rietveld outcomes, the formation of siliceous hydrogarnet post 28-day hydration exhibits the comparable extent for all phosphate-containing samples.

The temperature range of 40 to 200 °C is associated with mass loss generated from the removal of water in hydroxyapatite and C-S-H gel and the weight loss peaks exhibit an overlap. MKP0 shows a peak at around 150 °C, which is undoubtedly assosciated with the decomposition of C-S-H gel [73]. Hydroxyapatite shows a peak at a lower temperature around 100 °C compared to that of C-S-H gel. This water loss is reversible and does not affect lattice parameters [204,211]. The amount of the formed C-S-H gel in MKP2.5 and MKP5 is notably higher in comparison to MKP0 after 28 days of hydration. However, in MKP10, the distinctive mass loss peak of C-S-H gel is absent, suggesting a lower amount of C-S-H gel is formed compared to MKP2.5 and MKP5.

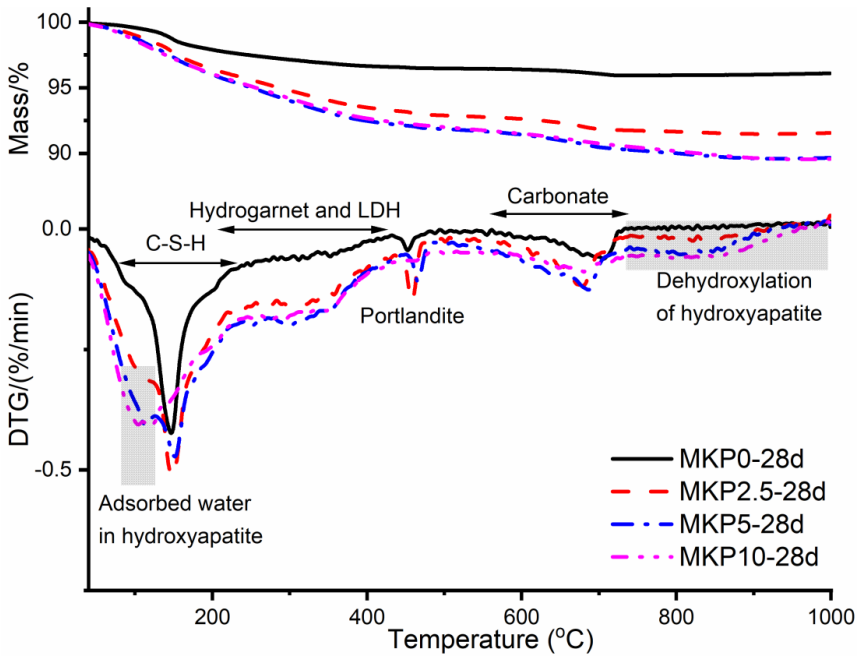

Fig. 5.5 *Thermal analysis (TG & DTG) of BOF slag pastes with dosages of MKP varying from 0 to 10 wt.% after 28 days of hydration.*

Nitrogen sorption analysis was employed to characterize the BET specific surface area of BOF slag pastes following 28 days of hydration, as illustrated in ***Fig. 5.6***. The observed evolution of the BET specific surface area mirrors the changes in the quantity of formed C-S-H gel, as gel pores (2-10 nm) within the C-S-H gel significantly contribute to the cumulative pore area in the Portland cement system [87,89,216]. The BET specific surface area experiences an increase with the incorporation of MKP in comparison to the reference sample. Notably, MKP5 exhibits the highest cumulative gel pore area, attributed to the maximum C-S-H content identified via the DTG method. However, a further MKP addition decreases the surface area. This suggests that, instead of C-S-H gel, silica gel also

does not form in MKP10 at 28 days, as silica gel contributes more to the increase in surface area compared to C-S-H gel [43,217]. Instead, a lower Ca/Si C-S-H gel in MKP10, compared to other samples, might form, and its contribution to the increase in surface area is diminished due to the filling effects of substantial hydroxyapatite. The water loss peak of C-S-H gel occurs at a lower temperature with a low Ca/Si molar ratio [218]. This also explains the distinctive mass loss peak at a lower temperature in MKP10.

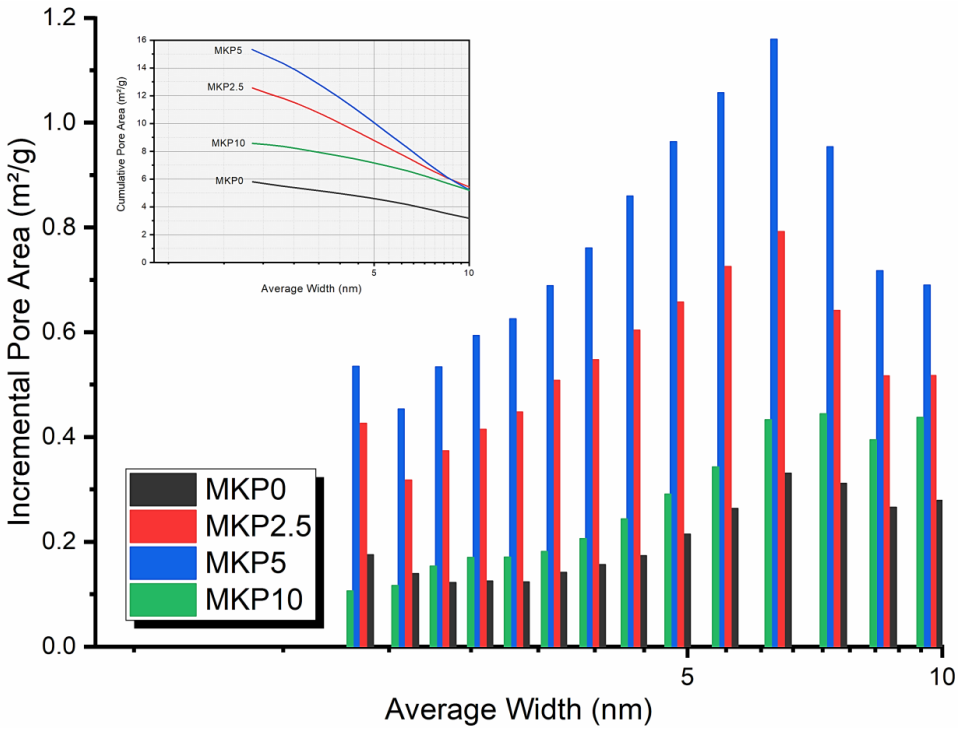

Fig. 5.6 *Specific surface area distribution of BOF slag pastes with dosages of MKP varying from 0 to 10 wt.% after 28 days of hydration.*

Fig. 5.7 shows the EDS based phase map of MKP5 after 28 days of curing, revealing a dense structure with visible macro pores. The crystalline and amorphous hydration products present in the sample have a very small particle size and are intermixed impeding the differentiation of individual phases like C-S-H, hydrogarnet, and others with EDS [198], which has a spatial resolution of around 1 micron. Therefore, all such phases are grouped together into a single hydration product. Portlandite, calcite and lime are grouped together as well, since differentiation is difficult based on EDS. Likewise, wuestite and magnetite are grouped together.

A discernible rim surrounding C_2S was observed, becoming more pronounced with increased phosphate addition, as depicted in ***Fig. 5.8***. It contains significantly less CaO than the adjacent C_2S (***Table 5.3***). This Si-rich layer covering the C_2S surface can be

attributed to the extraction of Ca by phosphate post mixing. ***Fig. 5.8*** also depicts the presence of large pores amidst the hydration products, attributed to the flash hardening from the drastic reaction following the mixture of BOF slag with abundant phosphate, leaving considerable unreacted water which becomes voids after drying.

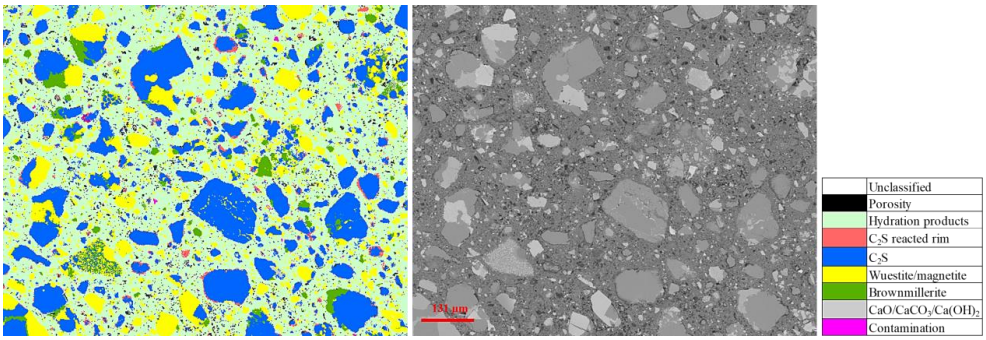

Fig. 5.7 *Representative PARC phase map and BSE image of 28-day hydrated slag paste with MKP dosage of 5 wt.%.*

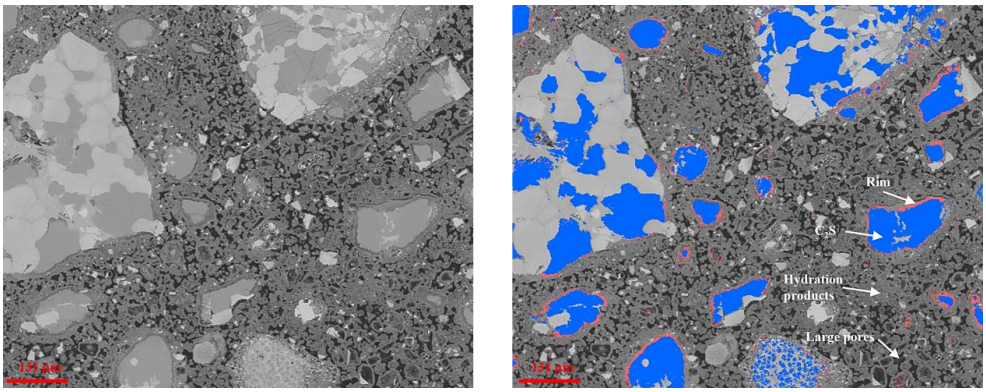

Fig. 5.8 *Representative BSE image of 28-day hydrated slag paste with MKP dosage of 10 wt.%.*

Table 5.3 displays the average chemical composition of the hydration products, which are rich in Ca, followed by Fe, Si and P. The hydration product contains both chromium and vanadium from the $C_2(A,F)$ and C_2S reacting. The considerable extraction of Ca upon phosphate addition is crucial for most hydration product formations. Hydroxyapatite and hydrogarnet can be assumed to have a Ca/P and Ca/(Al+Fe) molar ratios of 1.67 and 1.5, respectively. Consequently, based on detected P and Al+Fe amounts in the hydration products, the approximate amount of Ca bound by hydroxyapatite and hydrogarnet can be inferred. Any remaining Ca can primarily be attributed to C-S-H. Partially, Al and Fe contribute to hydrotalcite and pyroaurite formation, albeit in small quantities. ***Table 5.4*** illustrates Ca distribution in different hydration products, with hydrogarnet binding the most Ca in each sample, consistent with Rietveld results. As phosphate addition increases,

Ca consumption by hydroxyapatite rises, reducing available Ca for C-S-H since hydroxyapatite precipitates preferentially with respect to C-S-H [219]. Hence, this likely causes the formation of C-S-H with a lower Ca/Si ratio in MKP10 compared to that in MKP2.5 and MKP5.

Table 5.3 *The average chemical composition (wt.%) of hydration products and rims in samples containing different dosages of phosphate using PARC.*

	Sample ID	Na_2O	MgO	Al_2O_3	SiO_2	P_2O_5	SO_3	K_2O	CaO	TiO_2	V_2O_5	MnO	Fe_2O_3
Hydration products	MKP2.5	0.61	1.95	2.8	14.01	5.56	0.6	0.65	46.95	1.78	1.54	1.88	20.4
	MKP5	0.51	2.25	2.36	14.46	7.24	0.46	2.06	45.04	1.72	1.5	1.84	19.07
	MKP10	0.62	1.81	2.15	12.59	12.7	0.27	4.05	43.99	1.69	1.52	0.83	16.3
Rim	MKP2.5	0.5	0.49	0.65	30.43	3.15	1.11	0.77	52.95	1.63	0.46	0.53	4.08
	MKP5	0.73	0.48	3.42	30.47	2.61	1.17	1.95	44.53	2.41	0.99	0.9	7.59
	MKP10	0.36	0.32	2.78	32.22	2.17	1.23	3.3	43.66	1.84	1.14	0.38	7.45

Table 5.4 *The distribution of Ca in different hydration products calculated from the average chemical composition of the overall hydration product shown in* ***Table 5.3****.*

Sample ID	$Ca_5(PO_4)_3OH$	$Ca_3(Al_xFe_{1-x})_2(SiO_4)_y(OH)_{4(3-y)}$	C-S-H and others
MKP2.5	15.6%	55.6%	28.8%
MKP5	21.2%	53.2%	25.6%
MKP10	38.1%	47.1%	14.8%

5.3.3. Porosity and mechanical properties

The pore structure of 28-day hydrated BOF slag pastes was analyzed using MIP measurements, and the results are presented in ***Table 5.5***. MKP0 exhibits an overall porosity of 33.55% and a median pore size of 639.4 nm. Compared to this, all phosphate-containing samples demonstrate a reduction in both porosity and median pore size. The porosities of MKP2.5, MKP5, and MKP10 are measured at 22.42, 22.19, and 22.53%, respectively. However, there are significant variations in median pore size among these samples, with MKP5 showing the smallest pore size, followed by MKP2.5 and MKP10. This difference in median pore size suggests the different pore size distribution as shown in ***Fig. 5.9***. MKP10 exhibits a substantial presence of gel pores and microcapillary pores below 20 nm, along with numerous larger pores exceeding 1000 nm, consistent with the pore structure observed using SEM-BSE. Despite the presence of a certain amount of gel pores in MKP10, macrocapillary pores exceeding 1000 nm can be implicated in the

reduction of strength [87,220]. Additionally, it should be noticed that large amounts of macro pores above 10000 nm cannot be measured accurately due to MIP method limitation.

Table 5.5 *Porosity and pore size of 28-day hydrated BOF slag paste.*

Sample ID	Porosity [%]	Median pore size [nm]
MKP0	33.55	639.4
MKP2.5	22.42	33.7
MKP5	22.19	31.0
MKP10	22.53	160.0

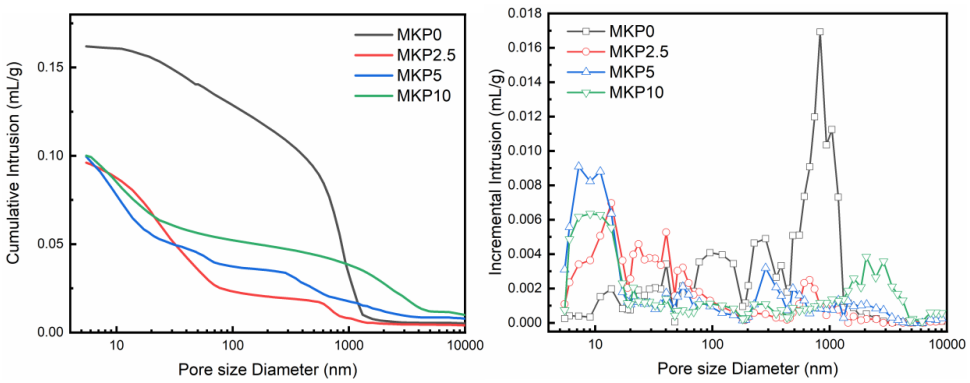

Fig. 5.9 *The cumulative and incremental pore volume of 28-day hydrated BOF slag paste.*

The mechanical performance of MKP0 is found to be relatively unsatisfactory, in line with its high porosity and large pore size, primarily due to its low hydraulic activity, as demonstrated in ***Fig. 5.10***. The addition of 2.5 wt.% MKP has minimal influence on the strength development after 7 days, attributed to the limited hydration of C_2S and $C_2(A,F)$ as detected via QXRD. However, at 28 days, a notable increase in compressive strength is observed, reaching 30.5 MPa. This trend is consistent with the heat release recorded via calorimetry, which starts after the prolonged induction period of 23 days (***Fig. 5.2***). A higher addition of 5 wt.% MKP significantly enhances the mechanical properties, resulting in a remarkable compressive strength of 19.9 and 44.5 MPa at 7 and 28 days, respectively. Nevertheless, a further increase in phosphate dosage leads to a decline in compressive strength both at 7 and 28 days, to as low as 7.9 and 14.4 MPa, respectively. The comparable porosities (***Table 5.5***) of phosphate-containing samples were expected to result in similar compressive strength. However, the observed variation in strength development correlates with differences in median pore size, where the lower median pore size leads to higher strength with comparable porosities. ***Fig. 5.11*** shows a clear

trend where the strength increases with the elevation of chemically bound water whereas MKP10 at 28 days is apparent out of this trend. Despite the comparable amount of chemically bound water in MKP10 and MKP5 at 28 days, the significant formation of hydration products in MKP10 does not yield the anticipated strength development seen in MKP2.5 and MKP5. This can be ascribed to the rapid reaction of BOF slag with phosphate at the early stages, resulting in the generation of numerous large pores detrimental to mechanical performance as detected by MIP and SEM at different pore size levels up to microns. Furthermore, the lower amount of C-S-H gel in MKP10 compared to MKP2.5 and MKP5 as estimated (***Table 5.4***) is notable. C-S-H gel exhibits favourable binding properties and is responsible for the strength development in Portland cement. These properties are uncertain for hydroxyapatite formed in the BOF slag system.

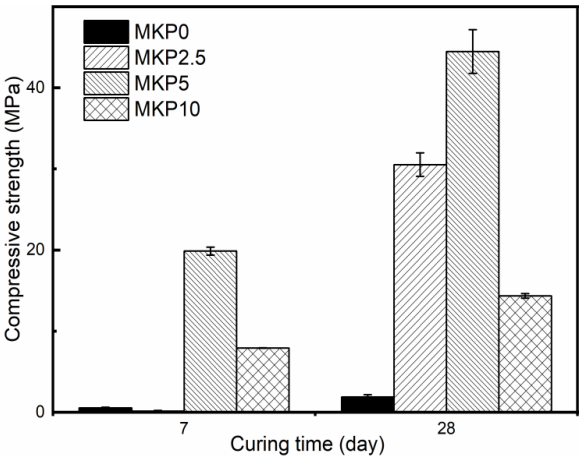

Fig. 5.10 *The strength development of 28-day hydrated BOF slag paste.*

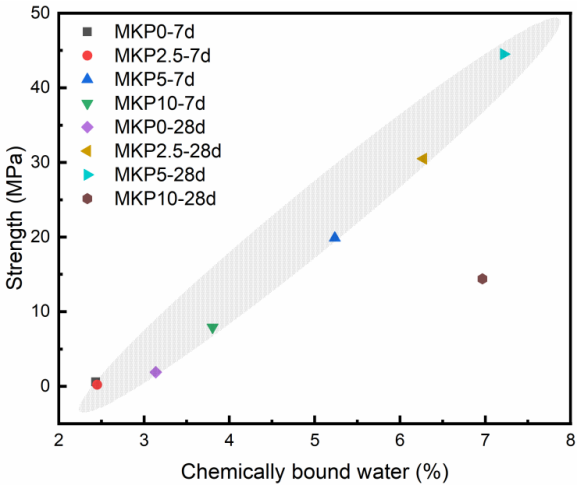

Fig. 5.11 *Correlations between chemically bound water and strength.*

5.3.4. Environmental impact

Table 5.6 *Leaching of inorganic contaminants measured by one stage batch leaching test and the SQD limit values and its pH.*

Parameter	Unshaped material (SQD)	MKP0	MKP2.5	MKP5	MKP10
	mg/kg	mg/kg	mg/kg	mg/kg	mg/kg
Antimony (Sb)	0.32	0.005	0.002	0.005	0.004
Arsenic (As)	0.90	0.007	0.005	0.007	0.004
Barium (Ba)	22.00	0.251	0.519	0.425	0.030
Cadmium (Cd)	0.04	bdl*	bdl	bdl	bdl
Chromium (Cr)	0.63	0.004	0.010	0.039	0.140
Cobalt (Co)	0.54	0.001	0.001	bdl	bdl
Coper (Cu)	0.90	0.001	0.001	0.002	0.003
Lead (Pb)	2.30	0.002	0.002	0.001	0.002
Molybdenum (Mo)	1.00	0.008	0.006	0.009	0.083
Nickel (Ni)	0.44	0.001	0.002	0.002	0.001
Tin (Sn)	0.40	bdl	bdl	bdl	bdl
Vanadium (V)	1.80	0.033	0.008	0.006	0.076
Zinc (Zn)	4.50	0.003	0.002	0.003	0.002
pH		12.4	12.7	13.0	13.0

**bdl - below detection limit.*

The one batch leaching test was conducted on 28-day cured slag pastes to assess the environmental impact of BOF slag-based building materials. Element concentrations were

compared with Dutch Soil Quality Decree (SQD) values [201], outlined in ***Table 5.6***. The BOF slag utilized in this study contains various heavy metals, predominantly Cr and V, incorporated mainly in wuestite/C_2(A,F) and C_2S, respectively [34,39]. The leaching of heavy metals from all 28-day hydrated BOF slag pastes was minimal and far below SQD values, consistent with prior research indicating BOF slag's ability to retain heavy metals post-hydration due to the formation of C-S-H gel and hydrogarnet [34,42]. QXRD results indicate that increased phosphate addition correlates with higher dissolution of C_2S and C_2(A,F), resulting in elevated leachable V and Cr levels. Despite the significant hydrogarnet formation, which can effectively immobilize heavy metals, the lower amount of C-S-H in MKP10 could also undermine its overall immobilization capacity. VO_4^{3-} can substitute PO_4^{3-} at high temperatures, incorporating into the hydroxyapatite structure to form $Ca_5(PO_4)_{3-x}(VO_4)_xOH$ [221,222]. However, the effectiveness of hydroxyapatite in immobilizing V under ambient conditions is unknown. Studies suggest that Cr uptake by hydroxyapatite is feasible within a controlled pH range, preferably below 7 [223,224]. This causes the uncertainty surrounding Cr removal by hydroxyapatite in alkaline BOF slag systems as all pH values are above 12 after 28-days hydration as shown in ***Table 5.6***.

5.3.5. Additional discussion on effects of MKP on BOF slag hydration

The pore fluid composition in the pastes, is reflected to some extent in the aqueous solutions from the 24-hour leaching test. ***Fig. 5.12*** shows that the Ca concentration reaches saturation and stabilizes after 2 hours of hydration in MKP0, consistent with the immediate formation of portlandite upon the start of hydration reactions, and even buffering the fluid phase in the 24-hour leaching test.

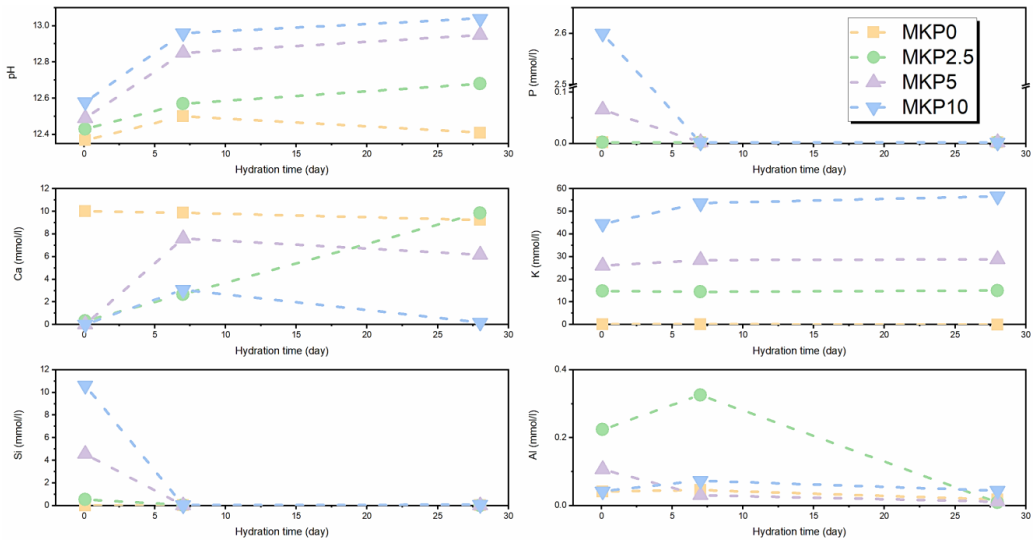

Fig. 5.12 *pH and ion concentration in leaching solution of BOF slag pastes with dosages of MKP varying from 0 to 10 wt.% at 2 hours, 7 and 28 days.*

MKP dissolved in water is acidic, however the pH increases rapidly upon mixing as explained by the following two equations:

$$5Ca_2SiO_4 + 3H_2O + 6H_2PO_4^- \rightarrow 2Ca_5(PO_4)_3OH + 5H_2SiO_3 + 6OH^- \quad \textbf{(5.1)}$$

$$5Ca_2(Al,Fe)_2O_5 + 3H_2O + 6H_2PO_4^- \rightarrow 2Ca_5(PO_4)_3OH + 10(Al,Fe)OOH + 6OH^- \quad \textbf{(5.2)}$$

At 2 hours, all pH values of the solutions in the 24-hour leaching test of phosphate-containing samples surpass 12.4, with PO_4^{3-} being the primary species. Apparently during setting, the rapid reaction between the added phosphate and C_2S and $C_2(A,F)$ results in the formation of a largely amorphous hydroxyapatite like phase, as indicated by the peak observed at 114 °C in ***Fig. 5.13***. This formation reduces the Ca concentrations in the pore solution which in turn enables the release of Si and Al at 2 hours as also reflected in the 24-hour leaching test of those samples (***Fig. 5.12***). MKP5 and MKP10 exhibit phosphate concentrations of 0.07 mmol/L and 2.6 mmol/L, respectively, indicating the excessive phosphate input suppressing the Ca and allowing Si and Al in solution at 2 hours [59]. Notably, the reaction of acidic phosphate with aluminium and iron is likely to occur before the pH rises above 7 upon mixing, as described by [59]:

$$(Al,Fe)O_2^- + 4H^+ + PO_4^{3-} \rightarrow (Al,Fe)PO_4 \cdot 2H_2O \quad \textbf{(5.3)}$$

This suggests that the unconsumed phosphate at phase saturation (***Eq. (5.3)***) controls the Al concentrations in the 2-hour pore fluid as reflected in the 24-hour leachate and preserved due to acidification prior to ICP test.

Thereafter, the Ca concentration becomes primarily controlled by the dissolution equilibrium among siliceous hydrogarnet, portlandite, C-S-H, and hydroxyapatite. Among these phases, hydroxyapatite exhibits the lowest solubility, followed by siliceous hydrogarnet, C-S-H, and portlandite [204,208,225,226]. The higher Ca concentration observed in MKP5 at 7 days compared to MKP2.5 and MKP10 can be attributed to the larger quantity of C-S-H. The main source of the lower Ca concentrations in MKP2.5 and MKP10 is predominantly the hydrogarnet and hydroxyapatite that have a lower solubility. The further increase in the Ca concentration in MKP2.5 at 28 days suggests ongoing primary hydration following a prolonged induction period, as shown in ***Fig. 5.2***. In other samples, the decrease in Ca concentrations is associated with the further stabilization and carbonation of hydration products after the main hydration process whereas in MKP2.5 the hydration still seems to be ongoing, as indicated by QXRD and DTG results.

Via calculation based on the initial MKP input, the theoretical K concentrations should be around 14.9, 29.2 and 55.7 mmol/L in MKP2.5, MKP5 and MKP10 if all K is part of the aqueous solution in the 24-hour leaching test. These results are indeed quite close to the measured K concentrations (15.0, 28.8 and 56.64 mmol/L in MKP2.5, MKP5 and MKP10) at 28 days and indicate that K is not incorporated into any stable hydration products. In MKP2.5, the K concentration remains stable over the entire 28-day hydration period, whereas MKP5 and MKP10 show lower K concentrations during the first 7 days. Though specific phases incorporating and later releasing potassium are not identified, previous studies suggest that the reaction of excess MKP with wollastonite (CS) may yield metastable $CaK_3H(PO_4)_2$, which can subsequently form hydroxyapatite at higher pH levels [227,228].

At 7 days, the tiny amount of Si is observed in all samples. The reaction of C_2S in MKP2.5 at 7 days (***Table 5.2***) is minimal, resulting in limited availability of Si leading to the formation primarily of OH-hydrogarnet with a higher solubility than Si-rich hydrogarnet. Consequently, the higher Al concentration in MKP2.5 at 7 days can be attributed to the increased solubility of OH-hydrogarnet [199,203]. In these other samples, the Al concentrations are similarly lower at 7 days which remain stable until 28 days. Si concentrations also stabilize in low level at 28 days, as Si plays a crucial role in the formation of less soluble C-S-H and Si-rich hydrogarnet. Furthermore, the limited Si concentration supports the absence of silica gel in all samples. The total reduction of C_2S in MKP10 is 19.5 wt.% at 28 days. Assuming that phosphate only reacts with C_2S as shown in ***Eq. (5.1)***, the theoretical consumption of C_2S would be 10.53 wt.%, thus leaving 0.06 mol Si per 100 g paste to form low Ca/Si C-S-H in addition of hydrogarnet.

Phosphate depletion in the leachate is observed at 7 days, while an increase in hydroxyapatite content at 28 days is noted across all phosphate-containing samples, with MKP10 exhibiting the most significant increase of 3.1 wt.%. This phenomenon can be attributed to two potential causes: the crystallization of amorphous hydroxyapatite formed at the first place or, more likely, the transformation of metastable phosphate-containing phases coexisting with hydroxyapatite. These metastable phases are likely rich in aluminum and iron and eventually convert into hydrogarnet, leaving phosphate to form hydroxyapatite. Consequently, the increase of 10 wt.% hydrogarnet coupled with a 3 wt.% decline in C_2(A,F) content in MKP10, as shown in ***Table 5.2***, is reasonable. A similar process is observed in MKP5.

The dosage of added phosphate plays a critical role in the hydration process. A low dosage of 2.5 wt.% phosphate has limited effects on the early dissolution of Si, resulting in retarded hydration despite enhanced overall hydration at 28 days. Increasing the phosphate input to 10 wt.% accelerates hydration but inhibits hydrogarnet formation at 7 days. This is primarily due to prominent calcium phosphate precipitation, although the potential for phosphate ions to react with iron and aluminum should not be overlooked [58,59,229]. The over-sequestration of calcium ions by hydroxyapatite, as indicated in ***Table 5.4***, leaves insufficient calcium for the formation of C-S-H, potentially resulting in

C-S-H with a low Ca/Si molar ratio. Additionally, the drastic acid-base reactions caused by excessive phosphate (10 wt.%) result in the formation of significant large pores, up to microns in size, which are detrimental to strength development despite the presence of abundant hydration products.

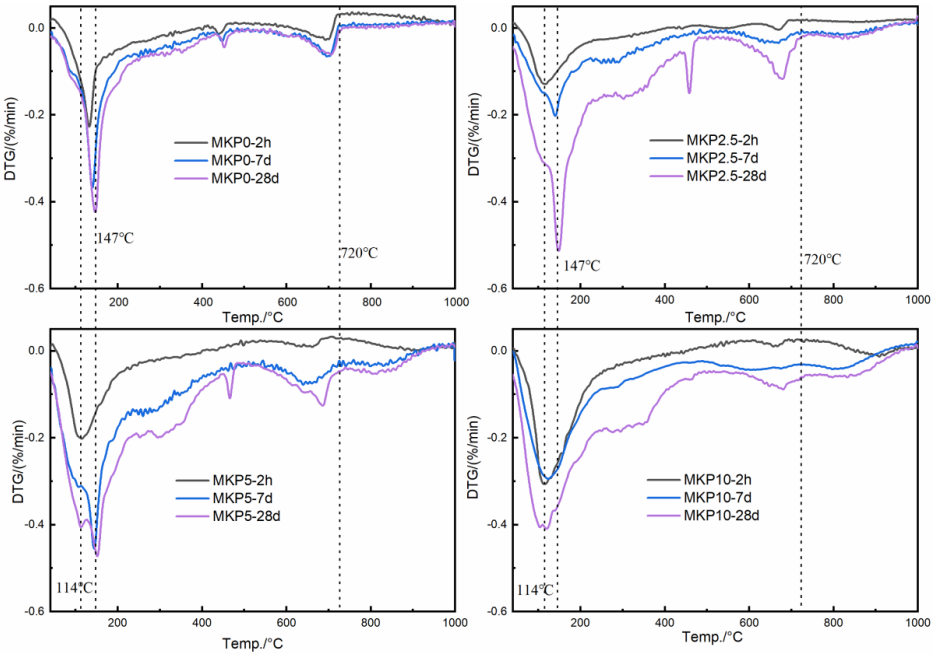

Fig. 5.13 *DTG curves at 2 hours, 7 and 28 days.*

5.4. Conclusions

This study introduces a novel approach to utilize BOF slag as cement-free binder, exhibiting satisfactory strength and leaching behaviour. Through comprehensive analysis, insights into the reactions between BOF slag and varying quantities of mono potassium phosphate were obtained, revealing the influence on microstructure and strength development. The experimental investigation leads to the following conclusions:

The incorporation of monopotassium phosphate (MKP) facilitates the dissolution and hydration of $C_2(A,F)$ and C_2S, enhancing mechanical properties compared to a reference samples where BOF slag reacts only with water. The principal hydration products identified include hydrotalcite, pyroaurite, hydrogarnet, C-S-H gel, and hydroxyapatite.

2.5 wt.% MKP addition shows little effects on hydration before 7 days because the insufficient dissolution of C_2S and $C_2(A,F)$ restricts the precipitation of hydration products. However, it still benefits overall hydration at 28 days.

Optimization of pore structure is achieved with the addition of 5 wt.% MKP, resulting in maximum strength at both 7 and 28 days. This formulation exhibits significant formation of C-S-H and hydrogarnet, along with some hydroxyapatite.

Excessive MKP addition (10 wt.%) leads to a drastic early-stage reaction, causing unexpectedly large pores in the matrix and hindering strength development. Additionally, Ca was bound in hydroxyapatite reducing available Ca for C-S-H formation. Balancing the extraction of Si, Al and Fe, and the fixation of Ca is therefore crucial.

Phosphate ions can interact with iron and aluminium ions, forming a metastable phase that decomposes over time, benefiting secondary formation of hydrogarnet. Further research is needed to investigate the behavior, microstructure, and composition of this metastable phase.

CHAPTER 6

6. Activation of BOF Slag with Dipotassium Hydrogen Phosphate: Enhancing Hydration, Carbonation Resistance, and Heavy Metal Leaching

For the development of a cement-free BOF slag binder, dipotassium hydrogen phosphate (DKP) was used as an activator at levels up to 3 wt.%. The heat release, phase assemblages, porosities, and mechanical performance of the hydrated BOF slag pastes were investigated to evaluate DKP's activation efficiency. The carbonation behaviours of both reference samples and DKP-activated samples were also examined to assess their carbonation resistance. The results demonstrate that DKP-activated BOF slag pastes exhibit satisfactory mechanical performance and promising carbonation resistance. Increasing DKP from 1 to 3 wt.% in BOF slag pastes extends the induction period while enhancing overall hydration heat. This enhancement aligns with greater consumption of belite and brownmillerite and increased formation of hydration products such as hydrogarnet, C-S-H gel, and LDH phases. The improved hydration optimizes the overall pore structure, reducing porosity from 40.73 to 22.36% with 3 wt.% DKP, thereby increasing strength from 1.9 to 42.5 MPa at 28 days. Additionally, the reference sample exhibits poor carbonation resistance, as indicated by significant vanadium (V) leaching. However, heavy metal leaching is effectively controlled in the presence of phosphate after carbonation, falling well below the limits stipulated by the Dutch Soil Quality Decree (SQD). This control is attributed to the abundance of hydration products capable of immobilizing heavy metals and the sustained high pH due to the strong buffering capacity of HPO_4^{2-}/PO_4^{3-}. This buffering capacity plays a crucial role in retarding calcium carbonate formation. The stabilized high pH during carbonation limits carbonic acid availability and portlandite dissolution, thereby mitigating the overall carbonation of DKP-activated BOF slag pastes and mortars in this chapter.

This chapter is reproduced from: Y. Tang, METHOD FOR ACTIVATING BASIC OXYGEN FURNACE STEEL SLAG, WO 2024/052265 A1, 2024. (International patent); Y. Tang, K. Schollbach, S.R. van der Laan, W. Chen, Activation of BOF Slag with Dipotassium Hydrogen Phosphate: Enhancing Hydration, Carbonation Resistance, and Heavy Metal Leaching, 2024 (submitted).

6.1. Introduction

Carbonation resistance is crucial for building materials. In conventional concrete, carbonation can naturally occur, reducing alkalinity and making the reinforcement more susceptible to chloride corrosion [230,231]. Alkali-activated materials (AAMs), developed as cement-free binders, tend to experience reduced durability at a higher rate than conventional concrete due to the absence or minimal formation of portlandite, which acts as an alkalinity buffer [232,233]. From an environmental perspective of BOF slag binder, carbonation influences the leaching behavior significantly. BOF slag can contain heavy metals like vanadium (V) and chromium (Cr). Previous studies indicate that hydrated BOF slag can retain heavy metals due to the formation of abundant hydration products [197]. However, after carbonation, the leaching of heavy metals from BOF slag pastes increases significantly [212]. Carbonation enhances the leachability of V in BOF slag. Non-weathered BOF slags release low quantities of the less mobile and toxic V(IV) compared to the more oxidized and mobile V(V) [234]. After carbonation, the leaching of V can increase substantially, with partial oxidation of V(IV) to V(V) [235]. This increase correlates with the drop in pH due to reaction of portlandite and dissolved CO_2, as V remains relatively immobile in highly alkaline environments [212,236,237]. The leaching values of Cr are generally much lower than those of V. The leaching of Cr tends to remain similar or even slightly reduced after carbonation [212,237].

The development of a cement-free BOF slag binder deserves more attention than its use as a supplementary cementitious material in conventional cement. Our previous research demonstrates that monopotassium phosphate (MKP) can achieve synergistic activation of both belite and ferrite phases, producing layered double hydroxide (LDH) phases, hydrogarnet, C-S-H gel, and hydroxyapatite as principal hydration products [197,238]. However, the hydration process varies significantly with different phosphate dosages ranging from 2.5 to 10 wt.%. An optimal addition of 5 wt.% phosphate results in improved pore structure and satisfactory compressive strengths of 19.9 MPa at 7 days and 44.5 MPa at 28 days. Lower phosphate dosages were anticipated to achieve comparable strength, but 2.5 wt.% phosphate only enhances overall hydration at 28 days, showing poor hydration at 7 days. This slow activation process is attributed to the initial low pH of approximately 4.2 and the strong buffering effect of $H_2PO_4^-/HPO_4^{2-}$ ions with pH around 7 [239].

Since natural carbonation is a slow process, accelerated carbonation is generally adopted to evaluate the carbonation resistance of building materials [154,232]. This involves exposing the building materials to significantly higher CO_2 concentrations than the ambient level (~0.03 wt.%) for a certain period, up to several months. Therefore, accelerated carbonation is necessary to predict the leaching behavior of heavy metals in shaped cement-free BOF slag building materials over time.

Following up on our previous study, we developed dipotassium hydrogen phosphate (DKP, K_2HPO_4)-activated BOF slag pastes with DKP dosages of up to 3 wt.%. The heat

release, phase assemblages, porosities, and mechanical performance of the hydrated BOF slag pastes were investigated to evaluate the activation efficiency of DKP. Additionally, the leaching of heavy metals was tested, including vanadium (V), chromium (Cr), and molybdenum (Mo), before and after accelerated carbonation. The carbonation behaviors of both reference samples and DKP-activated samples were examined, focusing on differences in mineralogical composition, pH, carbonation depth, and porosities. The results indicate that DKP-activated BOF slag exhibits satisfactory mechanical performance and promising carbonation resistance. These samples maintain a high pH level and effectively control the leaching of heavy metals upon carbonation.

6.2. Experiments and methodology

6.2.1. Raw materials

The BOF slag utilized in this study was sourced from standard production at Tata Steel (The Netherlands). A disc milling process (Retsch, RS300XL) was employed for 15 minutes to obtain BOF slag powder. The particle size distribution of the BOF slag powder, analyzed using a laser particle size analyzer (Model Malvern Mastersizer 2000, Malvern PANalytical), is depicted in ***Fig. 6.1***, indicating a median particle size of approximately 17 μm. Chemical composition analysis of the BOF slag powder was conducted via X-ray fluorescence (XRF, Model Axios Advanced, PANalytical.B.V), with results summarized in ***Table 6.1***. Furthermore, the mineral composition was determined through quantitative X-ray diffraction (QXRD) analysis, the findings of which are presented in ***Table 6.2***. Dipotassium hydrogen phosphate (DKP, K_2HPO_4) was selected as the additive, sourced as a commercially available technical-grade product (VWR Chemicals BDH®, purity $\geqslant$ 99.0 wt.% analytical reagent).

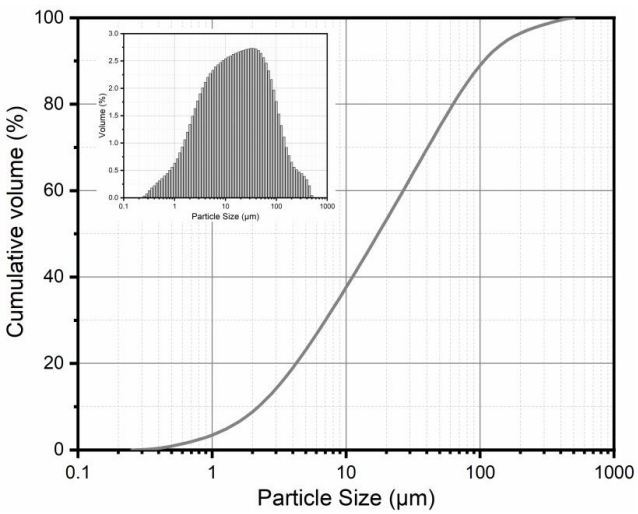

Fig. 6.1 *Particle size distribution of BOF slag.*

Table 6.1 *Mineralogical composition of BOF slag.*

Mineral compound	Brownmillerite	Magnetite	Belite	Wuestite	Lime	Calcite	Portlandite	Amorphous
Content [wt.%]	17.1	6.4	39.6	20.5	0.9	0.8	0.7	14.0

Table 6.2 *Chemical composition of BOF slag.*

Oxide	MgO	SiO_2	Al_2O_3	CaO	P_2O_5	TiO_2	V_2O_5	Cr_2O_3	MnO	Fe_2O_3	Others	GOI
Content [wt.%]	6.8	13.45	2.21	40.14	1.61	1.39	1.05	0.3	4.61	28.32	0.12	1.31

6.2.2. Mix design of DKP-activated BOF slag pastes

DKP, equivalent to 0, 1, 2, and 3 wt.% of BOF slag, was initially mixed with water to ensure homogeneous dispersion before blending. The pH values of all DKP solutions are around 8.8. The water-to-solid (BOF slag + DKP) ratio was set at 0.18. Initially, the BOF slag powder was mixed with the DKP solution at low speed for 30 seconds, followed by manual homogenization for an additional 30 seconds. Subsequently, another mixing session lasting 60 seconds at high speed was performed to produce the DKP-activated BOF slag pastes. The freshly prepared BOF slag pastes were then poured into foam molds ($40\times40\times160$ mm^3) and covered with plastic film before demolding. The pastes were air-cured at ambient temperature until the testing age. The samples in this study are denoted based on the amount of DKP added, labeled as DKP0, DKP1, DKP2, and DKP3 for 0, 1, 2, and 3 wt.% DKP dosages, respectively.

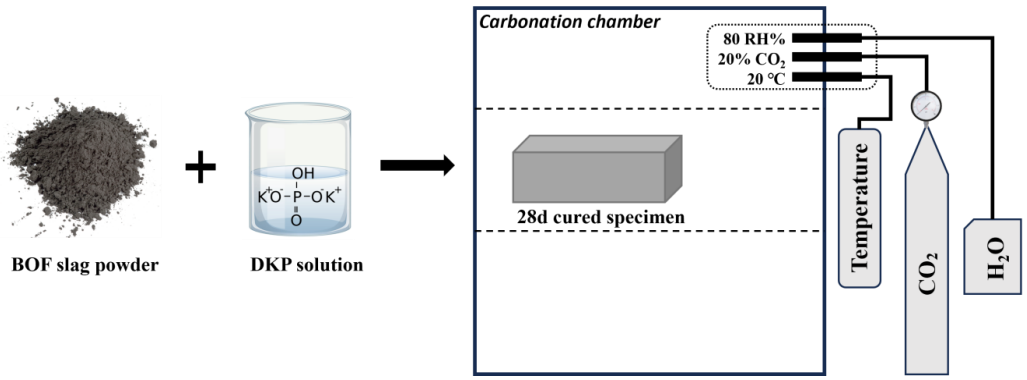

Fig. 6.2 *Schematic of samples preparation starting from mixing to carbonation process.*

6.2.3. Carbonation of DKP-activated BOF slag powders, pastes and mortars

Evaluation of carbonation resistance was conducted on 28-day cured samples powder, paste and mortar samples. Although no direct correlation has been established between

the carbonation rates of pastes, mortars, and concretes with a given binder type, the addition of inert or low-activity ingredients like sand can increase the carbonation coefficient [154,164,240,241]. Coarse aggregates in mortars introduce more voids and create weaker interface transition zones (ITZ), facilitating greater CO_2 penetration and thus a faster carbonation rate. This allows CO_2 to reach deeper sections more easily compared to the paste. Besides, the fine powder has a high surface area, allowing for increased contact between CO_2 in the atmosphere and the slag particles, facilitating faster carbonation.

The 28-day cured pastes were placed in a CO_2 chamber with a CO_2 concentration of 20 wt.% and a relative humidity of 80 wt.% for 14 days. The carbonated pastes in this study are denoted based on the amount of DKP added, labeled as CDKP0, CDKP1, CDKP2, and CDKP3 for 0, 1, 2, and 3 wt.% DKP dosages, respectively. The whole process is presented in ***Fig. 6.2***.

DKP-activated BOF slag mortar was prepared in the polystyrene mold (40×40×160 mm^3), using 2 wt.% DKP and a sand to binder ratio of 1. The water to binder ratio was 0.25 to ensure workability. The prepared mortar after 28-day hydration was placed into CO_2 chamber for 14 days with the same carbonation conditions as the pastes.

The powder sample was obtained via milling 28-day cured samples to be below 63 μm. The obtained fine powder was exposed to atmospheric CO_2 for 2 years.

6.2.4. Methodology

6.2.4.1. Calorimetric test

The rate of heat release was measured using an isothermal conduction calorimeter (TAM Air, Thermometric). To prepare a homogenous paste, BOF slag powders were internally mixed with distilled water or DKP solution for 2 minutes. The heat flow curve was integrated between 45 minutes and 14 days to assess the cumulative heat release.

6.2.4.2. Compressive strength

The compressive strength at 7 and 28 days was determined according to EN 196-1, applying a loading rate of 2400 N/s to all specimens, with three replicates for each composition.

6.2.4.3. Characterization

The pieces below 4 mm that were obtained from the manually crushed pastes after hydration or carbonation, underwent immersion in isopropanol for 72 hours to eliminate hydration. Subsequently, they were dried in a vacuum oven at 45 °C until a constant mass was achieved [73]. Following drying, partial pieces were finely ground to pass through a 63 μm sieve. The obtained powder and the remaining piece samples were stored in

desiccators. Calcium chloride pellets served as the drying agent, while sodium hydroxide pellets acted as a CO_2 trap until further testing.

The crystalline phases of the hydrated and carbonated slag pastes were quantified employing the Rietveld method, using a D4 ENDEAVOR X-ray Diffractometer equipped with a LynxEye detector and a Co X-ray tube, operating at 40 kV and 40 mA. The scanning range covered 10 to 90 °2θ with a step size of 0.019° and a counting time of 1 second per step. Si powder (Siltronix, France), serving as an internal standard with a mass comprising 10 wt.% of the tested samples, was thoroughly mixed with the samples using an XRD-Mill McCrone (RETSCH) operating at 75% speed for 5 minutes to ensure a homogeneous distribution of the powders. The quantification of crystalline and amorphous phases was conducted using the TOPAS 5.2 software from Bruker Corporation.

Nitrogen sorption analysis was conducted using a Brunauer-Emmett-Teller (BET) instrument, specifically the TriStar II 3020 from Micrometrics. The surface area and pore size distribution were determined from the adsorption branch of the sorption isotherm. The Brunauer-Emmett-Teller method [76] was employed to calculate the surface area, while the Barrett–Joyner–Hallenda method [77] was utilized to evaluate the pore size distribution.

Mercury Intrusion Porosimetry (MIP) measurements with the AutoPore V 9600 Micrometrics Series Mercury Porosimeter with the maximum pressure of 228 MPa was applied to analyse the porosity of hydrated or carbonated pastes.

Thermogravimetric analyses (TGA) were performed with a NETZSCH STA 449 F1 instrument. Ground powder samples, each weighing between 30 to 40 mg, underwent heating at a rate of 10 °C/min in a nitrogen atmosphere, covering temperatures from 40 to 1000 °C. The temperature range for quantifying carbonates was determined from approximately 500 to 800 °C [199].

6.2.4.4. Mass changing due to carbonation

Carbonation was applied to 28-day cured samples. The mass changing of these samples was recorded per day using a balance (PB3001, Mettler). The phenolphthalein test was applied for all 14-day carbonated samples. The phenolphthalein solution was sprayed on the surface of powder samples and the cross section after breaking pastes and mortars.

6.2.4.5. Leaching behavior

The leaching test followed the guidelines of EN 12457–2 (one stage batch leaching test) and was conducted on 28-day cured and 14-day carbonated slag pastes (mortars) [200]. Samples were prepared by crushing and sieving hydrated and carbonated specimens below 4 mm. Deionized water was added to the sieved samples at a liquid-to-solid ratio (L/S) of 10 using a dynamic shaker (ES SM-30, Edmund Buhler GmbH) at a constant speed of 250 rpm for 24 hours. After agitation, leachates were filtered through a syringe filter (pore diameter 0.22 μm, VWR). pH values were measured at ambient temperature using

a GMH-GREISINGER 5500 pH meter, with three readings taken and averaged for each sample. Liquid samples were either undiluted or diluted by a factor of 10 for further element concentration measurements. The concentrations of Ca^{2+}, K^{+}, and phosphate were determined using a Thermo Scientific Dionex ICS-1100 ion chromatography (IC) system. Acidified solutions with concentrated HNO_3 were analyzed using an inductively coupled plasma atomic emission spectrometer (ICP-OES, SPECTROBLUE), following NEN 6966. Finally, the obtained element concentrations were compared with the limit values specified in the Dutch Soil Quality Decree [201].

6.3. Results

6.3.1. Hydration

6.3.1.1. Isothermal calorimetric analysis

The results of isothermal calorimetry are depicted in ***Fig. 6.3***. A minor peak is evident at approximately 24 hours for DKP0, indicative of limited dissolution of BOF slag and precipitation of hydration products due to its low hydraulic reactivity [186]. Introducing 1 wt.% phosphate notably advances the exothermic peaks, with a significant increase in cumulative heat release. The further addition of phosphate delays the appearance of the main exothermic peaks, observed at approximately 64 hours and 72 hours in DKP2 and DKP3, respectively. However, this delay of the main heat flow peaks does not seem to affect cumulative heat. A clear increase between total heat release and higher phosphate additions is observed. In our previous study, varying amounts of monopotassium phosphate (KH_2PO_4) were found to elevate hydration heat, although strong retardation effects were observed with 2.5 wt.% KH_2PO_4, resulting in a 23-day induction period [197,238]. In contrast, the main reaction of BOF slag with DKP additions below 3 wt.% can be completed in just 3 days. This substantial difference underscores how phosphate alkalinity determines its accelerating or retarding role in BOF slag hydration. The initial pH of KH_2PO_4 solution, being below 7, requires the hydration system to pass through the buffering region of $H_2PO_4^-$ and HPO_4^{2-}, where the pH is kept in the range of 7-7.5 [239], hindering precipitation of hydration products like C-S-H and hydrogarnet [65,199,242]. Conversely, DKP solution not only promotes the dissolution of original phases in BOF slag but also establishes an appropriate pH range for hydration product precipitation due to its basic nature, supported by the first 3-day cumulative hydration heat.

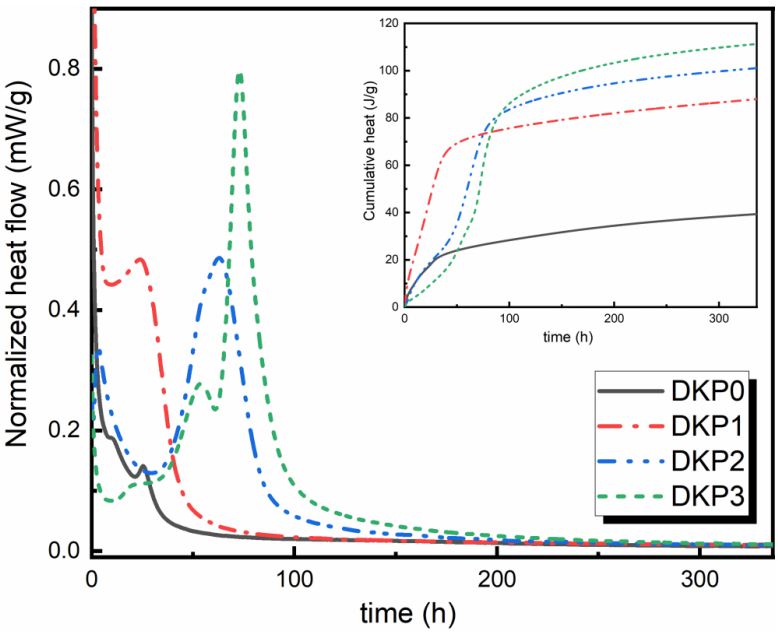

Fig. 6.3 *Cumulative heat evolution and heat flow of BOF slag pastes with dosages of DKP varying from 0 to 3 wt.%.*

6.3.1.2. Phase formation during hydration

Fig. 6.4 illustrates the phase composition of 7- and 28-day hydrated BOF slag pastes, with crystalline hydration products mainly comprising hydrogarnet, hydroxyapatite, and LDHs phases (pyroaurite/hydrotalcite). As depicted by the heat release profiles of these samples (***Fig. 6.3***), the hydration product development of DKP0 progresses slowly, whereas the addition of phosphate strongly influences the hydration kinetics and, consequently, the phase assemblage. Brownmillerite, being the most actively hydraulic phase in BOF slag, undergoes minimal alteration in DKP0, resulting in a modest increase in hydrogarnet and LDHs phases [39]. Belite begins to react after 7 days, accompanied by a notable increase in amorphous phases, likely attributed to C-S-H gels. The hydration of belite is influenced by various factors, including the added water content, pH, and anions in solution [187]. The low water-to-solids ratio (w/s) in this study significantly restricts the reactivity of belite in DKP0. Magnetite is inert whereas wuestite shows a slight decrease, whose reactivity increases with the increasing Mg content [241].

In the presence of phosphate, the hydration of both brownmillerite and belite is significantly enhanced during the first 7 days and continues until 28 days. The consumption of brownmillerite and belite correlates well with the dosages of phosphate, increasing with higher phosphate additions. Consequently, hydrogarnet becomes the most abundant crystalline hydration product, increasing over time. The precipitation of hydroxyapatite readily initiates in the presence of calcium and phosphate ions,

particularly in an alkaline environment [204]. The content of hydroxyapatite (1.7, 1.9 and 2.5 wt.% in DKP1, DKP2 and DKP3, respectively) increases with higher phosphate additions at 7 days, remaining relatively stable (1.6, 2.0 and 3.2 wt.% in DKP1, DKP2 and DKP3, respectively) at later ages. Generally, the amount of pyroaurite and hydrotalcite continues to increase throughout the hydration process, with slight growth observed from 7 to 28 days in DKP1 and more significant growth in samples with higher phosphate dosages. The mass ratios of pyroaurite/hydrotalcite vary with different phosphate dosages, suggesting that the detected hydrotalcite and pyroaurite in the BOF slag system can be locally different due to other involved anions replacement [245]. Magnetite remains relatively stable while wuestite exhibits a notable decrease in the presence of phosphate. This could influence the formation of LDHs as the partial dissolution of wuestite provides Mg. An increasing amount of portlandite in all phosphate containing samples is observed compared to DKP0, stabilizing after 7-day hydration.

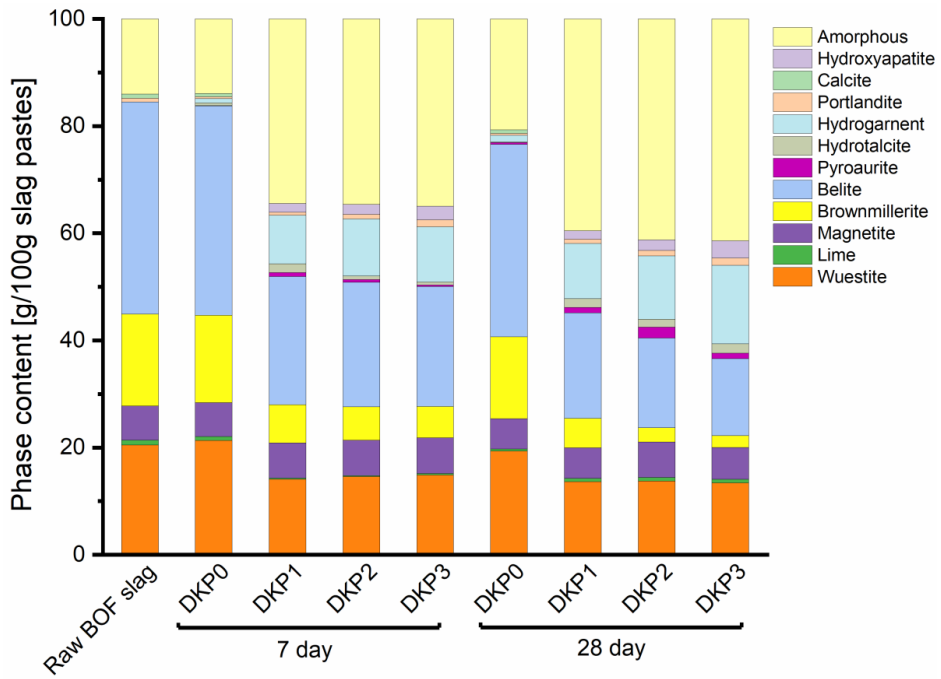

Fig. 6.4 *QXRD results of 7- and 28-day hydrated samples with dosages of DKP varying from 0 to 3 wt.%.*

6.3.1.3. Thermogravimetric analysis

To gain deeper insights into the overall hydration progress of BOF slag pastes, the TG-DTG method was employed to detect the water bound in hydrogarnet and other hydration products, particularly C-S-H gel, which remains undetectable via XRD due to its low crystallinity [48]. DKP0 exhibits the lowest mass loss, as depicted in ***Fig. 6.5***. A noticeable increase in mass loss with increasing phosphate concentration is observed at 7 days. At

28 days, all samples exhibit a further increase in mass loss, albeit at varying degrees, with DKP1 exhibiting a lower increase of 1.3% compared to DKP2 (2.6%) and DKP3 (2.0%). This disparity closely correlates with the differing consumption rates of belite and brownmillerite from 7 to 28 days in DKP1, DKP2 and DKP3, which are found to be 5.8, 10.1 and 11.6 wt.%, respectively, as determined by the Rietveld method.

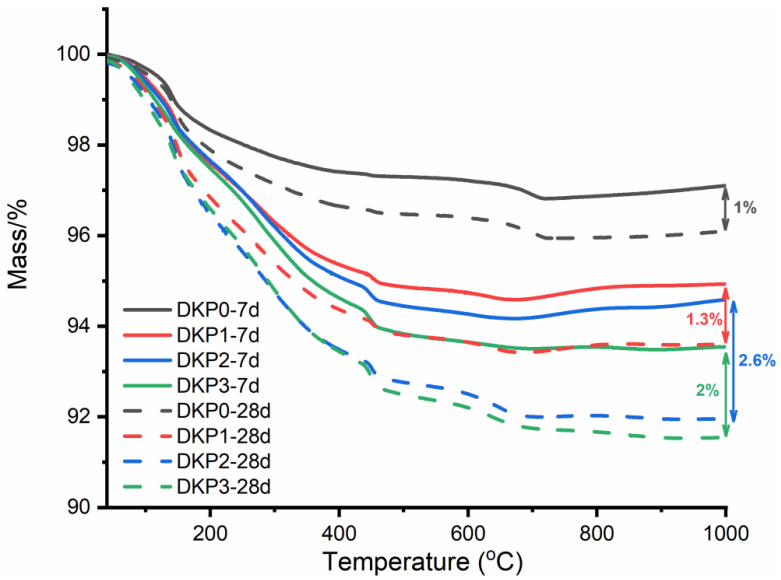

Fig. 6.5 *Mass loss of BOF slag pastes with dosages of DKP varying from 0 to 3 wt.% after 7 and 28 days of hydration.*

Fig. 6.6 provides insights into the weight loss occurring at distinct temperature stages, revealing the complex composition of the hydrated system. While the removal of adsorbed water in hydroxyapatite and the release of loosely chemically bound water from C-S-H gel overlap in the temperature range of 40 to 200 °C, their respective peaks are distinguishably situated at temperatures of 105 (hydroxyapatite) and 147 °C (C-S-H). Hydroxyapatite, has the ability to undergo reversible water removal between 40 and 200 °C without the lattice parameters being affected [204,211]. The dehydration of siliceous hydrogarnet and hydrotalcite-pyroaurite minerals (LDH) occurs within the temperature range of 200 to 400 °C [199,212]. However, the weight loss in this region is dominated by hydrogarnet due to its much higher amounts. The mass loss of hydrogarnet and LDH increases with the addition of phosphate, as well as an increase in age from 7 to 28 days. Notably, phosphate addition promotes the formation of portlandite, evident from its pronounced decomposition peaks in the temperature range from 400 to 450 °C [73]. This observation differs from previous research using KH_2PO_4 as the additive, where portlandite is absent during the first 7-day hydration [238] and only appears at 28d. This disparity can be attributed to the influence of the initial pH of the additives, where phosphates with higher pH (DKP) can enhance the hydration rate of belite at 7 days

compared to MKP, without the inbibition effects of the $H_2PO_4^-/HPO_4^{2-}$ buffering regime [239]. Another weight loss observed from 450 to 720 °C signifies the decomposition of carbonate groups in calcite in DKP0 [73]. Crystalline calcium carbonates are not detected in the phosphate-containing samples via XRD Rietveld method, suggesting that the mass loss in this temperature range may originate from amorphous calcium carbonate, stabilized by phosphates, which delay its transformation into crystalline forms [246]. A final weight loss range corresponding to the dehydroxylation from hydroxyapatite is observed above 720 °C for phosphate-containing samples [210,211].

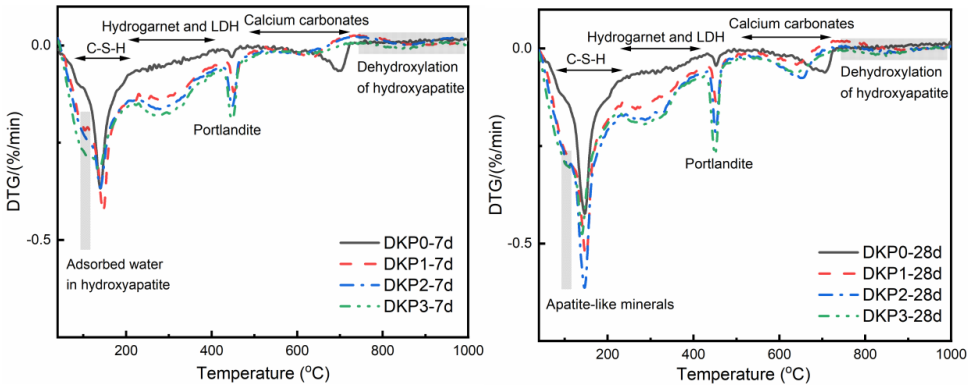

(a) ***(b)***

Fig. 6.6 *The first derivative of thermogravimetric analysis (DTG/TGA) of BOF slag pastes with dosages of DKP varying from 0 to 3 wt.% after (a) 7 and (b) 28 days of hydration.*

6.3.2. Porosities and its mechanical performance

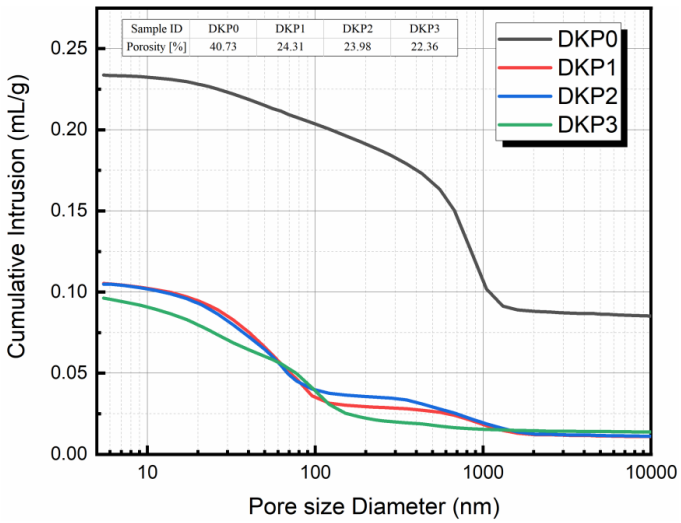

Fig. 6.7 *The cumulative pore volume and overall porosity of 28-day hydrated BOF slag pastes.*

Fig. 6.7 shows the pore structure of 28-day hydrated BOF slag pastes analyzed via MIP measurement. DKP0 shows a high porosity of 40.73 % in line with its low reaction extent. Its pore size distribution concentrates in the range of 10-1000 nm, more preferentially 100-1000 nm as indicated by the cumulative pore size. The overall hydration of phosphate activated BOF slag pastes has been greatly improved as previously discussed. Consequently, the total porosities of all samples containing phosphate decrease to 24.31, 23.98, and 22.36% for DKP1, DKP2, and DKP3, respectively, which are very similar but slightly decreased with the increasing phosphate addition.

Porosity is the main factor influencing the strength. The low strength of DKP0 is observed in ***Fig. 6.8***, showing a 7- and 28-day strength of 0.6 and 1.9 MPa, respectively. With 1 wt.% addition of DKP, the compressive strength is elevated to 15.7 and 27.0 MPa at 7 and 28 days, respectively. A further phosphate addition leads to higher strength, showing a maximum 28-day strength of 42.5 MPa with 3 wt.% DKP dosage. DKP1 at 28 days shows comparable porosity to the other two samples containing DKP but its strength development is less satisfactory. The porosities of DKP1, DKP2 and DKP3 are 24.31, 23.98, and 22.36%, respectively. Despite comparable porosities, the strength increases with the increasing amount of hydration products [247], which can be roughly determined by the final mass loss calculated from thermogravimetric analysis.

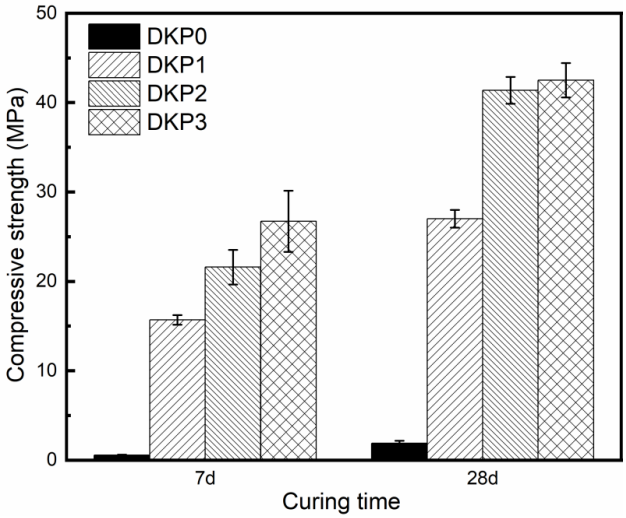

Fig. 6.8 *The strength development of 28-day hydrated BOF slag paste.*

6.3.3. Carbonation resistance evaluation

6.3.3.1. Leaching before and after carbonation

The BOF slag utilized in this study contains various heavy metals, with vanadium (V) exhibiting the highest concentration, followed by chromium (Cr), as indicated by the chemical composition. Cr is found mainly in wuestite and brownmillerite, whereas vanadium is primarily found in C2S and brownmillerite [34,39]. Despite molybdenum's

(Mo) concentration being below the detection limits of the XRF method, it is also investigated due to its common occurrence in iron-containing phases like brownmillerite [248]. Concentrations of V, Cr, and Mo obtained from the batch leaching test are compared with the Dutch Soil Quality Decree (SQD) values as shown in ***Fig. 6.9*** [201].

Before carbonation, all 28-day hydration BOF pastes exhibit minimal leaching of heavy metals that are below the SQD values. This is governed by the equilibrium between the release of heavy metals from the original slag phases (such as belite and brownmillerite) during hydration and the retention of heavy metals by hydration products (such as C-S-H gel and hydrogarnet) [34,42]. The reactivity of DKP0 is low, resulting in limited release of heavy metals. In contrast, phosphate activated BOF slag pastes demonstrate high hydration degrees, yet the leaching of heavy metals is effectively controlled and even lower than that of DKP0. This is attributed to the immobilization capacity of the abundant hydration products for heavy metals.

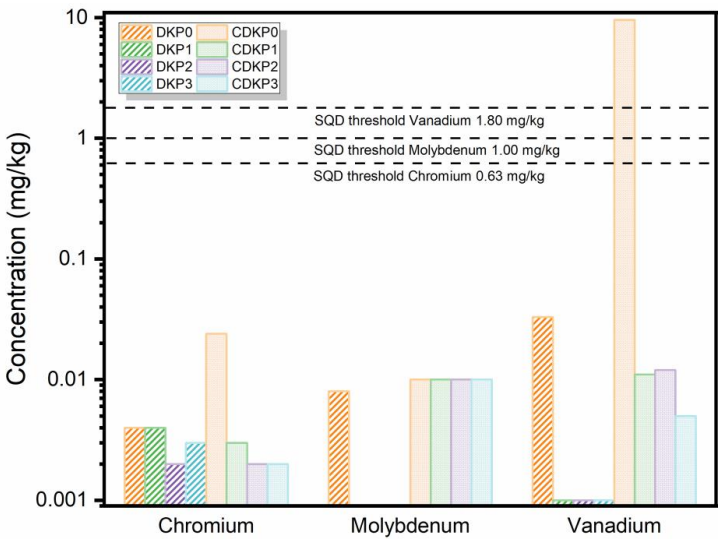

Fig. 6.9 *Leaching of inorganic contaminants before and after carbonation measured by one stage batch leaching test and the Dutch Soil Quality Decree (SQD) limit values.*

After carbonation, a significant increase in V leaching is observed in CDKP0, with concentrations over 300 times higher compared to DKP0. The V concentration in CDKP0 exceeds SQD values, whereas all phosphate-containing samples show only a slight increase in V leaching to around 0.01 mg/kg, well below the threshold. At high pH, V tends to form various oxyanions like VO_4^{3-}, which can be adsorbed on C-S-H gel, providing unspecific adsorption sites at positively charged calcium ions [249]. Additionally, V^{3+} can occupy the B site in hydrogarnet, substituting trivalent cations (Fe^{3+} and Al^{3+}) [34,249]. Nevertheless, it is important to note that V leaching is strongly influenced by pH, increasing as pH decreases [236]. ***Table 6.3*** illustrates the pH of leaching solutions of hydrated BOF slag pastes before and after carbonation. The noticeable decrease in pH of

DKP0 after carbonation from 12.6 to 11.4 contrasts with the slight drop in pH observed in phosphate-containing samples, which maintain pH at a high level (pH~13) more stably. This accounts for the significant V leaching observed in CDKP0 and the relatively low values in the phosphate-containing samples.

Despite that phosphate ions in the leaching solution are below the detection limit (0.2 mg/l) of IC methods due to the formation of hydroxyapatite with low solubility, phosphate buffering role in the limited pore solution cannot be ignored during the carbonation process. Alkaline phosphate has the capacity to stabilize high pH above 12 due to the buffering role of HPO_4^{2-}/PO_4^{3-} ions [204,239]. Additionally, the added K^+ can have the synergistic role in maintaining high alkalinity, reducing the carbonation rate [230,250]. This is also reflected in the changes in K and Ca concentrations before and after carbonation, as shown in ***Table 6.3***. A significant reduction in Ca concentration is noticed in CDKP0 whereas both K and Ca concentrations reduce with a relatively slight extent after carbonation, and the extent of this reduction decreases with increasing phosphate input.

Table 6.3 *The pH values and alkaline metal concentrations of leaching solutions of hydrated BOF slag pastes before and after 14-day carbonation.*

	Sample ID	DKP0	DKP1	DKP2	DKP3
pH	Before carbonation	12.6	13.1	13.2	13.3
	After carbonation	11.4	12.8	13.0	13.1
K [mmol/l]	Before carbonation	0.13	9	17	27
	After carbonation	0.04	7	16	26
Ca [mmol/l]	Before carbonation	10	11	10	8
	After carbonation	1.2	8	7	7

A reasonable increase in Cr concentration of CDKP0 is noticed, caused by the decomposition of hydration products rather than brownmillerite upon carbonation since brownmillerite is inert in CO_2 environment [212,236]. Cr and Mo belong to the same group in the periodic table (6th secondary group), and while the mechanisms of Mo immobilization are less complex than Cr, their concentrations in the leachate of samples containing phosphate change only slightly before and after carbonation since their leaching behavior is not as directly influenced by pH as V [164,249].

6.3.3.2. Mass change

Fig. 6.10 illustrates the mass effects of all samples during carbonation. CDKP0 exhibits a two-stage mass change, with a significant 10.85 wt.% decline within the first 3 days of carbonation, followed by a gradual increase until 14 days. In contrast, the mass change of phosphate-containing samples is relatively small. After a slight increase on the first day,

the overall mass increase remains below 1 wt.%. When samples are placed in the carbonation chamber, pore water evaporates due to the humidity difference, causing a mass decrease. Simultaneously, CO_2 uptake by original slag phases such as belite, and hydration products like portlandite and C–S–H, leads to the formation of calcium carbonates, amorphous silica gel, and new free water, resulting in a mass increase [31,164]. Thus, the mass change depends on the balance between CO_2 uptake and water evaporation. Excessive pore water can slow CO_2 diffusion [31]. The reference sample, CDKP0, has significant free water that remains unconsumed by the BOF slag over 28 days due to its low reactivity. Initially, the mass change in CDKP0 is dominated by water evaporation. The subsequent mass increase indicates substantial CO_2 uptake, consistent with the phenolphthalein test results shown in ***Fig. 6.10***. Conversely, phosphate-containing samples generate abundant hydration products at 28 days, leaving limited free water for evaporation. The mass change in these samples is most likely driven by CO_2 uptake, but the carbonation extent is minimal, with only a thin carbonation layer observed in the phenolphthalein test.

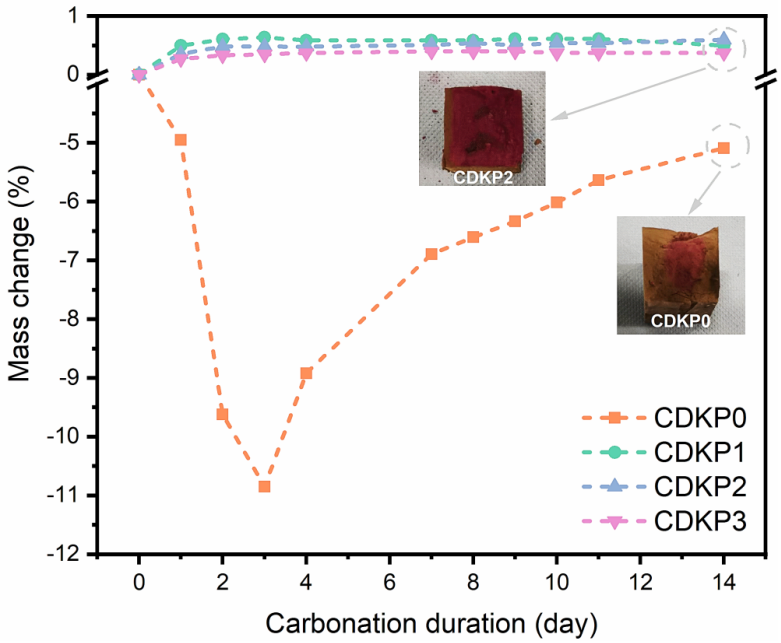

Fig. 6.10 *Mass change during carbonation and color change of 14-day carbonated samples after phenolphthalein test.*

6.3.3.3. Phase evolution

Further characterization of carbonated samples was conducted, with DKP0 and DKP2 chosen as representative samples. The DTG curves of hydrated samples before and after carbonation for 3 and 14 days are shown in ***Fig. 6.11***, and their mass loss from 500 to 800 °C is detailed in ***Table 6.4***.

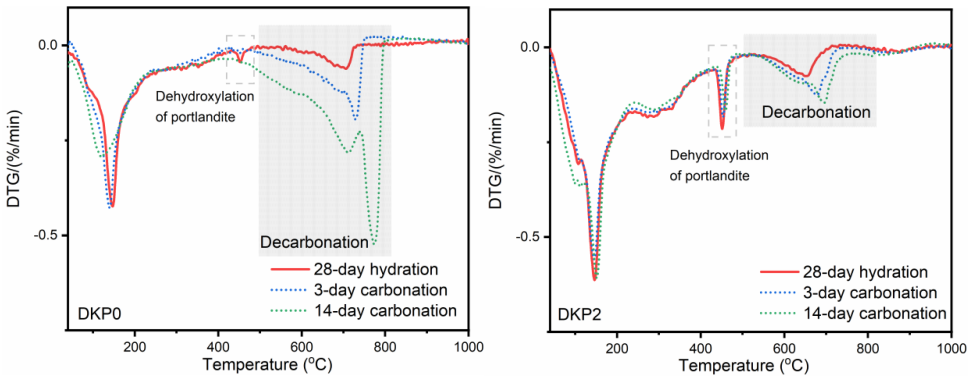

(a) ***(b)***

Fig. 6.11 *The first derivative of thermogravimetric analysis (DTG/TGA) of (a) DKP0, and (b) DKP2 before and after carbonation.*

Table 6.4 *The mass loss (500 to 800 °C) of hydrated BOF slag pastes before and after carbonation.*

Sample ID		DKP0	DKP2
Mass loss 500-800 °C [wt.%]	Before carbonation	0.52	0.74
	After 3-day carbonation	1.78	1.32
	After 14-day carbonation	5.89	1.72

After 3 days of carbonation of DKP0, portlandite is absent, and the intensity of the mass loss peak from 40 to 200 °C decreases after 14 days of carbonation, consistent with the decomposition of C-S-H (***Fig. 6.11(a)***) [217]. Correspondingly, the formation of calcium carbonates is notable as the weight loss peaks attributed to the decomposition of calcium carbonates become broader and larger during continued carbonation. The lower decomposition temperature of these carbonates compared to calcite indicates the presence of amorphous or poorly crystalline calcium carbonates [130]. The large mass loss peak at ~770 °C in DKP0 after 14-day carbonation is observed, demonstrating the presence of abundant crystalline carbonates which have not formed yet after 3 days of carbonation. Conversely, portlandite and C-S-H are well-preserved in DKP2, with only a minor decrease in hydrogarnet and a slight increase in calcium carbonates observed during carbonation (***Fig. 6.11(b)***). The mass loss from 500 to 800 °C of hydrated BOF slag pastes is used to estimate the amount of calcium carbonates [164]. DKP0 shows a significant increase from 0.52 wt.% before carbonation to 5.89 wt.% after 14 days of carbonation, whereas DKP2 exhibits a smaller increase from 0.74 to 1.72 wt.%. The

continuous increase in mass loss from 500 to 800 °C in DKP2 indicates that carbonation is not completely inhibited but occurs at a very low rate. There is a very limited presence of crystalline carbonates in DKP2, with decomposition above 700 °C, as confirmed with Rietveld-XRD analysis.

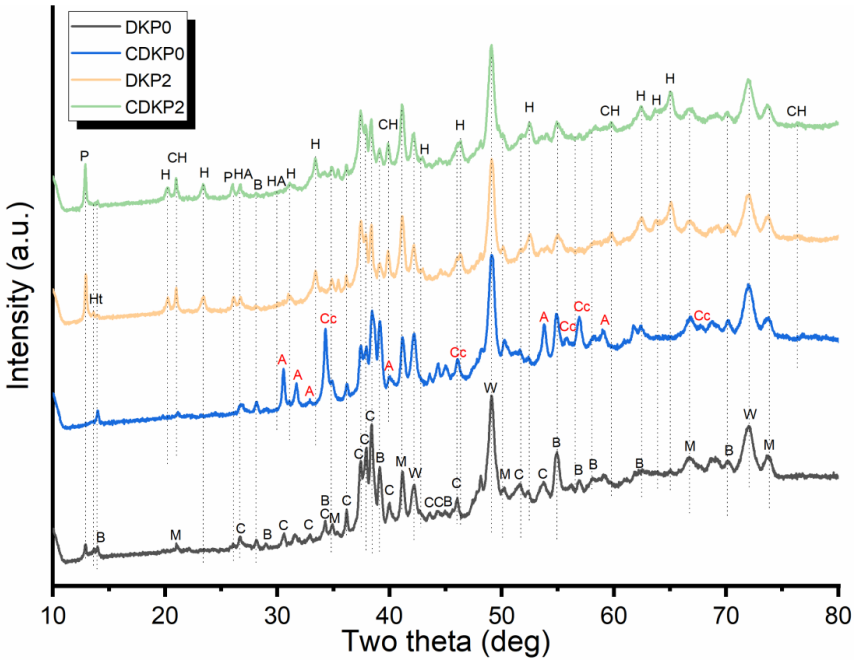

Fig. 6.12 *XRD data of 28-day hydrated samples before and after 14-day carbonation (Legend: B-Brownmillerite, C-Belite, M-Magnetite, W-Wuestite, P-Pyroaurite, H-Hydrogarnet, Ht-Hydrotalcite, HA-Hydroxyapatite, CH-Portlandite, A-Aragonite, Cc-Calcite).*

Further insights into the mineralogical composition of hydrated BOF slag pastes before and after carbonation were obtained using the XRD Rietveld method, as shown in ***Fig. 6.12*** and ***Table 6.5***. Aragonite and calcite are the primary crystalline carbonation products, constituting 7.9 and 7.4 wt.% of the CDKP0 matrix, respectively. Among the three common crystalline calcium carbonates (calcite, aragonite, and vaterite), vaterite is less stable and less crystalline than calcite and aragonite [251]. Additionally, vaterite may transform into the more thermodynamically stable phases of calcite and aragonite [233,252]. Carbonation significantly affects the original phases of the reference sample (DKP0), with portlandite, hydrogarnet, and LDH phases no longer visible, and belite showing a substantial decline from 35.9 to 16.7 wt.% after carbonation. Phases such as brownmillerite remain inert under carbonation, consistent with the literature [212,236]. In contrast, all diffraction peaks of hydration products are still evident in the samples containing phosphate. While portlandite is typically the main subject of carbonation in cementitious materials, it remains present post-carbonation with the addition of

phosphate [119]. The slight decrease in hydrogarnet in the phosphate-containing sample, from 11.8 to 8.3 wt.%, corresponds to the results obtained with TG/DTG, as shown in ***Fig. 6.11(b)***). An increase in crystalline carbonates (calcite) of 1.7 wt.% seems to correlate well with the off-set of the decomposition peak of carbonates in CDKP2 compared to DKP2.

Belite exhibits a decrease of 2.3 wt.% in the phosphate-containing sample after carbonation. This decrease is likely due to continuous hydration rather than carbonation, as both QXRD and TG/DTG methods indicate minor formation of calcium carbonates. Additionally, hydrogarnet shows a decrease of 3.5 wt.% due to carbonation. ***Fig. 6.13*** illustrates the specific surface area of 28-day hydrated samples before and after carbonation. CDKP2 shows an increase in the specific surface area, attributed to the expansion of gel pores from 2 to 10 nm. This finding further supports the continuous hydration of belite, as the formed C-S-H gel contains numerous gel pores contributing to elevating specific surface areas [87,89,216]. The porosity alterations observed through Mercury Intrusion Porosimetry (MIP) (***Fig. 6.14***) provide a clearer understanding of the changes in C-S-H gel pores. The increased mercury intrusion in pores smaller than 10 nm directly indicates the further formation of C-S-H gel in CDKP2 [48].

A significant increase in cumulative pore area is also observed in CDKP0, albeit for different reasons. The carbonation of belite and hydration products like C-S-H gel results in the formation of calcium carbonates and silica gel, which substantially elevates the surface area [43,217]. Similar phenomena have been observed in the carbonation of hydrated cement, where the formed silica gel has a higher surface area than C-S-H gel [217]. The formation of silica gel also explains the increase in amorphous phases in CDKP0 as measured with QXRD, as no additional C-S-H gel has formed in CDKP0, as illustrated in ***Fig. 6.11(a).***

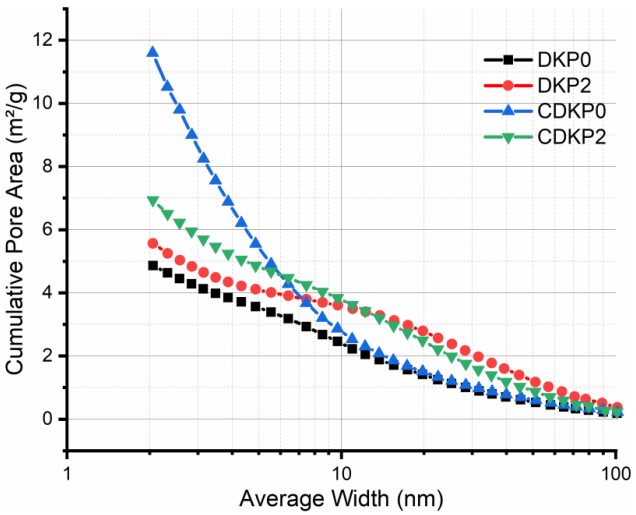

Fig. 6.13 *BET surface area tested of 28-day hydrated samples before and after carbonation showing the pore area contribution by pores smaller than 100 nm width.*

Table 6.5 *Phase composition of 28-day hydrated samples before and after 14 days of carbonation determined by XRD-Rietveld analysis [wt.%].*

Phase	DKP0	DKP2	CDKP0	CDKP2
Wuestite	19.4	13.7	17.2	11.7
Mangnetite	5.6	6.6	5.8	5.9
Belite	35.9	16.7	16.5	14.4
Brownmillerite	15.3	2.7	15.4	4.0
Lime	0.4	0.7	0.7	0.3
Calcite	0.6	-	7.4	1.7
Portlandite	0.4	1.0	-	0.7
Hydrogarnet	1.2	11.8	-	8.3
Hydroxyapatite	-	2.0	-	2.8
Pyroaurite	0.3	2.0	-	2.1
Hydrotalcite	0.1	1.5	-	0.7
Aragonite	-	-	7.9	-
Amorphous	20.7	41.2	29.2	47.3

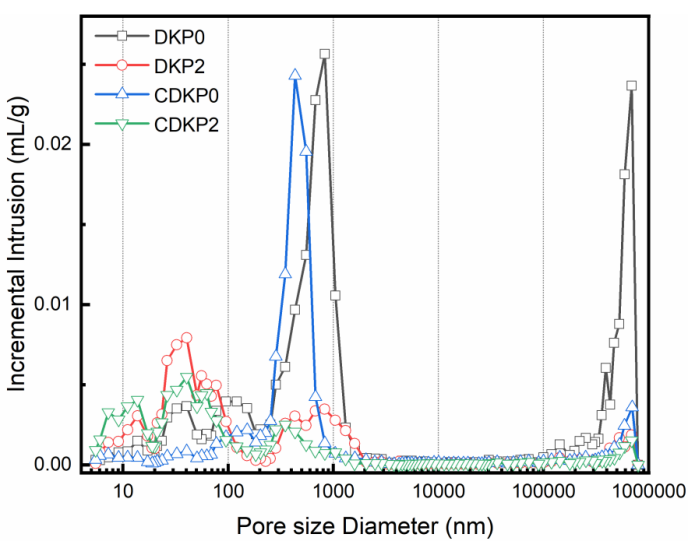

Fig. 6.14 *The incremental pore volume measured by MIP of 28-day hydrated samples before and after carbonation.*

Additionally, carbonation results in a denser structure for both CDKP0 and CDKP2, as shown in ***Table 6.6***. Carbonation has a greater impact on the pore structure of CDKP0, likely due to its initially higher porosity (40.73 %) before carbonation, which enhances CO_2 diffusivity. The significant reduction in pores larger than 100 μm in CDKP0 is particularly notable. The overall porosity decrease in CDKP2 is attributed to both slight carbonation and ongoing hydration during carbonation under high humidity conditions.

Table 6.6 *The overall porosity of hydrated BOF slag pastes from MIP before and after carbonation.*

Sample ID	DKP0	DKP2
Before carbonation [%]	40.73	23.98
After carbonation [%]	24.75	20.52

6.4. Discussion

The carbonation rate of BOF slag is influenced by various factors, including carbonation conditions (e.g., CO_2 concentration, humidity, temperature), chemical composition, porosity of the carbonated materials, additives, and water content [253,254]. The addition of phosphate enhances the hydration of BOF slag pastes, thereby optimizing the pore structure by reducing porosity, which adversely affects CO_2 diffusivity. Moreover, the higher pH maintained by the buffering action of combination of K^+ and HPO_4^{2-}/PO_4^{3-} ions inhibits the formation of calcium carbonates. Consequently, identifying the primary cause of carbonation mitigation in BOF slag pastes with phosphate addition remains challenging.

6.4.1. Carbonation behaviours of mortar and powder

Carbonating shaped mortar samples and milled fine powder can give certain understanding on the carbonation behaviors of the same matrices with different shapes.

The phosphate-activated BOF slag mortar after carbonation demonstrates a certain heavy metals retention capacity, as shown in ***Table 6.7***. The V and Cr concentrations show little change after 3 and 14 days of carbonation, which is attributed to the slow carbonation process. The pH values exhibit a slight decline from 13.1 before carbonation to 12.8 after 14 days of carbonation, as shown in ***Table 6.7***. The mortar surface sprayed with phenolphthalein solution indicates some carbonation depth as shown in ***Fig. 6.15***, but its extent is still slight compared to CDKP0 (***Fig. 6.10***). Both BOF slag pastes and mortars show negligible pH decreases and slight carbonation degrees upon carbonation, even though CO_2 diffusivity can be faster due to the addition of more aggregates in the mortar samples.

Table 6.7 *The Leaching of inorganic contaminants of BOF slag mortars after carbonation measured by one stage batch leaching test.*

Heavy metals concentrations[mg/l]	V	Cr	Mo	pH
Before carbonation	-	-	-	13.1
After 3-day carbonation	0.032	0.004	-	12.9
After 14-day carbonation	0.038	0.005	-	12.8

**Note: the ions concentrations of BOF slag mortars before carbonation were not tested since the leaching results of BOF slag pastes with phosphate before carbonation can be taken as a reference.*

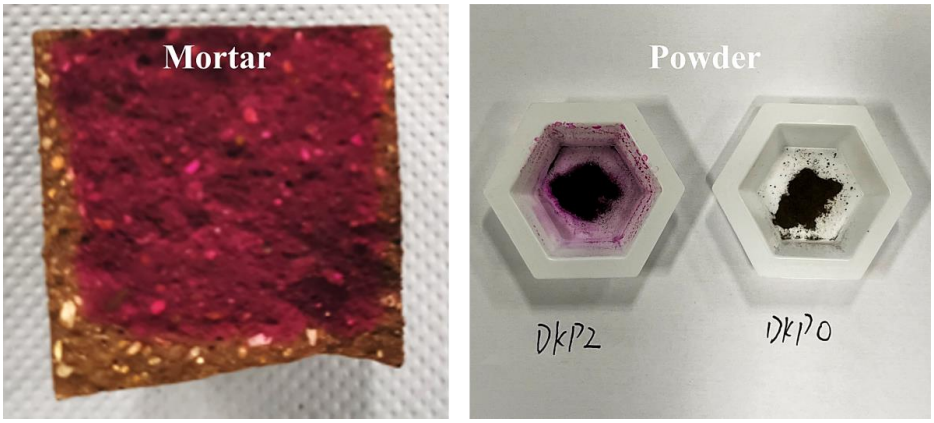

Fig. 6.15 *Color change by phenolphthalein test of the mortar sample after 14-day accelerated carbonation and the powder samples after 2-year natural carbonation.*

Additionally, after exposure to atmospheric CO_2 for two years, DKP2 powder demonstrates satisfactory carbonation resistance (***Fig. 6.15*** and ***Fig. 6.16***). The weight loss from 500 to 800 °C for DKP2 and DKP0 powder samples after 2-year natural carbonation is 1.02 and 4.42 wt.%, respectively. While some hydration products, such as C-S-H, seems to undergo carbonation, portlandite remains present and only small amount of calcium carbonates form even after long-term natural carbonation. In contrast, the powder without DKP shows a high extent of carbonation, as evidenced by its pronounced decarbonation peak and the complete absence of portlandite.

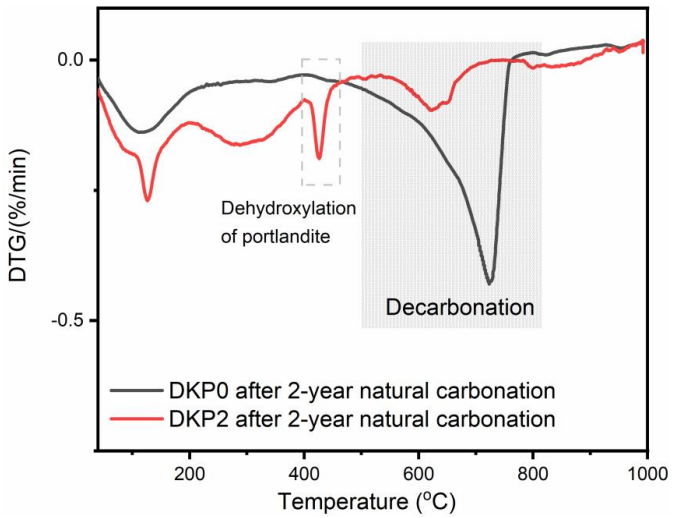

Fig. 6.16 *The first derivative of thermogravimetric analysis (DTG/TGA) of DKP0 and DKP2 powder after 2-year natural carbonation.*

6.4.2. pH buffering

Portlandite is commonly considered as the alkalinity buffer in cement matrices during carbonation, with higher portlandite levels correlating with better carbonation resistance [127]. DKP2 contains around 1 wt.% portlandite, significantly less than hydrated Portland cement, which typically exceeds 10 wt.% [255]. Normally, the dissolution of portlandite and subsequent formation of calcium carbonates occur upon carbonation [154,231]. The small amount of portlandite in hydrated BOF slag pastes may have limited capacity for reserving alkalinity.

The sustained high pH in DKP2 can be attributed to the synergetic roles of the introduced K^+ and PO_4^{3-}ions. Although alkali-activated materials (AAMs) exhibit faster carbonation rates than traditional cement due to the absence of portlandite, their high alkalinity, resulting from considerable K^+/Na^+ content, still provides significant buffering capacity [256]. During carbonation, the continuous consumption of K^+/Na^+ and OH^- occurs simultaneously with the dissolution of pozzolanic materials and the neutralization of alkalis in the pore solution, leading to a decrease in pH along with the reduction of K^+/Na^+ [232,256]. It has been reported that the pH of sodium carbonate alkali-activated ground blast furnace slag (GBS) falls below 11 after carbonation with 1% CO_2 for one month, alongwith a significant decomposition of hydration products [257]. These bulk AAMs exhibit a porosity of 25.7% before carbonation, which is comparable to the porosity of DKP2. In DKP2, a slight decline in K and Ca levels is observed after carbonation, suggesting their participation in buffering by consuming dissolved CO_2. However, the pH in DKP2 after carbonation remains stable at around 13, which is attributed to the strong buffering capacity of PO_4^{3-}. Overall, K^+ contributes to buffering the pH, a role that is further enhanced by the presence of PO_4^{3-}. The maintained high pH level slows down the

carbonation of portlandite, thereby protecting other calcium-rich phases from significant carbonation until portlandite is depleted. This results in a slower overall carbonation rate for DKP-activated BOF slag powders, pastes, and mortars in this study. Similar findings have been reported, indicating that higher pH levels in cement are associated with increased resistance to carbonation [230,247].

Additionally, the formation of hydroxyapatite may help mitigate carbonation. Hydroxyapatite is often used as a consolidant for damaged carbonate stones and as an additive in geothermal well applications due to its low solubility and high stability under weathering or extreme conditions, such as those involving CO_2 saturated brine with over 40,000 parts per million (ppm) of CO_2 at temperatures ranging from 200 to 320 °C [208,258–260]. During carbonation, OH^- and PO_4^{3-} ions in hydroxyapatite can be substituted by CO_3^{2-} leading to the formation of carbonated hydroxyapatite and the adsorption of certain amounts of CO_2 [213,214]. This process releases OH^- and PO_4^{3-} ions, which can further increase the pH level. These characteristics make hydroxyapatite an effective material for resisting carbonation.

6.5. Conclusions

This study delves into the hydration of BOF slag utilizing dipotassium hydrogen phosphate (DKP) as the activator at levels up to 3 wt.%. The tested samples demonstrate satisfactory strength, leaching behaviour, and carbonation resistance, leading to the following conclusions:

Compared to monopotassium phosphate (KH_2PO_4), DKP-activated BOF slag pastes facilitate the completion of the main exothermic reaction within 3 days, avoiding strong retardation effects with phosphate additions below 3 wt.%. Importantly, increasing DKP from 1 to 3 wt.% extends the induction period while enhancing overall hydration heat. This contributes to greater consumption of belite and brownmillerite, leading to increased formation of hydration products such as hydrogarnet, C-S-H gel, and LDHs phases by 7 days. Continuous hydration of belite and brownmillerite is observed up to 28 days, particularly pronounced with DKP levels above 1 wt.%.

The improved hydration optimizes the overall pore structure, reducing porosity from 40.73 % in DKP0 to 22.36 % in DKP3, thereby increasing strength from 1.9 MPa in DKP0 to 42.5 MPa in DKP3 at 28 days.

DKP0 exhibits poor carbonation resistance, evidenced by significant formation of calcium carbonates and unsatisfactory V leaching. After carbonation, heavy metal leaching of V, Cr, and Mo is effectively controlled in all DKP-containing samples, falling well below the limits stipulated by the Dutch Soil Quality Decree (SQD). This is attributed to the abundance of hydration products capable of immobilizing heavy metals and the sustained high pH due to the strong buffering capacity of HPO_4^{2-}/PO_4^{3-} and K^+.

All phosphate-activated BOF slag powders, pastes and mortars demonstrate good carbonation resistance. The stabilized high pH during carbonation plays a crucial role in retarding carbonation of portlandite, thereby mitigating overall carbonation of DKP-activated BOF slag samples.

CHAPTER 7

7. Understanding the difference between BOF slag hydration with acidic and alkaline phosphates

The interactions between BOF slag and phosphate solutions of varying pH were studied to understand their effects on hydration kinetics, microstructure, and strength development. Initially, belite dissolves in samples with acidic phosphates, forming hydroxyapatite-like phases instead of C-S-H, leading to a prolonged induction period of up to three weeks after the initial reaction. The retardation of hydration diminishes with increasing initial pH of the phosphate solutions. Once beyond the $H_2PO_4^-/HPO_4^{2-}$ buffering regime, hydration can be further enhanced. This buffering regime also impedes the formation of hydrogarnet and LDH phases. Higher initial pH levels lead to a greater hydration extent of belite, brownmillerite, and wuestite, accompanied by the formation of more C-S-H, hydrogarnet, and LDH phases. These results are supported by phase composition analysis, measurements of chemically bound water, and calorimetric data, along with reaction enthalpy calculations. The pore structure of all phosphate-containing samples shows comparable porosities at 28 days. However, sample strengths vary significantly, ranging from a minimum of 37.7 MPa to a maximum of 66.9 MPa. This variation is attributed to a higher proportion of capillary pores and a larger average pore size of 34.7 nm in samples reacting at a low pH (pH at 4.2) compared to those reacting with basic alkaline phosphates. Furthermore, increasing the initial pH from 11.5 to 12.8 decreases strength despite higher hydration extent, likely due to high potassium concentrations causing shrinkage during air curing.

This chapter is reproduced from: Y. Tang, METHOD FOR ACTIVATING BASIC OXYGEN FURNACE STEEL SLAG, WO 2024/052265 A1, 2024. (International patent); Y. Tang, K. Schollbach, Z. Liu, S.R. van der Laan, W. Chen, H.J.H. Brouwers, Understanding the difference between BOF slag hydration with acidic and alkaline phosphates, 2024 (submitted).

7.1. Introduction

The synergistic activation of both belite and brownmillerite in BOF slag can be achieved through the addition of phosphates, stimulating the formation of layered double hydroxide (LDH) phases, hydrogarnet, and calcium silicate hydrate (C-S-H) gel as principal hydration products [197,238,261]. Phosphates are commonly reported to be retarders in Portland cement by inhibiting the hydration of alite and tricalcium aluminate, the inherent hydraulic activities of which are significantly higher than those of belite and brownmillerite [48,202,219,262,263]. This may be different for BOF slags, since they contain mainly belite and brownmillerite, and phosphate could act as a trigger to promote phase dissolution. A 2.5 wt.% monopotassium phosphate (MKP) solution has been shown to enhance the overall hydration of belite and brownmillerite in BOF slag at 28 days, despite the observed extensive retardation compared to BOF slag with pure water [197]. This retardation was mitigated by increasing the MKP dosage to 10 wt.%. Yet, excessive phosphates shift the reaction pathway towards an acid-base mechanism, disrupting normal hydration reactions, instead extracting excessive Ca and forming calcium phosphate compounds [48,195,261]. Compared to MKP, dipotassium phosphate (DKP)-activated BOF slag pastes show very little retardation and the main exothermic reactions are completed within 3 days, with phosphate additions below 3 wt.% [261]. Notably, the pH values of MKP and DKP solutions are approximately 4.1 and 8.8, respectively.

Based on our previous studies, the hydration behaviour of BOF slag differs with respect to reaction kinetics, reaction products and strength development for acidic versus alkaline phosphates, i.e. phosphates of different pH. In comparison, under varying pH conditions (pH = 3, 7 and 12) with Portland cement, the hydration products generally remain the same, however the quantities of products are different, e.g. portlandite increases with rising pH levels [264]. Also, in cement variation is significantly influenced by acidic and alkaline curing environments impacting strength development. Acidic environments primarily affect early strength (1 – 3 days), while alkaline environments have a more pronounced effect on the later strength development of cement (7 – 28 days) [264,265]. Additionally, according to literature [266], the induction period of cement hydration is prolonged as pH decreases, and this induction period can be elongated with the simultaneous removal of both calcium and hydroxyl ions, derived from the lower undersaturation degree of alite, and later silicate reaction peak time.

While acid-base reactions have been studied intensively for chemically bonded phosphate ceramics (CBPCs) [194–196], detailed hydration mechanisms across a wide pH range of phosphate-activated systems have not been studied in any detail and warrant systematic investigation. Specifically for iron oxide rich systems such as slags which were shown to be responsive to phosphate activation. This helps to find the optimal way for activating BOF slag using phosphates.

Following up on our previous research, the reactions between BOF slag and phosphate across a pH range of 4.2 to 12.8 were investigated. To achieve this broad pH range,

monopotassium phosphate (MKP), dipotassium phosphate (DKP) and tripotassium phosphate (TKP) were used as the additives since they naturally provide different starting pH upon dissolving in water. Previous studies used varying amounts of phosphate, complicating the assessment of pH's critical role [197,238,261]. In this study, we standardized the phosphate solution concentration at 0.8 M. Additionally, it is noteworthy that the pH changes in the BOF slag system are moderated in case of using phosphate salt buffers. A comprehensive multi-technique approach was employed to elucidate the effects of acidic and alkaline phosphates on hydration kinetics, microstructure, and strength development. This approach included quantitative X-ray diffraction (XRD) analysis, thermogravimetric analysis (TGA), calorimetric measurements, and mercury intrusion porosimetry (MIP), to interpret reaction extent, product identification, heat release, and pore structure. In-situ pH and conductivity measurements, along with ion chromatography (IC) and inductively coupled plasma atomic emission spectroscopy (ICP-OES), were used to analyze early-stage dissolution and precipitation, as well as 28-day leaching behavior. This study provides a deeper understanding of the relationship between phosphate solutions of varying pH and the hydration behaviour of BOF slag.

7.2. Experiments and methodology

7.2.1 Raw materials

The BOF slag utilized in this study was supplied by Tata Steel in IJmuiden, The Netherlands. The grinding procedure was performed using a Retsch RS 300 XL disc mill at a constant speed of 912 min^{-1} for 15 min with 1 kg BOF slag grains (0-5.6 mm) in a grinding jar volume of 2l, and the particle size distribution of the BOF slag powder is given in ***Fig. 7.1*** and ***Table 7.1***. The chemical, mineralogical composition and other physical parameters are summarized in ***Table 7.1***. Monopotassium phosphate (MKP, KH_2PO_4), dipotassium phosphate (DKP, K_2HPO_4) and tripotassium phosphate (TKP, K_3PO_4) were selected as the additives, sourced as a commercially available technical-grade product (VWR Chemicals BDH®, purity ≥ 99.0 wt.% analytical reagent).

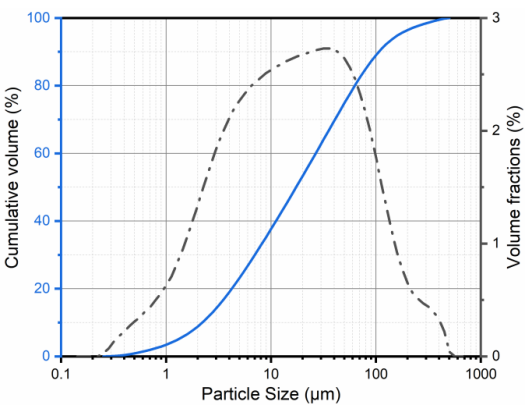

Fig. 7.1 *Particle size distribution of BOF slag.*

Table 7.1 *Chemical, mineralogical composition and other physical properties of BOF slag.*

Oxide	Content [wt.%][a]	Mineral	Content [wt.%][b]	Physical properties
MgO	6.8	Brownmillerite	17.1	D(0.1)[c] = 2.22 μm
SiO_2	13.45	Magnetite	6.4	D(0.5)[c] = 17.34 μm
Al_2O_3	2.21	Belite	39.6	D(0.9)[c] = 106.77 μm
CaO	40.14	Wuestite	20.5	ρ^d = 3.66 g/cm^3
P_2O_5	1.61	Lime	0.9	SSA_{BET}[e] = 1.1 m^2/g
TiO_2	1.39	Calcite	0.8	
V_2O_5	1.05	Portlandite	0.7	
Cr_2O_3	0.3	Amorphous	14.0	
MnO	4.61	Rwp	2.8	
Fe_2O_3	28.32			
Others	0.12			
GOI	1.31			

[a] *Tested via X-ray fluorescence (XRF, Model Axios Advanced, PANalytical.B.V).*

[b] *Quantitative X-ray diffraction (QXRD) analysis via Rietveld method.*

[c] *Analysed with a laser particle size analyser (Model Malvern Mastersizer 2000, Malvern PANalytical).*

[d] *Particle specific gravity from He pycnometer.*

[e] *Specific surface area determined by Brunauer-Emmett-Teller (BET) method.*

7.2.2. Mix design

Based on our preliminary research, the concentrations of phosphate solutions were fixed as 0.8M. The detailed mix proportions of the pastes are shown in ***Table 7.2***. The ratios of volume of phosphate solutions to mass of BOF slag were set as 0.2. The volumes of phosphate solutions were measured by pipette to ensure the constant phosphate molarities in each mixture. The varying initial pH values from 4.1 to 12.8 of the phosphate solutions were obtained via the combination of MKP, DKP and TKP solutions. The freshly mixed BOF slag pastes were poured into molds (20×20×20 mm^3) and covered with plastic film before demolding. The pastes were air-cured at ambient temperature until the testing age.

Table 7.2 *Mix proportions of BOF slag pastes.*

Sample ID	BOF slag	Water	MKP solution	DKP solution	TKP solution	Initial pH
	[g]			[ml]		
REF	100	20				6.9
M	100		20			4.1
MD	100		10	10		6.5
D	100			20		8.8
DT	100			10	10	11.5
T	100				20	12.8

7.2.3 Methodology

The hydration heat was recorded using an isothermal conduction calorimeter (TAM Air, Thermometric) from 45 minutes to 28 days. Before placing the samples into the calorimeter, BOF slag powders were mixed with distilled water or 0.8M phosphate solutions in the ampoule for 1 minute. The compressive strengths at 7 and 28 days were tested in an MTS Criterion equipped with a load cell of 100 kN at a speed of 0.6 mm/min until collapse according to EN 196-1, with three replicates for each composition.

After the designated curing time, the pastes were crushed and sieved to particles smaller than 2 mm, then immersed in isopropanol for 48 hours to stop hydration. The pieces were subsequently dried in a vacuum oven at 45 °C until a constant mass was achieved [73]. After drying, some pieces were finely ground to pass through a 63 μm sieve. The resulting powder and the remaining pieces were stored in desiccators with calcium chloride pellets as a drying agent and sodium hydroxide pellets as a CO_2 trap until further testing. The crystalline phases of the hydrated slag pastes were identified using a Bruker D2 X-ray Diffractometer with a LynxEye detector and a Co X-ray tube, set at 30 kV and 10 mA. The scans were performed over a range of 5 to 80 °2θ with a step size of 0.019° and a counting time of 1 s/step. For quantitative phase analysis via the Rietveld method, the counting time was increased to 2 s/step. Si powder (Siltronix, France) was used as an internal standard, making up 10 wt.% of the samples. To ensure homogeneity, the samples were mixed thoroughly with the Si powder using an XRD-Mill McCrone (RETSCH) at 75% speed for 5 minutes. The TOPAS 5.2 software from Bruker Corporation was utilized to quantify both crystalline and amorphous phases. Nitrogen sorption analysis was conducted using a TriStar II 3020 from Micrometrics based on Brunauer-Emmett-Teller (BET) methods [77]. Thermogravimetric analyses (TGA) were performed with NETZSCH STA 449 F1 and NETZSCH TG 209 F3 Tarsus instruments. Ground powder samples, each weighing

between 30 to 40 mg, underwent heating at a rate of 10 °C/min in a nitrogen atmosphere, covering temperatures from 40 to 1000 °C. The porosities of 28-day hydrated BOF slag pastes were obtained by Mercury Intrusion Porosimetry (MIP) measurements using the AutoPore IV 9500 Micromeritics Series Mercury Porosimeter with the maximum pressure of 227.53 MPa.

The leaching test of 28-day cured slag pastes was conducted according to EN 12457–2, a one-stage batch leaching test [200]. Deionized water was added to the crushed samples (below 4 mm in size) at a liquid-to-solid ratio of 10, and the mixture was agitated using a dynamic shaker (ES SM-30, Edmund Buhler GmbH) for 24 hours. After shaking, the leachates were filtered through a 0.22 μm syringe filter. The pH of the filtrates was measured using a Greisinger-GMH 5500 pH meter, with three readings taken and averaged for each sample. Liquid samples were either used undiluted or diluted by a factor of 10 for further elemental concentration analysis. The ion concentrations were determined using a Thermo Scientific Dionex ICS-1100 ion chromatography (IC) system or an inductively coupled plasma atomic emission spectrometer (ICP-OES, SPECTROBLUE) after acidification with concentrated HNO_3.

To study the early-stage dissolution of BOF slag, in-situ pH and conductivity measurements were performed using a handheld conductivity meter (Greisinger-GMH 3431) and a pH meter (Greisinger-GMH 5500). The experiments were conducted in a climate-controlled room maintained at 20 ± 0.5 °C and 60% relative humidity. An excess of solution with a liquid volume-to-slag mass ratio of 2 was added to ensure full contact of the probes with the liquid. Detailed mix proportions and initial conductivities of phosphate solutions with varying pH are provided in ***Table 7.3***. The probes were first immersed in distilled water or phosphate solutions until temperature, pH, and conductivity stabilization was achieved. BOF slag powder was then added to the liquid media and stirred for 30 seconds using a handheld mixer. Data logging was set at 1-minute intervals for a 90-minute duration. To prevent evaporation, the beaker used for measurements was sealed with parafilm and tape.

Table 7.3 *Mix proportions for in-situ pH and conductivity measurements.*

Sample ID	BOF slag	Water	MKP solution	DKP solution	TKP solution	Initial conductivity
	[g]			[ml]		[mS/cm]
REF*	50	100				0
M*	50		100			50.9
D*	50			100		98.9
T*	50				100	138.4

Ion concentrations at 10 and 90 minutes were measured. Due to the strong buffering effects of the phosphate, samples with phosphate solutions were not acidified but were diluted by factors of 10 or 100. Solids were separated by filtration and immersed in isopropanol for 2 hours to stop hydration. The isopropanol was then removed, and the solids were dried in a vacuum oven at 45 °C until a constant mass was achieved. The dried samples were subsequently used for XRD analysis.

7.3. Results and discussion

7.3.1. Hydration

7.3.1.1. Kinetics

The results of isothermal conduction calorimetry are depicted in ***Fig. 7.2***. A minor peak is evident at approximately 2 days for REF, with the cumulative hydration heat reaching 37.6 J/g at this time, which is more than 50% of the total heat release (62.3 J/g) at 28 days. After this initial peak, the increase in hydration heat for REF is slow. The exothermic reaction of brownmillerite hydration typically occurs within the first several hours [190,267]. Brownmillerite dissolves rapidly upon contact with water, forming a metastable C-(A,F)-H gel that coats the surface of brownmillerite. This gel coating retards further hydration of brownmillerite, although it eventually converts to stable hydrogarnet [190,267]. Additionally, the C-(A,F)-H gel in REF can be iron-rich and less soluble due to the higher iron content of brownmillerite in BOF slag compared to that in cement clinker [186,190,267]. These factors explain the delayed exothermic peak in REF. Belite has a low reactivity, leading to its complete hydration taking several weeks or even months [268]. The prolonged hydration of belite can contribute to the slow accumulation of heat at later stages.

The introduction of phosphate solutions significantly elevates the hydration heat at 28 days in all samples except M. M starts accelerating its reaction after 3 weeks, as shown in ***Fig. 7.2***, similar to our previous findings [261] and is expected to generate a higher heat release than REF at higher ages. The initial low pH (4.1) may restrict the hydration of brownmillerite and facilitate the fast dissolution of belite initially, but this is not recorded in the heat release. The buffering regime of $H_2PO_4^-$ and HPO_4^{2-} in maintains a pH range of 7-7.5, increasing the saturation level of hydration products like C-S-H and hydrogarnet and thereby hindering the further dissolution and precipitation [239,269]. This buffering role occurs in all samples whereas the buffered pH increases with the higher alkaline phosphate input. Consequently, the retardation effects diminish with increasing initial pH. T shows the highest hydraulic reactivity, with the main exothermic reaction completing within 3 days and a 28-day cumulative heat of approximately 145 J/g. High pH favours the dissolution of iron-containing phases, such as the original brownmillerite and the initially formed C-(A,F)-H gel and hydroferrite [203,270]. MD, D, DT, and T exhibit comparable overall hydration heat at 28 days, indicating that equal phosphate input can result in similar hydration extent once the buffering barrier of $H_2PO_4^-$ /HPO_4^{2-} is overcome.

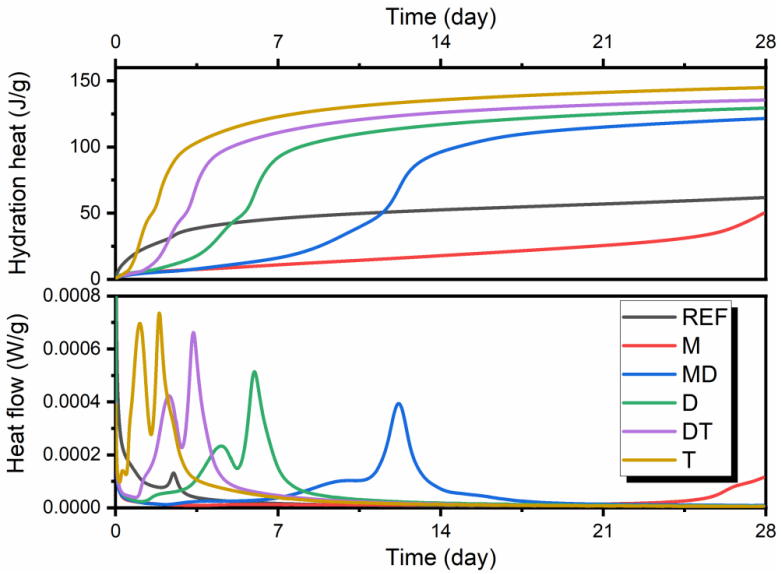

Fig. 7.2 *Heat flow and cumulative heat evolution of BOF slag pastes.*

7.3.1.2. Phase identification

Fig. 7.3 illustrates the phase composition of 7- and 28-day hydrated BOF slag pastes. Generally, hydrogarnet, pyroaurite, and hydrotalcite are the main crystalline hydration products, as detected via XRD. Hydrogarnet ($Ca_3(Al_xFe_{1-x})_2(OH)_{12}$) is a typical hydration product of brownmillerite in the absence of other phases like gypsum [190]. Notably, brownmillerite also apparently hydrates with consumption of some belite to produce siliceous hydrogarnets covered by the general formula $Ca_3(Al_xFe_{1-x})_2(SiO_4)_y(OH)_{4(3-y)}$, where the Al/Fe ratio is unknown [271]. The diffraction peak of hydroxy-AFm (OH-AFm, mainly $Ca_4Al_2O_7{\cdot}19H_2O$) is detected but with low intensity. This metastable phase, originating from brownmillerite, can gradually convert into hydrogarnet and portlandite over time [272–274]. The presence of hydroxy-AFm in some samples (D, DT, T) at 28 days might be due to the initial high pH and promoted brownmillerite hydration, as T also shows the peak of hydroxy-AFm at 7 days. The detection of pyroaurite and hydrotalcite, which are layer double hydroxides (LDHs) and can be represented by the general formula $Mg_3(Al,Fe)(OH)_8(CO_3)_{0.5}{\cdot}nH_2O$, indicates the hydration of wuestite since the release of magnesium is controlled by wuestite dissolution [34]. The precipitation of hydroxyapatite was expected but this phase can be present in small amounts with poor crystallinity [204,205], making hydroxyapatite invisible in XRD.

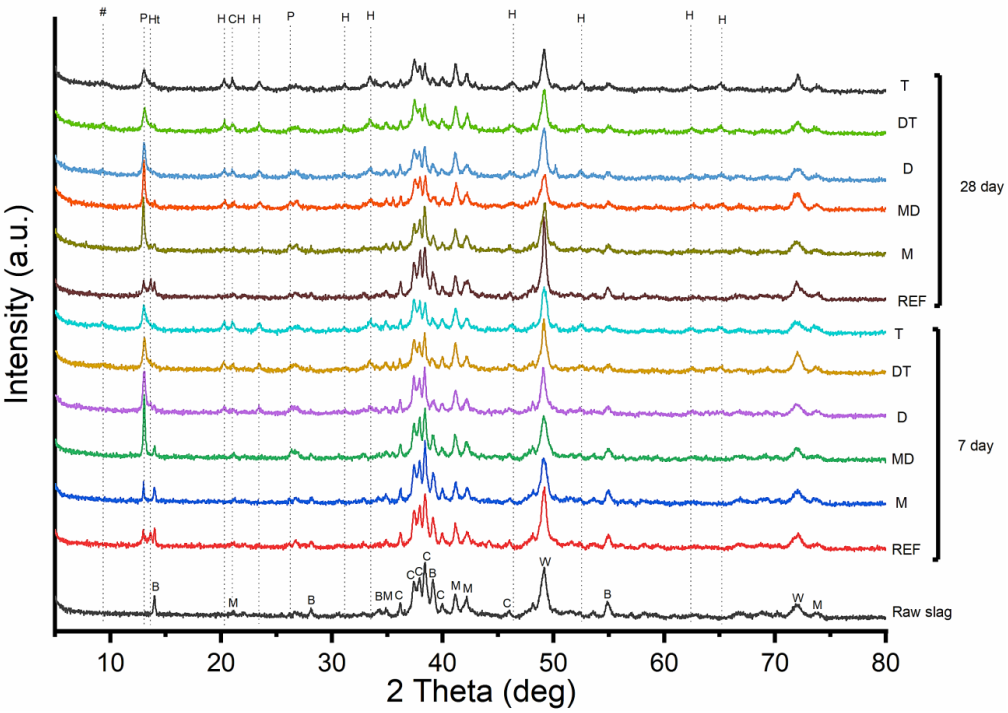

Fig. 7.3 *XRD data of 7- and 28-day hydrated samples (Legend: # -Hydroxy-AFm, P-Pyroaurite, Ht-Hydrotalcite, H-Hydrogarnet, CH-Portlandite, B-Brownmillerite, C-Belite, M-Magnetite, W-Wuestite).*

Table 7.4 illustrates the phase composition of 7- and 28-day hydrated BOF slag pastes. The decline of brownmillerite at 7 days in REF leads to a modest increase in hydrogarnet and LDH phases (pyroaurite and hydrotalcite), which likely benefit from the decreased wuestite [34,39]. Belite begins to react after 7 days, showing only a minor decline. The absence of portlandite further evidences the limited hydration of belite at 7 days. Magnetite remains stable throughout. At 28 days, both belite and brownmillerite in REF show continuous hydration, with belite decreasing to a larger extent, contributing to the increasing amorphous phase content.

In the presence of phosphate, the consumption of belite and brownmillerite shows a clear trend that higher initial pH leads to greater hydration. For M, the added phosphate shows limited effects on the brownmillerite hydration at 7 days but significant decrease in brownmillerite is observed at 28 days. The decline in belite at 7 days is not consistent with the heat release shown in ***Fig. 7.2***, indicating that the consumption of belite is probably caused by the immediate dissolution post-mixing due to the acidic nature of M rather than hydration. In MD, the noticeable decline in belite and brownmillerite does not correspond to a proportional increase in hydrogarnet and LDH phases at 7 days. The primary hydration of MD completes after about 2 weeks, as indicated in ***Fig. 7.2***. It can be

assumed that the decline in belite and brownmillerite in MD at 7 days promotes the formation of metastable phases with poor crystallinity, which gradually convert to stable hydrogarnet and LDHs, releasing heat in the process. The other samples D, DT, and T exhibit high degrees of hydration at 7 days, along with considerable amounts of hydration products. The highest amount of portlandite is detected in T at both 7 and 28 days, attributed to the significantly promoted hydration of belite. Additionally, belite can prompt a series of secondary reactions with brownmillerite and the formed Al/Fe hydroxides to produce straetlingite, siliceous hydrogarnets, and C-S-H, consuming portlandite in the process [275,276]. Magnetite remains relatively stable, while wuestite exhibits a notable decrease at 7 days in the presence of phosphate solutions with initial pH above 7. Pyroaurite is detected in greater amounts than hydrotalcite in all phosphate-containing samples, reflecting the iron-rich nature of the BOF slag system.

Table 7.4 *Phase composition of 7 and 28-day hydrated BOF slag pastes determined by XRD-Rietveld analysis.*

Sample ID		Phases										
		Wuestite	Magentite	Brownmillerite	Belite	Lime	Portlandite	Calcite	Hydrogarnet	Pyroaurite	Hydrotalcite	Amorphous
7 days	REF	18.2	5.8	13.7	38.0	0.6	0.0	0.0	1.3	0.9	1.1	20.4
	M	17.5	5.8	15.4	32.1	0.4	0.0	0.0	0.6	0.1	0.0	28.1
	MD	18.8	5.5	9.9	34.1	0.5	0.0	0.0	1.1	1.7	0.0	28.3
	D	15.4	5.4	5.7	27.8	0.4	0.0	0.0	5.0	2.7	0.8	36.8
	DT	13.7	5.2	5.0	24.2	0.4	0.6	0.0	6.4	2.2	1.0	41.2
	T	14.3	5.7	5.2	22.0	0.4	1.0	0.0	7.8	2.0	0.9	40.8
28 days	REF	18.3	5.6	11.6	33.0	0.5	0.1	0.2	1.2	1.1	1.8	26.7
	M	16.8	5.5	6.5	26.5	0.5	0.0	0.0	3.1	3.3	0.3	37.4
	MD	14.7	5.8	3.9	22.9	0.5	0.7	0.0	6.2	3.3	1.0	41.0
	D	14.4	5.3	5.3	22.8	0.6	0.6	0.0	6.5	2.6	1.0	41.0
	DT	13.6	5.6	5.1	21.2	0.4	1.0	0.0	8.8	1.9	0.9	41.5
	T	13.7	5.8	4.5	18.2	0.3	1.3	0.0	9.2	1.6	0.7	44.6
	Error	0.3	0.2	0.3	0.5	0.1	0.1	0.1	0.2	0.1	0.2	1.2

Note: Hydroxy-AFm is included in the amorphous phase due to its low content in hydration products and low crystallinity. The error is indicative, as obtained from Rietveld analysis.

7.3.1.3. Thermogravimetric analysis

The weight loss of the hydrated BOF slag pastes at various temperature stages is shown in ***Fig. 7.4***. The decomposition of hydrogarnet and other hydration products, particularly

X-ray amorphous C-S-H gel, upon heating provides an indication of the overall amount of hydration products [48]. C-S-H exhibits water loss over a wide temperature range from 40 to 600 °C due to the loss of water in the interlayer and dehydroxylation, with the main decomposition peak typically occurring between 40 and 200 °C [73]. Although hydroxyapatite is not detected via XRD, the added phosphate ultimately converts into hydroxyapatite through its reaction with calcium, owing to hydroxyapatite's high thermodynamic stability [227,277]. The removal of adsorbed water in hydroxyapatite at around 105 °C is also noted [204,211], which is lower than the decomposition peak of C-S-H at around 150 °C, as shown in ***Fig. 7.4***. It is evident that the addition of phosphate promotes the formation of C-S-H gel in all samples except M at 7 days, confirming the retardation effects of acidic phosphate on belite hydration.

The dehydration of hydrogarnet and LDHs occurs within the temperature range of 200 to 400 °C. The mass loss of these phases increases with the addition of phosphate at higher initial pH levels, with a continuous rise observed over time. The higher pH also results in a greater amount of portlandite, which decomposes at temperatures between 400 and 500 °C [73], consistent with the QXRD results. In the presence of phosphate, the formation of hydroxyapatite is favored over portlandite [278]. With equal phosphate input, samples D, DT, and T exhibit a more distinct dehydroxylation peak of portlandite compared to REF at 7 days, further demonstrating the accelerating effects of alkaline phosphate on belite hydration.

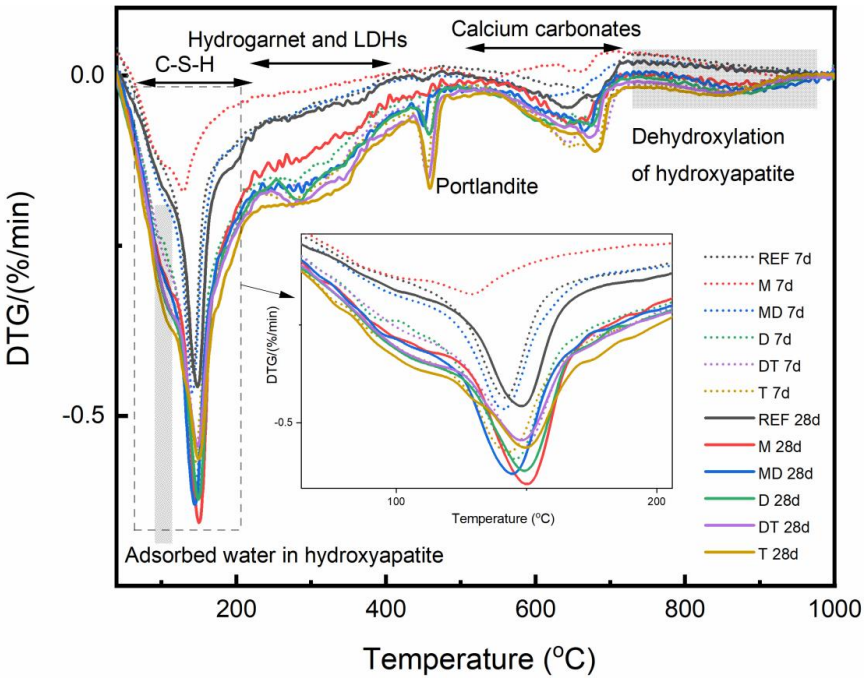

Fig. 7.4 *The first derivative of thermogravimetric analysis (DTG/TGA) of 7- and 28-day hydrated BOF slag pastes.*

Another weight loss observed from 500 to 720 °C signifies the decomposition of carbonate groups [73]. While the amount of calcite determined via XRD Rietveld method is negligible, this mass loss most likely originates from the carbonate compounds such as amorphous calcium carbonate and the formed LDHs, confirmed by the split carbonate peaks in some samples (DT and T at 7 days) [109]. It should be noted that B-type carbonated hydroxyapatite may form via the substitution of PO_4^{3-} by CO_3^{2-}, showing an overlapping temperature range of decarbonation from 500 to 1000 °C [213,214]. Additionally, a final weight loss range corresponding to the dehydroxylation of hydroxyapatite is observed above 720 °C in phosphate-containing samples [210,211]. However, this mass loss is absent in M and MD at 7 days, likely due to the formation of other metastable phosphate-containing phases like (Al,Fe)PO_4 formed at pH below 7, which can transform into hydroxyapatite as the pH increases over time [59].

7.3.1.4. Chemically bound water and heat of hydration

The weight loss between 105-600 °C is equivalent to the amount of chemically bound water of C-S-H, hydrogarnet, LDHs, portlandite etc. Therefore, the quantification of the amount of chemically bound water excluding portlandite provides an estimate of the total quantity of the other hydration products, as performed according to [73,217]:

$$W_{Chemically\ bound\ water} = (Water\ loss_{105-600\,°C} - Water\ loss_{OH\ group\ in\ Ca(OH)_2}) \times 100\% \quad \textbf{(7.1)}$$

Where $Water\ loss_{105-600\,°C}$ corresponds to the weight loss from 105 to 600 °C in the total mass fraction, $Water\ loss_{OH\ group\ in\ Ca(OH)_2}$ corresponds to the weight loss from approximately 400 to 500 °C in the total mass fraction.

Fig. 7.5 compares the overall cumulative heat release with the chemically bound water content measured from TGA for 7- and 28-day hydrated BOF slag pastes. The addition of phosphate increases the content of chemically bound water, which correlates with the higher initial pH, as shown in ***Fig. 7.5(a)***, using the indicated salt buffer as proxy (***Table 7.2***). One exception is M at 7 days, revealing its limited hydration. ***Fig. 7.5(b)*** shows that the total hydration heat is directly proportional to the chemically bound water, demonstrating a good correlation with an R2 value of 0.86. However, MD at 7 days and M at 28 days deviate from this trend, likely due to the exclusion of the first 45-minute heat release and the low heat release associated with the favoured formation of metastable phases at low initial pH.

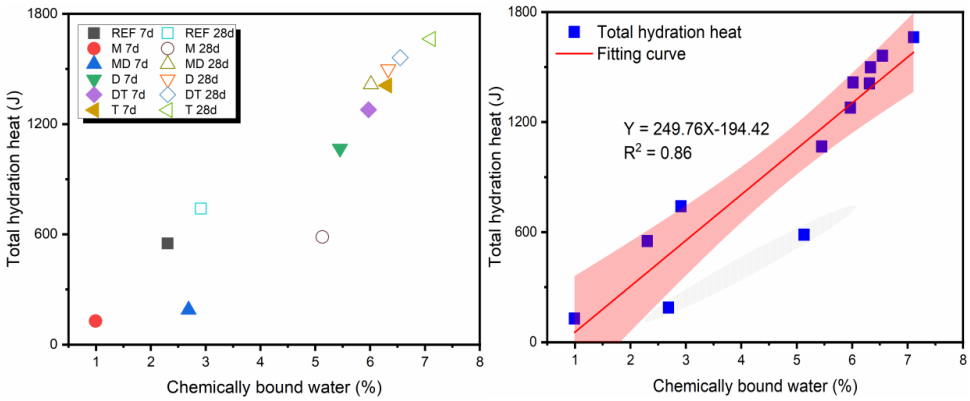

Fig. 7.5 *(a) The correlation between the chemically bound water of 7- and 28-day hydrated BOF slag pastes and its hydration heat, and (b) fitting curve.*

7.3.1.5. Reacted phases and hydration heat

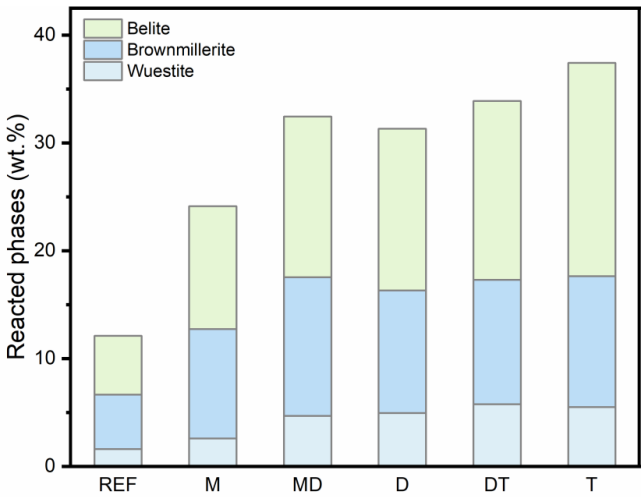

Fig. 7.6 *Amounts of reacted belite, brownmillerite and wuestite at 28 days with indicated phosphate salt buffer as pH-proxy.*

Fig. 7.6 illustrates the amounts of reacted belite, brownmillerite, and wuestite in 28-day hydrated BOF slag pastes with phosphate solutions at different initial pH values. The reaction amounts of these phases are normalized for water loss at 600 °C. Although the initial low pH in some samples retards hydration, the addition of phosphate ultimately leads to significantly more reacted phases compared to REF at 28 days. Higher initial pH enhances the reaction extent, with belite comprising the largest proportion of reacted phases. Brownmillerite shows a relatively higher reaction extent than belite, as its original amount is approximately half that of belite, as indicated in ***Table 7.1***. Despite variations

in pH affecting the reaction extent of belite, brownmillerite, and wuestite, the total hydration extent is more or less comparable for all samples containing phosphate, except for M.

Different clinker phases generate varying amounts of heat upon hydration. Based on the consumption of original phases in BOF slag pastes shown in ***Fig. 7.6***, the overall hydration heat at 28 days can be calculated. This allows for verification of the contributions from the dissolution and precipitation processes of specific phases in BOF slag to the overall heat release during hydration. The hydration of BOF slag involves multiple overlapping precipitation reactions that occur after dissolution. These precipitation reactions are difficult to study in isolation because they occur simultaneously and progressively as hydration advances. Besides, despite that the overall heat effect incorporates both dissolution and precipitation, the heat effect can be more allocated to the dissolution reaction depending on the thermodynamic data used, and dissolution of the clinker phases can be assumed to be the dominant heat contributing reaction [279]. Consequently, a simplified approach has been applied that dissolution enthalpy is used to represent the reaction enthalpy [279]. The dissolution reactions of brownmillerite and belite are represented by [187,280]:

$$Ca_2Fe_2O_5 + 5H_2O \rightarrow 2Ca^{2+} + 4OH^- + 2Fe(OH)_{3(am)} \qquad \Delta H_{R(Ca2Fe2O5)} = -485.67 \ [J/g] \qquad \textbf{(7.2)}$$

$$Ca_2SiO_4 + H_2O \rightarrow 2Ca^{2+} + 2OH^- + SiO_3^{2-} \qquad \Delta H_{R(Ca2SiO4)} = -298.95 \ [J/g] \qquad \textbf{(7.3)}$$

The hydration of wuestite releases certain amounts of Mg, Mn, and Fe, with Mg contributing more significantly than Mn and Fe to the formation of LDH phases [32,34]. Consequently, the reaction of wuestite can be simplified by considering MgO as the primary reacted phase, assuming the dissolution of Fe^{2+} and Mn^{2+} is minor. The reaction of wuestite is described using the simplified equation:

$$MgO + H_2O \rightarrow Mg^{2+} + 2OH^- \qquad \Delta H_{R(MgO)} = -959.25 \ [J/g] \qquad \textbf{(7.4)}$$

The reaction enthalpies of belite, brownmillerite, and wuestite are determined using the thermodynamic data listed in ***Table 7.5***. The overall heat release, calculated based on the amounts of reacted phases in the 28-day hydrated BOF slag pastes, is compared with the measured heat via calorimetry, as shown in ***Fig. 7.7***. The small deviation between the calculated and measured heat release in MD, D, DT, and T indicates the completed hydration of the reacted phases reached equilibrium, with the contribution of wuestite to the overall exothermic reaction being as comparable as that of belite and brownmillerite.

The measured heat higher than the calculated heat in REF can be attributed to the hydration of other original phases not included in the calculation. This exclusion of other hydrated original phases happens in all samples and affects more apparently the obtained value for REF. However, a large disparity is observed in M, where the calculated heat is much higher than the measured heat. This demonstrates that with acidic phosphate the hydration of BOF slag occurs differently from alkaline phosphate, initiating with an acid-base reaction where dissolution due to its acidic nature proceeds immediately upon mixing. This rapid dissolution concludes within the first 45 minutes, and thus, the corresponding heat release is omitted by the calorimeter measurement. Additionally, the reaction enthalpy is calculated based on the complete hydration. Hence, the formation of metastable phases with low heat release in M at 28 days is supported, indicating that the $H_2PO_4^-/HPO_4^{2-}$ buffering regime hinders the conversion of these metastable phases into stable hydrogarnet and LDH phases, similar to the observation in MD at 7 days.

Table 7.5 *Enthalpies of each phase/species used for the calculation of the overall heat release.*

Phases/species	ΔH_f [kJ/mol]	Reference
$Ca_2Fe_2O_5$	-2124.22	[280]
Ca_2SiO_4	-2307.6	[281]
MgO	-601.70	[282]
H_2O	-285.88	[283]
Ca^{2+}	-543.07	[283]
OH^-	−230.01	[283]
$Fe(OH)_{3(am)}$	-832	[280]
SiO_3^{2-}	−1098.74	[283]
Mg^{2+}	−465.93	[282]

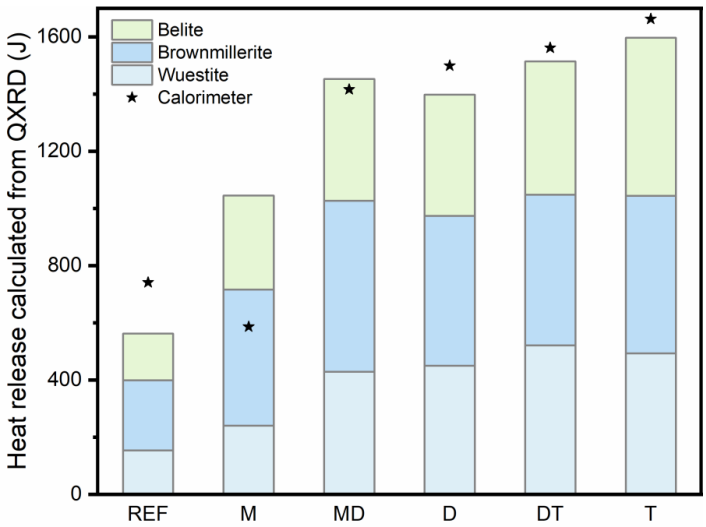

Fig. 7.7 *The comparison between heat release calculated based on the amounts of reacted phases and the measured heat from calorimeter of 28-day hydrated BOF slag pastes.*

7.3.2. Porosity and mechanical performance

The pore structure of 28-day hydrated BOF slag pastes was analyzed using MIP measurements, with the results shown in ***Fig. 7.8*** and ***Table 7.6***. REF exhibits the highest porosity at 21.2%, resulting in the lowest strength of 7.7 MPa at 28 days (***Fig. 7.9***). The addition of phosphate optimizes the pore structure by significantly reducing capillary porosity. Consequently, all phosphate-containing samples demonstrate a reduction in both porosity and average pore size at 28 days, consistent with enhanced hydration. The overall porosities of all phosphate-containing samples are comparable, as well as their workability observed during mixing and molding. However, the strengths of M and DT are significantly different, with 28-day strengths of 37.7 MPa for M and 66.9 MPa for DT. M has a higher proportion of capillary pores and a larger average pore size of 34.7 nm. The noticeable increase in strength from 7 to 28 days in M is attributed to its retarded hydration during the first 3 weeks. A similar significant increase in strength is observed in MD due to the formation of metastable phases rather than hydrogarnet and LDHs at 7 days, as explained with ***Fig. 7.5***. The contradiction between the higher hydration extent and lower strength of T compared to DT is notable. This can be explained by the higher potassium concentration in T, leading to shrinkage during air curing, particularly under low w/s conditions being more sensitive to alkali enrichment [284], consistent with the increased porosity and reduced bulk density of T (13.2% and 2.17 g/cm^3) and compared to DT (11.9% and 2.20 g/cm^3). Overall, while the elevated pH of phosphate solutions enhances the hydration extent of BOF slag pastes, attention should be given to potential shrinkage due to high alkali enrichment to ensure strength development. Further investigation should be conducted regarding the effects of alkalis on the pore structure and strength development in phosphate-activated BOF slag pastes.

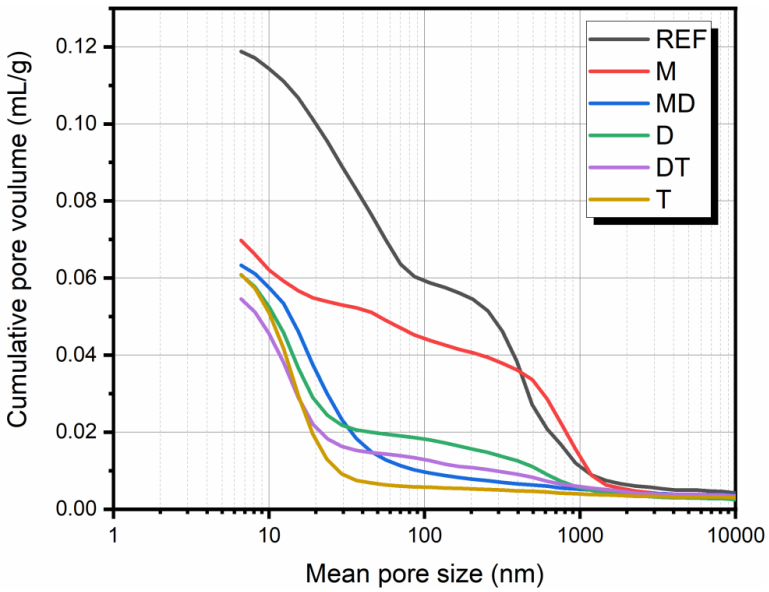

Fig. 7.8 *The cumulative pore volume of 28-day hydrated BOF slag pastes.*

Table 7.6 *Porosity and density of 28-day hydrated BOF slag pastes.*

Sample	Porosity [%]	Average pore size [nm]	Bulk density [g/cm^3]
REF	21.2	38.8	1.81
M	13.9	34.7	2.00
MD	13.8	13.3	2.20
D	13.9	17.4	2.30
DT	11.9	15.5	2.20
T	13.2	13.6	2.17

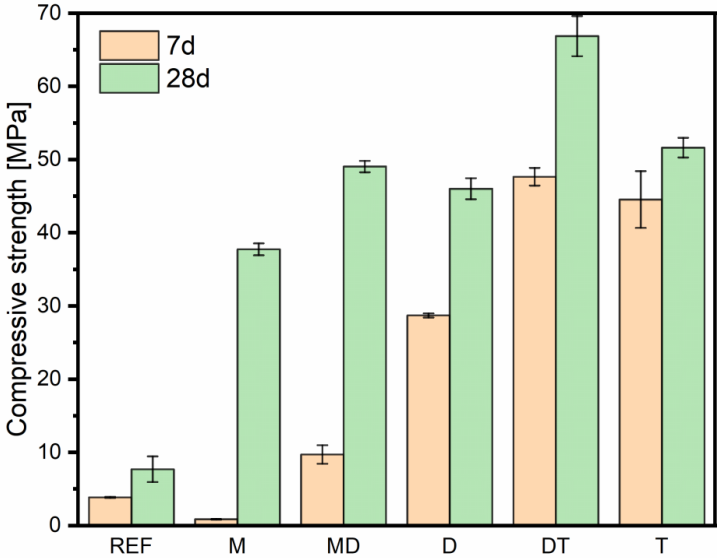

Fig. 7.9 *The strength development of 7- and 28-day hydrated BOF slag pastes.*

7.3.3. Leaching

The leaching of vanadium (V) and chromium (Cr) is of significant concern, as these are the two most concentrated heavy metals in the BOF slag used in this study, as indicated by the chemical composition (***Table 7.1***). V is primarily incorporated into belite and brownmillerite, while Cr resides in brownmillerite and wuestite [212]. The hydration of belite brownmillerite and wuestite can release these heavy metals, while their retention by hydration products like C-S-H gel and hydrogarnet can occur simultaneously [34,42]. This explains the lack of Cr leaching due to the immobilization capacity of the abundant hydration products, despite the significantly promoted hydration of brownmillerite and wuestite in the presence of phosphate. V remains relatively immobile in highly alkaline environments, and its leaching decreases with increasing pH [212,236,237]. A similar observation is noted in ***Table 7.7*** and ***Fig. 7.10***. The final pH is slightly higher with the initial higher pH of phosphate input, and while V leaching differences are minimal, they correlate well with the pH trend. Additionally, the final K concentrations are proportional to the initial K input for the phosphate-containing samples. Although C-S-H can adsorb small amounts of K, most K is dissolved during the leaching process [285].

Table 7.7 *Leaching of inorganic contaminants measured by one stage batch leaching test and the SQD limit values for unshaped materials.*

Elements	Unshaped material (SQD)	REF	M	MD	D	DT	T
	[mg/kg]						
Barium (Ba)	22.00	0.255	0.472	0.324	0.262	0.250	0.372
Chromium (Cr)	0.63	bdl*	bdl	0.001	bdl	0.001	bdl
Molybdenum (Mo)	1.00	<0.01	<0.01	<0.01	<0.01	<0.01	<0.01
Vanadium (V)	1.80	0.032	0.010	0.010	0.007	0.007	0.002
Zinc (Zn)	4.50	<0.01	<0.01	<0.01	<0.01	<0.01	<0.01

**bdl-below detection limit. Antimony (Sb), arsenic (As), cadmium (Cd), cobalt (Co), copper (Cu), lead (Pb), nickel (Ni) and tin (Sn) were also undetected by ICP measurement due to the detection limit.*

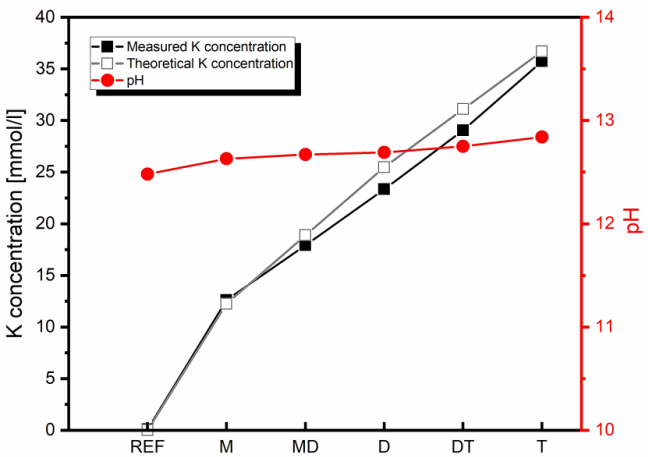

Fig. 7.10 *The pH values and K concentrations from leaching.*

7.3.4. Early-stage dissolution and precipitation

Due to the low water-to-solid (w/s) ratio, in-situ measurements of pH and conductivity are impractical. Therefore, a mixture of phosphate solution and BOF slag with a volume-to-slag mass ratio of 2 was used. Although this method significantly increases the phosphate amount, it closely simulates the early-stage dissolution of BOF slag under low w/s conditions, providing insights into pH evolution and ion concentration changes.

Upon mixing, REF* exhibits an immediate increase in conductivity and pH (***Fig. 7.11***). This increase can be attributed to the incongruent dissolution of belite and brownmillerite, as shown in ***Fig. 7.12*** that Ca shows a concentration of around 20 mmol/l and the concentrations of other elements (Fe, Al and Si) are at best around 0.01 mmol/l. The temperature in REF* remains stable, indicating the limited reactivity of BOF slag with water. At around 10 minutes, a slight pH increase is observed, stabilizing shortly after, along with a slight increase in Si concentration at 90 minutes, due to the further dissolution of belite. The decline in conductivity corresponds with a decrease in Al, Fe, and Mg concentrations, indicating the formation of pyroaurite (***Fig. 7.13***).

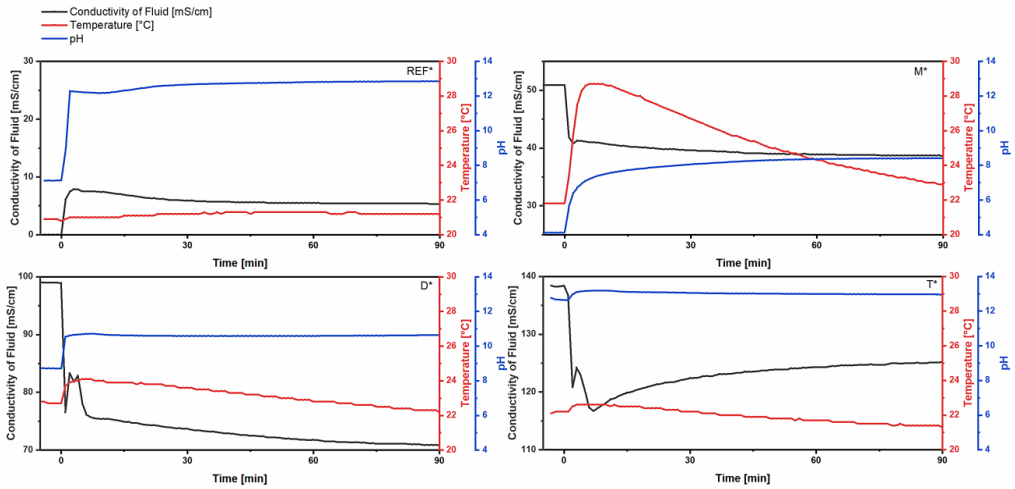

Fig. 7.11 *The in-situ pH and conductivity of different mixtures shown in* ***Table 7.3****.*

In mixtures containing phosphate, a significant decrease in conductivity is noted due to the rapid precipitation of various phosphates, as phosphate ions interact with iron, aluminum, magnesium, and calcium across a wide pH range [58]. Unlike M* and D*, T* starts increasing conductivity at around 10 minutes, indicating that dissolution is predominant instead of precipitation. In M*, a dramatic temperature rise occurs, due to acid-base reactions with a strong exothermic response [286]. Dissolution at alkaline conditions, as seen in D* and T* (***Fig. 7.11***), is more gradual. Phosphate addition enhances the dissolution of Al, Fe, and Si, which is more pronounced at higher pH levels. Variations in Ca and Mg concentrations are controlled by the saturation of different calcium and magnesium phosphate phases at specific pH levels, as the stabilized pH ranges of M*, D*,

and T* vary due to the buffering effects of different amounts of $H_2PO_4^-$, HPO_4^{2-}, and PO_4^{3-} ions [239]. The resulting precipitates differ with pH, including brushite ($CaHPO_4 \cdot 2H_2O$) at ~8.4, montgomeryite ($Al_4Ca_4Mg(PO_4)_6(OH)_4 \cdot 12H_2O$) at ~10.6, and vauxite ($FeAl_2(PO_4)_2(OH)_2 \cdot 6H_2O$) and bobierrite ($Mg_3(PO_4)_2 \cdot 8H_2O$) at ~13.0, as shown in ***Fig. 7.13***. Vauxite disappears at 90 minutes, likely converting into hydroxyapatite, a phase with higher thermodynamic stability at high pH [59,204]. These different formed phases indicate how phosphate reacts with various ions across a broad pH range. However, these reactions may not occur in BOF slag under low w/s conditions due to much lower phosphate content, or they may occur extremely rapidly upon mixing when the water to solid ratio still comprises only the surface of the slag particles and effectively is much higher.

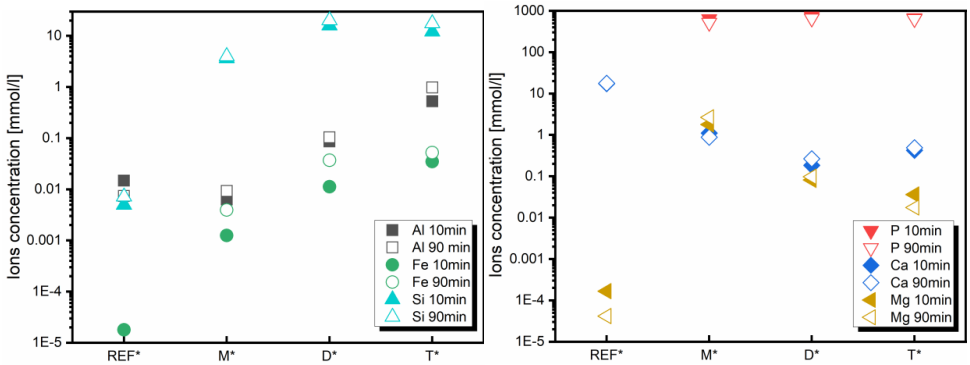

Fig. 7.12 *Ions concentration changing of different mixtures shown in* ***Table 7.3****.*

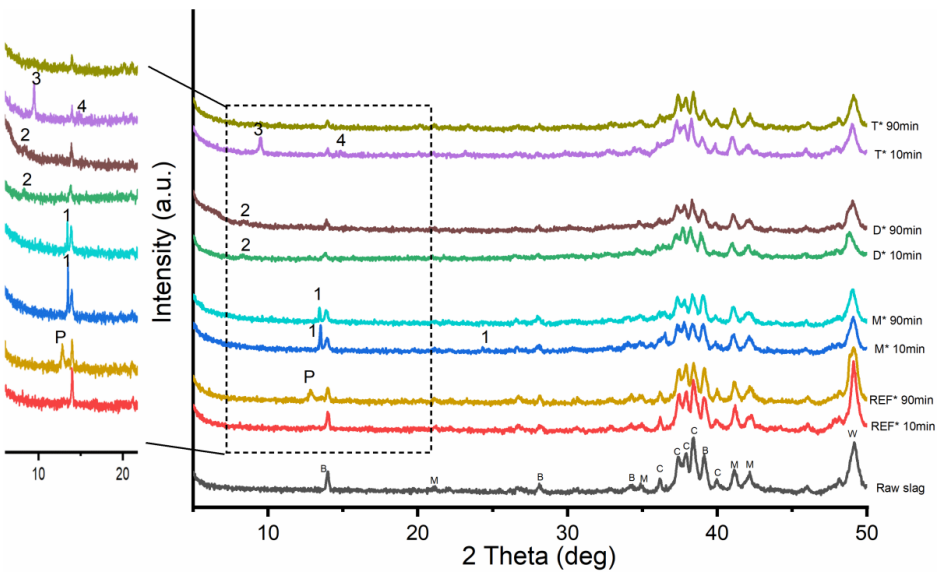

Fig. 7.13 *XRD data of BOF slag with different solutions (Legend: 1-Brushite, 2-Montgomeryite, 3-Vauxite, 4-Bobierrite, P-Pyroaurite, B-Brownmillerite, C-Belite, M-Magnetite, W-Wuestite).*

The preceding analysis provides valuable insights into the initial dissolution and precipitation processes of reacted BOF slag when activated with phosphates at different initial pH values. Further insights are drawn from the quantification of 1-day hydrated BOF slag pastes using XRD Rietveld analysis, as presented in ***Fig. 7.14***. It is evident that phosphate addition accelerates the reaction of belite. The reaction extent of belite in M and MD is more pronounced compared to that in samples with alkaline phosphate solutions. However, the reduction in belite content in M and MD does not lead to the formation of C-S-H. Instead, hydroxyapatite is detected via thermal analysis (***Fig. 7.15***), alongside other possible calcium phosphate compounds such as brushite and octacalcium phosphate, which form at pH levels below 7 [206,208]. The hydration extent of both belite and brownmillerite increases with higher pH in samples D, DT, and T, correlating well with the increase in hydration products. From the perspective of the formation of C-S-H gel, hydrogarnet and LDHs at an early stage, phosphate activators with high initial pH above 11, preferably above 12, are more effective.

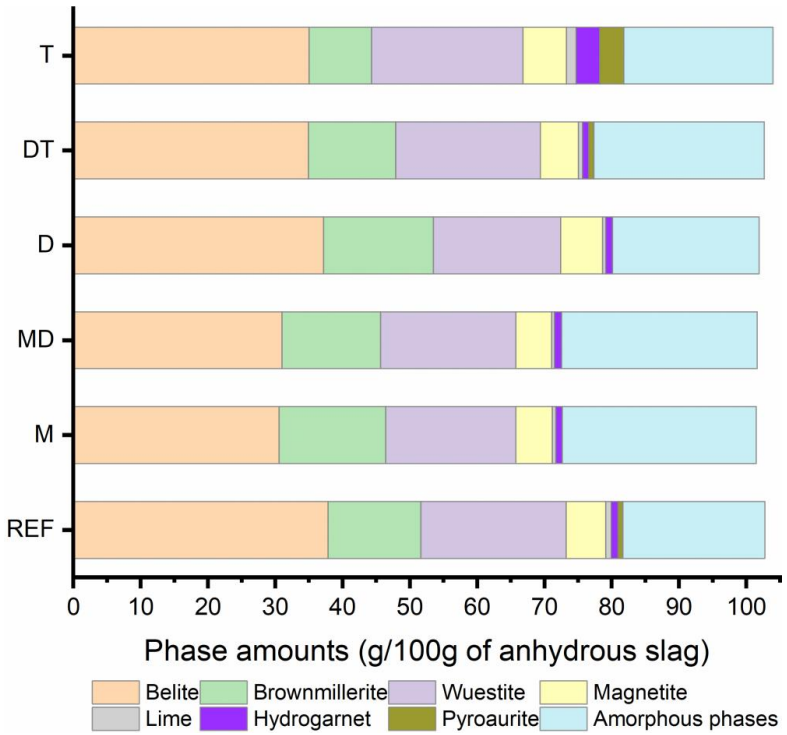

Fig. 7.14 *QXRD results of 1-day hydrated BOF slag pastes.*

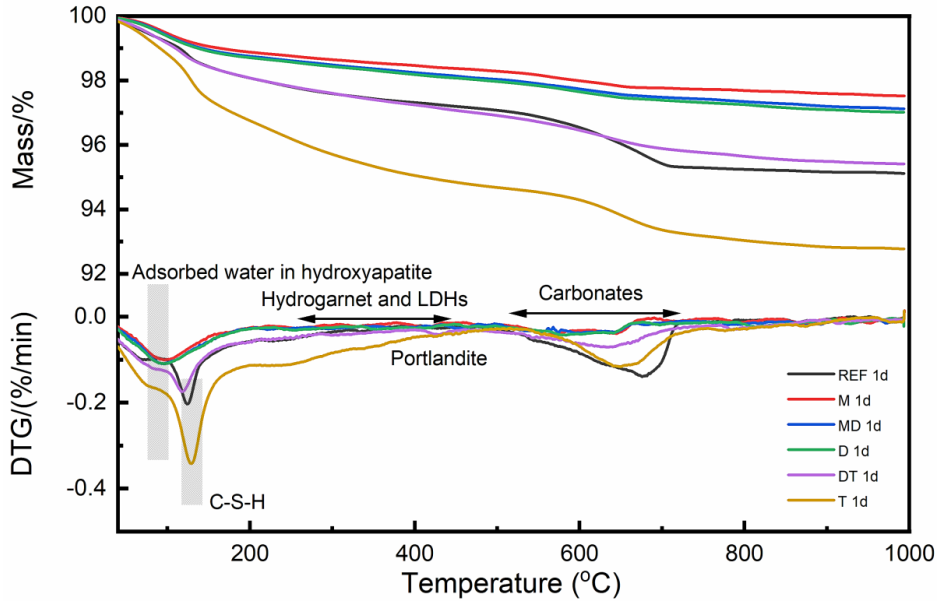

Fig. 7.15 *Thermal analysis (TG & DTG) of 1-day hydrated BOF slag pastes.*

7.3.5. Discussion

Upon mixing BOF slag with phosphate solutions, phosphate compounds form readily, but the reactions differ between acidic and alkaline phosphates, as shown in ***Fig. 7.16***. A certain amount of brownmillerite and belite is dissolved initially after mixing (***Fig. 7.12***). Acidic phosphate preferentially reacts with belite at an early stage, indicated by QXRD results of 1-day hydrated BOF slag pastes in ***Fig. 7.14***, forming a hydroxyapatite layer surrounding the belite surface, as described by:

$$5Ca_2SiO_4 + 7H_2PO_4^- \rightarrow 2Ca_5(PO_4)_3OH + 5HSiO_3^- + HPO_4^{2-} + 3H_2O \qquad \textbf{(7.5)}$$

This is corroborated by our previous findings, where a discernible rim containing mainly Ca, P, and Si was observed around belite in MKP-activated BOF slag pastes [238]. The formed layer can further inhibit the hydration of belite, resulting in slow increases in both pH and Ca concentration. As reported in [239], the addition of phosphoric acid significantly delays the dissolution of C_3A, and its hydration resumes only when the system exits the $H_2PO_4^-/HPO_4^{2-}$ buffering regime, which has a pH below 9 (***Fig. 7.11***). This process appears to occur in M, as only a small amount of brownmillerite reacts within 7 days compared to REF (***Table 7.4***). Additionally, the $H_2PO_4^-/HPO_4^{2-}$ buffering regime impedes the formation of hydrogarnet and LDH phases, evidenced by the discrepancy between the noticeable decline in brownmillerite and the small amounts of hydrogarnet and LDH phases observed in MD at 7 days (***Table 7.4*** and ***Fig. 7.4***).

It is assumed that alkaline phosphate reacts with the Ca^{2+} present in the pore solution rather than directly precipitating on the belite surface (***Fig. 7.16***), a process more pronounced at higher initial pH levels. This reaction decreases the Ca concentration in the pore solution at an early stage and increases the alkalinity, as higher alkaline phosphate consumes fewer hydroxy ions during hydroxyapatite formation, as described by:

$$5Ca^{2+} + 5OH^{-} + 4HPO_4^{2-} \rightarrow Ca_5(PO_4)_3OH + PO_4^{3-} + 4H_2O \quad \textbf{(7.6)}$$

$$5Ca^{2+} + OH^{-} + 3PO_4^{3-} \rightarrow Ca_5(PO_4)_3OH \quad \textbf{(7.7)}$$

Consequently, the dissolution of belite and brownmillerite is enhanced. Moreover, higher pH increases the solubilities of Fe, Al, and Si, making the oversaturation and subsequent precipitation of hydrogarnet and C-S-H more feasible [199,287,288]. This explains the varying induction periods observed in phosphate-containing samples with different initial pH levels (***Fig. 7.2***). The promoted hydration of belite further stabilizes hydrogarnet by providing sufficient SiO_3^{2-} to substitude OH^{-} sites [199].

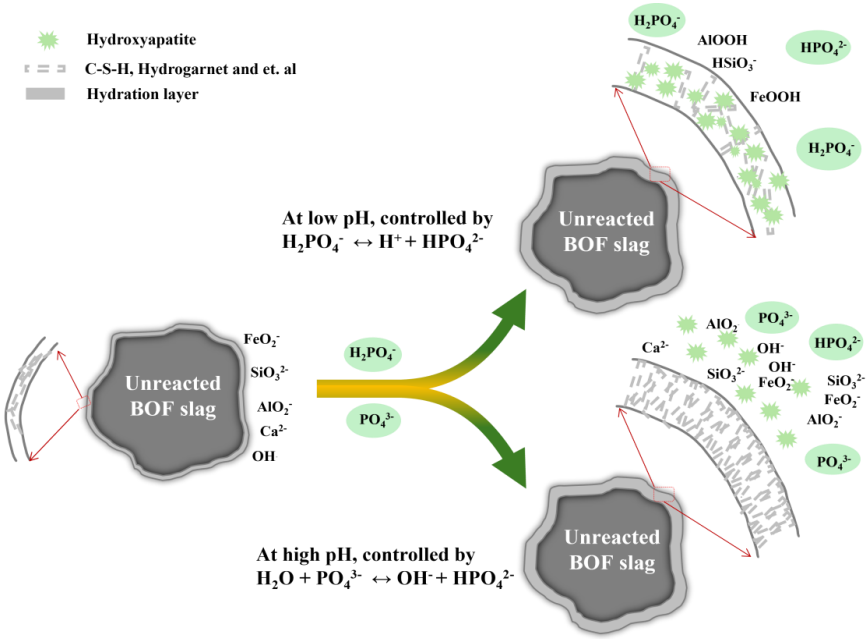

Fig. 7.16 *Hydration mechanism schematic of phosphate activated BOF slag at low and high pH.*

7.4. Conclusions

This study examined the reactions between BOF slag and phosphate across different pH levels, highlighting the effects of acidic and alkaline phosphates on hydration kinetics, microstructure, and strength development. The experimental findings are summarized as follows:

The reaction extent of belite in the samples with acidic phosphates are more pronounced compared to those in samples with alkaline phosphates at 1 day. This reduction in belite content in the samples with acidic phosphates leads to the formation of hydroxyapatite-like compounds via acid-base reaction instead of C-S-H. In contrast, a certain amount of C-S-H, hydrogarnent, and LDHs forms in the samples with high alkaline phosphates (pH at 11.5 and 12.8) at 1 day.

The acidic phosphate fails to react with the BOF slag after initial rapid dissolution due, instead leading to a prolonged induction period of up to 3 weeks.

The retardation effects on hydration diminish with increasing initial pH of phosphate solutions, influenced by the buffering effects of different amounts of $H_2PO_4^-$, HPO_4^{2-}, and PO_4^{3-} ions. Once leaving the $H_2PO_4^-/HPO_4^{2-}$ buffering regime, the hydration can still progress. Additionally, this buffering regime impedes the formation of hydrogarnet and LDH phases.

Higher initial pH leads to greater hydration extent of belite, brownmillerite and wuestite for equal phosphate input, accompanied by the formation of more C-S-H, hydrogarnet, and LDH phases, which are identified as the main hydration products. These findings are supported by phase composition, chemically bound water, and heat release obtained both from calorimetric measurements and calculations based on reaction enthalpies.

Despite variations in initial pH, the addition of phosphate promotes the hydration of BOF slag at 28 days, optimizing the pore structure. While the overall porosities of all phosphate-containing samples are comparable, ranging from 11.9 to 13.9%, their strengths vary significantly, with 28-day minimum and maximum strengths between 37.7 and 66.9 MPa. This variation is attributed to a higher proportion of capillary pores and a larger average pore size of 34.7 nm in the sample with low pH (pH 4.2) compared to those with alkaline phosphates. Furthermore, the contradiction between higher hydration extent and lower strength occurs in the sample with pH at 12.8 compared to the sample with lower pH at 11.5, likely due to high K concentration causing shrinkage during air curing.

CHAPTER 8

8. Conclusions and recommendations

8.1. Conclusions

This thesis explores a range of effective strategies aimed at reducing the environmental impact of cement and concrete production, focusing on innovative alternatives to traditional materials. These strategies include alternative clinker production using low-grade limestone, partial replacement of clinker with supplementary cementitious materials (SCMs), and the full replacement of clinker with cement-free binders, representing a promising pathway for sustainable construction. Furthermore, the replacement of natural aggregates with artificial aggregates derived from industrial wastes also plays a significant role in reducing CO_2 emissions.

Based on these approaches, this research investigates several key areas. It examines the structure of calcium silicate hydrate (C-S-H) when modified by magnesium, which may be introduced through the use of low-grade limestone for alternative clinker production. It also explores the valorization of concrete waste by utilizing it as artificial aggregates or new SCMs in blended Portland cement through carbonation. Finally, the thesis develops basic oxygen furnace (BOF) slag as a cement-free binder through chemical activation, offering a more radical solution to traditional cement, with the potential to significantly reduce the carbon footprint of the construction industry.

The introduction of Mg^{2+} into the C-S-H structure leads to substantial modifications, including increased cross-linking within silicate chains and reduced structural order. However, higher concentrations of Mg^{2+} can result in phase separation and structural instability, as shown by the formation of brucite. This suggests that while Mg^{2+} has potential in modifying binder properties, precise control of its content is crucial to maintain structural integrity. These results align with other studies that emphasize the need for balanced Mg^{2+} incorporation to leverage its benefits without compromising material performance.

In the area of concrete waste valorization, the research has demonstrated the feasibility of producing artificial lightweight aggregates (LWAs) and new supplementary cementitious materials (SCMs) from hydrated cement paste (HCP) powder. Carbonation plays a pivotal role in enhancing the mechanical properties of artificial aggregates, though careful calibration of carbonation duration is necessary to avoid shrinkage and internal

cracking. The incorporation of carbonated HCP with ground granulated blast furnace slag (GBS), fly ash (FA), and recycled glass powder (RGP) significantly improves the workability and strength of mortars. However, the CO_2 uptake capacity of the carbonated blends is reduced, and there are some issues with increased leaching of elements like Si and Na. This work supports the growing body of evidence that waste materials can be effectively valorized to reduce reliance on natural resources and minimize environmental impact.

The development of BOF slag as a cement-free binder through phosphate activation has emerged as one of the most promising solutions from this research. Phosphate activation significantly enhances hydration and mechanical properties, while controlling the leaching of heavy metals such as V, Cr, and Mo. However, the amount of phosphate must be carefully regulated to avoid rapid early reactions that can create large pores and hinder strength development. Despite these challenges, the ability of phosphate-activated BOF slag to control heavy metal leaching and maintain carbonation resistance makes it a particularly attractive option for industrial applications. This new binder type presents a strong opportunity for reducing clinker consumption and aligns well with ongoing efforts to integrate more sustainable practices in the cement industry.

From an industrial perspective, this research offers clear and actionable guidance for enhancing sustainability in the cement industry. One of the key recommendations is the optimization of alternative binders, such as phosphate-activated BOF slag. Notably, this development requires no special investments or additional equipment beyond what is already available in standard concrete or paste manufacturing. BOF slag-based building materials can be produced in existing concrete production facilities, with production costs primarily limited to the activator and water. This process offers a cost-effective and sustainable way to repurpose BOF slag, which is typically treated as waste, turning it into valuable construction materials. Moreover, the industry should focus on carefully managing the incorporation of magnesium to modify C-S-H structures. By controlling magnesium content, the potential for enhanced performance in cementitious materials can be achieved while maintaining stability. Additionally, effectively utilizing waste materials like concrete powder in production of LWAs and new SCMs offers another viable route to sustainability. By integrating waste products, the industry can significantly reduce CO_2 emissions and resource consumption, contributing to a circular economy in construction. These strategies not only reduce the environmental footprint but also ensure that the performance standards required for modern construction materials are met. Consistent with the findings of other researchers, this study underscores the potential for transformative change in the cement and concrete industry, driven by advances in materials science and waste valorization. Such innovations position the industry to achieve long-term sustainability goals without compromising material performance or economic feasibility.

8.2. Recommendations for future work

While the lab-based research presented here focuses on specific materials and controlled conditions and provides valuable insights into practical applications, there remain some general recommendations for future research that should be considered to further advance this field.

Understanding the Structure and Formation of C-S-H: The disordered and partially X-ray amorphous nature of synthesized calcium silicate hydrate (C-S-H) has left its exact structure and formation process unresolved. Future research should employ advanced techniques, such as synchrotron-based experiments combined with scanning transmission X-ray microscopy and solid-state nuclear magnetic resonance spectroscopy, to unravel the atomic structural details of synthesized C-S-H. Importantly, the C-S-H phase itself may have variable compositions, depending on the local environment in which it forms. The presence of new supplementary materials, such as those introducing abundant soluble ions, can significantly alter the chemistry of the surrounding environment, affecting the formation of C-S-H and potentially hampering cementitious reactions. These chemical effects, especially pH fluctuations, require detailed study, as they can disrupt C-S-H formation and affect the overall performance of the binder system. Understanding how these variables influence the structure and composition of C-S-H is critical for optimizing cementitious materials and ensuring their long-term durability. A deeper exploration into the composition–structure–property relationships of C-S-H during cement hydration is crucial, particularly considering that C-S-H formed during hydration is a heterogeneous mixture with hydrotalcite and hydrogarnet.

Variability in Industrial Waste Composition: The current focus on the chemistry and mineralogy of industrial wastes often overlooks the compositional variability within nominally similar by-products from different sources. Future studies should aim to isolate and examine individual phases of these by-products to gain comprehensive insights into the compound specific reactivity of single phases and their mixtures, during carbonation and activation processes. This approach will ensure more predictable performance and safety when using by-products with similar compositions in alternative binders.

Real Demolished Concrete Wastes: Unlike laboratory-made hydrated cement pastes (HCPs), real demolished concrete waste contains significant amounts of quartz, which dilutes the active components needed for carbonation, such as portlandite, C-(A)-S-H, and other hydrates. As a result, the performance of carbonated real demolished concrete wastes may be poorer compared to lab-made HCPs. Future research should focus on optimizing carbonation methods (e.g., wet, semi-dry, dry) and parameters (e.g., temperature, CO_2 concentration, relative humidity, pressure) to maximize the utilization of limited HCP content in real demolished concrete wastes.

Carbonation as an Alternative Activation Method for BOF Slag: While chemical activation has shown potential for developing BOF slag-based, cement-free binders with

satisfactory mechanical properties, carbonation could also serve as an effective activation method. However, the associated leaching issues must be addressed. Combining phosphate activation with carbonation might offer the benefit of captured CO_2, enhanced strength and controlled leaching.

Scale-up to Mortar and Concrete Mixtures: Research on BOF slag products has predominantly focused on paste-level investigations. Future work should extend to the design of mortar and concrete mixtures, emphasizing optimized particle packing and an engineered interfacial transition zone (ITZ) between the paste and aggregate to enhance overall material performance.

Exploring Alternative Activators for BOF Slag: Although phosphate has demonstrated promising results in enhancing both mechanical properties and heavy metal leaching control in BOF slag-based binders, the search for alternative activators is warranted. Future research should explore the potential of using lower phosphate dosages or identifying more economical activators to achieve similar or improved performance.

Bibliography

[1] Global Cement and Concrete Association, Concrete Future - The GCCA 2050 Cement and Concrete Industry Roadmap for Net Zero Concrete, 2021. www.gccassociation.org.

[2] A. Machner, M. Zajac, M. Ben Haha, K.O. Kjellsen, M.R. Geiker, K. De Weerdt, Limitations of the hydrotalcite formation in Portland composite cement pastes containing dolomite and metakaolin, Cem. Concr. Res. 89 (2018) 89–106. https://doi.org/10.1016/j.cemconcomp.2018.02.013.

[3] S.A. Walling, J.L. Provis, Magnesia-Based Cements: A Journey of 150 Years, and Cements for the Future?, Chem. Rev. 116 (2016) 4170–4204. https://doi.org/10.1021/acs.chemrev.5b00463.

[4] E. Gartner, H. Hirao, A review of alternative approaches to the reduction of CO2emissions associated with the manufacture of the binder phase in concrete, Cem. Concr. Res. 78 (2015) 126–142. https://doi.org/10.1016/j.cemconres.2015.04.012.

[5] I.-H. Jung, S.A. Decterov, A.D. Pelton, Critical Thermodynamic Evaluation and Optimization of the MgO-Al2O3, CaO-MgO-Al2O3, and MgO-Al2O3-SiO2 Systems, Proc. Sci. 25 (2010) 329–345. https://doi.org/10.1361/15477030420106.

[6] H. Wu, J. Zuo, G. Zillante, J. Wang, H. Yuan, Status quo and future directions of construction and demolition waste research: A critical review, J. Clean. Prod. 240 (2019) 118163. https://doi.org/10.1016/J.JCLEPRO.2019.118163.

[7] R. Islam, T.H. Nazifa, A. Yuniarto, A.S.M. Shanawaz Uddin, S. Salmiati, S. Shahid, An empirical study of construction and demolition waste generation and implication of recycling, Waste Manag. 95 (2019) 10–21. https://doi.org/10.1016/J.WASMAN.2019.05.049.

[8] B. Lu, C. Shi, J. Zhang, J. Wang, Effects of carbonated hardened cement paste powder on hydration and microstructure of Portland cement, Constr. Build. Mater. 186 (2018) 699–708. https://doi.org/10.1016/j.conbuildmat.2018.07.159.

[9] R. Serpell, M. Lopez, Reactivated cementitious materials from hydrated cement paste wastes, Cem. Concr. Compos. 39 (2013) 104–114. https://doi.org/10.1016/j.cemconcomp.2013.03.020.

[10] J. Yang, J. Huang, Y. Su, X. He, H. Tan, W. Yang, B. Strnadel, Eco-friendly treatment of low-calcium coal fly ash for high pozzolanic reactivity: A step towards waste utilization in sustainable building material, J. Clean. Prod. 238 (2019) 117962. https://doi.org/10.1016/j.jclepro.2019.117962.

[11] P.M.F. van de Wouw, E. Loginova, M.V.A. Florea, H.J.H. Brouwers, Compositional modelling and crushing behaviour of MSWI bottom ash material classes, Waste Manag. 101 (2020) 268–282. https://doi.org/10.1016/j.wasman.2019.10.013.

[12] X. He, Z. Zheng, J. Yang, Y. Su, T. Wang, B. Strnadel, Feasibility of incorporating autoclaved aerated concrete waste for cement replacement in sustainable building materials, J. Clean. Prod. 250 (2020) 119455. https://doi.org/10.1016/j.jclepro.2019.119455.

[13] C. Shi, Y. Li, J. Zhang, W. Li, L. Chong, Z. Xie, Performance enhancement of recycled concrete aggregate - A review, J. Clean. Prod. 112 (2016) 466–472. https://doi.org/10.1016/j.jclepro.2015.08.057.

[14] A. Singh, S. Arora, ; Vaibhav Sharma, B. Bhardwaj, Workability Retention and Strength

Development of Self-Compacting Recycled Aggregate Concrete Using Ultrafine Recycled Powders and Silica Fume, J. Hazardous, Toxic, Radioact. Waste. 23 (2019) 04019016. https://doi.org/10.1061/(ASCE)HZ.2153-5515.0000456.

[15] K. Kalinowska-Wichrowska, M. Kosior-Kazberuk, E. Pawluczuk, The Properties of Composites with Recycled Cement Mortar Used as a Supplementary Cementitious Material, Mater. 2020, Vol. 13, Page 64. 13 (2019) 64. https://doi.org/10.3390/MA13010064.

[16] M. Frías, S. Martínez-Ramírez, R.V. de la Villa, L. Fernández-Carrasco, R. García, Reactivity in cement pastes bearing fine fraction concrete and glass from construction and demolition waste: Microstructural analysis of viability, Cem. Concr. Res. 148 (2021) 106531. https://doi.org/10.1016/J.CEMCONRES.2021.106531.

[17] V.W.Y. Tam, M. Soomro, A.C.J. Evangelista, A review of recycled aggregate in concrete applications (2000–2017), Constr. Build. Mater. 172 (2018) 272–292. https://doi.org/10.1016/J.CONBUILDMAT.2018.03.240.

[18] EN 197-1, (2000). https://doi.org/10.1016/0005-2736(80)90400-9.

[19] A. Dixit, G. Geng, H. Du, S.D. Pang, The role of age on carbon sequestration and strength development in blended cement mixes, Cem. Concr. Compos. 133 (2022) 104644. https://doi.org/10.1016/J.CEMCONCOMP.2022.104644.

[20] M.C.G. Juenger, R. Siddique, Recent advances in understanding the role of supplementary cementitious materials in concrete, Cem. Concr. Res. 78 (2015) 71–80. https://doi.org/10.1016/J.CEMCONRES.2015.03.018.

[21] M.C.G. Juenger, R. Snellings, S.A. Bernal, Supplementary cementitious materials: New sources, characterization, and performance insights, Cem. Concr. Res. 122 (2019) 257–273. https://doi.org/10.1016/J.CEMCONRES.2019.05.008.

[22] J. Yang, J. Zeng, X. He, H. Hu, Y. Su, H. Bai, H. Tan, Eco-friendly UHPC prepared from high volume wet-grinded ultrafine GGBS slurry, Constr. Build. Mater. 308 (2021) 125057. https://doi.org/10.1016/j.conbuildmat.2021.125057.

[23] O.R. Ogirigbo, L. Black, Chloride binding and diffusion in slag blends: Influence of slag composition and temperature, Constr. Build. Mater. 149 (2017) 816–825. https://doi.org/10.1016/J.CONBUILDMAT.2017.05.184.

[24] J. Yang, J. Zeng, X. He, Y. Zhang, Y. Su, H. Tan, Sustainable clinker-free solid waste binder produced from wet-ground granulated blast-furnace slag, phosphogypsum and carbide slag, Constr. Build. Mater. 330 (2022) 127218. https://doi.org/10.1016/j.conbuildmat.2022.127218.

[25] O. Kayali, M. Sharfuddin Ahmed, Assessment of high volume replacement fly ash concrete – Concept of performance index, Constr. Build. Mater. 39 (2013) 71–76. https://doi.org/10.1016/J.CONBUILDMAT.2012.05.009.

[26] G. Liu, M.V.A. Florea, H.J.H. Brouwers, Characterization and performance of high volume recycled waste glass and ground granulated blast furnace slag or fly ash blended mortars, J. Clean. Prod. 235 (2019) 461–472. https://doi.org/10.1016/j.jclepro.2019.06.334.

[27] B. Taha, G. Nounu, Properties of concrete contains mixed colour waste recycled glass as sand and cement replacement, Constr. Build. Mater. 22 (2008) 713–720. https://doi.org/10.1016/j.conbuildmat.2007.01.019.

[28] M.U. Hossain, C.S. Poon, I.M.C. Lo, J.C.P. Cheng, Comparative LCA on using waste materials in the cement industry: A Hong Kong case study, Resour. Conserv. Recycl. 120 (2017) 199–208. https://doi.org/10.1016/J.RESCONREC.2016.12.012.

[29] Y. Jiang, T.C. Ling, C. Shi, S.Y. Pan, Characteristics of steel slags and their use in cement and

concrete—A review, Resour. Conserv. Recycl. 136 (2018) 187–197. https://doi.org/10.1016/j.resconrec.2018.04.023.

[30] R. Ragipani, S. Bhattacharya, A.K. Suresh, A review on steel slag valorisation: Via mineral carbonation, React. Chem. Eng. 6 (2021) 1152–1178. https://doi.org/10.1039/d1re00035g.

[31] P.S. Humbert, J. Castro-Gomes, CO2 activated steel slag-based materials: A review, J. Clean. Prod. 208 (2019) 448–457. https://doi.org/10.1016/j.jclepro.2018.10.058.

[32] K. Schollbach, M.J. Ahmed, S.R. van der Laan, The mineralogy of air granulated converter slag, Int. J. Ceram. Eng. Sci. 3 (2021) 21–36. https://doi.org/10.1002/ces2.10074.

[33] J. Zhao, P. Yan, D. Wang, Research on mineral characteristics of converter steel slag and its comprehensive utilization of internal and external recycle, J. Clean. Prod. 156 (2017) 50–61. https://doi.org/10.1016/j.jclepro.2017.04.029.

[34] W. Franco Santos, K. Schollbach, S. Melzer, S.R. van der Laan, H.J.H. Brouwers, Quantitative analysis and phase assemblage of basic oxygen furnace slag hydration, J. Hazard. Mater. 450 (2023) 131029. https://doi.org/10.1016/j.jhazmat.2023.131029.

[35] Euroslag, (2018). https://www.euroslag.com/products/statistics/statistics-2018/.

[36] B. Das, S. Prakash, P.S.R. Reddy, V.N. Misra, An overview of utilization of slag and sludge from steel industries, Resour. Conserv. Recycl. 50 (2007) 40–57. https://doi.org/10.1016/j.resconrec.2006.05.008.

[37] G. Liu, K. Schollbach, P. Li, H.J.H. Brouwers, Valorization of converter steel slag into eco-friendly ultra-high performance concrete by ambient CO2 pre-treatment, Constr. Build. Mater. 280 (2021) 122580. https://doi.org/10.1016/j.conbuildmat.2021.122580.

[38] Q. Zhao, L. Pang, D. Wang, Adverse Effects of Using Metallurgical Slags as Supplementary Cementitious Materials and Aggregate: A Review, Materials (Basel). 15 (2022) 1–21. https://doi.org/10.3390/ma15113803.

[39] A.M. Kaja, K. Schollbach, S. Melzer, S.R. van der Laan, H.J.H. Brouwers, Q. Yu, Hydration of potassium citrate-activated BOF slag, Cem. Concr. Res. 140 (2021) 106291. https://doi.org/10.1016/j.cemconres.2020.106291.

[40] Y.M. Kim, S.H. Hong, Influence of minor ions on the stability and hydration rates of β-dicalcium silicate, J. Am. Ceram. Soc. 87 (2004) 900–905. https://doi.org/10.1111/j.1551-2916.2004.00900.x.

[41] W. Kurdowski, Cement and Concrete Chemistry, 2018. https://medium.com/@arifwicaksanaa/pengertian-use-case-a7e576e1b6bf.

[42] M.J. Ahmed, R. Cuijpers, K. Schollbach, S.R. van der Laan, M. Van Wijngaarden-Kroft, T. Verhoeven, H.J.H. Brouwers, V and Cr substitution in dicalcium silicate under oxidizing and reducing conditions – Synthesis, reactivity, and leaching behavior studies, J. Hazard. Mater. 442 (2023) 130032. https://doi.org/10.1016/j.jhazmat.2022.130032.

[43] G. Liu, Y. Tang, J. Wang, Effects of carbonation degree of semi-dry carbonated converter steel slag on the performance of blended cement mortar – Reactivity, hydration, and strength, J. Build. Eng. 63 (2023) 105529. https://doi.org/10.1016/j.jobe.2022.105529.

[44] Q. Wang, P.Y. Yan, S. Han, The influence of steel slag on the hydration of cement during the hydration process of complex binder, Sci. China Technol. Sci. 54 (2011) 388–394. https://doi.org/10.1007/s11431-010-4204-0.

[45] S. Zhuang, Q. Wang, Inhibition mechanisms of steel slag on the early-age hydration of cement, Cem. Concr. Res. 140 (2021) 106283. https://doi.org/10.1016/j.cemconres.2020.106283.

[46] I.G. Richardson, The calcium silicate hydrates, Cem. Concr. Res. 38 (2008) 137–158. https://doi.org/10.1016/j.cemconres.2007.11.005.

[47] J. Li, G. Geng, R. Myers, Y.S. Yu, D. Shapiro, C. Carraro, R. Maboudian, P.J.M. Monteiro, The chemistry and structure of calcium (alumino) silicate hydrate: A study by XANES, ptychographic imaging, and wide- and small-angle scattering, Cem. Concr. Res. 115 (2019) 367–378. https://doi.org/10.1016/j.cemconres.2018.09.008.

[48] H.F.W. Taylor, Cement chemistry. 2nd ed., Acad. Press. (1997). https://doi.org/10.1016/S0958-9465(98)00023-7.

[49] A. Nonat, The structure and stoichiometry of C-S-H, Cem. Concr. Res. 34 (2004) 1521–1528. https://doi.org/10.1016/j.cemconres.2004.04.035.

[50] F.P. Glasser, E.E. Lachowski, D.E. Macphee, Compositional Model for Calcium Silicate Hydrate (C-S-H) Gels, Their Solubilities, and Free Energies of Formation, J. Am. Ceram. Soc. 70 (1987) 481–485. https://doi.org/10.1111/j.1151-2916.1987.tb05680.x.

[51] J. Hill, A.W. Harris, M. Manning, A. Chambers, S.W. Swanton, The effect of sodium chloride on the dissolution of calcium silicate hydrate gels, Waste Manag. 26 (2006) 758–768. https://doi.org/10.1016/j.wasman.2006.01.022.

[52] M. Santhanam, M. Cohen, J. Olek, Differentiating seawater and groundwater sulfate attack in Portland cement mortars, Cem. Concr. Res. 36 (2006) 2132–2137. https://doi.org/10.1016/j.cemconres.2006.09.011.

[53] G. Plusquellec, A. Nonat, Interactions between calcium silicate hydrate (C-S-H) and calcium chloride, bromide and nitrate, Cem. Concr. Res. 90 (2016) 89–96. https://doi.org/10.1016/j.cemconres.2016.08.002.

[54] E.M.J. Bérodier, A.C.A. Muller, K.L. Scrivener, Effect of sulfate on C-S-H at early age, Cem. Concr. Res. 138 (2020). https://doi.org/10.1016/j.cemconres.2020.106248.

[55] X. Liu, P. Feng, W. Li, G. Geng, J. Huang, Y. Gao, S. Mu, J. Hong, Effects of pH on the nano/micro structure of calcium silicate hydrate (C-S-H) under sulfate attack, Cem. Concr. Res. 140 (2021) 106306. https://doi.org/10.1016/j.cemconres.2020.106306.

[56] B.J. Zhan, D.X. Xuan, C.S. Poon, K.L. Scrivener, Characterization of interfacial transition zone in concrete prepared with carbonated modeled recycled concrete aggregates, Cem. Concr. Res. 136 (2020) 106175. https://doi.org/10.1016/j.cemconres.2020.106175.

[57] D. Xuan, B. Zhan, C.S. Poon, Assessment of mechanical properties of concrete incorporating carbonated recycled concrete aggregates, Cem. Concr. Compos. 65 (2016) 67–74. https://doi.org/10.1016/j.cemconcomp.2015.10.018.

[58] Q. Wang, Z. Liao, D. Yao, Z. Yang, Y. Wu, C. Tang, Phosphorus immobilization in water and sediment using iron-based materials: A review, Sci. Total Environ. 767 (2021) 144246. https://doi.org/10.1016/j.scitotenv.2020.144246.

[59] C.J. Penn, J.J. Camberato, A critical review on soil chemical processes that control how soil ph affects phosphorus availability to plants, Agric. 9 (2019) 1–18. https://doi.org/10.3390/agriculture9060120.

[60] L. Fernandez, C. Alonso, A. Hidalgo, C. Andrade, The role of magnesium during the hydration of C3S and C-S-H formation. Scanning electron microscopy and mid-infrared studies, Adv. Cem. Res. 17 (2005) 9–21. https://doi.org/10.1680/adcr.2005.17.1.9.

[61] L. Fernandez, C. Alonso, C. Andrade, A. Hidalgo, The interaction of magnesium in hydration of C3S and CSH formation using 29Si MAS-NMR, J. Mater. Sci. 43 (2008) 5772–5783. https://doi.org/10.1007/s10853-008-2889-2.

[62] N.Y. Mostafa, E.A. Kishar, S.A. Abo-El-Enein, FTIR study and cation exchange capacity of

Fe3+- and Mg2+-substituted calcium silicate hydrates, J. Alloys Compd. 473 (2009) 538–542. https://doi.org/10.1016/j.jallcom.2008.06.029.

[63] S. Diamond, W. L. Dolch, J. L. White, Studies on Tobermorite-Like Calcium Silicate Hydrates, Jt. Highw. Res. Proj. (1963). https://doi.org/10.5703/1288284313642.

[64] G. Qian, G. Xu, H. Li, A. Li, Mg-Xonotlite and its coexisting phases, Cem. Concr. Res. 27 (1997) 315–320. https://doi.org/10.1016/S0008-8846(97)00018-5.

[65] E. Bernard, B. Lothenbach, F. Le Goff, I. Pochard, A. Dauzères, Effect of magnesium on calcium silicate hydrate (C-S-H), Cem. Concr. Res. 97 (2017) 61–72. https://doi.org/10.1016/j.cemconres.2017.03.012.

[66] E. Bernard, B. Lothenbach, C. Cau-Dit-Coumes, C. Chlique, A. Dauzères, I. Pochard, Magnesium and calcium silicate hydrates, Part I: Investigation of the possible magnesium incorporation in calcium silicate hydrate (C-S-H) and of the calcium in magnesium silicate hydrate (M-S-H), Appl. Geochemistry. 89 (2018) 229–242. https://doi.org/10.1016/j.apgeochem.2017.12.005.

[67] E. Bernard, A. Dauzères, B. Lothenbach, Magnesium and calcium silicate hydrates, Part II: Mg-exchange at the interface "low-pH" cement and magnesium environment studied in a C-S-H and M-S-H model system, Appl. Geochemistry. 89 (2018) 210–218. https://doi.org/c.

[68] O.P. Shrivastava, S. Komarneni, E. Breval, Mg2+uptake by synthetic tobermorite and xonotlite, Cem. Concr. Res. 21 (1991) 83–90. https://doi.org/10.1016/0008-8846(91)90034-F.

[69] Y. Tang, W. Chen, Effect of magnesium on the structure and chemical composition of calcium silicate hydrate at elevated temperature, Constr. Build. Mater. 240 (2020) 117925. https://doi.org/10.1016/j.conbuildmat.2019.117925.

[70] L. Galvánková, J. Másilko, T. Solný, E. Štěpánková, Tobermorite Synthesis under Hydrothermal Conditions, Procedia Eng. 151 (2016) 100–107. https://doi.org/10.1016/j.proeng.2016.07.394.

[71] B. Lothenbach, D. Nied, E. L'Hôpital, G. Achiedo, A. Dauzères, Magnesium and calcium silicate hydrates, Cem. Concr. Res. 77 (2015) 60–68. https://doi.org/10.1016/j.cemconres.2015.06.007.

[72] F. Battocchio, P.J.M. Monteiro, H.R. Wenk, Rietveld refinement of the structures of 1.0 C-S-H and 1.5 C-S-H, Cem. Concr. Res. 42 (2012) 1534–1548. https://doi.org/10.1016/j.cemconres.2012.07.005.

[73] K. Scrivener, R. Snellings, B. Lothenbach, F. Group, A Practical Guide to Microstructural Analysis of Cementitious Materials, 2018. https://doi.org/10.1201/b19074.

[74] A.A. Coelho, TOPAS and TOPAS-Academic: An optimization program integrating computer algebra and crystallographic objects written in C++: An, J. Appl. Crystallogr. 51 (2018) 210–218. https://doi.org/10.1107/S1600576718000183.

[75] E.P. Barrett, L.G. Joyner, P.P. Halenda, The Determination of Pore Volume and Area Distributions in Porous Substances. I. Computations from Nitrogen Isotherms, J. Am. Chem. Soc. 73 (1951) 373–380. https://doi.org/10.1021/ja01145a126.

[76] S. Brunauer, P.H. Emmett, E. Teller, Adsorption of Gases in Multimolecular Layers, J. Am. Chem. Soc. 60 (1938) 309–319. https://doi.org/10.1021/ja01269a023.

[77] L.G. Joyner, E.P. Barrett, R. Skold, The Determination of Pore Volume and Area Distributions in Porous Substances. II. Comparison between Nitrogen Isotherm and Mercury Porosimeter Methods, J. Am. Chem. Soc. 73 (1951) 3155–3158. https://doi.org/10.1021/ja01151a046.

[78] P. Yu, R.J. Kirkpatrick, B. Poe, P.F. McMillan, X. Cong, Structure of Calcium Silicate Hydrate (C-S-H): Near-, Mid-, and Far-Infrared Spectroscopy, J. Am. Ceram. Soc. 82 (1999) 742–748. https://doi.org/10.1111/j.1151-2916.1999.tb01826.x.

[79] F.. Wilburn, Handbook of Thermal Analysis of Construction Materials, Thermochim. Acta. 406 (2003) 249. https://doi.org/10.1016/s0040-6031(03)00230-2.

[80] H.F.W. Taylor, Bound Water in Cement Pastes and its Significance for Pore Solution Compositions, MRS Online Proc. Libr. 85 (1986) 47–54. https://doi.org/10.1557/PROC-85-47.

[81] F. Jin, K. Gu, A. Al-Tabbaa, Strength and drying shrinkage of reactive MgO modified alkali-activated slag paste, Constr. Build. Mater. 51 (2014) 395–404. https://doi.org/10.1016/j.conbuildmat.2013.10.081.

[82] J.J. Thomas, S.A. FitzGerald, D.A. Neumann, R.A. Livingston, State of Water in Hydrating Tricalcium Silicate and Portland Cement Pastes as Measured by Quasi-Elastic Neutron Scattering, J. Am. Ceram. Soc. 84 (2004) 1811–1816. https://doi.org/10.1111/j.1151-2916.2001.tb00919.x.

[83] E.T. Rodriguez, I.G. Richardson, L. Black, E. Boehm-Courjault, A. Nonat, J. Skibsted, Composition, silicate anion structure and morphology of calcium silicate hydrates (C-S-H) synthesised by silica-lime reaction and by controlled hydration of tricalcium silicate (C3S), Adv. Appl. Ceram. 114 (2015) 362–371. https://doi.org/10.1179/1743676115Y.0000000038.

[84] J. Li, W. Zhang, K. Xu, P.J.M. Monteiro, Fibrillar calcium silicate hydrate seeds from hydrated tricalcium silicate lower cement demand, Cem. Concr. Res. 137 (2020). https://doi.org/10.1016/j.cemconres.2020.106195.

[85] N. Krautwurst, L. Nicoleau, M. Dietzsch, I. Lieberwirth, C. Labbez, A. Fernandez-Martinez, A.E.S. Van Driessche, B. Barton, S. Leukel, W. Tremel, Two-Step Nucleation Process of Calcium Silicate Hydrate, the Nanobrick of Cement, Chem. Mater. 30 (2018) 2895–2904. https://doi.org/10.1021/acs.chemmater.7b04245.

[86] W.S. Chiang, G. Ferraro, E. Fratini, F. Ridi, Y.Q. Yeh, U.S. Jeng, S.H. Chen, P. Baglioni, Multiscale structure of calcium- and magnesium-silicate-hydrate gels, J. Mater. Chem. A. 2 (2014) 12991–12998. https://doi.org/10.1039/c4ta02479f.

[87] H.M. Jennings, J.J. Thomas, J.J. Chen, D. Rothstein, Cement Paste as a Porous Material, Handb. Porous Solids. (2002) 2971–3028. https://doi.org/10.1002/9783527618286.

[88] R.M. Espinosa, L. Franke, Influence of the age and drying process on pore structure and sorption isotherms of hardened cement paste, Cem. Concr. Res. 36 (2006) 1954–1968. https://doi.org/10.1016/j.cemconres.2006.06.011.

[89] N. De Belie, J. Kratky, S. Van Vlierberghe, Influence of pozzolans and slag on the microstructure of partially carbonated cement paste by means of water vapour and nitrogen sorption experiments and BET calculations, Cem. Concr. Res. 40 (2010) 1723–1733. https://doi.org/10.1016/j.cemconres.2010.08.014.

[90] Y. Suda, T. Saeki, T. Saito, Relation between chemical composition and physical properties of C-S-H generated from cementitious materials, J. Adv. Concr. Technol. 13 (2015) 275–290. https://doi.org/10.3151/jact.13.275.

[91] Y.X. Chen, F. Wu, Q. Yu, H.J.H. Brouwers, Bio-based ultra-lightweight concrete applying miscanthus fibers: Acoustic absorption and thermal insulation, Cem. Concr. Compos. 114 (2020). https://doi.org/10.1016/j.cemconcomp.2020.103829.

[92] A. Kan, R. Demirboğa, A novel material for lightweight concrete production, Cem. Concr. Compos. 31 (2009) 489–495. https://doi.org/10.1016/j.cemconcomp.2009.05.002.

[93] Q.L. Yu, P. Spiesz, H.J.H. Brouwers, Development of cement-based lightweight composites - Part 1: Mix design methodology and hardened properties, Cem. Concr. Compos. 44 (2013) 17–29. https://doi.org/10.1016/j.cemconcomp.2013.03.030.

[94] P. Spiesz, Q.L. Yu, H.J.H. Brouwers, Development of cement-based lightweight composites - Part 2: Durability-related properties, Cem. Concr. Compos. 44 (2013) 30–40. https://doi.org/10.1016/j.cemconcomp.2013.03.029.

[95] T.Y. Lo, W.C. Tang, H.Z. Cui, The effects of aggregate properties on lightweight concrete, Build. Environ. 42 (2007) 3025–3029. https://doi.org/10.1016/j.buildenv.2005.06.031.

[96] F. Tajra, M.A. Elrahman, D. Stephan, The production and properties of cold-bonded aggregate and its applications in concrete: A review, Constr. Build. Mater. 225 (2019) 29–43. https://doi.org/10.1016/j.conbuildmat.2019.07.219.

[97] P. Tang, H.J.H. Brouwers, Integral recycling of municipal solid waste incineration (MSWI) bottom ash fines (0–2 mm) and industrial powder wastes by cold-bonding pelletization, Waste Manag. 62 (2017) 125–138. https://doi.org/10.1016/j.wasman.2017.02.028.

[98] P. Tang, H.J.H. Brouwers, The durability and environmental properties of self-compacting concrete incorporating cold bonded lightweight aggregates produced from combined industrial solid wastes, Constr. Build. Mater. 167 (2018) 271–285. https://doi.org/10.1016/j.conbuildmat.2018.02.035.

[99] P. Tang, D. Xuan, J. Li, H.W. Cheng, C.S. Poon, D.C.W. Tsang, Investigation of cold bonded lightweight aggregates produced with incineration sewage sludge ash (ISSA) and cementitious waste, J. Clean. Prod. 251 (2020) 119709. https://doi.org/10.1016/j.jclepro.2019.119709.

[100] H. Yıldırım, T. Özturan, Mechanical properties of lightweight concrete made with cold bonded fly ash pellets, 2nd Int. Balk. Conf. Challenges Civ. Eng. BCCCE, 23-25 May 2013, Epoka Univ. Tirana, Albania. (2013).

[101] M. Shi, T.C. Ling, B. Gan, M.Z. Guo, Turning concrete waste powder into carbonated artificial aggregates, Constr. Build. Mater. 199 (2019) 178–184. https://doi.org/10.1016/j.conbuildmat.2018.12.021.

[102] Y. Jiang, T.C. Ling, M. Shi, Strength enhancement of artificial aggregate prepared with waste concrete powder and its impact on concrete properties, J. Clean. Prod. 257 (2020) 120515. https://doi.org/10.1016/j.jclepro.2020.120515.

[103] E. Güneyisi, M. Gesoɨlu, I. Altan, H.Ö. Öz, Utilization of cold bonded fly ash lightweight fine aggregates as a partial substitution of natural fine aggregate in self-compacting mortars, Constr. Build. Mater. 74 (2015) 9–16. https://doi.org/10.1016/j.conbuildmat.2014.10.021.

[104] M. Gesoğlu, E. Güneyisi, H.Ö. Öz, Properties of lightweight aggregates produced with cold-bonding pelletization of fly ash and ground granulated blast furnace slag, Mater. Struct. Constr. 45 (2012) 1535–1546. https://doi.org/10.1617/s11527-012-9855-9.

[105] P. Tang, M.V.A. Florea, H.J.H. Brouwers, Employing cold bonded pelletization to produce lightweight aggregates from incineration fine bottom ash, J. Clean. Prod. 165 (2017) 1371–1384. https://doi.org/10.1016/j.jclepro.2017.07.234.

[106] S. Geetha, K. Ramamurthy, Properties of geopolymerised low-calcium bottom ash aggregate cured at ambient temperature, Cem. Concr. Compos. 43 (2013) 20–30. https://doi.org/10.1016/j.cemconcomp.2013.06.007.

[107] V. Vasugi, K. Ramamurthy, Identification of design parameters influencing manufacture and properties of cold-bonded pond ash aggregate, Mater. Des. 54 (2014) 264–278. https://doi.org/10.1016/j.matdes.2013.08.019.

[108] Y. Jiang, L. Li, J. Lu, P. Shen, T. Ling, C. Sun, Mechanism of carbonating recycled concrete fines in aqueous environment : The particle size effect, Cem. Concr. Compos. 133 (2022) 104655. https://doi.org/10.1016/j.cemconcomp.2022.104655.

[109] H. Mehdizadeh, X. Cheng, K.H. Mo, T.C. Ling, Upcycling of waste hydrated cement paste containing high-volume supplementary cementitious materials via CO2 pre-treatment, J. Build. Eng. 52 (2022) 104396. https://doi.org/10.1016/j.jobe.2022.104396.

[110] H. Mehdizadeh, T.C. Ling, X. Cheng, K.H. Mo, Effect of particle size and CO2 treatment of waste cement powder on properties of cement paste, Can. J. Civ. Eng. 48 (2021) 522–531. https://doi.org/10.1139/cjce-2019-0574.

[111] Y. Zhang, H. Chen, Q. Wang, Accelerated carbonation of regenerated cementitious materials from waste concrete for CO2 sequestration, J. Build. Eng. 55 (2022) 104701. https://doi.org/10.1016/j.jobe.2022.104701.

[112] R. V. Silva, R. Neves, J. De Brito, R.K. Dhir, Carbonation behaviour of recycled aggregate concrete, Cem. Concr. Compos. 62 (2015) 22–32. https://doi.org/10.1016/j.cemconcomp.2015.04.017.

[113] B.J. Zhan, D.X. Xuan, W. Zeng, C.S. Poon, Carbonation treatment of recycled concrete aggregate: Effect on transport properties and steel corrosion of recycled aggregate concrete, Cem. Concr. Compos. 104 (2019) 103360. https://doi.org/10.1016/j.cemconcomp.2019.103360.

[114] H. Zanni, M. Cheyrezy, V. Maret, S. Philippot, P. Nieto, Investigation of hydration and pozzolanic reaction in reactive powder concrete (RPC) using 29Si NMR, Cem. Concr. Res. 26 (1996) 93–100. https://doi.org/10.1016/0008-8846(95)00197-2.

[115] P. Tang, D. Xuan, C.S. Poon, D.C.W. Tsang, Valorization of concrete slurry waste (CSW) and fine incineration bottom ash (IBA) into cold bonded lightweight aggregates (CBLAs): Feasibility and influence of binder types, J. Hazard. Mater. 368 (2019) 689–697. https://doi.org/10.1016/j.jhazmat.2019.01.112.

[116] X. Zhu, C. Qian, B. He, Q. Chen, Z. Jiang, Experimental study on the stability of C-S-H nanostructures with varying bulk CaO / SiO 2 ratios under cryogenic attack, Cem. Concr. Res. 135 (2020) 106114. https://doi.org/10.1016/j.cemconres.2020.106114.

[117] X. Liu, P. Hou, H. Chen, Effects of nanosilica on the hydration and hardening properties of slag cement, Constr. Build. Mater. 282 (2021) 122705. https://doi.org/10.1016/j.conbuildmat.2021.122705.

[118] M. Zajac, J. Skibsted, J. Skocek, P. Durdzinski, F. Bullerjahn, M. Ben Haha, Phase assemblage and microstructure of cement paste subjected to enforced, wet carbonation, Cem. Concr. Res. 130 (2020) 105990. https://doi.org/10.1016/j.cemconres.2020.105990.

[119] B. Šavija, M. Luković, Carbonation of cement paste: Understanding, challenges, and opportunities, Constr. Build. Mater. 117 (2016) 285–301. https://doi.org/10.1016/j.conbuildmat.2016.04.138.

[120] C. Liang, B. Pan, Z. Ma, Z. He, Z. Duan, Utilization of CO2 curing to enhance the properties of recycled aggregate and prepared concrete: A review, Cem. Concr. Compos. 105 (2020) 103446. https://doi.org/10.1016/j.cemconcomp.2019.103446.

[121] K. Sisomphon, L. Franke, Carbonation rates of concretes containing high volume of pozzolanic materials, Cem. Concr. Res. 37 (2007) 1647–1653. https://doi.org/10.1016/j.cemconres.2007.08.014.

[122] B. Chen, M. Horgnies, B. Huet, V. Morin, K. Johannes, F. Kuznik, Comparative kinetics study on carbonation of ettringite and meta-ettringite based materials, Cem. Concr. Res. 137 (2020) 106209. https://doi.org/10.1016/j.cemconres.2020.106209.

[123] E. Güneyisi, M. Gesoğlu, Ö. Pürsünlü, K. Mermerdaş, Durability aspect of concretes composed of cold bonded and sintered fly ash lightweight aggregates, Compos. Part B Eng. 53 (2013) 258–266. https://doi.org/10.1016/j.compositesb.2013.04.070.

[124] M. Gesoğlu, E. Güneyisi, R. Alzeebaree, K. Mermerdaş, Effect of silica fume and steel fiber on the mechanical properties of the concretes produced with cold bonded fly ash aggregates, Constr. Build. Mater. 40 (2013) 982–990. https://doi.org/10.1016/j.conbuildmat.2012.11.074.

[125] G. Perumal, S. Anandan, Performance evaluation of alkali activated fly ash lightweight aggregates, Eng. J. 18 (2014) 77–85. https://doi.org/10.4186/ej.2014.18.1.77.

[126] I. Hager, T. Tracz, M. Choińska, K. Mróz, Effect of cement type on the mechanical behavior and permeability of concrete subjected to high temperatures, Materials (Basel). 12 (2019). https://doi.org/10.3390/ma12183021.

[127] P.H.R. Borges, J.O. Costa, N.B. Milestone, C.J. Lynsdale, R.E. Streatfield, Carbonation of CH and C-S-H in composite cement pastes containing high amounts of BFS, Cem. Concr. Res. 40 (2010) 284–292. https://doi.org/10.1016/j.cemconres.2009.10.020.

[128] I. Pajares, S. Martínez-Ramírez, M.T. Blanco-Varela, Evolution of ettringite in presence of carbonate, and silicate ions, Cem. Concr. Compos. 25 (2003) 861–865. https://doi.org/10.1016/S0958-9465(03)00113-6.

[129] J. Yang, H. Hu, X. He, Y. Su, Y. Wang, H. Tan, H. Pan, Effect of steam curing on compressive strength and microstructure of high volume ultrafine fly ash cement mortar, Constr. Build. Mater. 266 (2021) 120894. https://doi.org/10.1016/j.conbuildmat.2020.120894.

[130] A. Morandeau, M. Thiéry, P. Dangla, Investigation of the carbonation mechanism of CH and C-S-H in terms of kinetics, microstructure changes and moisture properties, Cem. Concr. Res. 56 (2014) 153–170. https://doi.org/10.1016/j.cemconres.2013.11.015.

[131] J. Skocek, M. Zajac, M. Ben Haha, Carbon Capture and Utilization by mineralization of cement pastes derived from recycled concrete, Sci. Rep. 10 (2020) 1–12. https://doi.org/10.1038/s41598-020-62503-z.

[132] V. Shah, K. Scrivener, B. Bhattacharjee, S. Bishnoi, Changes in microstructure characteristics of cement paste on carbonation, Cem. Concr. Res. 109 (2018) 184–197. https://doi.org/10.1016/j.cemconres.2018.04.016.

[133] K. Ndiaye, M. Cyr, S. Ginestet, Durability and stability of an ettringite-based material for thermal energy storage at low temperature, Cem. Concr. Res. 99 (2017) 106–115. https://doi.org/10.1016/j.cemconres.2017.05.001.

[134] K. McNeil, T. Kang, International Journal of Concrete Structures and Materials, Int. J. Concr. Struct. Mater. 7 (2013) 119–125.

[135] S.C.B. Myneni, S.J. Traina, G.A. Waychunas, T.J. Logan, Vibrational spectroscopy of functional group chemistry and arsenate coordination in ettringite, Geochim. Cosmochim. Acta. 62 (1998) 3499–3514. https://doi.org/10.1016/s0016-7037(98)00221-x.

[136] L. Qin, X. Gao, T. Chen, Influence of mineral admixtures on carbonation curing of cement paste, Constr. Build. Mater. 212 (2019) 653–662. https://doi.org/10.1016/j.conbuildmat.2019.04.033.

[137] B.J. Zhan, D.X. Xuan, C.S. Poon, C.J. Shi, S.C. Kou, Characterization of C–S–H formed in coupled CO2–water cured Portland cement pastes, Mater. Struct. Constr. 51 (2018) 1–15. https://doi.org/10.1617/s11527-018-1211-2.

[138] N. Li, N. Farzadnia, C. Shi, Microstructural changes in alkali-activated slag mortars induced by accelerated carbonation, Cem. Concr. Res. 100 (2017) 214–226.

https://doi.org/10.1016/j.cemconres.2017.07.008.

[139] I. García Lodeiro, D.E. Macphee, A. Palomo, A. Fernández-Jiménez, Effect of alkalis on fresh C-S-H gels. FTIR analysis, Cem. Concr. Res. 39 (2009) 147–153. https://doi.org/10.1016/j.cemconres.2009.01.003.

[140] J.J. Thomas, J. Hsieh, H.M. Jennings, Effect of carbonation on the nitrogen BET surface area of hardened Portland cement paste, Adv. Cem. Based Mater. 3 (1996) 76–80. https://doi.org/10.1016/S1065-7355(96)90074-7.

[141] B. Johannesson, P. Utgenannt, Microstructural changes caused by carbonation of cement mortar, Cem. Concr. Res. 31 (2001) 925–931. https://doi.org/10.1016/S0008-8846(01)00498-7.

[142] M. Oltulu, R. Şahin, Pore structure analysis of hardened cement mortars containing silica fume and different nano-powders, Constr. Build. Mater. 53 (2014) 658–664. https://doi.org/10.1016/j.conbuildmat.2013.11.105.

[143] J.M. Chi, R. Huang, C.C. Yang, Effects of carbonation on mechanical properties and durability of concrete using accelerated testing method, J. Mar. Sci. Technol. 10 (2002) 14–20.

[144] J.J. Chen, J.J. Thomas, H.M. Jennings, Decalcification shrinkage of cement paste, Cem. Concr. Res. 36 (2006) 801–809. https://doi.org/10.1016/j.cemconres.2005.11.003.

[145] Y. Jiang, T.C. Ling, Production of artificial aggregates from steel-making slag: Influences of accelerated carbonation during granulation and/or post-curing, J. CO2 Util. 36 (2020) 135–144. https://doi.org/10.1016/j.jcou.2019.11.009.

[146] A. Neves Junior, R.D.T. Filho, E.D.M.R. Fairbairn, J. Dweck, A study of the carbonation profile of cement pastes by thermogravimetry and its effect on the compressive strength, J. Therm. Anal. Calorim. 116 (2014) 69–76. https://doi.org/10.1007/s10973-013-3556-7.

[147] M. Zajac, J. Skocek, P. Durdzinski, F. Bullerjahn, J. Skibsted, M. Ben Haha, Effect of carbonated cement paste on composite cement hydration and performance, Cem. Concr. Res. 134 (2020) 106090. https://doi.org/10.1016/J.CEMCONRES.2020.106090.

[148] X. Ouyang, L. Wang, S. Xu, Y. Ma, G. Ye, Surface characterization of carbonated recycled concrete fines and its effect on the rheology, hydration and strength development of cement paste, Cem. Concr. Compos. 114 (2020) 103809. https://doi.org/10.1016/J.CEMCONCOMP.2020.103809.

[149] P. Shen, Y. Sun, S. Liu, Y. Jiang, H. Zheng, D. Xuan, J. Lu, C.S. Poon, Synthesis of amorphous nano-silica from recycled concrete fines by two-step wet carbonation, Cem. Concr. Res. 147 (2021) 106526. https://doi.org/10.1016/j.cemconres.2021.106526.

[150] M. Zajac, J. Skibsted, P. Durdzinski, F. Bullerjahn, J. Skocek, M. Ben Haha, Kinetics of enforced carbonation of cement paste, Cem. Concr. Res. 131 (2020) 106013. https://doi.org/10.1016/J.CEMCONRES.2020.106013.

[151] M. Zajac, J. Skibsted, F. Bullerjahn, J. Skocek, Semi-dry carbonation of recycled concrete paste, J. CO2 Util. 63 (2022) 102111. https://doi.org/10.1016/J.JCOU.2022.102111.

[152] C.B. Cheah, L.L. Tiong, E.P. Ng, C.W. Oo, The engineering performance of concrete containing high volume of ground granulated blast furnace slag and pulverized fly ash with polycarboxylate-based superplasticizer, Constr. Build. Mater. 202 (2019) 909–921. https://doi.org/10.1016/J.CONBUILDMAT.2019.01.075.

[153] R. Bucher, P. Diederich, G. Escadeillas, M. Cyr, Service life of metakaolin-based concrete exposed to carbonation: Comparison with blended cement containing fly ash, blast furnace slag and limestone filler, Cem. Concr. Res. 99 (2017) 18–29. https://doi.org/10.1016/J.CEMCONRES.2017.04.013.

[154] S. von Greve-Dierfeld, B. Lothenbach, A. Vollpracht, B. Wu, B. Huet, C. Andrade, C. Medina, C. Thiel, E. Gruyaert, H. Vanoutrive, I.F. Saéz del Bosque, I. Ignjatovic, J. Elsen, J.L. Provis, K. Scrivener, K.C. Thienel, K. Sideris, M. Zajac, N. Alderete, Ö. Cizer, P. Van den Heede, R.D. Hooton, S. Kamali-Bernard, S.A. Bernal, Z. Zhao, Z. Shi, N. De Belie, Understanding the carbonation of concrete with supplementary cementitious materials: a critical review by RILEM TC 281-CCC, Mater. Struct. Constr. 53 (2020). https://doi.org/10.1617/s11527-020-01558-w.

[155] X. Liu, P. Feng, Y. Cai, X. Yu, C. Yu, Q. Ran, Carbonation behavior of calcium silicate hydrate (C-S-H): Its potential for CO2 capture, Chem. Eng. J. 431 (2022) 134243. https://doi.org/10.1016/J.CEJ.2021.134243.

[156] Y. Guo, Y. Li, F. Cheng, M. Wang, X. Wang, Role of additives in improved thermal activation of coal fly ash for alumina extraction, Fuel Process. Technol. 110 (2013) 114–121. https://doi.org/10.1016/J.FUPROC.2012.12.003.

[157] B.L. Damineli, F.M. Kemeid, P.S. Aguiar, V.M. John, Measuring the eco-efficiency of cement use, Cem. Concr. Compos. 32 (2010) 555–562. https://doi.org/10.1016/j.cemconcomp.2010.07.009.

[158] S. Monkman, Y. Shao, Integration of carbon sequestration into curing process of precast concrete, Can. J. Civ. Eng. 37 (2010) 302–310. https://doi.org/10.1139/L09-140.

[159] M.F. Alnahhal, U.J. Alengaram, M.Z. Jumaat, F. Abutaha, M.A. Alqedra, R.R. Nayaka, Assessment on engineering properties and CO2 emissions of recycled aggregate concrete incorporating waste products as supplements to Portland cement, J. Clean. Prod. 203 (2018) 822–835. https://doi.org/10.1016/j.jclepro.2018.08.292.

[160] E.T. Bueno, J.M. Paris, K.A. Clavier, C. Spreadbury, C.C. Ferraro, T.G. Townsend, A review of ground waste glass as a supplementary cementitious material: A focus on alkali-silica reaction, J. Clean. Prod. 257 (2020) 120180. https://doi.org/10.1016/J.JCLEPRO.2020.120180.

[161] R. Chang, S. Kim, S. Lee, S. Choi, M. Kim, Y. Park, Calcium carbonate precipitation for CO 2 storage and utilization: A review of the carbonate crystallization and polymorphism, Front. Energy Res. 5 (2017) 1–12. https://doi.org/10.3389/fenrg.2017.00017.

[162] N. V. Vagenas, A. Gatsouli, C.G. Kontoyannis, Quantitative analysis of synthetic calcium carbonate polymorphs using FT-IR spectroscopy, Talanta. 59 (2003) 831–836. https://doi.org/10.1016/S0039-9140(02)00638-0.

[163] Z. Tu, M.Z. Guo, C.S. Poon, C. Shi, Effects of limestone powder on CaCO3 precipitation in CO2 cured cement pastes, Cem. Concr. Compos. 72 (2016) 9–16. https://doi.org/10.1016/J.CEMCONCOMP.2016.05.019.

[164] G. Liu, K. Schollbach, S.R. van der Laan, P. Tang, M.V.A. Florea, H.J.H. Brouwers, Recycling and utilization of high volume converter steel slag into CO2 activated mortars – The role of slag particle size, Resour. Conserv. Recycl. 160 (2020) 104883. https://doi.org/10.1016/j.resconrec.2020.104883.

[165] F. Puertas, M. Torres-Carrasco, Use of glass waste as an activator in the preparation of alkali-activated slag. Mechanical strength and paste characterisation, Cem. Concr. Res. 57 (2014) 95–104. https://doi.org/10.1016/j.cemconres.2013.12.005.

[166] R. Baciocchi, G. Costa, A. Polettini, R. Pomi, Effects of thin-film accelerated carbonation on steel slag leaching, J. Hazard. Mater. 286 (2015) 369–378. https://doi.org/10.1016/j.jhazmat.2014.12.059.

[167] K.L. Scrivener, B. Lothenbach, N. De Belie, E. Gruyaert, J. Skibsted, R. Snellings, A. Vollpracht, TC 238-SCM: hydration and microstructure of concrete with SCMs, Mater. Struct. 2015 484.

48 (2015) 835–862. https://doi.org/10.1617/S11527-015-0527-4.

[168] J. Skibsted, R. Snellings, Reactivity of supplementary cementitious materials (SCMs) in cement blends, Cem. Concr. Res. 124 (2019) 105799. https://doi.org/10.1016/J.CEMCONRES.2019.105799.

[169] G. Le Saoût, V. Kocaba, K. Scrivener, Application of the Rietveld method to the analysis of anhydrous cement, Cem. Concr. Res. 41 (2011) 133–148. https://doi.org/10.1016/J.CEMCONRES.2010.10.003.

[170] B. Lothenbach, G. Le Saout, E. Gallucci, K. Scrivener, Influence of limestone on the hydration of Portland cements, Cem. Concr. Res. 38 (2008) 848–860. https://doi.org/10.1016/j.cemconres.2008.01.002.

[171] K. Scrivener, F. Martirena, S. Bishnoi, S. Maity, Calcined clay limestone cements (LC3), Cem. Concr. Res. 114 (2018) 49–56. https://doi.org/10.1016/J.CEMCONRES.2017.08.017.

[172] J. Tang, S. Wei, W. Li, S. Ma, P. Ji, X. Shen, Synergistic effect of metakaolin and limestone on the hydration properties of Portland cement, Constr. Build. Mater. 223 (2019) 177–184. https://doi.org/10.1016/J.CONBUILDMAT.2019.06.059.

[173] F. Zunino, K. Scrivener, The reaction between metakaolin and limestone and its effect in porosity refinement and mechanical properties, Cem. Concr. Res. 140 (2021) 106307. https://doi.org/10.1016/j.cemconres.2020.106307.

[174] F. Moghaddam, V. Sirivivatnanon, K. Vessalas, The effect of fly ash fineness on heat of hydration, microstructure, flow and compressive strength of blended cement pastes, Case Stud. Constr. Mater. 10 (2019) e00218. https://doi.org/10.1016/J.CSCM.2019.E00218.

[175] F. Zunino, K. Scrivener, The influence of the filler effect on the sulfate requirement of blended cements, Cem. Concr. Res. 126 (2019) 105918. https://doi.org/10.1016/J.CEMCONRES.2019.105918.

[176] P. Ren, B. Li, J.-G. Yu, T.-C. Ling, Utilization of recycled concrete fines and powders to produce alkali-activated slag concrete blocks, J. Clean. Prod. 267 (2020) 122115. https://doi.org/10.1016/J.JCLEPRO.2020.122115.

[177] M. Mejdi, W. Wilson, M. Saillio, T. Chaussadent, L. Divet, A. Tagnit-Hamou, Hydration and microstructure of glass powder cement pastes – A multi-technique investigation, Cem. Concr. Res. 151 (2022) 106610. https://doi.org/10.1016/J.CEMCONRES.2021.106610.

[178] M. Mejdi, W. Wilson, M. Saillio, T. Chaussadent, L. Divet, A. Tagnit-Hamou, Quantifying glass powder reaction in blended-cement pastes with the Rietveld-PONKCS method, Cem. Concr. Res. 130 (2020) 105999. https://doi.org/10.1016/J.CEMCONRES.2020.105999.

[179] X. Liu, P. Feng, Y. Cai, X. Yu, Q. Liu, Carbonation behaviors of calcium silicate hydrate (C-S-H): Effects of aluminum, Constr. Build. Mater. 325 (2022) 126825. https://doi.org/10.1016/J.CONBUILDMAT.2022.126825.

[180] S. Steiner, B. Lothenbach, T. Proske, A. Borgschulte, F. Winnefeld, Effect of relative humidity on the carbonation rate of portlandite, calcium silicate hydrates and ettringite, Cem. Concr. Res. 135 (2020) 106116. https://doi.org/10.1016/j.cemconres.2020.106116.

[181] G. Liu, M.V.A. Florea, H.J.H. Brouwers, The role of recycled waste glass incorporation on the carbonation behaviour of sodium carbonate activated slag mortar, J. Clean. Prod. 292 (2021) 126050. https://doi.org/10.1016/J.JCLEPRO.2021.126050.

[182] A. Schöler, B. Lothenbach, F. Winnefeld, M. Zajac, Hydration of quaternary Portland cement blends containing blast-furnace slag, siliceous fly ash and limestone powder, Cem. Concr. Compos. 55 (2015) 374–382. https://doi.org/10.1016/j.cemconcomp.2014.10.001.

[183] A. Mistri, S.K. Bhattacharyya, N. Dhami, A. Mukherjee, S. V. Barai, A review on different

treatment methods for enhancing the properties of recycled aggregates for sustainable construction materials, Constr. Build. Mater. 233 (2020) 117894. https://doi.org/10.1016/J.CONBUILDMAT.2019.117894.

[184] J.A. Bogas, A. Carriço, M.F.C. Pereira, Mechanical characterization of thermal activated low-carbon recycled cement mortars, J. Clean. Prod. 218 (2019) 377–389. https://doi.org/10.1016/J.JCLEPRO.2019.01.325.

[185] C. Shi, Z. Wu, Z. Cao, T.C. Ling, J. Zheng, Performance of mortar prepared with recycled concrete aggregate enhanced by CO2 and pozzolan slurry, Cem. Concr. Compos. 86 (2018) 130–138. https://doi.org/10.1016/J.CEMCONCOMP.2017.10.013.

[186] E. Belhadj, C. Diliberto, A. Lecomte, Characterization and activation of Basic Oxygen Furnace slag, Cem. Concr. Compos. 34 (2012) 34–40. https://doi.org/10.1016/j.cemconcomp.2011.08.012.

[187] M.J. Ahmed, K. Lambrechts, X. Ling, K. Schollbach, H.J.H. Brouwers, Effect of hydroxide, carbonate, and sulphate anions on the β-dicalcium silicate hydration rate, Cem. Concr. Res. 173 (2023). https://doi.org/10.1016/j.cemconres.2023.107302.

[188] M.J. Sánchez-Herrero, A. Fernández-Jiménez, A. Palomo, C3S and C2S hydration in the presence of Na2CO3 and Na2SO4, J. Am. Ceram. Soc. 100 (2017) 3188–3198. https://doi.org/10.1111/jace.14855.

[189] M.J. Sánchez-Herrero, A. Fernández-Jiménez, Á. Palomo, L. Klein, Alkaline Hydration of C2S and C3S, J. Am. Ceram. Soc. 99 (2016) 604–611. https://doi.org/10.1111/jace.13985.

[190] A. Cuesta, I. Santacruz, S.G. Sanfélix, F. Fauth, M.A.G. Aranda, A.G. De La Torre, Hydration of C4AF in the presence of other phases: A synchrotron X-ray powder diffraction study, Constr. Build. Mater. 101 (2015) 818–827. https://doi.org/10.1016/j.conbuildmat.2015.10.114.

[191] M. Collepardi, S. Monosi, G. Moriconi, M. Corradi, Combined effect of lignosulfonate and carbonate on pure portland clinker compounds hydration. I. Tetracalcium aluminoferrite hydration, Cem. Concr. Res. 10 (1980) 455–462. https://doi.org/10.1016/0008-8846(80)90122-2.

[192] Q. Wang, J.W. Yang, P.Y. Yan, Influence of initial alkalinity on the hydration of steel slag, Sci. China Technol. Sci. 55 (2012) 3378–3387. https://doi.org/10.1007/s11431-012-4830-9.

[193] J. Wang, L. Chang, D. Yue, Y. Zhou, H. Liu, Y. Wang, S. Yang, S. Cui, Effect of chelating solubilization via different alkanolamines on the dissolution properties of steel slag, J. Clean. Prod. 365 (2022) 132824. https://doi.org/10.1016/j.jclepro.2022.132824.

[194] C. Cárdenas, P. Mácová, M. Gómez, L. Zárybnická, R. Ševčík, A. Viani, Formation, Properties, and Microstructure of a New Steel Slag–Based Phosphate Cement, J. Mater. Civ. Eng. 33 (2021) 04021330. https://doi.org/10.1061/(asce)mt.1943-5533.0003958.

[195] C.A. Cárdenas Balaguera, M.A. Gómez Botero, Characterization of steel slag for the production of chemically bonded phosphate ceramics (CBPC), Constr. Build. Mater. 241 (2020). https://doi.org/10.1016/j.conbuildmat.2020.118138.

[196] Y. Ma, Y. Luo, H. Ma, X. Zhou, Z. Luo, Upcycling steel slag in producing eco-efficient iron–calcium phosphate cement, J. Clean. Prod. 371 (2022) 133688. https://doi.org/10.1016/j.jclepro.2022.133688.

[197] Y. Tang, METHOD FOR ACTIVATING BASIC OXYGEN FURNACE STEEL SLAG, WO 2024/052265 A1, 2024.

[198] K. Schollbach, S.R. van der Laan, Microstructure analysis with quantitative phase mapping using SEM-EDS and Phase Recognition and Characterization (PARC) Software: Applied to steelmaking slag, 2022. https://doi.org/10.1515/9783110674941-003.

[199] B.Z. Dilnesa, B. Lothenbach, G. Renaudin, A. Wichser, D. Kulik, Synthesis and characterization of hydrogarnet Ca3(Al xFe1 - X)2(SiO4)y(OH) 4(3 - y), Cem. Concr. Res. 59 (2014) 96–111. https://doi.org/10.1016/j.cemconres.2014.02.001.

[200] European Committee for Standardizaiton, EN 12457-1, Characterisation of Waste. Leaching. Compliance Test for Leaching of Granular Waste Materials and Sludges, (2014).

[201] Soil Quality Decree, (2015). https://wetten.overheid.nl/BWBR0023085/2015-07-01#BijlageA.

[202] T. Zhang, B. Ma, H. Tan, H. Qi, T. Shi, Effect of sodium carbonate and sodium phosphate on hydration of cement paste, J. Build. Eng. 45 (2022) 103577. https://doi.org/10.1016/j.jobe.2021.103577.

[203] B.Z. Dilnesa, E. Wieland, B. Lothenbach, R. Dähn, K.L. Scrivener, Fe-containing phases in hydrated cements, Cem. Concr. Res. 58 (2014) 45–55. https://doi.org/10.1016/j.cemconres.2013.12.012.

[204] S.V. Dorozhkin, Calcium orthophosphates (CaPO 4): Occurrence and properties, Morphologie. 101 (2017) 125–142. https://doi.org/10.1016/j.morpho.2017.03.007.

[205] J. Vecstaudza, M. Gasik, J. Locs, Amorphous calcium phosphate materials: Formation, structure and thermal behaviour, J. Eur. Ceram. Soc. 39 (2019) 1642–1649. https://doi.org/10.1016/j.jeurceramsoc.2018.11.003.

[206] I.A. Karampas, C.G. Kontoyannis, Characterization of calcium phosphates mixtures, Vib. Spectrosc. 64 (2013) 126–133. https://doi.org/10.1016/j.vibspec.2012.11.003.

[207] Y. Liu, B. Chen, Z. Qin, D. Pen, M. Aminul Haque, Experimental research on properties and microstructures of magnesium-iron phosphate cement, Constr. Build. Mater. 257 (2020) 119570. https://doi.org/10.1016/j.conbuildmat.2020.119570.

[208] E. Sassoni, E. Franzoni, Lime and cement mortar consolidation by ammonium phosphate, Constr. Build. Mater. 245 (2020) 118409. https://doi.org/10.1016/j.conbuildmat.2020.118409.

[209] M.A. Haque, B. Chen, Research progresses on magnesium phosphate cement: A review, Constr. Build. Mater. 211 (2019) 885–898. https://doi.org/10.1016/j.conbuildmat.2019.03.304.

[210] T. Wang, A. Dorner-Reisel, E. Müller, Thermogravimetric and thermokinetic investigation of the dehydroxylation of a hydroxyapatite powder, J. Eur. Ceram. Soc. 24 (2004) 693–698. https://doi.org/10.1016/S0955-2219(03)00248-6.

[211] M. Tonsuaadu, K., Gross, K. A., Plūduma, L., Veiderma, A review on the thermal stability of calcium apatites, J. Therm. Anal. Calorim. 110 (2012) 647–956.

[212] A.M. Kaja, A. Delsing, S.R. van der Laan, H.J.H. Brouwers, Q. Yu, Effects of carbonation on the retention of heavy metals in chemically activated BOF slag pastes, Cem. Concr. Res. 148 (2021) 106534. https://doi.org/10.1016/j.cemconres.2021.106534.

[213] T. Kubota, A. Nakamura, K. Toyoura, K. Matsunaga, The effect of chemical potential on the thermodynamic stability of carbonate ions in hydroxyapatite, Acta Biomater. 10 (2014) 3716–3722. https://doi.org/10.1016/j.actbio.2014.05.007.

[214] S.P. Parthiban, I.Y. Kim, K. Kikuta, C. Ohtsuki, Effect of ammonium carbonate on formation of calcium-deficient hydroxyapatite through double-step hydrothermal processing, J. Mater. Sci. Mater. Med. 22 (2011) 209–216. https://doi.org/10.1007/s10856-010-4201-7.

[215] K. Rozov, U. Berner, C. Taviot-Gueho, F. Leroux, G. Renaudin, D. Kulik, L.W. Diamond, Synthesis and characterization of the LDH hydrotalcite-pyroaurite solid-solution series, Cem. Concr. Res. 40 (2010) 1248–1254.

https://doi.org/10.1016/j.cemconres.2009.08.031.

[216] Z. Zhang, Y. Zhu, H. Zhu, Y. Zhang, J.L. Provis, H. Wang, Effect of drying procedures on pore structure and phase evolution of alkali-activated cements, Cem. Concr. Compos. 96 (2019) 194–203. https://doi.org/10.1016/j.cemconcomp.2018.12.003.

[217] Y. Tang, G. Liu, K. Schollbach, Y. Chen, W. Chen, H.J.H. Brouwers, Re-cementation effects by carbonation and the pozzolanic reaction on LWAs produced by hydrated cement paste powder, J. Clean. Prod. 377 (2022) 134529. https://doi.org/10.1016/j.jclepro.2022.134529.

[218] X. Liu, P. Feng, X. Yu, X. Shen, G. Geng, B. Lothenbach, The physiochemical alterations of calcium silicate hydrate (C-S-H) under magnesium attack, Cem. Concr. Res. 160 (2022) 106901. https://doi.org/10.1016/j.cemconres.2022.106901.

[219] P. Bénard, S. Garrault, A. Nonat, C. Cau-Dit-Coumes, Hydration process and rheological properties of cement pastes modified by orthophosphate addition, J. Eur. Ceram. Soc. 25 (2005) 1877–1883. https://doi.org/10.1016/j.jeurceramsoc.2004.06.017.

[220] R. Kumar, B. Bhattacharjee, Porosity, pore size distribution and in situ strength of concrete, Cem. Concr. Res. 33 (2003) 155–164. https://doi.org/10.1016/S0008-8846(02)00942-0.

[221] C.H. Yoder, M.D. Havlusch, R.N. Dudrick, J.T. Schermerhorn, L.K. Tran, A.C. Deymier, The synthesis of phosphate and vanadate apatites using an aqueous one-step method, Polyhedron. 127 (2017) 403–409. https://doi.org/10.1016/j.poly.2016.10.007.

[222] C.B. Boechat, J.G. Eon, A.M. Rossi, C.A. De Castro Perez, R.A. Da Silva San Gil, Structure of vanadate in calcium phosphate and vanadate apatite solid solutions, Phys. Chem. Chem. Phys. 2 (2000) 4225–4230. https://doi.org/10.1039/b004339g.

[223] S. Campisi, C. Evangelisti, G. Postole, A. Gervasini, Combination of interfacial reduction of hexavalent chromium and trivalent chromium immobilization on tin-functionalized hydroxyapatite materials, Appl. Surf. Sci. 539 (2021) 148227. https://doi.org/10.1016/j.apsusc.2020.148227.

[224] S. Hokkanen, A. Bhatnagar, E. Repo, S. Lou, M. Sillanpää, Calcium hydroxyapatite microfibrillated cellulose composite as a potential adsorbent for the removal of Cr(VI) from aqueous solution, Chem. Eng. J. 283 (2016) 445–452. https://doi.org/10.1016/j.cej.2015.07.035.

[225] J. Siramanont, B.J. Walder, L. Emsley, P. Bowen, Iron incorporation in synthetic precipitated calcium silicate hydrates, Cem. Concr. Res. 142 (2021) 106365. https://doi.org/10.1016/j.cemconres.2021.106365.

[226] C. Roosz, P. Vieillard, P. Blanc, S. Gaboreau, H. Gailhanou, D. Braithwaite, V. Montouillout, R. Denoyel, P. Henocq, B. Madé, Thermodynamic properties of C-S-H, C-A-S-H and M-S-H phases: Results from direct measurements and predictive modelling, Appl. Geochemistry. 92 (2018) 140–156. https://doi.org/10.1016/j.apgeochem.2018.03.004.

[227] B. Xu, F. Winnefeld, B. Lothenbach, Effect of temperature curing on properties and hydration of wollastonite blended magnesium potassium phosphate cements, Cem. Concr. Res. 142 (2021) 106370. https://doi.org/10.1016/j.cemconres.2021.106370.

[228] B. Xu, B. Lothenbach, F. Winnefeld, Influence of wollastonite on hydration and properties of magnesium potassium phosphate cements, Cem. Concr. Res. 131 (2020) 106012. https://doi.org/10.1016/j.cemconres.2020.106012.

[229] C.E. Boyd, Water Quality, in: Springer, 2019: pp. 291–309.

[230] V. Shah, S. Bishnoi, Carbonation resistance of cements containing supplementary cementitious materials and its relation to various parameters of concrete, Constr. Build.

Mater. 178 (2018) 219–232. https://doi.org/10.1016/j.conbuildmat.2018.05.162.

[231] Q. Pu, L. Jiang, J. Xu, H. Chu, Y. Xu, Y. Zhang, Evolution of pH and chemical composition of pore solution in carbonated concrete, Constr. Build. Mater. 28 (2012) 519–524. https://doi.org/10.1016/j.conbuildmat.2011.09.006.

[232] G. Lamaa, A.P.C. Duarte, R.V. Silva, J. de Brito, Carbonation of Alkali-Activated Materials: A Review, Materials (Basel). 16 (2023). https://doi.org/10.3390/ma16083086.

[233] N. Li, N. Farzadnia, C. Shi, Microstructural changes in alkali-activated slag mortars induced by accelerated carbonation, Cem. Concr. Res. 100 (2017) 214–226. https://doi.org/10.1016/j.cemconres.2017.07.008.

[234] J.F.P. Gomes, C.G. Pinto, Leaching of heavy metals from steelmaking slags, Rev. Metal. 42 (2006) 409–416.

[235] P. Chaurand, J. Rose, V. Briois, L. Olivi, J.L. Hazemann, O. Proux, J. Domas, J.Y. Bottero, Environmental impacts of steel slag reused in road construction: A crystallographic and molecular (XANES) approach, J. Hazard. Mater. 139 (2007) 537–542. https://doi.org/10.1016/j.jhazmat.2006.02.060.

[236] A. van Zomeren, S.R. van der Laan, H.B.A. Kobesen, W.J.J. Huijgen, R.N.J. Comans, Changes in mineralogical and leaching properties of converter steel slag resulting from accelerated carbonation at low CO 2 pressure, Waste Manag. 31 (2011) 2236–2244. https://doi.org/10.1016/j.wasman.2011.05.022.

[237] G. Costa, A. Polettini, R. Pomi, A. Stramazzo, Leaching modelling of slurry-phase carbonated steel slag, J. Hazard. Mater. 302 (2016) 415–425. https://doi.org/10.1016/j.jhazmat.2015.10.005.

[238] Y. Tang, K. Schollbach, S.R. van der Laan, W. Chen, H.J.H. Brouwers, A novel BOF slag binder based on monopotassium phosphate activation (submitted), (n.d.).

[239] T. Manninger, D. Jansen, J. Neubauer, F. Goetz-Neunhoeffer, The retarding effect of phosphoric acid during CAC hydration, Cem. Concr. Res. 122 (2019) 83–92. https://doi.org/10.1016/j.cemconres.2019.04.020.

[240] Q. Zhao, X. He, J. Zhang, J. Jiang, Long-age wet curing effect on performance of carbonation resistance of fly ash concrete, Constr. Build. Mater. 127 (2016) 577–587. https://doi.org/10.1016/j.conbuildmat.2016.10.065.

[241] P. Gaikwad, S. Sathe, Effect of fly ash on compressive strength, carbonation and corrosion resistance of reinforced concrete: a systematic review, World J. Eng. (2023). https://doi.org/10.1108/WJE-07-2023-0240.

[242] Y. Tang, K. Schollbach, H.J.H. Brouwers, W. Chen, Effects of soluble magnesium on the structure of calcium silicate hydrate, Constr. Build. Mater. 302 (2021) 124402. https://doi.org/10.1016/j.conbuildmat.2021.124402.

[243] G.R. Qian, D.D. Sun, J.H. Tay, Z.Y. Lai, Hydrothermal reaction and autoclave stability of Mg bearing RO phase in steel slag, Br. Ceram. Trans. 101 (2002) 159–164. https://doi.org/10.1179/096797802225003415.

[244] L. De Windt, P. Chaurand, J. Rose, Kinetics of steel slag leaching: Batch tests and modeling, Waste Manag. 31 (2011) 225–235. https://doi.org/10.1016/j.wasman.2010.05.018.

[245] A.N. Ay, B. Zümreoglu-Karan, A. Temel, L. Mafra, Layered double hydroxides with interlayer borate anions: A critical evaluation of synthesis methodology and pH-independent orientations in nano-galleries, Appl. Clay Sci. 51 (2011) 308–316. https://doi.org/10.1016/j.clay.2010.12.015.

[246] L. Cheng, Y. Chen, T. Liu, H.J.H. Brouwers, Q. Yu, Understanding the CaCO3 phase transition

of carbonated wollastonite composites caused by sodium tripolyphosphate: From amorphous to crystalline, Cem. Concr. Compos. 148 (2024) 105477. https://doi.org/10.1016/j.cemconcomp.2024.105477.

[247] I. Odler, M. Rößler, Investigations on the relationship between porosity, structure and strength of hydrated Portland cement pastes. II. Effect of pore structure and of degree of hydration, Cem. Concr. Res. 15 (1985) 401–410. https://doi.org/10.1016/0008-8846(85)90113-9.

[248] M. Spanka, T. Mansfeldt, R. Bialucha, Sequential extraction of chromium, molybdenum, and vanadium in basic oxygen furnace slags, Environ. Sci. Pollut. Res. 25 (2018) 23082–23090. https://doi.org/10.1007/s11356-018-2361-z.

[249] A. Vollpracht, W. Brameshuber, Binding and leaching of trace elements in Portland cement pastes, Cem. Concr. Res. 79 (2016) 76–92. https://doi.org/10.1016/j.cemconres.2015.08.002.

[250] L. Urbonas, V. Leno, D. Heinz, Effect of carbonation in supercritical CO2 on the properties of hardened cement paste of different alkalinity, Constr. Build. Mater. 123 (2016) 704–711. https://doi.org/10.1016/j.conbuildmat.2016.07.040.

[251] Z. Liu, C. Lv, F. Wang, S. Hu, Research Recent advances in carbonatable binders, Cem. Concr. Res. 173 (2023) 107286. https://doi.org/10.1016/j.cemconres.2023.107286.

[252] P. Liu, L. Mo, Z. Zhang, Effects of carbonation degree on the hydration reactivity of steel slag in cement-based materials, Constr. Build. Mater. 370 (2023) 130653. https://doi.org/10.1016/j.conbuildmat.2023.130653.

[253] Q. Zhang, P. Feng, X. Shen, J. Lu, S. Ye, H. Wang, T.C. Ling, Q. Ran, Utilization of solid wastes to sequestrate carbon dioxide in cement-based materials and methods to improve carbonation degree: A review, J. CO2 Util. 72 (2023) 102502. https://doi.org/10.1016/j.jcou.2023.102502.

[254] A. Baras, J. Li, W. Ni, Z. Hussain, M. Hitch, Evaluation of Potential Factors Affecting Steel Slag Carbonation, Processes. 11 (2023). https://doi.org/10.3390/pr11092590.

[255] K.L. Scrivener, T. Füllmann, E. Gallucci, G. Walenta, E. Bermejo, Quantitative study of Portland cement hydration by X-ray diffraction/Rietveld analysis and independent methods, Cem. Concr. Res. 34 (2004) 1541–1547. https://doi.org/10.1016/j.cemconres.2004.04.014.

[256] M. Nedeljković, B. Ghiassi, S.R. van der Laan, Z. Li, G. Ye, Effect of curing conditions on the pore solution and carbonation resistance of alkali-activated fly ash and slag pastes, Cem. Concr. Res. 116 (2019) 146–158. https://doi.org/10.1016/j.cemconres.2018.11.011.

[257] P. Azar, C. Patapy, G. Samson, F. Cussigh, L. Frouin, M. Cyr, Effect of natural and accelerated carbonation on microstructure and pH of sodium carbonate alkali-activated slag, Cem. Concr. Res. 181 (2024). https://doi.org/10.1016/j.cemconres.2024.107525.

[258] E. Sassoni, S. Naidu, G.W. Scherer, The use of hydroxyapatite as a new inorganic consolidant for damaged carbonate stones, J. Cult. Herit. 12 (2011) 346–355. https://doi.org/10.1016/j.culher.2011.02.005.

[259] R. Ahmed, S. Salehi, A. Srivastava, Evaluation of hydroxyapatite-based cement for geothermal well applications, Geothermics. 104 (2022) 102462. https://doi.org/10.1016/j.geothermics.2022.102462.

[260] A. Srivastava, R. Ahmed, S. Shah, Carbonic acid resistance of hydroxyapatite based cement, Proc. - SPE Int. Symp. Oilf. Chem. 2019 (2019) 8–9. https://doi.org/10.2118/193585-ms.

[261] Y. Tang, K. Schollbach, S.R. van der Laan, W. Chen, Activation of BOF Slag with Dipotassium

Hydrogen Phosphate: Enhancing Hydration, Carbonation Resistance, and Heavy Metal Leaching (submitted), (n.d.).

[262] P. Bénard, S. Garrault, A. Nonat, C. Cau-dit-Coumes, Influence of orthophosphate ions on the dissolution of tricalcium silicate, Cem. Concr. Res. 38 (2008) 1137–1141. https://doi.org/10.1016/j.cemconres.2008.03.019.

[263] M. Bishop, S.G. Bott, A.R. Barron, A new mechanism for cement hydration inhibition: Solid-state chemistry of calcium nitrilotris(methylene)triphosphonate, Chem. Mater. 15 (2003) 3074–3088. https://doi.org/10.1021/cm0302431.

[264] Y. Zhu, Y. Liu, J. Zhang, Monitoring the hydration behavior of hardened cement paste affected by different environmental pH regimes, Front. Mater. 9 (2022) 1–13. https://doi.org/10.3389/fmats.2022.980887.

[265] P. Šiler, I. Kolářová, T. Sehnal, J. Másilko, T. Opravil, The Determination of the Influence of pH Value of Curing Conditions on Portland Cement Hydration, Procedia Eng. 151 (2016) 10–17. https://doi.org/10.1016/j.proeng.2016.07.393.

[266] H. Chen, P. Feng, S. Ye, W. Sun, The coupling effect of calcium concentration and pH on early hydration of cement, Constr. Build. Mater. 185 (2018) 391–401. https://doi.org/10.1016/j.conbuildmat.2018.07.067.

[267] G. Zhang, Q. Ren, J. He, S. Jiang, X. Cheng, Y. Yu, S. Huang, C. Zhang, M. Zhou, New understanding of early hydration of C4AF under surface vitrification, Powder Technol. 377 (2021) 372–378. https://doi.org/10.1016/j.powtec.2020.08.098.

[268] A. Cuesta, A. Ayuela, M.A.G. Aranda, Belite cements and their activation, Cem. Concr. Res. 140 (2021) 106319. https://doi.org/10.1016/j.cemconres.2020.106319.

[269] D.D. Nguyen, L.P. Devlin, P. Koshy, C.C. Sorrell, Effects of acetic acid on early hydration of Portland cement, J. Therm. Anal. Calorim. 123 (2016) 489–499. https://doi.org/10.1007/s10973-015-4942-0.

[270] F.E. Furcas, B. Lothenbach, O.B. Isgor, S. Mundra, Z. Zhang, U.M. Angst, Solubility and speciation of iron in cementitious systems, Cem. Concr. Res. 151 (2022) 106620. https://doi.org/10.1016/j.cemconres.2021.106620.

[271] E.M. Gartner, D.E. MacPhee, A physico-chemical basis for novel cementitious binders, Cem. Concr. Res. 41 (2011) 736–749. https://doi.org/10.1016/j.cemconres.2011.03.006.

[272] T. Matschei, B. Lothenbach, F.P. Glasser, The AFm phase in Portland cement, Cem. Concr. Res. 37 (2007) 118–130. https://doi.org/10.1016/j.cemconres.2006.10.010.

[273] G. Geng, R.J. Myers, Y.S. Yu, D.A. Shapiro, R. Winarski, P.E. Levitz, D.A.L. Kilcoyne, P.J.M. Monteiro, Synchrotron X-ray nanotomographic and spectromicroscopic study of the tricalcium aluminate hydration in the presence of gypsum, Cem. Concr. Res. 111 (2018) 130–137. https://doi.org/10.1016/j.cemconres.2018.06.002.

[274] L. Black, C. Breen, J. Yarwood, C.S. Deng, J. Phipps, G. Maitland, Hydration of tricalcium aluminate (C3A) in the presence and absence of gypsum - Studied by Raman spectroscopy and X-ray diffraction, J. Mater. Chem. 16 (2006) 1263–1272. https://doi.org/10.1039/b509904h.

[275] Loth, A. Blandine, M. Vincent, G. Ellis, Hydration of Belite-Ye ' elimite-Ferrite cements : thermodynamic modeling, 14th Int. Congr. Chem. Cem. (2015). https://www.researchgate.net/profile/Barbara_Lothenbach/publication/283320461_Hydration_of_Belite-Ye'elimite-Ferrite_cements_thermodynamic_modeling/links/56332e0e08aefa44c3694637.pdf%0A http://www.iccc2015beijing.org/dct/page/1.

[276] L.U.D. Tambara, M. Cheriaf, J.C. Rocha, A. Palomo, A. Fernández-Jiménez, Effect of alkalis content on calcium sulfoaluminate (CSA) cement hydration, Cem. Concr. Res. 128 (2020) 105953. https://doi.org/10.1016/j.cemconres.2019.105953.

[277] Q. Li, Z. Liu, W. Chen, B. Yuan, X. Liu, W. Chen, A novel bio-inspired bone-mimic self-healing cement paste based on hydroxyapatite formation, Cem. Concr. Compos. 104 (2019) 103357. https://doi.org/10.1016/j.cemconcomp.2019.103357.

[278] M.D. Mullen, Phosphorus in Soils - Biological Interactions, Encycl. Soils Environ. 4 (2004) 210–216. https://doi.org/10.1016/B0-12-348530-4/00161-2.

[279] D. Ectors, J. Neubauer, F. Goetz-Neunhoeffer, The hydration of synthetic brownmillerite in presence of low Ca-sulfate content and calcite monitored by quantitative in-situ-XRD and heat flow calorimetry, Cem. Concr. Res. 54 (2013) 61–68. https://doi.org/10.1016/j.cemconres.2013.08.011.

[280] A.M. Kaja, S. Melzer, H.J.H. Brouwers, Q. Yu, On the optimization of BOF slag hydration kinetics, Cem. Concr. Compos. 124 (2021) 104262. https://doi.org/10.1016/j.cemconcomp.2021.104262.

[281] K.D. Grevel, F. Bellmann, J. Majzlan, E. Dachs, A. Benisek, H.M. Ludwig, Thermodynamic data of belite polymorphs, Cem. Concr. Res. 152 (2022) 106621. https://doi.org/10.1016/j.cemconres.2021.106621.

[282] X. Jia, J. Li, P. Wang, J. Qian, M. Tang, Preparation and mechanical properties of magnesium phosphate cement for rapid construction repair in ice and snow, Constr. Build. Mater. 229 (2019) 116927. https://doi.org/10.1016/j.conbuildmat.2019.116927.

[283] B. Lothenbach, D.A. Kulik, T. Matschei, M. Balonis, L. Baquerizo, B. Dilnesa, G.D. Miron, R.J. Myers, Cemdata18: A chemical thermodynamic database for hydrated Portland cements and alkali-activated materials, Cem. Concr. Res. 115 (2019) 472–506. https://doi.org/10.1016/j.cemconres.2018.04.018.

[284] G. Sant, A. Kumar, C. Patapy, G. Le Saout, K. Scrivener, The influence of sodium and potassium hydroxide on volume changes in cementitious materials, Cem. Concr. Res. 42 (2012) 1447–1455. https://doi.org/10.1016/j.cemconres.2012.08.012.

[285] Y. Yan, S.Y. Yang, G.D. Miron, I.E. Collings, E. L'Hôpital, J. Skibsted, F. Winnefeld, K. Scrivener, B. Lothenbach, Effect of alkali hydroxide on calcium silicate hydrate (C-S-H), Cem. Concr. Res. 151 (2022). https://doi.org/10.1016/j.cemconres.2021.106636.

[286] G. Mestres, M.P. Ginebra, Novel magnesium phosphate cements with high early strength and antibacterial properties, Acta Biomater. 7 (2011) 1853–1861. https://doi.org/10.1016/j.actbio.2010.12.008.

[287] E. Wieland, G.D. Miron, B. Ma, G. Geng, B. Lothenbach, Speciation of iron(II/III) at the iron-cement interface: a review, Mater. Struct. Constr. 56 (2023). https://doi.org/10.1617/s11527-023-02115-x.

[288] P. V. Brady, J. V. Walther, Controls on silicate dissolution rates in neutral and basic pH solutions at 25°C, Geochim. Cosmochim. Acta. 53 (1989) 2823–2830. https://doi.org/10.1016/0016-7037(89)90160-9.

Abbreviations

AAMs	Alkali-activated materials
AFm	Alumina-ferric oxide-mono
AFt	Alumina-ferric oxide-tri /Ettringite
BET	Brunauer–Emmett–Teller
BOF	Basic oxygen furnace
BSE	Backscattered electrons
C_2S	Dicalcium silicate
C_3S	Tricalcium silicate
C_3A	Tricalcium aluminate
$C_4AF/C_2(A,F)$	Tetracalcium aluminoferrite
C-A-S-H	Aluminum-substituted calcium silicate hydrate
CBPCs	chemically bonded phosphate ceramics
C-RBCPs	Carbonated recycled blended cement paste powders
C-S-H	Calcium silicate hydrate
DKP	Dipotassium hydrogen phosphate
DTG	Derivative thermogravimetric
EDS/EDX	Energy dispersive X-ray spectrometry
FA	Fly ash
FTIR	Fourier-transform infrared spectroscopy
GBS/GGBS	Ground granulated blast furnace slag
HCP	Hydrated cement paste
IC	Ion chromatography
ICD	Increased carbonation degree
ICP-OES	Inductively coupled plasma atomic emission spectrometry
LDH	Layered double hydroxides
L/S	Liquid to solid ratios

LWAs	Lightweight aggregates
MKP	Monopotassium phosphate
MIP	Mercury intrusion porosimetry
M-S-H	Magnesium silicate hydrate
OPC	Ordinary Portland cement
PARC	PhAse Recognition and Characterization
QXRD	Quantitative X-ray diffraction
RBCPs	Recycled blended cement paste powders
RGP	Recycled glass powder
RH	Relative humidity
SAI	Strength activity index
SCMs	Supplementary cementitious materials
SEM	Scanning electron microscope
SF	Silica fume
SI	Spectral imaging
SQD	Soil Quality Decree
SSA	Specific surface area
TEM	Transmission electron microscope
TGA/TG	Thermogravimetric analysis
TKP	Tripotassium phosphate
w/b	Water-to-binder ratio

Nomenclatures

Roman symbols		SI unit
A	Area	m^2
C	Concentration	mg/l
d/h	Diameter	m
H	Enthalpy	kJ/mol
M	Mass	mg/g
P	Load	N
T	Temperature	°C
V	Volume	ml
W	Mass loss	%

Greek symbols		SI unit
σ	Strength	MPa
θ	Angle	°
λ	Wavelength	m
ρ	Density	g/cm^3

List of publications

- **Peer-reviewed journal papers**

[1] ***Y. Tang***, K. Schollbach, H.J.H. Brouwers, W. Chen, Effects of soluble magnesium on the structure of calcium silicate hydrate, Constr. Build. Mater. 302 (2021) 124402.

[2] ***Y. Tang***, L. Zhao, B. Li, W. Chen, Controlling the soundness of Portland cement clinker synthesized with solid wastes based on phase transition of $MgNiO_2$, Cem. Concr. Res. 157 (2022) 106832.

[3] ***Y. Tang***, G. Liu, K. Schollbach, Y. Chen, W. Chen, H.J.H. Brouwers, Re-cementation effects by carbonation and the pozzolanic reaction on LWAs produced by hydrated cement paste powder, J. Clean. Prod. 377 (2022) 134529.

[4] G. Liu, ***Y. Tang*** *(Corresponding author)*, J. Wang, Recycling and valorization of hydrated cement blends in mortars via semi-dry carbonation – The role of waste glass, granulated blast furnace slag and fly ash, Constr. Build. Mater. 401 (2023) 132987.

[5] ***Y. Tang***, Y. Li, X. Liu, W. Chen, K. Schollbach, W. Chen, Biomimetic-induced hydroxyapatite for rebar corrosion mitigation in self-healing concrete beam, J. Build. Eng. 84 (2024) 108666.

[6] ***Y. Tang***, W. Chen, Effect of magnesium on the structure and chemical composition of calcium silicate hydrate at elevated temperature, Constr. Build. Mater. 240 (2020) 117925.

[7] ***Y. Tang***, K. Schollbach, S.R. van der Laan, W. Chen, H.J.H. Brouwers, A novel BOF slag binder based on monopotassium phosphate activation, submitted.

[8] ***Y. Tang***, K. Schollbach, S. Melzer, S.R. van der Laan, W. Chen, Activation of BOF Slag with Dipotassium Hydrogen Phosphate: Enhancing Hydration, Carbonation Resistance, and Heavy Metal Leaching, submitted.

[9] ***Y. Tang***, K. Schollbach, S. Melzer, S.R. van der Laan, W. Chen, H.J.H. Brouwers, Effects of pH on hydration kinetics of phosphate activated BOF slag, under internal review.

[10] Z. Liu, ***Y. Tang*** *(Corresponding author)*, K. Schollbach, H.J.H. Brouwers, Effect of potassium citrate on hydration and strength development of ternary Portland cement blends containing calcined low-grade Dutch clay and carbonated BOF slag, under internal review.

- **Patent**

[1] ***Y. Tang***, METHOD FOR ACTIVATING BASIC OXYGEN FURNACE STEEL SLAG, WO 2024/052265 A1, 2024. (International patent).

- **Conferences**

[1] **Y. Tang**, K. Schollbach, H.J.H Brouwers. Effects of soluble magnesium on the structure of calcium silicate hydrate. The 4th International Conference on the Chemistry of Construction Materials (ICCCM 2023), 26-28 September 2022, Karlsruhe, Germany.

[2] **Y. Tang**, K. Schollbach, H.J.H Brouwers. Effects of phosphate on BOF slag hydration. The 7th International Conference of Non-Traditional Cement & Concrete (NTCC2023), 25-28 June 2023, Brno, Czech Republic.

[3] ***Y. Tang***, K. Schollbach, W. Chen, H.J.H. Brouwers, Carbonation effects on mechanical performance and microstructure of LWAs produced with hydrated cement paste powder, The 16th International Congress on the Chemistry of Cement 2023 (ICCC2023) "Further Reduction of CO2 -Emissions and Circularity in the Cement and Concrete Industry", September 18–22 2023, Bangkok, Thailand.

[4] ***Y. Tang***, Y. Li, X. Liu, W. Chen, K. Schollbach, H.J.H Brouwers. Biomimetic-Induced Hydroxyapatite for Autonomous Self-Healing in Cementitious Materials: Crack Repair and Rebar Corrosion Mitigation. The 3rd International Conference of Sustainable Building Materials (ICSBM 2023), 25-27 September 2023 Wuhan, China.

[5] ***Y. Tang***, K. Schollbach, S.R. van der Laan, H.J.H Brouwers. Enhancing hydration of BOF slag pastes through monopotassium phosphate addition. 78TH RILEM WEEK & RILEM CONFERENCE ON SMART MATERIALS AND STRUCTURES: MEETING THE MAJOR CHALLENGES OF THE 21ST CENTURY SMS 2024, 25-30 August, Toulouse, France.

- **M2i meetings and reports**

[1] ***Y. Tang***, Activation of BOF slag using potassium phosphate - phase formation and microstructure. Materials innovation institute (M2i) Cluster 6 Meeting, 21 April, 2023, Utrecht, the Netherlands.

[2] ***Y. Tang***. Enhancing BOF Slag Hydration through Phosphate Addition. Materials innovation institute (M2i) Conference, 11-12 December, 2023, Arnhem, the Netherlands.

[3] ***Y. Tang***, K. Schollbach, H.J.H Brouwers. Mitigating BOF slag-leaching of oxy-anions Vanadate, Chromate, Molybdenate. (External report for Materials innovation institute (M2i), biannual project report 2023H1)

[4] ***Y. Tang***, K. Schollbach, H.J.H Brouwers. Mitigating BOF slag-leaching of oxy-anions Vanadate, Chromate, Molybdenate. (External report for Materials innovation institute (M2i), biannual project report 2023H2)

[5] ***Y. Tang***, K. Schollbach, H.J.H Brouwers. Mitigating BOF slag-leaching of oxy-anions Vanadate, Chromate, Molybdenate. (External report for Materials innovation institute (M2i), biannual project report 2024H1)

[6] ***Y. Tang***, K. Schollbach, H.J.H Brouwers. Mitigating BOF slag-leaching of oxy-anions Vanadate, Chromate, Molybdenate. (External report for Materials innovation institute (M2i), biannual project report 2024H2)

Curriculum vitae

Yanjie Tang was born in Changzhou, Jiangsu Province, China on February 9, 1995. After finishing his primary, middle, and high school education in Changzhou, he started his studies at Wuhan University of Technology (WUT) in September 2013. In June 2017, he received his bachelor's degree majoring in Materials Science and Engineering. In September 2017, he started to study at the School of Materials Science and Engineering (WUT) as a doctoral student supervised by Prof. dr. Wei Chen. In December 2020, he continued his Ph.D. study at the Department of the Built Environment, Eindhoven University of Technology (TU/e), supported by the China Scholarship Council (CSC), under supervision of Prof. dr. ir. H.J.H. Brouwers, Prof. dr. Sieger van der Laan, and Asst. Prof. dr. Katrin Schollbach. In October 2022, he was employed at TU/e, supported by Tata Steel Europe and Materials innovation institute (M2i), the Netherlands. In March 2023, he stayed at Tata Steel Europe as a guest researcher. His research interests include the design of sustainable building materials, synthesis and characterization of aluminosilicate structures, self-healing, etc.

Bouwstenen is een publicatiereeks
van de Faculteit Bouwkunde,
Technische Universiteit Eindhoven.
Zij presenteert resultaten van
onderzoek en andere activiteiten op
het vakgebied der Bouwkunde,
uitgevoerd in het kader van deze
Faculteit.

Bouwstenen en andere proefschriften van de
TU/e zijn online beschikbaar via:
https://research.tue.nl/

Reeds verschenen in de serie
Bouwstenen

nr 1
Elan: A Computer Model for Building Energy Design: Theory and Validation
Martin H. de Wit
H.H. Driessen
R.M.M. van der Velden

nr 2
Kwaliteit, Keuzevrijheid en Kosten: Evaluatie van Experiment Klarendal, Arnhem
J. Smeets
C. le Nobel
M. Broos
J. Frenken
A. v.d. Sanden

nr 3
Crooswijk: Van 'Bijzonder' naar 'Gewoon'
Vincent Smit
Kees Noort

nr 4
Staal in de Woningbouw
Edwin J.F. Delsing

nr 5
Mathematical Theory of Stressed Skin Action in Profiled Sheeting with Various Edge Conditions
Andre W.A.M.J. van den Bogaard

nr 6
Hoe Berekenbaar en Betrouwbaar is de Coëfficiënt k in x-ksigma en x-ks?
K.B. Lub
A.J. Bosch

nr 7
Het Typologisch Gereedschap: Een Verkennende Studie Omtrent Typologie en Omtrent de Aanpak van Typologisch Onderzoek
J.H. Luiten

nr 8
Informatievoorziening en Beheerprocessen
A. Nauta
Jos Smeets (red.)
Helga Fassbinder (projectleider)
Adrie Proveniers
J. v.d. Moosdijk

nr 9
Strukturering en Verwerking van Tijdgegevens voor de Uitvoering van Bouwwerken
ir. W.F. Schaefer
P.A. Erkelens

nr 10
Stedebouw en de Vorming van een Speciale Wetenschap
K. Doevendans

nr 11
Informatica en Ondersteuning van Ruimtelijke Besluitvorming
G.G. van der Meulen

nr 12
Staal in de Woningbouw, Korrosie-Bescherming van de Begane Grondvloer
Edwin J.F. Delsing

nr 13
Een Thermisch Model voor de Berekening van Staalplaatbetonvloeren onder Brandomstandigheden
A.F. Hamerlinck

nr 14
De Wijkgedachte in Nederland: Gemeenschapsstreven in een Stedebouwkundige Context
K. Doevendans
R. Stolzenburg

nr 15
Diaphragm Effect of Trapezoidally Profiled Steel Sheets: Experimental Research into the Influence of Force Application
Andre W.A.M.J. van den Bogaard

nr 16
Versterken met Spuit-Ferrocement: Het Mechanische Gedrag van met Spuit-Ferrocement Versterkte Gewapend Betonbalken
K.B. Lubir
M.C.G. van Wanroy

nr 17
De Tractaten van Jean Nicolas Louis Durand
G. van Zeyl

nr 18
Wonen onder een Plat Dak: Drie Opstellen over Enkele Vooronderstellingen van de Stedebouw
K. Doevendans

nr 19
Supporting Decision Making Processes: A Graphical and Interactive Analysis of Multivariate Data
W. Adams

nr 20
Self-Help Building Productivity: A Method for Improving House Building by Low-Income Groups Applied to Kenya 1990-2000
P. A. Erkelens

nr 21
De Verdeling van Woningen: Een Kwestie van Onderhandelen
Vincent Smit

nr 22
Flexibiliteit en Kosten in het Ontwerpproces: Een Besluitvormingondersteunend Model
M. Prins

nr 23
Spontane Nederzettingen Begeleid: Voorwaarden en Criteria in Sri Lanka
Po Hin Thung

nr 24
Fundamentals of the Design of Bamboo Structures
Oscar Arce-Villalobos

nr 25
Concepten van de Bouwkunde
M.F.Th. Bax (red.)
H.M.G.J. Trum (red.)

nr 26
Meaning of the Site
Xiaodong Li

nr 27
Het Woonmilieu op Begrip Gebracht: Een Speurtocht naar de Betekenis van het Begrip 'Woonmilieu'
Jaap Ketelaar

nr 28
Urban Environment in Developing Countries
editors: Peter A. Erkelens
George G. van der Meulen (red.)

nr 29
Stategische Plannen voor de Stad: Onderzoek en Planning in Drie Steden
prof.dr. H. Fassbinder (red.)
H. Rikhof (red.)

nr 30
Stedebouwkunde en Stadsbestuur
Piet Beekman

nr 31
De Architectuur van Djenné: Een Onderzoek naar de Historische Stad
P.C.M. Maas

nr 32
Conjoint Experiments and Retail Planning
Harmen Oppewal

nr 33
Strukturformen Indonesischer Bautechnik: Entwicklung Methodischer Grundlagen für eine 'Konstruktive Pattern Language' in Indonesien
Heinz Frick arch. SIA

nr 34
Styles of Architectural Designing: Empirical Research on Working Styles and Personality Dispositions
Anton P.M. van Bakel

nr 35
Conjoint Choice Models for Urban Tourism Planning and Marketing
Benedict Dellaert

nr 36
Stedelijke Planvorming als Co-Produktie
Helga Fassbinder (red.)

nr 37
Design Research in the Netherlands
editors: R.M. Oxman
M.F.Th. Bax
H.H. Achten

nr 38
Communication in the Building Industry
Bauke de Vries

nr 39
Optimaal Dimensioneren van Gelaste Plaatliggers
J.B.W. Stark
F. van Pelt
L.F.M. van Gorp
B.W.E.M. van Hove

nr 40
Huisvesting en Overwinning van Armoede
P.H. Thung
P. Beekman (red.)

nr 41
Urban Habitat:
The Environment of Tomorrow
George G. van der Meulen
Peter A. Erkelens

nr 42
A Typology of Joints
John C.M. Olie

nr 43
Modeling Constraints-Based Choices for Leisure Mobility Planning
Marcus P. Stemerding

nr 44
Activity-Based Travel Demand Modeling
Dick Ettema

nr 45
Wind-Induced Pressure Fluctuations on Building Facades
Chris Geurts

nr 46
Generic Representations
Henri Achten

nr 47
Johann Santini Aichel: Architectuur en Ambiguiteit
Dirk De Meyer

nr 48
Concrete Behaviour in Multiaxial Compression
Erik van Geel

nr 49
Modelling Site Selection
Frank Witlox

nr 50
Ecolemma Model
Ferdinand Beetstra

nr 51
Conjoint Approaches to Developing Activity-Based Models
Donggen Wang

nr 52
On the Effectiveness of Ventilation
Ad Roos

nr 53
Conjoint Modeling Approaches for Residential Group preferences
Eric Molin

nr 54
Modelling Architectural Design Information by Features
Jos van Leeuwen

nr 55
A Spatial Decision Support System for the Planning of Retail and Service Facilities
Theo Arentze

nr 56
Integrated Lighting System Assistant
Ellie de Groot

nr 57
Ontwerpend Leren, Leren Ontwerpen
J.T. Boekholt

nr 58
Temporal Aspects of Theme Park Choice Behavior
Astrid Kemperman

nr 59
Ontwerp van een Geïndustrialiseerde Funderingswijze
Faas Moonen

nr 60
Merlin: A Decision Support System for Outdoor Leisure Planning
Manon van Middelkoop

nr 61
The Aura of Modernity
Jos Bosman

nr 62
Urban Form and Activity-Travel Patterns
Daniëlle Snellen

nr 63
Design Research in the Netherlands 2000
Henri Achten

nr 64
Computer Aided Dimensional Control in Building Construction
Rui Wu

nr 65
Beyond Sustainable Building
editors: Peter A. Erkelens
Sander de Jonge
August A.M. van Vliet
co-editor: Ruth J.G. Verhagen

nr 66
Das Globalrecyclingfähige Haus
Hans Löfflad

nr 67
Cool Schools for Hot Suburbs
René J. Dierkx

nr 68
A Bamboo Building Design Decision Support Tool
Fitri Mardjono

nr 69
Driving Rain on Building Envelopes
Fabien van Mook

nr 70
Heating Monumental Churches
Henk Schellen

nr 71
Van Woningverhuurder naar Aanbieder van Woongenot
Patrick Dogge

nr 72
Moisture Transfer Properties of Coated Gypsum
Emile Goossens

nr 73
Plybamboo Wall-Panels for Housing
Guillermo E. González-Beltrán

nr 74
The Future Site-Proceedings
Ger Maas
Frans van Gassel

nr 75
Radon transport in Autoclaved Aerated Concrete
Michel van der Pal

nr 76
The Reliability and Validity of Interactive Virtual Reality Computer Experiments
Amy Tan

nr 77
Measuring Housing Preferences Using Virtual Reality and Belief Networks
Maciej A. Orzechowski

nr 78
Computational Representations of Words and Associations in Architectural Design
Nicole Segers

nr 79
Measuring and Predicting Adaptation in Multidimensional Activity-Travel Patterns
Chang-Hyeon Joh

nr 80
Strategic Briefing
Fayez Al Hassan

nr 81
Well Being in Hospitals
Simona Di Cicco

nr 82
Solares Bauen: Implementierungs- und Umsetzungs-Aspekte in der Hochschulausbildung in Österreich
Gerhard Schuster

nr 83
Supporting Strategic Design of Workplace Environments with Case-Based Reasoning
Shauna Mallory-Hill

nr 84
ACCEL: A Tool for Supporting Concept Generation in the Early Design Phase
Maxim Ivashkov

nr 85
Brick-Mortar Interaction in Masonry under Compression
Ad Vermeltfoort

nr 86
Zelfredzaam Wonen
Guus van Vliet

nr 87
Een Ensemble met Grootstedelijke Allure
Jos Bosman
Hans Schippers

nr 88
On the Computation of Well-Structured Graphic Representations in Architectural Design
Henri Achten

nr 89
De Evolutie van een West-Afrikaanse Vernaculaire Architectuur
Wolf Schijns

nr 90
ROMBO Tactiek
Christoph Maria Ravesloot

nr 91
External Coupling between Building Energy Simulation and Computational Fluid Dynamics
Ery Djunaedy

nr 92
Design Research in the Netherlands 2005
editors: Henri Achten
Kees Dorst
Pieter Jan Stappers
Bauke de Vries

nr 93
Ein Modell zur Baulichen Transformation
Jalil H. Saber Zaimian

nr 94
Human Lighting Demands: Healthy Lighting in an Office Environment
Myriam Aries

nr 95
A Spatial Decision Support System for the Provision and Monitoring of Urban Greenspace
Claudia Pelizaro

nr 96
Leren Creëren
Adri Proveniers

nr 97
Simlandscape
Rob de Waard

nr 98
Design Team Communication
Ad den Otter

nr 99
Humaan-Ecologisch Georiënteerde Woningbouw
Juri Czabanowski

nr 100
Hambase
Martin de Wit

nr 101
Sound Transmission through Pipe Systems and into Building Structures
Susanne Bron-van der Jagt

nr 102
Het Bouwkundig Contrapunt
Jan Francis Boelen

nr 103
A Framework for a Multi-Agent Planning Support System
Dick Saarloos

nr 104
Bracing Steel Frames with Calcium Silicate Element Walls
Bright Mweene Ng'andu

nr 105
Naar een Nieuwe Houtskeletbouw
F.N.G. De Medts

nr 106 and 107
Niet gepubliceerd

nr 108
Geborgenheid
T.E.L. van Pinxteren

nr 109
Modelling Strategic Behaviour in Anticipation of Congestion
Qi Han

nr 110
Reflecties op het Woondomein
Fred Sanders

nr 111
On Assessment of Wind Comfort by Sand Erosion
Gábor Dezsö

nr 112
Bench Heating in Monumental Churches
Dionne Limpens-Neilen

nr 113
RE. Architecture
Ana Pereira Roders

nr 114
Toward Applicable Green Architecture
Usama El Fiky

nr 115
Knowledge Representation under Inherent Uncertainty in a Multi-Agent System for Land Use Planning
Liying Ma

nr 116
Integrated Heat Air and Moisture Modeling and Simulation
Jos van Schijndel

nr 117
Concrete Behaviour in Multiaxial Compression
J.P.W. Bongers

nr 118
The Image of the Urban Landscape
Ana Moya Pellitero

nr 119
The Self-Organizing City in Vietnam
Stephanie Geertman

nr 120
A Multi-Agent Planning Support System for Assessing Externalities of Urban Form Scenarios
Rachel Katoshevski-Cavari

nr 121
Den Schulbau Neu Denken, Fühlen und Wollen
Urs Christian Maurer-Dietrich

nr 122
Peter Eisenman Theories and Practices
Bernhard Kormoss

nr 123
User Simulation of Space Utilisation
Vincent Tabak

nr 125
In Search of a Complex System Model
Oswald Devisch

nr 126
Lighting at Work: Environmental Study of Direct Effects of Lighting Level and Spectrum on Psycho-Physiological Variables
Grazyna Górnicka

nr 127
Flanking Sound Transmission through Lightweight Framed Double Leaf Walls
Stefan Schoenwald

nr 128
Bounded Rationality and Spatio-Temporal Pedestrian Shopping Behavior
Wei Zhu

nr 129
Travel Information: Impact on Activity Travel Pattern
Zhongwei Sun

nr 130
Co-Simulation for Performance Prediction of Innovative Integrated Mechanical Energy Systems in Buildings
Marija Trčka

nr 131
Niet gepubliceerd

nr 132
Architectural Cue Model in Evacuation Simulation for Underground Space Design
Chengyu Sun

nr 133
Uncertainty and Sensitivity Analysis in Building Performance Simulation for Decision Support and Design Optimization
Christina Hopfe

nr 134
Facilitating Distributed Collaboration in the AEC/FM Sector Using Semantic Web Technologies
Jacob Beetz

nr 135
Circumferentially Adhesive Bonded Glass Panes for Bracing Steel Frame in Façades
Edwin Huveners

nr 136
Influence of Temperature on Concrete Beams Strengthened in Flexure with CFRP
Ernst-Lucas Klamer

nr 137
Sturen op Klantwaarde
Jos Smeets

nr 139
Lateral Behavior of Steel Frames with Discretely Connected Precast Concrete Infill Panels
Paul Teewen

nr 140
Integral Design Method in the Context of Sustainable Building Design
Perica Savanović

nr 141
Household Activity-Travel Behavior: Implementation of Within-Household Interactions
Renni Anggraini

nr 142
Design Research in the Netherlands 2010
Henri Achten

nr 143
Modelling Life Trajectories and Transport Mode Choice Using Bayesian Belief Networks
Marloes Verhoeven

nr 144
Assessing Construction Project Performance in Ghana
William Gyadu-Asiedu

nr 145
Empowering Seniors through Domotic Homes
Masi Mohammadi

nr 146
An Integral Design Concept for Ecological Self-Compacting Concrete
Martin Hunger

nr 147
Governing Multi-Actor Decision Processes in Dutch Industrial Area Redevelopment
Erik Blokhuis

nr 148
A Multifunctional Design Approach for Sustainable Concrete
Götz Hüsken

nr 149
Quality Monitoring in Infrastructural Design-Build Projects
Ruben Favié

nr 150
Assessment Matrix for Conservation of Valuable Timber Structures
Michael Abels

nr 151
Co-simulation of Building Energy Simulation and Computational Fluid Dynamics for Whole-Building Heat, Air and Moisture Engineering
Mohammad Mirsadeghi

nr 152
External Coupling of Building Energy Simulation and Building Element Heat, Air and Moisture Simulation
Daniel Cóstola

nr 153
Adaptive Decision Making In Multi-Stakeholder Retail Planning
Ingrid Janssen

nr 154
Landscape Generator
Kymo Slager

nr 155
Constraint Specification in Architecture
Remco Niemeijer

nr 156
A Need-Based Approach to Dynamic Activity Generation
Linda Nijland

nr 157
Modeling Office Firm Dynamics in an Agent-Based Micro Simulation Framework
Gustavo Garcia Manzato

nr 158
Lightweight Floor System for Vibration Comfort
Sander Zegers

nr 159
Aanpasbaarheid van de Draagstructuur
Roel Gijsbers

nr 160
'Village in the City' in Guangzhou, China
Yanliu Lin

nr 161
Climate Risk Assessment in Museums
Marco Martens

nr 162
Social Activity-Travel Patterns
Pauline van den Berg

nr 163
Sound Concentration Caused by Curved Surfaces
Martijn Vercammen

nr 164
Design of Environmentally Friendly Calcium Sulfate-Based Building Materials: Towards an Improved Indoor Air Quality
Qingliang Yu

nr 165
Beyond Uniform Thermal Comfort on the Effects of Non-Uniformity and Individual Physiology
Lisje Schellen

nr 166
Sustainable Residential Districts
Gaby Abdalla

nr 167
Towards a Performance Assessment Methodology using Computational Simulation for Air Distribution System Designs in Operating Rooms
Mônica do Amaral Melhado

nr 168
Strategic Decision Modeling in Brownfield Redevelopment
Brano Glumac

nr 169
Pamela: A Parking Analysis Model for Predicting Effects in Local Areas
Peter van der Waerden

nr 170
A Vision Driven Wayfinding Simulation-System Based on the Architectural Features Perceived in the Office Environment
Qunli Chen

nr 171
Measuring Mental Representations Underlying Activity-Travel Choices
Oliver Horeni

nr 172
Modelling the Effects of Social Networks on Activity and Travel Behaviour
Nicole Ronald

nr 173
Uncertainty Propagation and Sensitivity Analysis Techniques in Building Performance Simulation to Support Conceptual Building and System Design
Christian Struck

nr 174
Numerical Modeling of Micro-Scale Wind-Induced Pollutant Dispersion in the Built Environment
Pierre Gousseau

nr 175
Modeling Recreation Choices over the Family Lifecycle
Anna Beatriz Grigolon

nr 176
Experimental and Numerical Analysis of Mixing Ventilation at Laminar, Transitional and Turbulent Slot Reynolds Numbers
Twan van Hooff

nr 177
Collaborative Design Support: Workshops to Stimulate Interaction and Knowledge Exchange Between Practitioners
Emile M.C.J. Quanjel

nr 178
Future-Proof Platforms for Aging-in-Place
Michiel Brink

nr 179
Motivate: A Context-Aware Mobile Application for Physical Activity Promotion
Yuzhong Lin

nr 180
Experience the City: Analysis of Space-Time Behaviour and Spatial Learning
Anastasia Moiseeva

nr 181
Unbonded Post-Tensioned Shear Walls of Calcium Silicate Element Masonry
Lex van der Meer

nr 182
Construction and Demolition Waste Recycling into Innovative Building Materials for Sustainable Construction in Tanzania
Mwita M. Sabai

nr 183
Durability of Concrete with Emphasis on Chloride Migration
Przemysław Spiesz

nr 184
Computational Modeling of Urban Wind Flow and Natural Ventilation Potential of Buildings
Rubina Ramponi

nr 185
A Distributed Dynamic Simulation Mechanism for Buildings Automation and Control Systems
Azzedine Yahiaoui

nr 186
Modeling Cognitive Learning of Urban Networks in Daily Activity-Travel Behavior
Şehnaz Cenani Durmazoğlu

nr 187
Functionality and Adaptability of Design Solutions for Public Apartment Buildings in Ghana
Stephen Agyefi-Mensah

nr 188
A Construction Waste Generation Model for Developing Countries
Lilliana Abarca-Guerrero

nr 189
Synchronizing Networks: The Modeling of Supernetworks for Activity-Travel Behavior
Feixiong Liao

nr 190
Time and Money Allocation Decisions in Out-of-Home Leisure Activity Choices
Gamze Zeynep Dane

nr 191
How to Measure Added Value of CRE and Building Design
Rianne Appel-Meulenbroek

nr 192
Secondary Materials in Cement-Based Products: Treatment, Modeling and Environmental Interaction
Miruna Florea

nr 193
Concepts for the Robustness Improvement of Self-Compacting Concrete: Effects of Admixtures and Mixture Components on the Rheology and Early Hydration at Varying Temperatures
Wolfram Schmidt

nr 194
Modelling and Simulation of Virtual Natural Lighting Solutions in Buildings
Rizki A. Mangkuto

nr 195
Nano-Silica Production at Low Temperatures from the Dissolution of Olivine - Synthesis, Tailoring and Modelling
Alberto Lazaro Garcia

nr 196
Building Energy Simulation Based Assessment of Industrial Halls for Design Support
Bruno Lee

nr 197
Computational Performance Prediction of the Potential of Hybrid Adaptable Thermal Storage Concepts for Lightweight Low-Energy Houses
Pieter-Jan Hoes

nr 198
Application of Nano-Silica in Concrete
George Quercia Bianchi

nr 199
Dynamics of Social Networks and Activity Travel Behaviour
Fariya Sharmeen

nr 200
Building Structural Design Generation and Optimisation including Spatial Modification
Juan Manuel Davila Delgado

nr 201
Hydration and Thermal Decomposition of Cement/Calcium-Sulphate Based Materials
Ariën de Korte

nr 202
Republiek van Beelden:
De Politieke Werkingen van het Ontwerp in Regionale Planvorming
Bart de Zwart

nr 203
Effects of Energy Price Increases on Individual Activity-Travel Repertoires and Energy Consumption
Dujuan Yang

nr 204
Geometry and Ventilation:
Evaluation of the Leeward Sawtooth Roof Potential in the Natural Ventilation of Buildings
Jorge Isaac Perén Montero

nr 205
Computational Modelling of Evaporative Cooling as a Climate Change Adaptation Measure at the Spatial Scale of Buildings and Streets
Hamid Montazeri

nr 206
Local Buckling of Aluminium Beams in Fire Conditions
Ronald van der Meulen

nr 207
Historic Urban Landscapes:
Framing the Integration of Urban and Heritage Planning in Multilevel Governance
Loes Veldpaus

nr 208
Sustainable Transformation of the Cities:
Urban Design Pragmatics to Achieve a Sustainable City
Ernesto Antonio Zumelzu Scheel

nr 209
Development of Sustainable Protective Ultra-High Performance Fibre Reinforced Concrete (UHPFRC):
Design, Assessment and Modeling
Rui Yu

nr 210
Uncertainty in Modeling Activity-Travel Demand in Complex Uban Systems
Soora Rasouli

nr 211
Simulation-based Performance Assessment of Climate Adaptive Greenhouse Shells
Chul-sung Lee

nr 212
Green Cities:
Modelling the Spatial Transformation of the Urban Environment using Renewable Energy Technologies
Saleh Mohammadi

nr 213
A Bounded Rationality Model of Short and Long-Term Dynamics of Activity-Travel Behavior
Ifigeneia Psarra

nr 214
Effects of Pricing Strategies on Dynamic Repertoires of Activity-Travel Behaviour
Elaheh Khademi

nr 215
Handstorm Principles for Creative and Collaborative Working
Frans van Gassel

nr 216
Light Conditions in Nursing Homes: Visual Comfort and Visual Functioning of Residents
Marianne M. Sinoo

nr 217
Woonsporen: De Sociale en Ruimtelijke Biografie van een Stedelijk Bouwblok in de Amsterdamse Transvaalbuurt
Hüseyin Hüsnü Yegenoglu

nr 218
Studies on User Control in Ambient Intelligent Systems
Berent Willem Meerbeek

nr 219
Daily Livings in a Smart Home: Users' Living Preference Modeling of Smart Homes
Erfaneh Allameh

nr 220
Smart Home Design: Spatial Preference Modeling of Smart Homes
Mohammadali Heidari Jozam

nr 221
Wonen: Discoursen, Praktijken, Perspectieven
Jos Smeets

nr 222
Personal Control over Indoor Climate in Offices: Impact on Comfort, Health and Productivity
Atze Christiaan Boerstra

nr 223
Personalized Route Finding in Multimodal Transportation Networks
Jianwe Zhang

nr 224
The Design of an Adaptive Healing Room for Stroke Patients
Elke Daemen

nr 225
Experimental and Numerical Analysis of Climate Change Induced Risks to Historic Buildings and Collections
Zara Huijbregts

nr 226
Wind Flow Modeling in Urban Areas Through Experimental and Numerical Techniques
Alessio Ricci

nr 227
Clever Climate Control for Culture: Energy Efficient Indoor Climate Control Strategies for Museums Respecting Collection Preservation and Thermal Comfort of Visitors
Rick Kramer

nr 228
Fatigue Life Estimation of Metal Structures Based on Damage Modeling
Sarmediran Silitonga

nr 229
A multi-agents and occupancy based strategy for energy management and process control on the room-level
Timilehin Moses Labeodan

nr 230
Environmental assessment of Building Integrated Photovoltaics: Numerical and Experimental Carrying Capacity Based Approach
Michiel Ritzen

nr 231
Performance of Admixture and Secondary Minerals in Alkali Activated Concrete: Sustaining a Concrete Future
Arno Keulen

nr 232
World Heritage Cities and Sustainable Urban Development:
Bridging Global and Local Levels in Monitoring the Sustainable Urban Development of World Heritage Cities
Paloma C. Guzman Molina

nr 233
Stage Acoustics and Sound Exposure in Performance and Rehearsal Spaces for Orchestras:
Methods for Physical Measurements
Remy Wenmaekers

nr 234
Municipal Solid Waste Incineration (MSWI) Bottom Ash:
From Waste to Value Characterization, Treatments and Application
Pei Tang

nr 235
Large Eddy Simulations Applied to Wind Loading and Pollutant Dispersion
Mattia Ricci

nr 236
Alkali Activated Slag-Fly Ash Binders: Design, Modeling and Application
Xu Gao

nr 237
Sodium Carbonate Activated Slag: Reaction Analysis, Microstructural Modification & Engineering Application
Bo Yuan

nr 238
Shopping Behavior in Malls
Widiyani

nr 239
Smart Grid-Building Energy Interactions: Demand Side Power Flexibility in Office Buildings
Kennedy Otieno Aduda

nr 240
Modeling Taxis Dynamic Behavior in Uncertain Urban Environments
Zheng Zhong

nr 241
Gap-Theoretical Analyses of Residential Satisfaction and Intention to Move
Wen Jiang

nr 242
Travel Satisfaction and Subjective Well-Being: A Behavioral Modeling Perspective
Yanan Gao

nr 243
Building Energy Modelling to Support the Commissioning of Holistic Data Centre Operation
Vojtech Zavrel

nr 244
Regret-Based Travel Behavior Modeling: An Extended Framework
Sunghoon Jang

nr 245
Towards Robust Low-Energy Houses: A Computational Approach for Performance Robustness Assessment using Scenario Analysis
Rajesh Reddy Kotireddy

nr 246
Development of sustainable and functionalized inorganic binder-biofiber composites
Guillaume Doudart de la Grée

nr 247
A Multiscale Analysis of the Urban Heat Island Effect: From City Averaged Temperatures to the Energy Demand of Individual Buildings
Yasin Toparlar

nr 248
Design Method for Adaptive Daylight Systems for buildings covered by large (span) roofs
Florian Heinzelmann

nr 249
Hardening, high-temperature resistance and acid resistance of one-part geopolymers
Patrick Sturm

nr 250
Effects of the built environment on dynamic repertoires of activity-travel behaviour
Aida Pontes de Aquino

nr 251
Modeling for auralization of urban environments: Incorporation of directivity in sound propagation and analysis of a framework for auralizing a car pass-by
Fotis Georgiou

nr 252
Wind Loads on Heliostats and Photovoltaic Trackers
Andreas Pfahl

nr 253
Approaches for computational performance optimization of innovative adaptive façade concepts
Roel Loonen

nr 254
Multi-scale FEM-DEM Model for Granular Materials: Micro-scale boundary conditions, Statics, and Dynamics
Jiadun Liu

nr 255
Bending Moment - Shear Force Interaction of Rolled I-Shaped Steel Sections
Rianne Willie Adriana Dekker

nr 256
Paralympic tandem cycling and handcycling: Computational and wind tunnel analysis of aerodynamic performance
Paul Fionn Mannion

nr 257
Experimental characterization and numerical modelling of 3D printed concrete: Controlling structural behaviour in the fresh and hardened state
Robert Johannes Maria Wolfs

nr 258
Requirement checking in the building industry: Enabling modularized and extensible requirement checking systems based on semantic web technologies
Chi Zhang

nr 259
A Sustainable Industrial Site Redevelopment Planning Support System
Tong Wang

nr 260
Efficient storage and retrieval of detailed building models: Multi-disciplinary and long-term use of geometric and semantic construction information
Thomas Ferdinand Krijnen

nr 261
The users' value of business center concepts for knowledge sharing and networking behavior within and between organizations
Minou Weijs-Perrée

nr 262
Characterization and improvement of aerodynamic performance of vertical axis wind turbines using computational fluid dynamics (CFD)
Abdolrahim Rezaeiha

nr 263
In-situ characterization of the acoustic impedance of vegetated roofs
Chang Liu

nr 264
Occupancy-based lighting control: Developing an energy saving strategy that ensures office workers' comfort
Christel de Bakker

nr 265
Stakeholders-Oriented Spatial Decision Support System
Cahyono Susetyo

nr 266
Climate-induced damage in oak museum objects
Rianne Aleida Luimes

nr 267
Towards individual thermal comfort: Model predictive personalized control of heating systems
Katarina Katic

nr 268
Modelling and Measuring Quality of Urban Life: Housing, Neighborhood, Transport and Job
Lida Aminian

nr 269
Optimization of an aquifer thermal energy storage system through integrated modelling of aquifer, HVAC systems and building
Basar Bozkaya

nr 270
Numerical modeling for urban sound propagation: developments in wave-based and energy-based methods
Raúl Pagán Muñoz

nr 271
Lighting in multi-user office environments: improving employee wellbeing through personal control
Sanae van der Vleuten-Chraibi

nr 272
A strategy for fit-for-purpose occupant behavior modelling in building energy and comfort performance simulation
Isabella I. Gaetani dell'Aquila d'Aragona

nr 273
Een architectuurhistorische waardestelling van naoorlogse woonwijken in Nederland: Het voorbeeld van de Westelijke Tuinsteden in Amsterdam
Eleonore Henriette Marie Mens

nr 274
Job-Housing Co-Dependent Mobility Decisions in Life Trajectories
Jia Guo

nr 275
A user-oriented focus to create healthcare facilities: decision making on strategic values
Emilia Rosalia Catharina Maria Huisman

nr 276
Dynamics of plane impinging jets at moderate Reynolds numbers – with applications to air curtains
Adelya Khayrullina

nr 277
Valorization of Municipal Solid Waste Incineration Bottom Ash - Chemical Nature, Leachability and Treatments of Hazardous Elements
Qadeer Alam

nr 278
Treatments and valorization of MSWI bottom ash - application in cement-based materials
Veronica Caprai

nr 279
Personal lighting conditions of office workers - input for intelligent systems to optimize subjective alertness
Juliëtte van Duijnhoven

nr 280
Social influence effects in tourism travel: air trip itinerary and destination choices
Xiaofeng Pan

nr 281
Advancing Post-War Housing: Integrating Heritage Impact, Environmental Impact, Hygrothermal Risk and Costs in Renovation Design Decisions
Lisanne Claartje Havinga

nr 282
Impact resistant ultra-high performance fibre reinforced concrete: materials, components and properties
Peipeng Li

nr 283
Demand-driven Science Parks: The Perceived Benefits and Trade-offs of Tenant Firms with regard to Science Park Attributes
Wei Keat Benny Ng

nr 284
Raise the lantern; how light can help to maintain a healthy and safe hospital environment focusing on nurses
Maria Petronella Johanna Aarts

nr 285
Modelling Learning and Dynamic Route and Parking Choice Behaviour under Uncertainty
Elaine Cristina Schneider de Carvalho

nr 286
Identifying indoor local microclimates for safekeeping of cultural heritage
Karin Kompatscher

nr 287
Probabilistic modeling of fatigue resistance for welded and riveted bridge details. Resistance models and estimation of uncertainty.
Davide Leonetti

nr 288
Performance of Layered UHPFRC under Static and Dynamic Loads: Effects of steel fibers, coarse aggregates and layered structures
Yangyueye Cao

nr 289
Photocatalytic abatement of the nitrogen oxide pollution: synthesis, application and long-term evaluation of titania-silica composites
Yuri Hendrix

nr 290
Assessing knowledge adoption in post-disaster reconstruction: Understanding the impact of hazard-resistant construction knowledge on reconstruction processes of self-recovering communities in Nepal and the Philippines
Eefje Hendriks

nr 291
Locating electric vehicle charging stations: A multi-agent based dynamic simulation
Seheon Kim

nr 292
De invloed van Lean Management op de beheersing van het bouwproces
Wim van den Bouwhuijsen

nr 293
Neighborhood Environment and Physical Activity of Older Adults
Zhengying Liu

nr 294
Practical and continuous luminance distribution measurements for lighting quality
Thijs Willem Kruisselbrink

nr 295
Auditory Distraction in Open-Plan Study Environments in Higher Education
Pieternella Elizabeth Braat-Eggen

nr 296
Exploring the effect of the sound environment on nurses' task performance: an applied approach focusing on prospective memory
Jikke Reinten

nr 297
Design and performance of water resistant cementitious materials– Mechanisms, evaluation and applications
Zhengyao Qu

nr 298
Design Optimization of Seasonal Thermal Energy Storage Integrated District Heating and Cooling System: A Modeling and Simulation Approach
Luyi Xu

nr 299
Land use and transport: Integrated approaches for planning and management
Zhongqi Wang

nr 300
Multi-disciplinary optimization of building spatial designs: co-evolutionary design process simulations, evolutionary algorithms, hybrid approaches
Sjonnie Boonstra

nr 301
Modeling the spatial and temporal relation between urban land use, temperature, and energy demand
Hung-Chu Chen

nr 302
Seismic retrofitting of masonry walls with flexible deep mounted CFRP strips
Ömer Serhat Türkmen

nr 303
Coupled Aerostructural Shape and Topology Optimization of Horizontal-Axis Wind Turbine Rotor Blades
Zhijun Wang

nr 304
Valorization of Recycled Waste Glass and Converter Steel Slag as Ingredients for Building Materials: Hydration and Carbonation Studies
Gang Liu

nr 305
Low-Carbon City Development based on Land Use Planning
Gengzhe Wang

nr 306
Sustainable energy transition scenario analysis for buildings and neighborhoods - Data driven optimization
Shalika Saubhagya Wickramarachchi Walker

nr 307
In-between living and manufactured: an exploratory study on biobuilding components for building design
Berrak Kirbas Akyurek

nr 308
Development of alternative cementitious binders and functionalized materials: design, performance and durability
Anna Monika Kaja

nr 309
Development a morphological approach for interactive kinetic façade design: Improving multiple occupants' visual comfort
Seyed Morteza Hosseini

nr 310
PV in urban context: modeling and simulation strategies for analyzing the performance of shaded PV systems
Ádám Bognár

nr 311
Life Trajectory, Household Car Ownership Dynamics and Home Renewable Energy Equipment Adoption
Gaofeng Gu

nr 312
Impact of Street-Scale Built Environment on Walking/Cycling around Metro Stations
Yanan Liu

nr 313
Advances in Urban Traffic Network Equilibrium Models and Algorithms
Dong Wang

nr 314
Development of an uncertainty analysis framework for model-based consequential life cycle assessment: application to activity-based modelling and life cycle assessment of multimodal mobility
Paul Martin Baustert

nr 315
Variable stiffness and damping structural joints for semi-active vibration control
Qinyu Wang

nr 316
Understanding Carsharing-Facilitating Neighborhood Preferences
Juan Wang

nr 317
Dynamic alignment of Corporate Real Estate to business strategies: An empirical analysis using historical data and in-depth modelling of decision making
Howard Cooke

nr 318
Local People Matter: Towards participatory governance of cultural heritage in China
Ji Li

nr 319
Walkability and Walkable Healthy Neighborhoods
Bojing Liao

nr 320
Light directionality in design of healthy offices: exploration of two methods
Parisa Khademagha

nr 321
Room acoustic modeling with the time-domain discontinuous Galerkin method
Huiqing Wang

nr 322
Sustainable insulating lightweight materials for enhancing indoor building performance: miscanthus, aerogel and nano-silica
Yuxuan Chen

nr 323
Computational analysis of the impact of façade geometrical details on wind flow and pollutant dispersion
Xing Zheng

nr 324
Analysis of urban wind energy potential around high-rise buildings in close proximity using computational fluid dynamics
Yu-Hsuan Jang

nr 325
A new approach to automated energy performance and fault detection and diagnosis of HVAC systems: Development of the 4S3F method
Arie Taal

nr 326
Innovative Admixtures for Modifying Viscosity and Volume Change of Cement Composites
Hossein Karimi

nr 327
Towards houses with low grid dependency: A simulation-based design optimization approach
Zahra Mohammadi

nr 328
Activation of demand flexibility for heating systems in buildings: Real-life demonstration of optimal control for power-to-heat and thermal energy storage
Christian Finck

nr 329
A computational framework for analysis and optimisation of automated solar shading systems
Samuel B. de Vries

nr 330
Challenges and potential solutions for cultural heritage adaptive reuse: a comparative study employing the Historic Urban Landscape approach
Nadia Pintossi

nr 331
Shared control in office lighting systems
Tatiana Aleksandrovna Lashina

nr 332
Comfort in Urban Public Spaces
You Peng

nr 333
Numerical modelling of metal soap formation in historical oil paintings
Gerardus Johannes Anna Maria Eumelen

nr 334
A transdisciplinary decision-making approach to food-water-energy nexus: A guide towards sustainable development
Maryam Ghodsvali

nr 335
Numerical modelling of transient low-frequency sound propagation and vibration in buildings
Indra Sihar

nr 336
Characterization of impact sound from lightweight joist floors
Yi Qin

nr 337
Cities for Children: Supporting Children and Caregivers in Participatory Urban Planning
Özlemnur Ataol

nr 338
Engaging the unengaged: Exploring citizen participation in nature-based solutions in China
Li Dai

nr 339
Municipal Solid Waste Incineration Residues: analysis, treatments, and applications
Ekaterina Loginova

nr 340
Enhancing the Uptake of Nature-Based Solutions in Urban Settings: An Information Systems Approach
Shahryar Ershad Sarabi

nr 341
Work Schedule Arrangements in Two-Adult Households with Children
Bilin Han

nr 342
Increasing awareness of urban cultural heritage using digital technologies: empirical design and analysis of a new multi-media web platform
Benshuo Wang

nr 343
Mechanical and physical properties of fibre-cement composites using alternative natural fibres
Katerina Kochova

nr 344
Numerical and experimental investigation of urban microclimate in a real compact heterogeneous urban area
Nestoras Antoniou

nr 345
Examining in-class activities to facilitate academic achievement in higher education: A framework for optimal indoor environmental conditions
Henk W. Brink

nr 346
High-temperature resistant geopolymers: composition, microstructure and performance
Kinga Malgorzata Klima

nr 347
Individual and household decision-making in shared parking
Qianqian Yan

nr 348
In-situ formation of LDHs in Alkali activated binders
Tao Liu

nr 349
Condition assessment of concrete sewer pipes through an integrated experimental-numerical approach
Irene C. Scheperboer

nr 350
In situ PU-based characterization of sound absorbing materials for room acoustic modeling purposes
Baltazar Briere de La Hosseraye

nr 351
Uncertainty analysis and management in building energy data mining: A bottom-up approach considering the temporal and spatial aspect of data
Waqas Khan

nr 352
Personalized Heating Control Systems to improve thermal comfort and reduce energy consumption
Michal Veselý

nr 353
Restorative value of the urban greenscape: Urban residential streets as restorative environments
Robert P. van Dongen

nr 354
Urban ventilation and the compact Mediterranean city: numerical investigations of the dynamic relationships between density, morphology and wind flow
Olga Palusci

nr 355
Data science for buildings: a multi-scale approach bridging occupants to smart-city energy planning
Julien Leprince

nr 356
Class Association Rule Models for Predicting Transportation Mode Choice
Jiajia Zhang

nr 357
Acceptance and use of autonomous vehicles
Zhihui Tian

nr 358
Consumer Acceptance of Crowdshipping Services
Chenyu Wang

nr 359
Determinants of habitual participation in leisure-time physical activity and active travel in life trajectories
Xiaoyue Chen

nr 360
Analysis of Citizens' Motivation and Intention Using Modern Information Technology in Urban Planning Public Participation
Wenshu Li

nr 361
Linking smart and physical port cities. Port-city interface areas: from obsolete/isolated to smart environments.
Mercè de Miguel Capdevila

nr 362
Assessment and improvement of indoor thermal comfort and energy demand of Chinese heritage apartment buildings under climate change
Muxi Lei

nr 363
Indoor airflow and heat transfer in a cross-ventilated generic building: wind tunnel experiments and computational fluid dynamics analyses
Katarina Kosutova

nr 364
A Robotic Construction Simulation Platform for Light-weight Prefabricated Structures.
Aiyu Zhu

nr 365
Lifetime prediction of vertical-axis wind turbines based on CFD simulations and high-cycle fatigue modeling
Feiyu Geng

nr 366
Computational modeling of convective heat transfer at building surfaces
Samy Iousef

nr 367
Numerical simulation of the atmospheric boundary layer with application to natural ventilation
Raffaele Vasaturo

nr 368
Bouwen zonder scrupules. De Nederlandse bouwnijverheid tijdens de bezetting en de eerste jaren van wederopbouw (1940-1950)
Geert-Jan Mellink

nr 369
Factors Promoting a Positive Experienced Neighborhood Public Space--A Virtual Environment-based analysis.
Yuwen Zhao

nr 370
Place quality making in high-speed railway station areas: Devising place quality indicators for urban design, beyond the transport-land use divide
Jinglun Du

nr 371
Sustainable Bio-based Adsorptive Concrete for Phosphorus Removal
Fan Wu

nr 372
The physical workplace as a resource for mental health: A salutogenic approach to a mentally healthy workplace design at home and at the office
Lisanne Bergefurt

nr 373
High-end application of basic oxygen furnace steel slag as sustainable building materials
Muhammad Jawad Ahmed

nr 374
Energy-Efficient Urban Rail Transit Operations: Models, Algorithms, and Applications
Kang Huang

nr 375
Household Energy Efficiency Adoption: Influencing Factors and Diffusion Interventions
Hua Du

nr 376
High-temperature resistant geopolymer-based materials out of industrial residuals.
Yan Luo

nr 377
A Simulation Approach Exploring the Impacts of Land Use Variables on Travel Behavior.
Xiaoming Lyu

nr 378
Understanding and modelling individual preferences for Mobility as a Service
Valeria Caiati

nr 379
Linking the physical and digital built environment - Enabling occupant-centric decision-making using cross-domain semantic digital twins
Alex Donkers

nr 380
Indoor Air Quality in Daycare Centers: Assessing and Mitigating Indoor Exposure on Young Children
Hailin Zheng

nr 381
A Data-Driven Approach to Understanding Visitors' Behavior to Reduce the Negative Effects of Tourism in Historical Cities
Sezi Karayazi

nr 382
Wind effects on internal depressurization for asbestos abatement
Anjali Radhakrishnan Jayakumari

nr 383
Spatiotemporal Graph Convolutional Neural Network for Robust and Accurate Traffic Flow Prediction
Yutian Liu

nr 384
Photo-responsive functional aluminosilicate cementitious materials - Design, Performance and Durability
Daoru Liu

nr 385
High-end applications of basic oxygen furnace slag as a cementitious binder. Phase Assemblage, Mechanical & Chemical Activation, Composites Application
Winnie Franco Santos

nr 386
Towards improved performance modelling of distributed PV systems in the built environment
Bin Meng

nr 387
Development of sustainable insulation materials. Design, performance and applications
Alex Koh Chuen Hon

nr 388
Simulations of Sandwich Panel Systems under Fire: Two-Scale Methods for Connections, Pyrolysis for Insulation, Experimental Validations
Qingfeng Xu

nr 389
Long-term Mechanical Performance of the Flax Fiber Reinforced Polymer Composites Considering the Environmental Effects
Bowen Xu

nr 390
Quality engineering and control for digital fabrication with concrete
Derk Bos

nr 391
Structural Engineering of 3D Printed Strain Hardening Cementitious Composites. From micro-scale analysis to application
Karsten Nefs

nr 392
Children's Outdoor Play in the Digital Age; The Role of Digital Interventions in Stimulating Children's Outdoor Play Behavior
Avin Khalilollahi

nr 393
Biophilic design and integrating nature in architecture: Guidelines for three-dimensional green spaces to innovate architectural typologies and create impact for sustainability
Weijie Zhong

nr 394
Crafting Smart Homes: Innovative Design Strategies to Enhance Housing Quality for Ageing Well
Chuan Ma

nr 395
Valorization of Natural Fibers and Municipal Solid Waste Incineration (MSWI) Bottom Ash in Building Composite
Helong Song

nr 396
Digital Placemaking and Healthy Ageing. A user-centric approach for empowering senior citizens in inclusive decision-making of future healthy ageing neighbourhoods
Peyman Najafi

nr 397
Optimizing aerodynamic performance in cycling. - Analyses of drafting strategies and skinsuit design through computational simulations and wind tunnel experiments
Thijs Druenen

nr 398
A simulation-based analytical framework for heat battery in residential use cases.
Shuwei Wang

This thesis addresses the environmental impact of the cement and concrete industry by focusing on reducing CO_2 emissions and minimizing the consumption of raw materials and energy. Clinker production, a significant source of these issues, is targeted through innovative strategies such as using low-grade limestone, partially replacing clinker with supplementary cementitious materials (SCMs), and fully substituting it with cement-free binders–offering a more sustainable approach to construction. Additionally, replacing natural aggregates with those derived from industrial wastes provides another avenue for reducing emissions. Given the unique properties of various industrial wastes, tailored valorization strategies are essential to unlock their potential as sustainable construction materials.

The thesis explores key solutions to these challenges. First, it examines the structure of calcium silicate hydrate (C-S-H) modified by magnesium, which could be introduced through low-grade limestone. Second, it investigates the valorization of concrete waste as artificial aggregates or SCMs through carbonation, contributing to waste reduction. Finally, the research develops basic oxygen furnace (BOF) slag as a cement-free binder via chemical activation, offering a transformative solution for traditional cement replacement. These approaches advance efforts toward low-carbon, sustainable construction and support global goals for circular economy.

DEPARTMENT OF THE BUILT ENVIRONMENT

TU/e EINDHOVEN UNIVERSITY OF TECHNOLOGY